



Experimental and theoretical investigation of a radiative heat pipe ceiling for uniform cooling and heat recovery in a ceramic roller hearth kiln

A thesis submitted for the degree of Doctor of Philosophy (PhD)

By:

Bertrand Delpech

Department of Mechanical, Aerospace and Civil Engineering College of Engineering,
Design and Physical Sciences
Brunel University London

July 2020

Abstract

The ceramics manufacturing sector is among the most energy intensive industry in Europe. The greenhouse gas generated by this industry represents a large amount of the greenhouse gas generated across the industrials sectors. During the tile manufacturing process, the slow cooling of the tile is among the most important step as the strength and lifespan of the tile will be determined by the quality of cooling.

The main objective of this study is to investigate and apply a radiative heat pipe ceiling solution that will provide a uniform tile surface temperature across the kiln section to reduce the internal stresses of the tile and to recover heat from the slow cooling process. To provide a uniform tile temperature, a heat pipe with a near horizontal evaporator was proposed. In a first approach, a cylindrical single heat pipe with a near horizontal evaporator section and cooling water jacket was tested. The single heat pipe was exposed to a radiative ceramic heat source in a fully instrumented laboratory kiln. The system was studied at different filling ratios to assess the effect of the filling ratio on the heat transfer rate, the heat pipe thermal resistance, and the heat pipe temperatures. The geyser boiling occurring at low heat flux was discussed and analysed to avoid this phenomenon in the full-scale system.

By using the experience gathered during the single heat pipe test, module heat pipes were proposed with different evaporator heat transfer area. The module heat pipes were composed of a near horizontal evaporator section with different number of parallel pipes connected to a bottom collector and a shell and tube header. The impact of the change in the evaporator surface area by changing the number of evaporator pipes for the same overall heat pipe dimensions on the heat transfer rate, the heat pipe thermal resistances and the heat pipe working temperatures were discussed. The impact of the filling ratio was assessed to verify the assumptions made in the single heat pipe study. The systems were tested at flow rates from 5 L/min to 20 L/min and heater temperatures from 200 °C and 500 °C.

A theoretical modelling tool was developed using VBA to predict the performance of the single heat pipe and the module heat pipes. The modelling tool was built based on an electrical analogy approach, considering the different thermal resistance within the system. Each thermal resistance was based on correlations validated by the experimental data. The modelling tool was then used to predict the heat transfer rate for all the tests carried out in this study. The prediction obtained was within 10%. The modelling tool predicted the impact of the heat pipe ceiling on the tile temperature. The potential heat recovered by the system was predicted to be 1277 MWh per year.

Declaration

No section of this PhD thesis has been submitted in any other application for a degree or qualification at Brunel University or other university or Institute of learning

Acknowledgement

Firstly, I would like to express my sincere gratitude to my supervisor, Prof. Hussam Jouhara for presenting the opportunity of taking on a PhD at Brunel University. The support and guidance provided throughout my study, leading to this thesis have been invaluable. The experience and knowledge learnt on Heat Pipe Technology and Heat Transfer is priceless and no doubt it will help me overcome challenges in the future.

I would like to thank Prof. Brian Axcell for his valuable advice and support.

Similarly, I cannot thank enough my fellow peers from the research team; Dr. Sulaiman Almahmoud, Dr. Amisha Chauhan for their support and encouragement. I am very grateful to Darem Ahmad and Nicolas Serey for their assistance in the laboratory.

Thank you Lujean Ahmad for putting up with me as your desk neighbour over the years and appreciate your patience and kindness.

Last but not the least, I am ever so thankful towards my parents and my brothers for their tremendous emotional support provided during this period; also special thanks to my partner who kept me motivated over these challenging years.

Publications

Published Journal paper

- [1] Delpech B, Axcell B, Jouhara H. Experimental investigation of a radiative heat pipe for waste heat recovery in a ceramics kiln. *Energy* 2019;170:636–51.
<https://doi.org/10.1016/j.energy.2018.12.133>.
- [2] Delpech B, Milani M, Montorsi L, Boscardin D, Chauhan A, Almahmoud S, et al. Energy efficiency enhancement and waste heat recovery in industrial processes by means of the heat pipe technology: Case of the ceramic industry. *Energy* 2018;158:656–65. <https://doi.org/10.1016/j.energy.2018.06.041>.
- [3] Jouhara H, Khordehgah N, Almahmoud S, Delpech B, Chauhan A, Tassou SA. Waste heat recovery technologies and applications. *Therm Sci Eng Prog* 2018;6:268–89.
<https://doi.org/10.1016/j.tsep.2018.04.017>.
- [4] Jouhara H, Almahmoud S, Chauhan A, Delpech B, Nannou T, Tassou SA, et al. Experimental investigation on a flat heat pipe heat exchanger for waste heat recovery in steel industry. *Energy Procedia* 2017;123:329–34.
<https://doi.org/10.1016/j.egypro.2017.07.262>.
- [5] Jouhara H, Almahmoud S, Chauhan A, Delpech B, Bianchi G, Tassou SA, et al. Experimental and theoretical investigation of a flat heat pipe heat exchanger for waste heat recovery in the steel industry. *Energy* 2017;141:1928–39.
<https://doi.org/10.1016/j.energy.2017.10.142>.

International conferences

SEEP 2018 - 11th international conference on sustainable energy & environmental protection

Radiative heat pipe for waste heat recovery in ceramics kiln

Award for the best paper in SEEP 2018

SEEP 2017 - 10th International Conference on Sustainable Energy & Environmental Protection

Erva mate drying using Heat pipe technology

ASEE 2017 - International conference on advances in energy systems and environmental engineering

Waste heat recovery from exhaust in ceramics industry

ASEE 2019 - International conference on advances in energy systems and environmental engineering

Experimental investigation of a Heat Pipe Heat Exchanger in the ceramics industry

HEXAG 2018 – HEAT EXCHANGER ACTION GROUP

Experimental investigation of a radiative heat pipe for waste heat recovery in ceramics industry

HEXAG 2019 – HEAT EXCHANGER ACTION GROUP

Experimental investigation of a single radiative heat pipe for waste heat recovery in ceramics industry

Table of Contents

Abstract.....	III
Declaration.....	IV
Acknowledgement.....	V
Publications	VI
Published Journal paper.....	VI
International conferences.....	VII
Table of Contents.....	VIII
List of figures	XII
List of tables.....	XVII
Nomenclature	XVIII
Chapter 1: Introduction.....	1
Chapter 2: State of the arts	7
2.1 State of the arts in the ceramics industry.....	7
2.1.1 Manufacturing process of tiles	7
2.1.2 Roof tile manufacturing process.....	8
2.1.3 Waste heat recovery technologies in tile manufacturing.....	11
2.1.4 Defects in the ceramic tile manufacturing sector.....	15
2.2 State of the art of heat pipe technology.....	19
2.2.1 Heat pipe technology overview	19
2.2.2 Heat pipe applications	38
Chapter 3: Experimental apparatus and equipment	42
3.1 Introduction	42
3.2 Data collection at tile manufacturing plant	43
3.2.1 Datapaq instrument.....	43
3.2.2 Results.....	48
3.3 Single radiative heat pipe.....	52
3.3.1 Mechanical design	52
3.3.2 Kiln set up.....	54
3.3.3 Heating elements	57
3.3.4 Water supply.....	58
3.3.5 Control system	59
3.3.6 Instrumentation	60
3.3.7 Experimental test plan	67
3.4 Modular radiative heat pipes.....	68
3.4.1 Module 15.....	68

3.4.2 Module 25	73
3.4.3 Module 35	78
3.4.4 Experimental plan	85
Chapter 4: Theoretical modelling	87
4.1 Introduction	87
4.2 Heat transfer background	87
4.2.1 Natural convection.....	87
4.2.2 Radiation	90
4.2.3 Two phase heat transfer	107
4.2.4 Conduction heat transfer	118
4.2.5 Internal forced convection heat transfer.....	118
4.2.6 External forced convection heat transfer	121
4.3 Theoretical modelling of the single heat pipe	121
4.3.1 Thermal network approach	122
4.3.2 Natural convection.....	124
4.3.3 Radiation	124
4.3.4 Conduction.....	128
4.3.5 Boiling.....	128
4.3.6 Condensation	131
4.3.7 Forced convection.....	131
4.4 Theoretical modelling of the radiative modules.....	133
4.4.1 Thermal network model for radiative modules.....	135
4.4.2 Natural convection.....	136
4.4.3 Conduction.....	136
4.4.4 Radiation	137
4.4.5 Boiling.....	139
4.4.6 Condensation over tube bundle	139
4.4.7 Forced convection in tubes.....	141
4.5 Theoretical modelling of a full-scale system.....	141
4.5.1 Thermal network model for radiative modules.....	141
4.5.2 Radiation heat transfer	145
4.5.3 Conduction heat transfer	152
4.5.4 Natural convection.....	152
4.5.5 External forced convection	153
4.5.6 Boiling heat transfer.....	154
4.5.7 Condensation heat transfer	154

4.6 Theoretical modelling tool.....	155
Chapter 5: Data reduction	157
5.1 Introduction	157
5.2 Power input.....	157
5.3 Heat transfer rate	157
5.4 Equivalent radiation thermal resistance.....	157
5.5 Radiation space resistance.....	158
5.6 Conduction thermal resistance at the evaporator section.....	158
5.7 Conduction thermal resistance at the condenser section.....	158
5.8 Overall conductance of the condenser.....	158
5.9 Average evaporator temperature.....	159
5.10 Two phase thermal resistances.	159
5.10.1 Boiling thermal resistance	159
5.10.2 Condensation thermal resistance.....	159
5.11 Forced convection thermal resistance.....	160
5.12 Boiling Heat flux.....	160
Chapter 6: Results and discussion	161
6.1 Introduction	161
6.2 Single heat pipe results and discussion	161
6.2.1 Single pipe experimental results.....	162
6.2.2 Experimental versus theoretical boiling thermal resistance.	181
6.2.3 Experimental versus theoretical condenser thermal resistance.	187
6.2.4 Radiation thermal resistance analysis	188
6.2.5 Theoretical analysis of the forced convection at the condenser.....	189
6.2.6 Total thermal resistances.....	190
6.2.7 Validation of the single heat pipe theoretical modelling predictions	191
6.3 Multi module laboratory-scale radiative heat pipe ceiling.....	192
6.3.1 Module experimental results.....	193
6.3.2 Boiling thermal resistance.	200
6.3.3 Condenser thermal resistance.....	207
6.3.4 Experimental overall thermal resistance.....	213
6.3.5 Validation of the theoretical modelling predictions.....	214
6.4 General discussion on lab test modules	218
6.5 Industrial application of the radiative heat pipe ceiling.	220
6.5.1 Introduction	220
6.5.2 Description of the full scale set up.....	221

6.5.3 Prediction for the full-scale model.....	225
6.5.4 Discussion and conclusion	226
Chapter 7: Conclusion from the study and suggestions for future work	228
7.1 Conclusion from study	228
7.2 Impact of the study on the research field.....	231
7.3 Suggestions for future work.....	232
References	234
Appendices	243
Appendix 1: Error analysis	243
Background	243
Results	244
Appendix 2: Pressure drop measurements	248
Introduction	248
Experimental set up	248
Experimental procedures.....	248
Results	249
Conclusion.....	250

List of figures

Figure 1 2015 ceramics industry production [4].....	2
Figure 2 production value (2015) [4].....	2
Figure 3 Location of the tile ceramics production in Europe	2
Figure 4 European ceramics industry by energy consumption[6]	3
Figure 5 Tile manufacturing process	4
Figure 6 Cross-section of a roller hearth kiln [8]	8
Figure 7 Section view of a tunnel kiln[8]	10
Figure 8 Operating data of tunnel kilns [8].....	10
Figure 9 Percentage of energy wasted in the USA in 2008	11
Figure 10 Waste heat recovery process	12
Figure 11 Schematic of an Organic Rankine Cycle [10].	13
Figure 12 Schematic view of a combined heat recycling system	14
Figure 13 Schematic view of hot air generation using a cogeneration system[16].	15
Figure 14 Calculation of the evolution of the curvature deflection in a tile body during industrial cooling [25]	18
Figure 15 Schematic heat pipe principle.....	19
Figure 16 Variable conductance heat pipe [31]	21
Figure 17 Schematic of a Pulsating Heat Pipe [33]	22
Figure 18 Wrap-around heat pipe schematic.....	23
Figure 19 (a) Exploded assembly details, (b) mechanical design of the wraparound heat pipe [36].....	24
Figure 20 HPHE in the ceramics industry [7].....	25
Figure 21 Selection of typical wick structure [38].....	26
Figure 22 Loop heat pipe [25]	27
Figure 23 Six LHP orientations [42].....	27
Figure 24 Cross section of a grooved heat pipe [44]	28
Figure 25 Cut view sintered heat pipe	29
Figure 26 Figure of merit for common working fluids in wicked heat pipes	33
Figure 27 Figure of merit of common working fluids used in thermosyphons.....	33
Figure 28 Operational limitations.....	34
Figure 29 Flat Heat Pipe on cooling line.....	39
Figure 30 Test rig Closed-loop heat pipe.....	40
Figure 31 HPHE in bakery test rig	41
Figure 32 Tpaq 21 data logger	43
Figure 33 "carpet" tile on the conveyer.....	45
Figure 34 Thermocouple arrangement	45
Figure 35 Thermocouple distance from the tile.....	46
Figure 36 Arrangement of the thermocouple on the tile.....	46
Figure 37 Data logger box.....	47
Figure 38 Full arrangement of the thermocouples on the tile.....	47
Figure 39 State of the Datapaq after the test.....	48
Figure 40 Single radiative heat pipe 5 degrees	52
Figure 41 Single heat pipe in the kiln	53
Figure 42 3D view of the Single Heat Pipe	53
Figure 43 Kiln arrangement.....	54
Figure 44 a) ceramic pad heater b) ceramic pad installed in the kiln	57
Figure 45 Ceramic heater parts.....	58
Figure 46 Water cooling system	59
Figure 47 Electrical board	60

Figure 48 Thermocouples in the kiln	61
Figure 49 Thermocouples outside the kiln.....	62
Figure 50 Thermocouple locations, single radiative heat pipe	63
Figure 51 Welded thermocouples.....	64
Figure 52 a) Flow meter display; b) flow meter.....	65
Figure 53 Data logging system.....	66
Figure 54 Module 15 GA.....	69
Figure 55 Module 15 condenser detail	70
Figure 56 Module 15 detail: Front view	71
Figure 57 Thermocouple wiring, module 15	72
Figure 58 Thermocouple locations, Module 15.....	73
Figure 59 Module 25 GA.....	74
Figure 60 Module 25 Condenser details.....	75
Figure 61 Module 25 front view	76
Figure 62 Thermocouples wiring Module 25.....	77
Figure 63 Thermocouple positions, module 25.....	78
Figure 64 Module 35	79
Figure 65 Shell and tube condenser.....	79
Figure 66 Module 35 GA.....	80
Figure 67 Module 35 condenser detail	81
Figure 68 Module 25 front view	82
Figure 69 Thermocouples wiring, module 35.....	83
Figure 70 Thermocouples location, Module 35.....	84
Figure 71 (a) Electromagnetic spectrum. (b) Thermal radiation portion of the electromagnetic spectrum. [72].....	91
Figure 72 Spectral blackbody emissive power [73].....	92
Figure 73 Emission of radiation from a differential area dA_1 into a solid angle $d\omega$ subtended by dA_n at a point on dA_1 [73]	93
Figure 74 The solid angle subtended by dA_n at a point on dA_1 in the spherical coordinate [73].....	93
Figure 75 Emission from a differential surface dA_1 to a differential surface dA_n [73]	95
Figure 76 Radiation at a surface. (a) Reflection, absorption, and transmission of irradiation for a semi-transparent medium. (b) The radiosity for an opaque medium.[73].....	96
Figure 77 Illustration of superposition rule.....	100
Figure 78 Illustration of summation rule	100
Figure 79 Schematic of two infinite planes with a common edge at an angle of 90° from each other	101
Figure 80 Schematic of the geometry of two rectangles in a parallel plane	102
Figure 81 Schematic of the geometry of two rectangles in a perpendicular plane	103
Figure 82 Illustration of the view factor between a cylinder and a strip	104
Figure 83 Schematic of the resistance approach of radiation leaving a surface i	105
Figure 84 Schematic of the radiation resistance approach for receiving surfaces.....	106
Figure 85 Schematic of the radiation resistance approach for an enclosure with two surfaces.	106
Figure 86 Boiling curve for water at 1 atm [81]	107
Figure 87 Schematic of the boiling heat transfer	109
Figure 88 Schematic of the condensation heat transfer.....	113
Figure 89 Laminar flow on an horizontal tube [57].....	116
Figure 90 Schematic of the heat transfer principles in the test rig	122
Figure 91 Model of the electrical resistance analogy for the radiative heat pipe	123

Figure 92 Model of the electrical resistance analogy applied to the radiation heat transfer for the radiative heat pipe.....	125
Figure 93 Simplified radiation model	126
Figure 94 Different boiling regime under various filling ratio	129
Figure 95 Thermal network schematic including the two boiling regimes.....	131
Figure 96 Detailed drawing of the single heat pipe condenser section	132
Figure 97 Heat transfer regime in radiative module 1	134
Figure 98 Heat transfer regime in radiative module 2.....	134
Figure 99 Thermal network modelling of radiative heat pipe modules	135
Figure 100 Thermal radiation network.....	137
Figure 101 Schematic of view factor from the heater to the tube bundle	139
Figure 102 Schematic of condenser section.....	141
Figure 103 Temperature distribution in the kiln.....	142
Figure 104 Heat transfer in the radiative heat pipe ceiling.....	143
Figure 105 Schematic thermal model heat pipe ceiling	144
Figure 106 Radiation heat transfer schematic	146
Figure 107 Simplified radiation network schematic.....	149
Figure 108 External forced convection	153
Figure 109 Heat pipe theoretical model tool.....	156
Figure 110 Filling ratio in single heat pipe	163
Figure 111 Experimental Evaporator temperature of the single heat pipe against the external evaporator heat flux	164
Figure 112 Temperature distribution at the evaporator section for low heat flux <math> < 4.5 \text{ W/m}^2 </math>.....	165
Figure 113 Geyser Boiling at 25% FR and 200°C heat source	166
Figure 114 Experimental temperatures of the single heat pipe for heat flux between 4.2 kW/m ² and 5.5 kW/m ²	167
Figure 115 Geyser boiling occurrence in a heat pipe [112].....	169
Figure 116 Experimental temperatures of the single heat pipe at heat flux > 11 kW/m ²	171
Figure 117 Excess temperature for various filling ratios	172
Figure 118 Experimental boiling thermal resistance versus heat flux under various filling ratios.....	173
Figure 119 Experimental overall condenser thermal resistance	175
Figure 120 Experimental condenser thermal resistance.....	176
Figure 121 Impact of the filling ratio on the evaporator ΔT	177
Figure 122 Fluctuation of the heat recovery during geyser boiling.....	178
Figure 123 Heat transfer rate by natural convection.....	179
Figure 124 Influence of natural convection on the overall heat transfer rate.....	180
Figure 125 Heat transfer rate by radiation	181
Figure 126 Surface area occupied by the pool at a filling ratio of 75%	182
Figure 127 Experimental and predicted boiling thermal resistance FR25%	183
Figure 128 Experimental and predicted boiling thermal resistance FR50%	183
Figure 129 Experimental and predicted boiling thermal resistance FR75%	183
Figure 130 Experimental and predicted boiling thermal resistance FR100%	184
Figure 131 Experimental versus predicted boiling thermal resistance FR25%	185
Figure 132 Experimental versus predicted boiling thermal resistance FR50%	186
Figure 133 Experimental versus predicted boiling thermal resistance FR75%	186
Figure 134 Experimental versus predicted boiling thermal resistance FR100%.....	187
Figure 135 Comparison between the experimental and predicted condensation thermal resistance	188
Figure 136 Experimental vs Theoretical thermal radiation resistance.....	189
Figure 137 Experimental overall thermal resistance of the single heat pipe	190

Figure 138 Experimental vs predicted heat transfer rate	191
Figure 139 Experimental vs predicted heat pipe temperatures, case study 1	192
Figure 140 Experimental vs predicted heat pipe temperatures, case study 2	192
Figure 141 Variation of the temperature measurements of module 15 heat pipe system at various flow rates for a heater temperature of 500°C	194
Figure 142 Experimental heat recovery under varying conditions.	195
Figure 143 Heat pipe module temperature at filling ratios of 25% and 75% for a tile temperature of 500°C.....	195
Figure 144 Heat recovery at similar conditions for a FR of 25% and 75% at 500 °C	196
Figure 145 Heat pipe module temperatures at various flow rates.....	197
Figure 146 Heat recovered at a flow rate of 5 L/min at various heater temperatures.....	198
Figure 147 Heat recovered at a flow rate of 10 L/min at various heater temperatures.....	199
Figure 148 Influence of natural convection overall heat transfer rate for modules 15 and 35 under a flow rate of 15 L/min.....	200
Figure 149 Experimental boiling thermal resistance for three evaporator designs	201
Figure 150 Experimental and predicted boiling thermal resistance for Module 15	202
Figure 151 Experimental and predicted boiling thermal resistance for Module 25	203
Figure 152 Experimental and predicted boiling thermal resistance for Module 35	204
Figure 153 Comparison between the theoretical and experimental thermal resistance	205
Figure 154 A comparison between the experimental boiling thermal resistance for Module 15 at FR 25% and FR 75%	206
Figure 155 Experimental and predicted boiling thermal resistance Module 15 25%	207
Figure 156 Experimental vs theoretical prediction boiling thermal resistance for Module 15 at FR 25%.....	207
Figure 157 Experimental condensation resistance modules.....	208
Figure 158 U values for the heat pipe module condenser section	209
Figure 159 Experimental vs theoretical condenser thermal resistance for module 15 at FR =75%	210
Figure 160 Experimental and theoretical prediction of the condensation heat transfer coefficient against the condensation heat flux.	211
Figure 161 Experimental vs predicted condensation thermal resistance for Module 15 at 75% FR.....	212
Figure 162 Experimental and theoretical condensation thermal resistance vs the heat flux for module 35 with 75% FR.....	213
Figure 163 Heat pipe modules overall thermal resistance	214
Figure 164 Experimental and predicted heat pipe temperatures, module 15, FR 75%, 10 L/min.....	215
Figure 165 Experimental and predicted heat pipe temperatures, module 15, FR 75%, 15 L/min.....	215
Figure 166 Experimental and predicted heat pipe temperatures, module 35, FR 75%, 15 L/min.....	216
Figure 167 Theoretical versus experimental heat transfer rate module 15	217
Figure 168 Theoretical versus experimental heat transfer rate module 35	217
Figure 169 Cross section of the kiln with the heat pipe ceiling installed.....	221
Figure 170 Heat pipe ceiling assembly.....	222
Figure 171 Heat Pipe Ceiling 25-35	223
Figure 172 Heat pipe ceiling 15.....	224
Figure 173 Heat transfer rate distribution across the kiln at a tile temperature of 500 °C...	225
Figure 174 Heat transfer rate distribution across the kiln at a tile temperature of 200°C....	226
Figure 175 Pressure drop experimental set up.....	248
Figure 176 modelling of the pressure resistances at the coolant	248

Figure 177 Pressure drop in the water for module 35 vs flow rate..... 249

List of tables

Table 1 Summary of tiles defects detected[18].....	15
Table 2 Working fluids and temperature ranges	31
Table 3 Compatibility between materials and working fluids.....	34
Table 4 Tpaq specifications.....	43
Table 5 Results of the temperature measurement of the tile	48
Table 6 Insulation specifications	54
Table 7 Brick specifications.....	55
Table 8 Specification of the heaters	57
Table 9 Technical specifications - FTB371-G.....	65
Table 10 Thermocouple type K measurement accuracy (°C)	66
Table 11 Experimental plan single radiative heat pipe.....	67
Table 12 Flow value used for the tests.....	67
Table 13 Module 15 Test Plan	85
Table 14 Module 25 Test Plan	85
Table 15 Module 35 Test Plan	85
Table 16 Value and error associated with n, m and Nusselt number	89
Table 17 Radiative fluxes[73].....	96
Table 18 List of correlations for boiling in the evaporator liquid pool.....	109
Table 19 List of correlations for falling film boiling	111
Table 20 Common correlations for condensation heat transfer coefficient.....	113
Table 21 Nusselt number correlations for forced convection in a tube.....	119
Table 22 Forced convection thermal resistance	189
Table 23 Error analysis equations	243
Table 24 Associated errors	244
Table 25 Error propagations.....	245
Table 26 Error analysis for the single heat pipe.....	245
Table 27 Error analysis for module 15 testing	246
Table 28 Pressure drop results for various flow rates and vapour temperature	249

Nomenclature

Symbol

A	Surface area (m^2)
C_p	Specific heat ($J/kg.K$)
C_{sf}	constant,
D	Diameter (m)
E	Emitted heat per surface area (W/m^2)
F	View factor
F_{12}	View factor between the heater surface and the surface of the heat pipe
F_{13}	View factor between the heater surface and the walls
F_{21}	View factor between the heat pipe surface and the surface of the heater
F_{23}	View factor between the heat pipe surface and the surface of the walls
G	Irradiation (W/m^2)
g	Gravitational acceleration (m/s^2)
h	Heat transfer Coefficient ($W/m^2.K$)
h_{fg}	Latent heat of vaporisation (J/kg)
I	Radiation intensity (W/m^2)
J	Radiosity (W/m^2)
k	Thermal conductivity ($W/m.K$)
L, l	Length (m)
\dot{m}	mass flow rate (kg/s)
N	number of pipes
P	Pressure (N/m^2)
Q	Heat transfer rate (W)
q	Heat flux (W/m^2)
R	Thermal resistance (K/W)
r	Radius
T	Temperature (K)

Non Dimensional number

Gr	Grashof number
Ja	Jakob number
Nu	Nusselt number
Pr	Prandtl number
Ra	Rayleigh number, $Ra = Gr.Pr$

Re Reynolds number

Greek Symbols

α Absorptivity
 ε Radiation emissivity
 θ contact angle of the fluid-wick combination
 η Efficiency
 λ Wavelength (μm)
 μ Dynamic viscosity (kg/m.s)
 ρ Density (kg/m³)
 σ Surface tension (N/m)
 σ_0 Stefan–Boltzmann constant which is equal to $5.67 \times 10^{-8} \text{ W}/(\text{m}^2 \cdot \text{K}^4)$
 τ Transmissivity

Subscripts

c Condenser section
ci Condenser inner wall
co Condenser outer wall
cold Cooling fluid
water, in Cooling fluid inlet
water, out Cooling fluid outlet
Cond, e Evaporator wall conduction
Cond, c Condenser wall conduction
e Evaporator
ei Evaporator inner wall
eo Evaporator outer wall
f Film
hp Heat pipe
h Heat source, heaters
l Liquid
rad radiation
v Vapour

Superscripts

n experimental constant that depends on fluid
 λ spectral

Chapter 1: Introduction

Following the energy crisis in 1980s, many energy saving technologies have been investigated with attempts to implement them into various industries, among them the field of ceramics. In order to comply with energy saving trends and environmental issues, the European ceramic industry sector has developed energy efficient systems which have significantly reduced production times and costs and reduced total energy consumption and greenhouse gas emissions.

Ceramics components are defined as a non-organic, non-metallic materials that develop mechanical properties when exposed to heat. The application of heat to produce high strength material is by definition an energy intensive process [1]. Studies on the energy balance and the opportunities of energy savings in ceramic industries have highlighted that the development of energy saving technologies and waste heat recovery is crucial in response to the worldwide environmental crisis but also for the reduction of production costs and the quality of the final products[2]. Seven types of ceramic productions can be identified, wall and floor tiles, brick roof tiles and pipes, refractories, sanitary ware, table and ornamental ware, technical ceramics and abrasives. The production of ceramics takes place in a large variety of kilns depending on the types of ceramics produced. Among the production costs, almost 30% is related to the energy input in the production process which make the ceramics sector the second most energy intensive manufacturing process in Europe with a consumption of 1.67 TWh of energy[3]. Tile production represents the largest production and market share in the ceramics industry with 51% of the total ceramics production (14 billion Euros) as seen in Figure 1 and Figure 2.

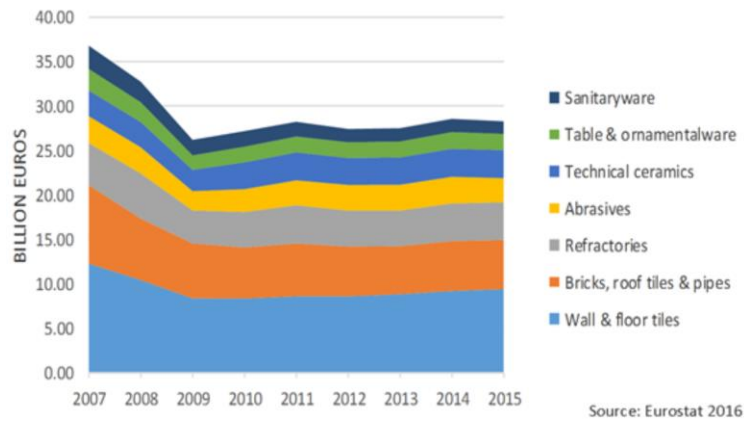


Figure 1 2015 ceramics industry production [4]



Figure 2 production value (2015) [4]

Four types of production can be identified in the traditional ceramics sector: Tiles, Tableware, Sanitary ware and Brick and Heavy clay pipes. Most of the manufacturing companies are based in Italy, Spain and Poland (Figure 3).

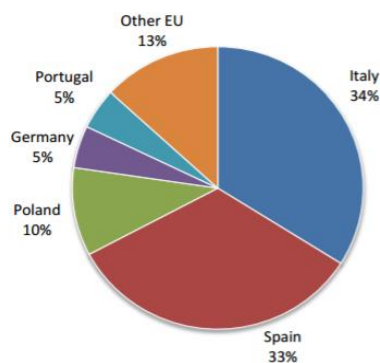


Figure 3 Location of the tile ceramics production in Europe

The tile manufacturing sector groups all the items used for covering roofs, floors, walls, showers and other objects such as furniture for bathrooms and kitchens. The tile ceramic industry is the largest sector within the traditional ceramics sector. Tile manufacture represents a market of 14 billion euros and 75% of the total energy consumption for the other ceramics sector, excluding brick and heavy clay pipes (Figure 4). The tiles ceramics sector consumes

large amounts of natural gas, the emissions related to the natural gas consumption are evaluated at about 265kg of CO₂ per tonne of fired tile. The energy used in the manufacturing of tiles is around 28kWh/m² [5].

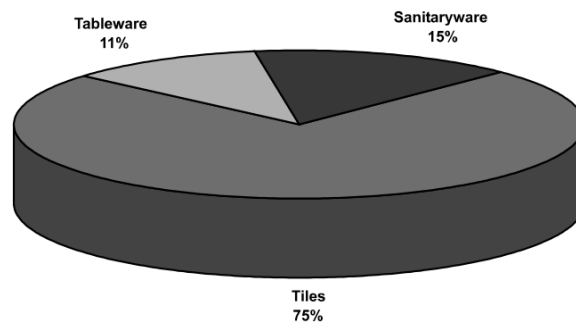


Figure 4 European ceramics industry by energy consumption[6]

The main challenges of the tiles ceramics industry are the competition in mass volumes of tiles fired for low prices with a good product quality to compete with emerging economies, the high energy demands of the tiles manufacturing process and the reduction of greenhouse gas emissions. To overcome those challenges, the tiles ceramics sector needs to develop ways to reduce the consumption of energy (in roller kilns, 50% of the total energy consumption is used for the firing). The increase in production required to compete with emerging economies comes with issues such as defects that will affect the production quality. Technologies need to be developed to reduce those defects. The EU legislation regarding greenhouse gas emissions implies a reduction of the emissions in tile manufacturing. By reducing the energy consumption, emissions will also reduce. In ceramics manufacturing, some gaseous pollutants are produced such as SO_x, NO_x, HF, and HCL. Reducing the emissions of these gases will be achieved by developing new filter technologies and reducing the energy consumption.

The tiles can be identified in 3 groups:

- Roof tiles used to protect buildings against the rain, they can be made of terracotta or slate but also concrete and plastic in certain applications.
- Floor and wall tiles used to cover the interior as a decorative part.
- Ceiling tiles used inside buildings as a decorative feature but also to improve the acoustics.

Brick and roof tiles follow a different manufacturing process than the wall and floor tiles. The manufacturing process of the tiles will depend on the type of tiles produced. In this thesis, the process investigated is based on the roller hearth kiln technology. The tile can be unglazed, single glazed or double glazed. Five main steps can be identified in the process, the raw

material and body preparation, the shaping, the drying, the firing and the final product shipping. A process flow chart can be seen in Figure 5.

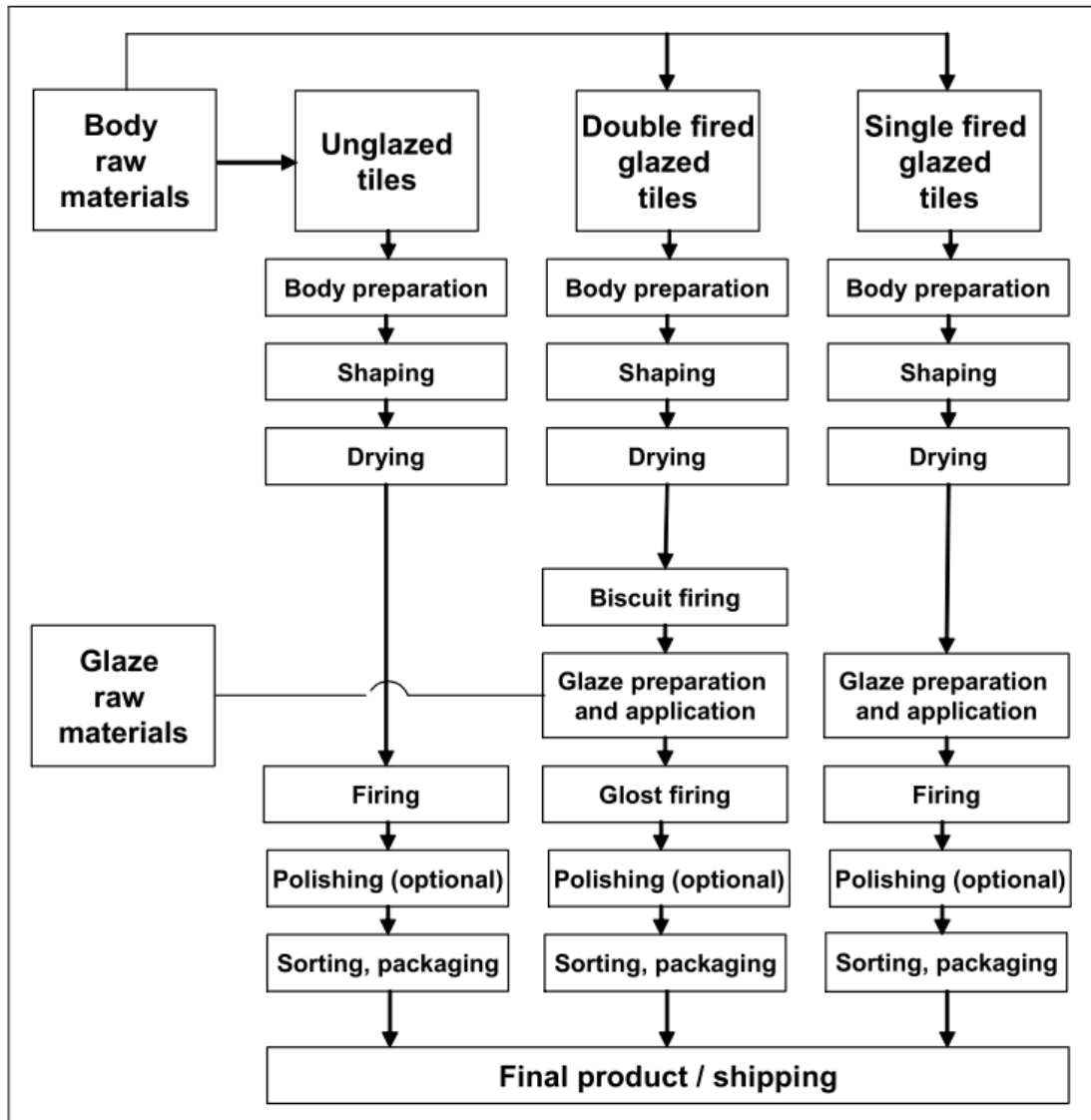


Figure 5 Tile manufacturing process

The baking of the tile is of great importance as the energy consumption of the ceramic process accounts for a significant percentage of the total production costs. More precisely, the firing stage consumes the highest amount of energy during the whole ceramic production process. The use of roller kilns, fired by natural gas, involves a loss of 50% of the input energy via the flue gas and the cooling gas exhausts. Most of the heat used in the firing process is then disposed of during the cooling stage where the tiles go through a cooling tunnel in four stages. During the first stage, air from the factory is blown onto the tile to decrease the temperature from 1100°C to 700°C. The second stage consists of a radiative ceiling roof composed of stainless-steel tubes arranged in a bundle with similar distances between each other, The heat

is transferred from the tile to the pipes using radiation heat transfer. The tubes are cooled by air. The hot air generated by the cooling is then sent to the dryers' burner. The indirect cooling section is used to cool down the tile slowly to 300°C to ensure that the crystallisation takes place in the most uniform way. The tiles are then cooled to ambient temperature using air. The main issue discovered during testing campaign on the roller earth kiln was the difference of cooling temperature taking place during the indirect cooling. The temperature gradient between the side of the tile and the middle was 100°C on average. This temperature gradient will impact the life span of the tile as internal stresses will weaken the tile. It also has been noticed through extensive simulation work that the temperature gradient between the top of the tile and the bottom was 150°C which will also impact on defects in the tile. The difficult environment of the kiln could not allow a proper testing of all of the stage and so the data used in this thesis are based on a simulation model.

Heat pipes have been used in a variety of applications. In recent years the heat pipe technology relying on gravity has been applied in different sectors as the price of heat pipe manufacturing decreases. Heat pipes rely on boiling and condensation regimes to transfer heat from the evaporator section to the condenser section. The heat pipe technology using radiation heat transfer has been used in different sectors such as the steel industry and solar collectors. The use of this technology in the ceramics industry has been investigated for recovering heat from the cooling stage [7], but the use of such a technology to cool down materials such as tiles has not been investigated.

Therefore, an attempt to fill the gaps in scientific research has been made in the current investigation. The heat pipe technology has been applied to the indirect cooling section in order to fine tune the temperature gradient and recover a larger amount of heat. The high conductivity and the reliability of the heat pipe technology has made it the best suitable solution for a novel radiative heat pipe ceiling.

The main objective of this investigation is to demonstrate that the heat pipe technology, using different variables such as the heat transfer area, the filling ratio and the flow rate in the condenser section can reduce the temperature variations along the tile during the cooling section with remote cooling in an industrial setting.

In order to achieve the objective, a test rig has been developed to demonstrate the concept experimentally and theoretically. The test rig is composed of three modules with different heat transfer areas for the evaporator section and a kiln with a heat source composed of a ceramic pad heater. A single radiative heat pipe has also been tested to validate the methods and hypothesis of the view factor for a larger scale system.

The thesis is structured as follows. An extensive review of previous work in waste heat recovery in the ceramics industry, radiative technologies and heat pipe technologies have been reported in Chapter 2. The experimental apparatus and instrumentations and the testing procedures for the radiative ceiling are described in Chapter 3. The theoretical investigation of the single radiative heat pipe and the characterisation of the view factor and emissivity have been investigated in Chapter 4. A data reduction analysis was carried out to assess the data and results from the experimental tests and is presented in Chapter 5. The results and the discussions on the single heat pipe and the modules test are presented in Chapter 6. The theoretical modelling tool developed is presented in Chapter 6 with the prediction of the heat transfer rate across the kiln cross section. The conclusions and suggestions for future work have been drawn in Chapter 7.

Chapter 2: State of the arts

2.1 State of the arts in the ceramics industry

2.1.1 Manufacturing process of tiles

2.1.1.1 Body preparation and shaping

The preparation of the tile body is one of the most crucial stages in the manufacturing process. The composition of the tile needs to be carefully selected in order to produce a high-quality tile matching the mechanical and aspect requirements. The tile is composed of a combination of natural and synthetic materials such as aluminium silicates, based clay and small amounts of pigment, metal oxides or colorants. The prepared raw material is mixed in a controlled environment using water as a bonding agent (35%). Then, the preparation is dried using spray drying at a temperature between 350 °C and 450 °C to a water content of 5%-9%. The resulting product is a powder with a moisture content of 5%.

2.1.1.2 Shaping

The shaping can be done using impact toggle presses, screw presses or hydraulic presses with a pressure of about 35MPa

2.1.1.3 Process of the drying stage

The tile is then dried. The dryer technology depends on the production: tunnel dryers, roller dryers or vertical dryers. The drying is performed at temperatures that vary depending on the dryer technologies used (200-220 °C for vertical dryers, 300-350 °C for tunnel dryers). The tiles are dried for between one to four hours depending on the moisture content. The moisture content at the end of the drying stage cannot exceed one percent to avoid fissure or explosion of the material during the firing stage. The heat required for the dryers is supplied via waste heat from the kiln or by natural gas. The main issue with the waste heat recovered from the kiln is the composition of the exhaust gas that will impact on the quality of the final product.

2.1.1.4 The firing stages.

The main purpose of the firing stage is to bind molecules of the tile together to increase the mechanical properties and guarantee a good integrity of the tiles. The firing process depends on the technology used. Two main kiln technologies can be used in the ceramics process, the tunnel kiln and the roller hearth kiln. Nowadays the most used technology in tile manufacturing processes is the roller hearth kiln but some technologies used in tunnel kilns can be applied in roller hearths regarding the waste heat recovery of exhaust stack gases. Four stages can be identified in the firing process. The firing stage, where the tile is heated up to 1300 °C, the direct cooling using air streams on the tile (1300 °C to 700 °C), the indirect cooling using

radiative cooling (700 °C to 300 °C), and the slow cooling using air to cool down the tile to 30 °C. a cut view of the kiln can be seen in Figure 6.

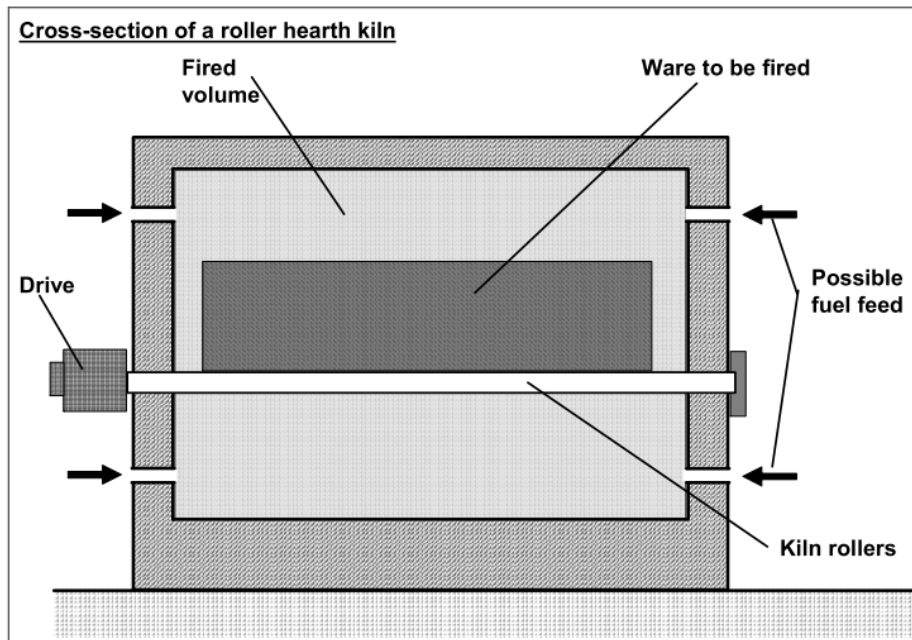


Figure 6 Cross-section of a roller hearth kiln [8]

Recent data suggest that the firing stage contributes 57% of the total CO₂ emissions of the ceramic tile process[9].

	Unit	Tunnel kiln biscuit firing	Roller hearth kiln	
			final firing	single firing
Product		Tiles with higher water absorption		
Throughput	t/h	2.8	1.2	1.6
Kiln length	m	120	60	80
Cross-section	m ²	1.5 – 2.0	0.8 – 1.2	0.5 – 1.0
Setting density	kg/m ³	500 – 700	10 – 30	10 – 30
Firing temperature	°C	1100	1250	1300
Specific energy requirement	kJ/kg	3500	2900	2200
Flue-gas volume flow	m ³ /h	15000	10000	13000
Flue-gas temperature	°C	180	160	200

2.1.2 Roof tile manufacturing process

The roof tile manufacturing process follows the same steps as for wall and floor tiles but with a different technology used. Five steps can be identified: raw material preparation, shaping, drying and glazing, firing and subsequent treatments.

2.1.2.1 Raw material

The raw material selection is one of the most important steps in the manufacture of roof tiles. Indeed, across Europe, the roof tile will be of different shapes, colour and composition. Most of the roof tile clays are sedimentary: marine fluvial or river glacier sediments. The composition of the roof tile will also have an impact on the mechanical properties of the final product and the gaseous emissions realised during the firing stages. Production sites mainly manufacture only one type of roof tile, depending on the region where they are. The raw materials are stored in large open-air storage. In most of the cases, the raw materials come from a brickyard next to the manufacturing plant.

2.1.2.2 Raw material preparation

Two type of preparations can be identified in roof tile manufacture, dry preparation and semi-wet preparation. The selection of the preparation method will be determined by the available materials, the quality required for the final product, the shaping methods and the product price. Dry preparation is used when dry material with low plasticity is used or for a high-quality product. The purpose of the dry preparation is to smash the product with a hammer or suspended roller mills to reduce the size of the particle and also to decrease the water content to six percent. Additives are used to fix the moisture content and to maintain a good plasticity of the raw materials. These additives will facilitate the cutting of the clay during the shaping in the extrusion process. Dry preparation can be applied to roof tiles, but it is mostly used with brick manufacturing. Semi-wet preparation is mainly used for the roof tile clay. The raw materials are mixed in a large volume feeder. The mixing of the materials requires a high-water content, about 20%. The material is then crushed to reduce the particle size to between 0.5 to 0.8 mm. To crush the materials, clay crushers, knife crushers, double roll crushers or a wet pan can be used depending on the material characteristics.

2.1.2.3 Shaping

The wet preparation is shaped using a press. The material is pressed under a die at a pressure of between 0.6 and 1.5 MPa and the die will form a column of formed clay; this column will be then cut using a wire cutter. This is the typical method used in building bricks and extruded roof tile production. Roof tiles can also be manufactured using presses. The raw material is formed into a cakes or lumps. The cakes will then be pressed again to the correct geometry.

2.1.2.4 Drying

Roof tiles are dried in tunnel dryers or chambers at a temperature between 60 °C to 90 °C for 12 to 48 hours. The dryer will decrease the water content of the body to less than three percent. Dryers are usually heated using the waste hot air from the cooling stage of the firing stage, by natural gas or fuel oil burner and cogeneration.

2.1.2.5 Firing

The main technology used to fire the roof tile is the tunnel kiln in an oxidising atmosphere. This will cause the appearance of special colour effect. The roof tile is placed on a kiln car going through the kiln as it heats up. The placement of the roof tile on the car has a great importance. It needs to allow the oxidising air to circulate around the product in a uniform way. The roof tile is heated up to a temperature between 1000 °C to 1150 °C. Depending on the shape of the tile, the product will be baked for 10 to 40 hours. The temperature of the flue gas within the kiln will depend on the dew point. The temperature of the flue gas needs to be higher than the dew point to avoid condensation on the tile while heating up. The temperature will depend on the composition of the roof tile fired. Then the product will be cooled to 50 °C. A cut view of the kiln can be seen in Figure 7. The different operating conditions for tunnel kilns are shown in Figure 8.

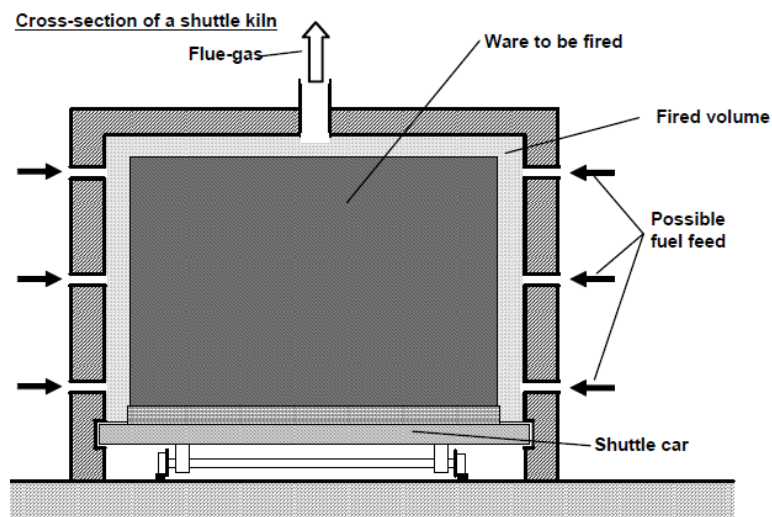


Figure 7 Section view of a tunnel kiln[8]

Tunnel kilns	Unit	Facing bricks and clay pavers	Clay blocks	Horizontally perforated clay blocks	Roof tiles
Throughput	t/h	1 – 15	3 – 15	3 – 15	3 – 6
Kiln length	m	35 – 160	60 – 120	60 – 120	80 – 140
Cross-section	m ²	1.3 – 6.0	4 – 12	4 – 12	4 – 10
Setting density	kg/m ³	650 – 1500	350 – 500	250 – 750	200 – 400
Firing temperature	°C	1000 – 1300	900 – 1050	950 – 1050	1000 – 1150
Specific energy requirement (drying + firing)	kJ/kg	1600 – 3000	1000 – 2500 ^{*)}	1000 – 2500	1600 – 3500
Flue-gas volume flow	m ³ /h	5000 – 20000	10000 – 50000	10000 – 50000	10000 – 40000
Flue-gas temperature	°C	100 – 230	100 – 300	100 – 150	170 – 200

^{*)} Including heat content of the pore-forming agent

Figure 8 Operating data of tunnel kilns [8]

The use of hearth roller kilns can also be applied in roof tile manufacturing depending on certain criteria. It will depend on the surface of the product and the possibility of perfusion by hot firing gases. A roller hearth kiln will allow a reduction of energy consumption and greenhouse gas emissions.

2.1.3 Waste heat recovery technologies in tile manufacturing

Waste heat recovery has been widely investigated due to global warming and climate change. Indeed, companies and governments are trying to reduce greenhouse emissions and waste energy e.g. the United States of America wasted 57% of the energy produced [10] as shown in Figure 9.

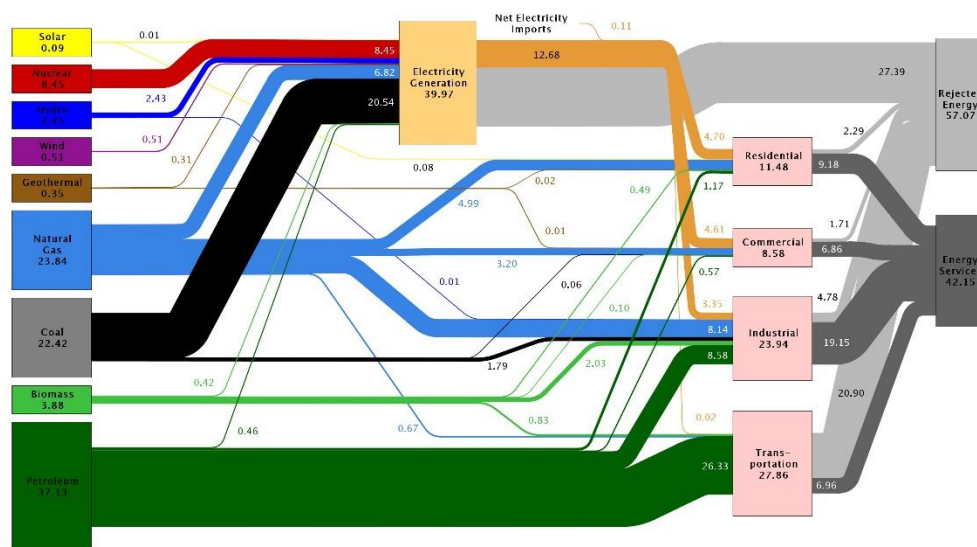


Figure 9 Percentage of energy wasted in the USA in 2008

To prevent such issues, universities and companies developed technology to recover heat from high- or low-grade temperatures. Those actions can prevent global warming but also can reduce manufacturing and energy costs.

The main areas of energy consumption during the manufacture of tiles are the firing, accounting for 55% of total energy consumption, the spray drying (36%), and the drying (9%)[5]. Also, the CO₂ emissions of the firing process are estimated to be about 265 kg CO₂ /t of fired tile[11]. High energy-demanding processes need to decrease energy consumption in order to remain competitive and to lower the production cost [2]. To match this objective, energy saving technologies have been investigated in the tile ceramics industry.

2.1.3.1 Optimisation of the drying stage

Several optimisations have been tested and applied in the drying stage such as [6]:

- Optimisation of the recirculation of drying air: using more sophisticated ventilation techniques to control fundamental parameters such as relative humidity, temperature and flow rate improved the efficiency of the hot-air dryer.
- Waste heat recovery: Clean hot air from the cooling exhaust of the firing kilns is available and can significantly improve the efficiency of the process. Waste heat recovery can provide up to 100% of potential energy saving for the drying process.
- Pulsed hot air: A periodically interrupted flow allows the use of a higher drying air temperature; this solution allows enough time for the moisture to migrate from the centroid to the surface. These higher drying air temperatures allow a reduction of 40 min when compared with the process with a classical roller dryer.
- Microwave drying: Microwave assisted drying has two obvious advantages. First of all, only the object is heated, whilst the chamber remains cool and so the energy to heat the drying chamber is saved. The microwave also heats the centre of the body and not only the surface; this promotes moisture migration to the surface. Water absorbs the microwaves better than the raw materials, which considerably accelerates the drying. The use of microwave technology can significantly reduce the drying time (from 30 to 7 minutes, depending on the object/material), with a higher energy efficiency.[12]

A significant number of investigations have been conducted regarding waste heat recovery from the kiln cooling stage.

2.1.3.2 Energy recovery using air to air heat exchanger

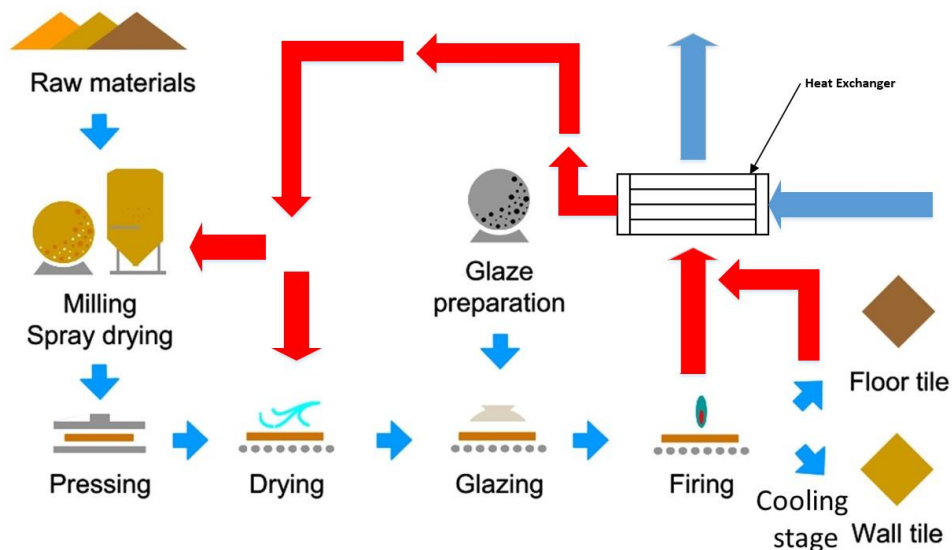


Figure 10 Waste heat recovery process

Luwa air engineering have investigated the use of a heat exchanger to recover the hot air from the firing section of a roller hearth kiln to heat up air in order to feed the burners of the driers.

The process flow chart can be seen in Figure 10. The heat exchanger located next to the kiln was able to recover heat and feed hot air to the burner hence decreasing the overall gas consumption of the plant. The main challenge with this technology is the composition of the flue gas exiting the firing section of the kiln. The sulphuric acid present in every burner's flue gas can be highly corrosive if the flue gas temperature is lower than the dew point. Also, the fouling effect could have a major contribution to the condensation of the flue gas in the system. The use of a shell and tube heat exchanger might not be ideal as the presence of cold spots/areas in the heat exchanger could generate a condensation of the flue gas and a corrosion of the heat exchanger shell. The maintenance cost of such a unit will impact on the return on investment. In order to tackle the corrosion problem, a suitable solution to avoid the appearance of cold spots could be investigated. Also, the fouling effect could have a major contribution to the condensation of the flue gas in the system.

2.1.3.3 Organic Rankine cycle

The application of the ORC for the ceramic industry has been investigated by Peris et al. [13]. The ORC has proven its efficiency for waste heat recovery from low grade heat sources. Similar to the Rankine cycle, the operative principle consists of recovering the waste thermal energy from a heat source via a working fluid to an expander in order to produce mechanical work which is subsequently converted to electricity.

The heat is taken from exhaust gases from a ceramic furnace via a collector heat exchanger to the ORC (Figure 11).

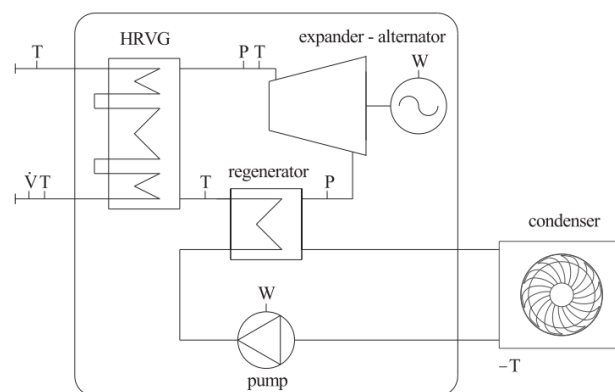


Figure 11 Schematic of an Organic Rankine Cycle [10].

A simulation of the ORC system during a typical year of production has been conducted. The results show an energy production for the whole year in excess of 115 MWh[13,14]. This ORC could save around 237 MWh of primary energy and avoid about 31 tonnes per year of atmospheric CO₂ emissions [13]. The payback of the ORC is around 4-5 years[13].

2.1.3.4 Recovery of excess heat from tunnel kilns

Hot air from the cooling zones of tunnel kilns is usually used in the drying stage and added to the hot air from gas burners. This method of recovering hot air can be managed only if the length of the pipes (distance between the cooling and the drying zone) is limited. A significant amount of insulation is needed over the pipe section to limit thermal losses. A large amount of energy is saved using this technique of heat recovery. Some processes also use a heat exchanger to recover the heat from the cooling zone to preheat the combustion air and the air for the drying stage as seen in Figure 12. The application is limited due to the production of acidic combustion gases and other implications such as foaming. Some applications use a thermal oil as a working fluid to transfer the recovered heat to the drying and firing stages. [8,15]

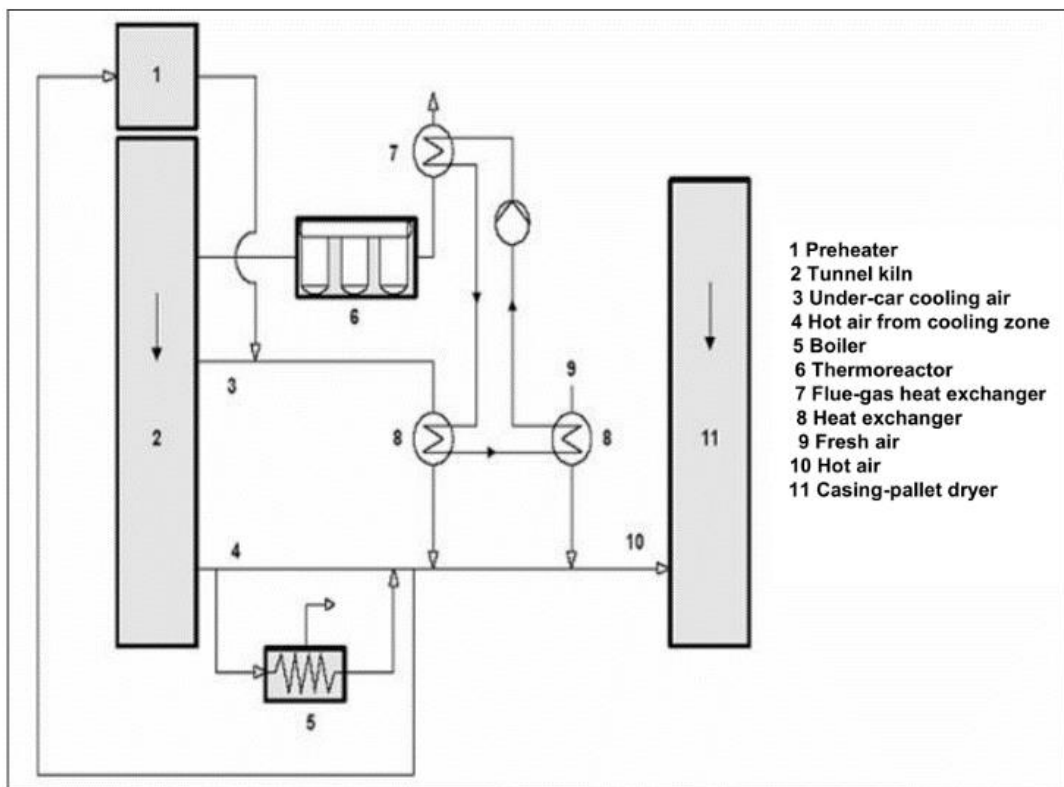


Figure 12 Schematic view of a combined heat recycling system

2.1.3.5 Cogeneration/combined heat and power plant

Cogeneration systems can be applied in the ceramic sector due to the simultaneous need of heat and electricity. Cogeneration technology has been applied in the ceramic industry to recover the waste heat from the cooling stage [8]. Figure 13 highlights a possible configuration. The hot air from the drying stage is used in the dryer and in the cogeneration system via a heat exchanger placed in the kiln cooling zone. Fresh air from the factory is injected into the system (high radiation from the kiln and the drying can be recovered). The fresh air is mixed

with the hot air coming from the cooling stage and the hot air coming from the cogeneration system and other gas engine emissions from the factory. Then, the hot air is sent into the dryer and a gas burner maintains the desired heat in the dryer. If the hot air temperature is too high, the uncooled gases from engines are withdrawn immediately. With this process, 10% to 50% of the heat input can be saved [16].[17]

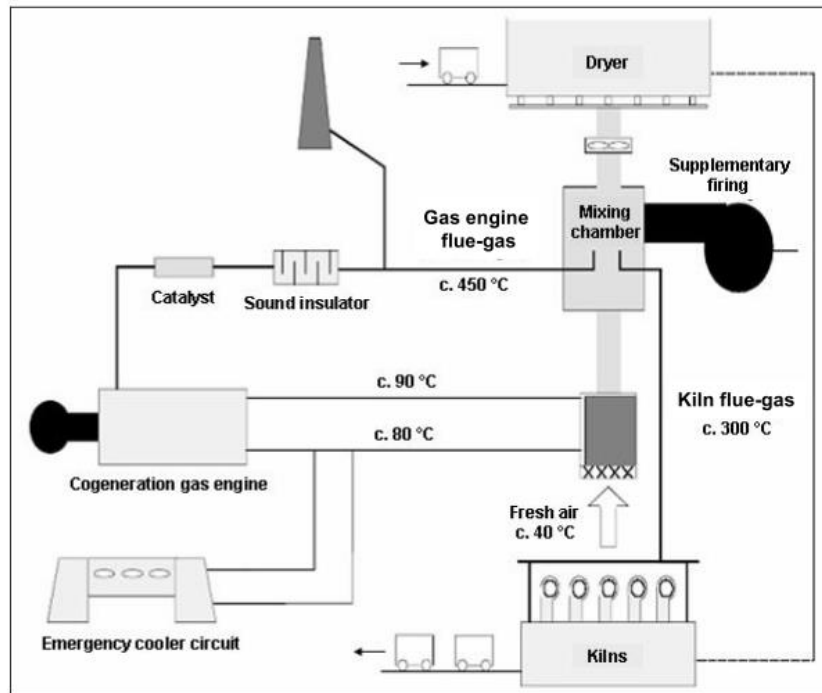


Figure 13 Schematic view of hot air generation using a cogeneration system[16].

2.1.4 Defects in the ceramic tile manufacturing sector

Defects in tile manufacturing have been investigated for the past decade. Indeed, the use of new technology in modern kilns decrease the firing time in the manufacturing process. Due to this reduction of firing time, defects appeared. The product quality is an important requirement for the client. Defects and their causes have been summarized by [18] :

Table 1 Summary of tiles defects detected[18]

Process phase	Defect	Cause
Preparation	Black core	Low grinding residue
	Size	Incorrect particles size distribution
	High H ₂ O absorption. Low bending strength	Grinding too coarse, insufficient moisture

	Stains, cratering, specks	Screening or iron removal error
Pressing	Black core	Pressure too high or not homogenous
	Small side cracks	Ejection too fast or imbalanced
	Size	Incorrect filling
	Dimensional defects	Incorrect press settings
	Low bending strength	Low pressing force, Low moisture content
	Explosions at kiln inlet	Pressing force too high, lamination
Drying	Cracks	Incorrect regulation, high temperature
	Explosions at kiln inlet	Residual moisture content high, incorrect regulation
	Glaze defects	Incorrect drier outlet temperature
	Soluble salt stains	Unsuitable drying cycle
Glazing	Cracks	Unsuitable temperatures, tiles knocked along the lines
	Explosions at kiln inlet	Excessive wetting
	Cracks in middle of the tile	Unfired tiles stored too long
	Stains, holes, cratering	Incorrect application, glaze not aged correctly
	Planarity defects	Poor glaze-body thermal expansion match
	Colour, surface defects	Engobe of poor quality
Firing	Side cracks	Preheating too fast
	Side cracks – cooling cracks	Cooling too fast

	Explosions at kiln inlet	High kiln inlet temperature
	Planarity defects	Poor temperature control
	Black heart, glaze defects	Unsuitable cycle, erroneous atmosphere
	Size	Incorrect temperature distributions
	Surfaces stains	Accumulations of glaze condensate
	Crater, holes	Preheating temperatures too high

Many investigations have been carried out to detect the defects in the ceramic tiles using different technologies such as automatic processing systems [19–21], ultrasonic inspections [22], infrared thermography [23,24]. The most common defect is convexity. Convexity can occur during the firing stage when the heating temperature is not uniform but also during the cooling stage. The cooling process in ceramic tiles is separated into three steps, the initial cooling, indirect cooling and final cooling. Even though the cooling time needs to be as short as possible, the integrity of the tiles needs to be ensured, and a higher cooling rate can cause a series of stresses resulting in the deterioration of the tile known as dunting. *Cantavella et al.* [25] investigated the behaviour of a porous body during the cooling process regarding stress and curvature. It can be observed from the results that when the temperature ranges of the tile are between 550 °C and 300 °C the curvature of the body is at a maximum as shown in Figure 14. We can also observe that the temperatures at the bottom and the top of tile are almost the same. Those temperatures correspond to the indirect cooling.

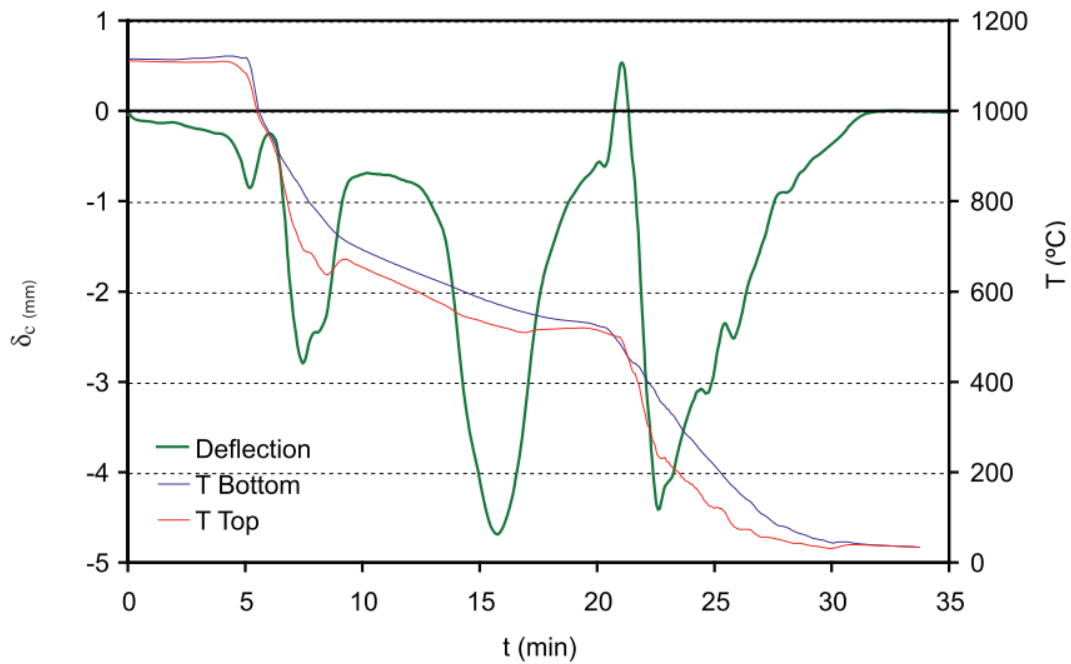


Figure 14 Calculation of the evolution of the curvature deflection in a tile body during industrial cooling [25]

The curvature deflection is impacted by different non uniformity of temperature at the surface and the temperature differential through the thickness of the tile. The temperature distribution on the tile surface will tend to increase the curvature as the temperatures in the middle of the surface will take more time to cool down than on the outsides. The tile will shrink on the outside before the middle does so, resulting in the development of stress and convexity defects. The curvature defects also occur when the glaze-body coupling temperature is not the same. The glaze will soften during heating, absorbing all the tension in the element, and solidify during the cooling, creating tensions. If the coupling temperatures of both materials are different, this will create defects such as crazing, peeling or planarity defects. [26] Convexity defects can also be managed by a better partition of heat between the bottom and the top of the tile. [18] studied the impact of the temperature below the roller in the initial section of the kiln and the temperature above the roller at the end of the firing section. By modifying those temperatures, the convexity defect decreased by 41%. Investigation into defects in ceramics tiles have been carried out but none of them propose novel solutions to improve the indirect cooling process. The indirect cooling process directly impacts on the quality of the final product and it needs to be improved. The installation of a system that could provide a uniform cooling along the tile and reduce defects in the final product needs to be investigated.

2.2 State of the art of heat pipe technology

2.2.1 Heat pipe technology overview

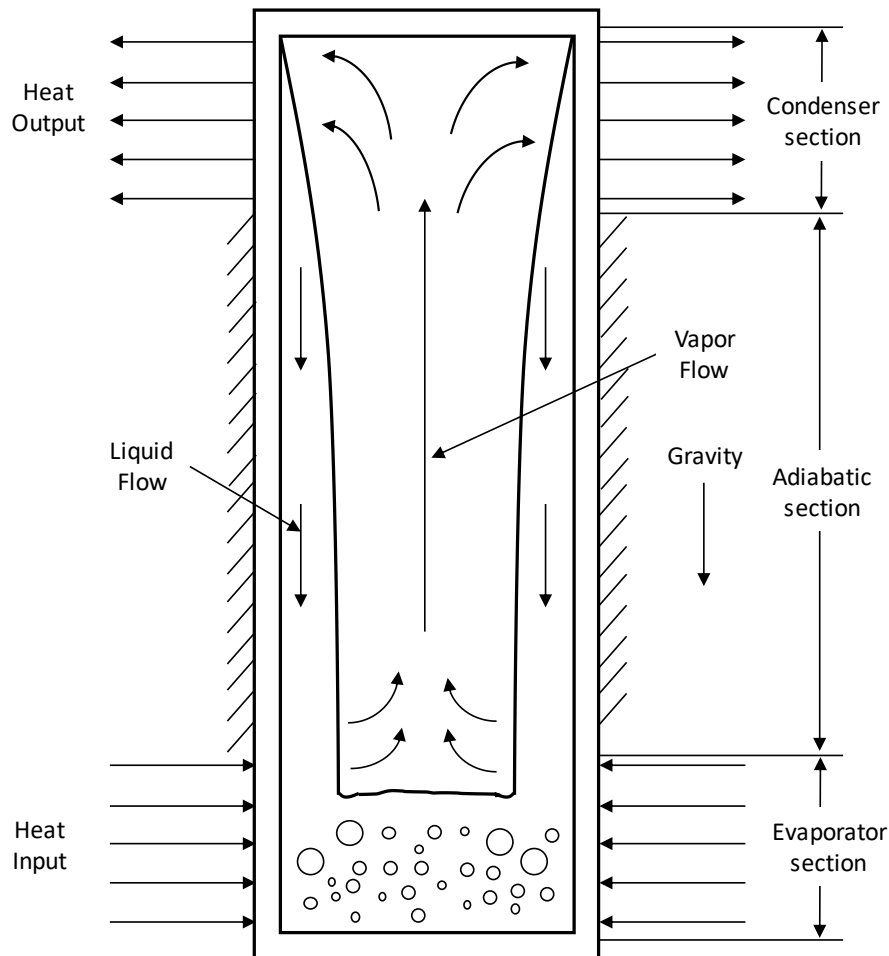


Figure 15 Schematic heat pipe principle

Heat pipes are considered as one of the most efficient and passive ways to transfer the heat from a hot source to a heat sink. A heat pipe is composed of three sections, the evaporator section where the heat is input into the heat pipe. The working fluid inside the pipe will boil and change phase into saturated vapour. This saturated vapour will travel upwards through the adiabatic section to the condenser section. The working fluid will release the latent heat to the heat sink, then, the working fluid will travel back to the evaporator. The cycle will then start again (Figure 15). The heat pipe system has multiple benefits such as an isothermal operation, avoiding any cold spots and the risk of condensation, which will increase the lifetime of the system. The heat pipe is considered as a passive device. No pumping/mechanical components are needed to send the condensed working fluid back to the evaporator. The reactivity of heat pipes is higher than other heat transfer system, which offers different control options.

Due to their advantages such as isothermal surfaces, high thermal conductivity and the independency of each heat pipe in the system, the heat pipe heat exchanger technology is a good candidate for most of the corrosive, high fouling and high temperature exhaust applications.

Heat pipe systems are composed of different shapes and technologies to move the fluid in the tubes.

Heat pipe technology can use two methods to move the fluid and the vapour between the condenser and the evaporator. Gravity can be used to send the fluid back to the condenser, this method is the easiest and cheapest way. The second way is to use a wick structure in the inner wall of the heat pipe. This method allows the possibility of having the evaporator section above the condenser section.

2.2.1.1 Heat pipe technology

Wickless heat pipe

Thermosyphon

Thermosyphon heat pipes rely on two-phase heat transfer to transfer heat from the evaporator section to the condenser section. The return of the liquid relies only on gravity, which allows the thermosyphon not to have a wick, thus making the manufacturing of the heat pipe cheaper than the other technology. The thermosyphon presents many advantages such as passive means to transfer heat, near isothermal surfaces, high conductivity etc. The thermosyphon can handle different working fluids such as water, refrigerants, liquid metals, or thermal oils. The effects of the types of working fluid was investigated by [27]. Filling ratios were investigated. Water, FC-84, FC-77 and FC-3283 were tested in a 200 mm long pipe with an inner diameter of 6mm. The evaporator and condenser lengths were respectively 40 mm and 60 mm. The results highlighted the capacity, at higher heat fluxes, of water as a working fluid. At low heat fluxes, FV-84 outperformed water; this is due to a lower boiling point compared to the other working fluids. Thermosyphons have also been investigated using R134a and R404a by [28] using CFD modelling of the two phase concept. The aim was to investigate the behaviour of low temperature boiling point fluids to transfer heat in an efficient way. It was highlighted that the refrigerant was able to transfer heat at low temperature and the CFD model developed was in good accordance with the experimental results

The use of thermosyphon to transfer heat from a heat source to a heat sink have been widely investigated in different industrial and commercial applications. Heat pipe applications in industrial setups vary from ceramics to metal and pharmaceutical.

Variable conductance heat pipe VCHP

Variable conductance heat pipes allow a better control of the heat flux by adding a variable amount of working fluid into the evaporator section or a reservoir of inert gas attached to the condenser that will reduce the space occupied by the vapour in the heat pipe. VCHPs rely on the use of an inert gas on the condenser section. By modifying the heat transfer area in the condenser section, the heat flux can be tuned to respect the temperatures of the condenser and the evaporator. This technique allows a better control of the temperatures of both sections and a modification of the heat flux independently of the power of the heat source. An illustration of the process can be seen in Figure 16.

[29] developed a VCHP for the thermal management of vehicles. The aim of the investigation was the reduction of engine energy consumption after a cold start through the control of the heating and cooling cycle of the oil. The results shown the importance of the angle to have a satisfactory heat transfer between the condenser and evaporator. VCHPs have also been applied by [30] to air pre-heating in corrosive and high particulate environments. The results highlighted that the VCHP has an excellent performance on anti-corrosion and particulates deposition. The inclination of the VCHP was also investigated. The effect of the VCHP on the vehicle as it is operated can have a large impact on the system performance. The results highlighted that a small inclination angle improved the performance of the heat pipe as the gravity aid the liquid to return to the evaporator section.

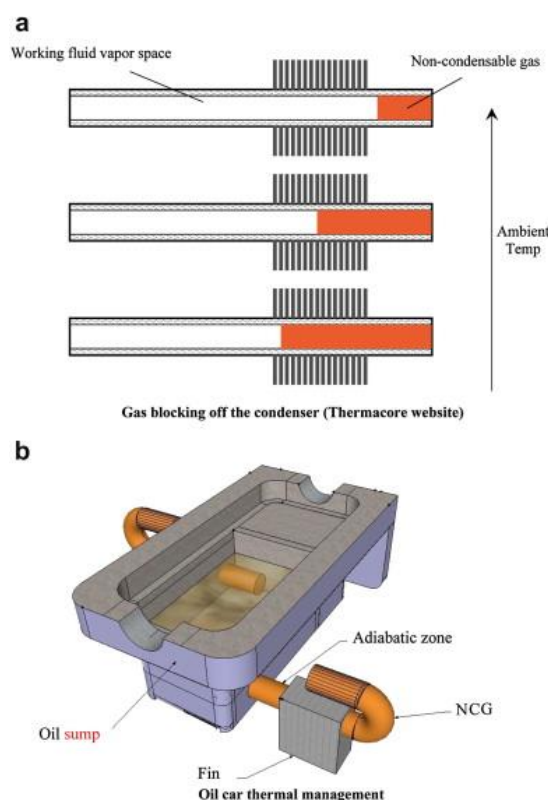


Figure 16 Variable conductance heat pipe [31]

Oscillating or pulsating heat pipes (PHP)

The oscillating heat pipe is a recent development in heat pipe technology. The heat transfer mechanism of OHPs rely on the coexistence of vapour bubbles and liquid in the evaporator section as seen in Figure 17. The heat pipe consists of a single tube with turns where the condenser and the evaporator are located. The vapour will form at the hottest spot of the evaporator section, the bubble will start to expand and the vapour pressure will increase. The bubble will then reach the condenser where the pressure is lower. The condenser will extract the heat and condense the vapour back to liquid. The liquid will then travel back to the evaporator section. The OHP presents some advantages such as the lack of wicks in both evaporator and condenser sections. The system is completely passive as no pump is needed to force the liquid in the evaporator. OHPs can operate at higher heat fluxes than wicked heat pipes. Four types of OHP can be identified, closed loop OHP, closed loop with check valve, open loop OHP and pump assisted OHP[32]. Recent improvements in the PHP technologies have been summarized by [29].

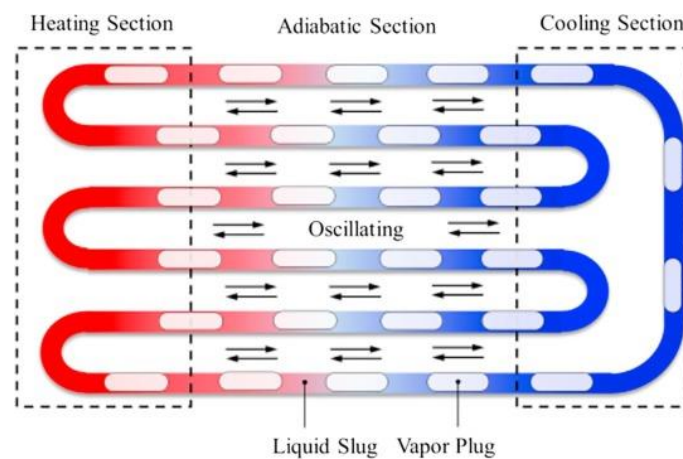


Figure 17 Schematic of a Pulsating Heat Pipe [33]

Wrap-around heat pipe (WLHP)

Wrap around heat pipes are designed to wrap around a cooling coil in air conditioning units for buildings. WLHPs rely on gravity to send the working fluid back to the evaporator section. An illustration of the WLHP can be seen in Figure 18.

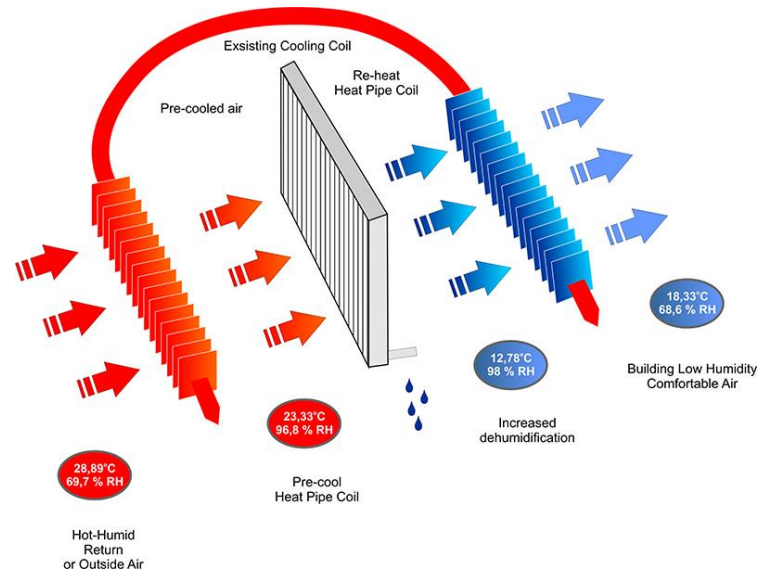


Figure 18 Wrap-around heat pipe schematic

The WLHPs aim to reduce the humidity content reaching the cooling coil by pre-cooling the air before the chiller unit. The air exiting the chiller is most of the time too cold to be sent to the building. In order to warm up the air to the desired temperature, the condenser section of the heat pipe is located after the chiller. This technology can be used for air conditioning in buildings, in hot countries such as in coastal regions in the Middle East. A significant reduction in energy consumption can be achieved due to the precooling and dehumidification of the air before the chiller unit and to the reheating done by the heat pipe instead of a traditional reheating system [34]. The technology was investigated by [35] using R134A as a working fluid. The use of a refrigerant as a working fluid shown good results and an overall effective thermal resistance as low as 0.078 °C/W. The maximum heat flux of the heat pipe was never reached during the experiment which shows a good potential for heat transfer capacity of such systems. [36] investigated the use of water instead of refrigerant in the WLHP which will decrease the overall price of the equipment while decreasing the environmental impact of the system lifetime. The test rig developed was composed of a WLHP, a chiller unit, a heater at the inlet of the ducting and a fan at the outlet of the ducting. The results showed an increase in effectiveness of the system compare to R134A, but the results might not apply for other types of coils. Hence more investigations will need to be carried out for this technology to be applied on an industrial scale. A full scale application of the WLHP can be seen in Figure 19.

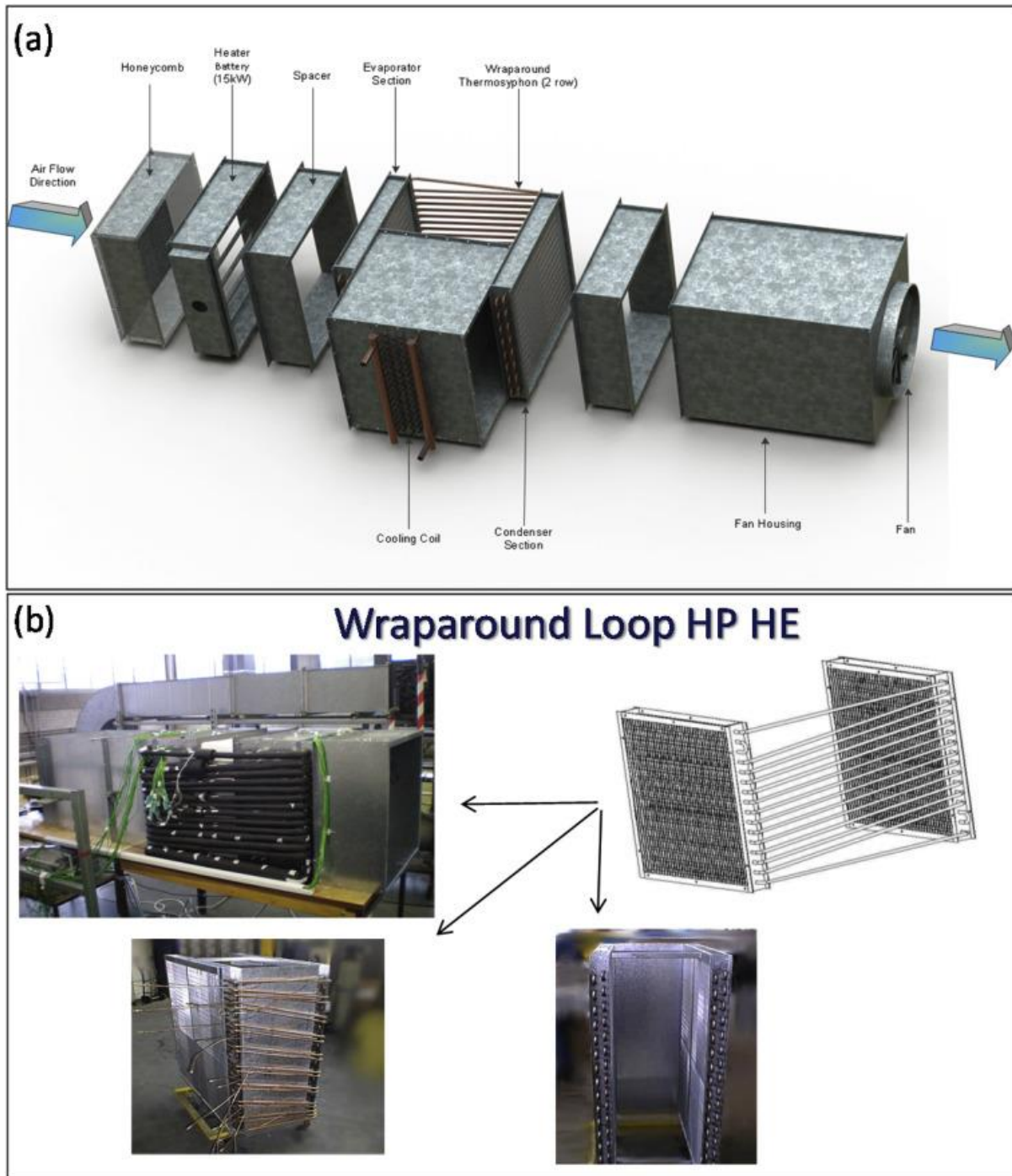


Figure 19 (a) Exploded assembly details, (b) mechanical design of the wraparound heat pipe [36]

Heat Pipe Heat Exchanger (HPHE)

Heat pipe heat exchangers are mainly used in industrial applications to recover heat from a flue gas exhaust to generate hot air, water or any heat transfer fluid. The heat pipe heat exchanger is composed of rows of thermosyphons arranged in a bundle. The heat pipe can be finned if the HPHE needs to be compact. The main advantage of the heat pipe heat exchanger is the total separation between the hot fluid or gas and the heat sink. Indeed, in order to have cross contamination, one of the heat pipes in the tube bundle will have to open

in both the evaporator and the condenser section. This is unlikely to happen. Also, heat pipes have an essentially uniform temperature along the evaporator and the condenser thus, no cold spot can form avoiding condensation problems that can occur in flue gases with sulphuric acid for example. The Heat Pipe Heat Exchanger is a recent development in heat pipe technology as heat pipe manufacturing costs used to be rather high. The price of heat pipes has been reduced over the years which now make the HPHE a good and affordable option for industries. An illustration of the HPHE can be seen in Figure 20.

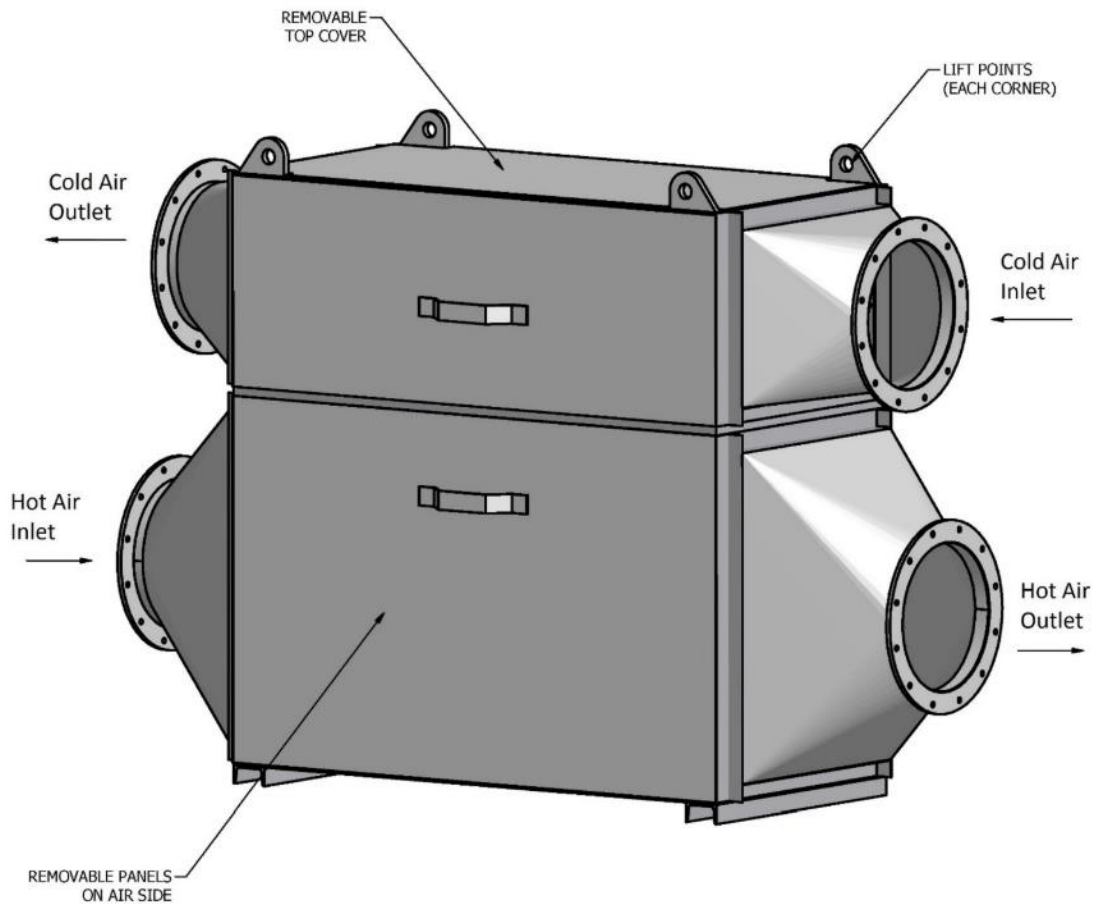


Figure 20 HPHE in the ceramics industry [7]

2.2.1.2 Wicked heat pipe

A wicked heat pipe is composed of a tube, working fluid and a wick structure inside the tube which uses capillarity to transport the fluid from one end of the heat pipe to the other. Wicks are used mainly in small scale applications such as electronics (computer cooling systems) or cryogenic applications[37]. Also, the wick allows the evaporator section to be above the condenser section. Different types of wicks have been developed to accommodate the working fluid and/or improve the capillarity effect and the overall heat transfer capability. The three properties of the wicks that will be important for the heat pipe design are:

- Minimum capillary radius.
- Permeability
- Effective thermal conductivity

A high thermal conductivity and permeability coupled to a low minimum radius are contradictory in the design of a wick. A balance needs to be investigated for the design of wick heat pipe between all the parameters to allow an optimal working condition. Different types of wick are shown in Figure 21.

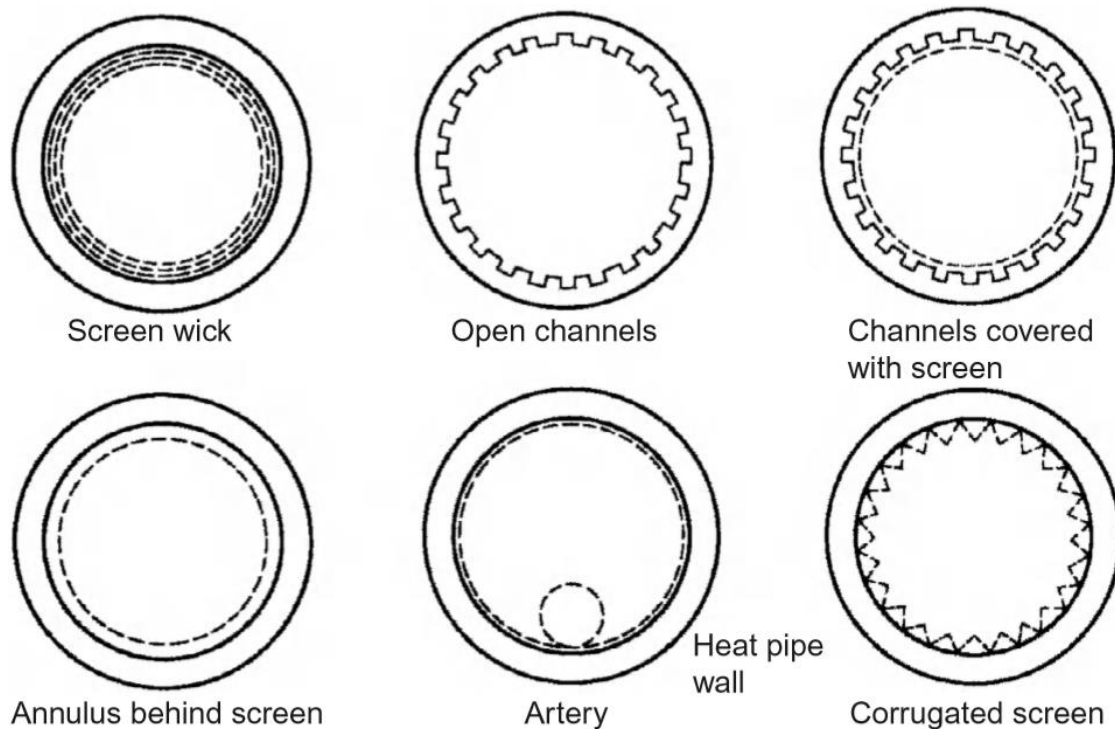


Figure 21 Selection of typical wick structure [38]

Some recent innovations have been made in the development of new wick structures involving the use of nanoparticles to modify the characteristics of the wick [39]. [40,41] reported a significant improvement in capillarity performance, in heat transfer coefficient and critical heat flux for the use of nanostructure micro wick.

Loop heat pipe (LHP)

Loop heat pipes can be used for applications where the evaporator section is located next to or above the condenser section. The inside of the tube is composed of channels where the liquid flows using the capillarity effect. LHPs are mainly used as thermal links between cryo coolers and the receiver components, LHP are not sensible to vibration, increase the thermal transport possibility, etc. An illustration of LHP can be seen in Figure 22.

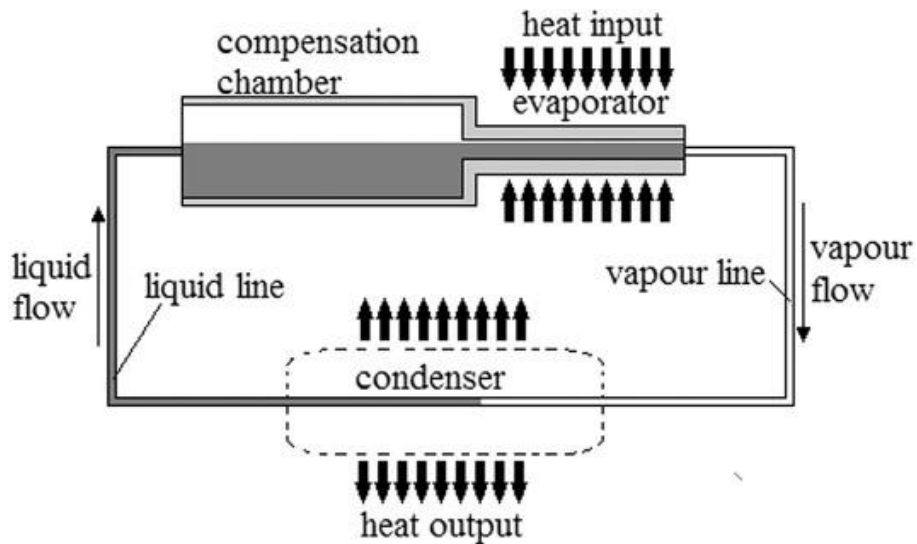


Figure 22 Loop heat pipe [25]

The main benefit of LHPs is the ability to work in an anti-gravity way. This aspect was investigated by [42]. A loop heat pipe exposed to high heat fluxes were tested in six different configurations, as shown on Figure 23.

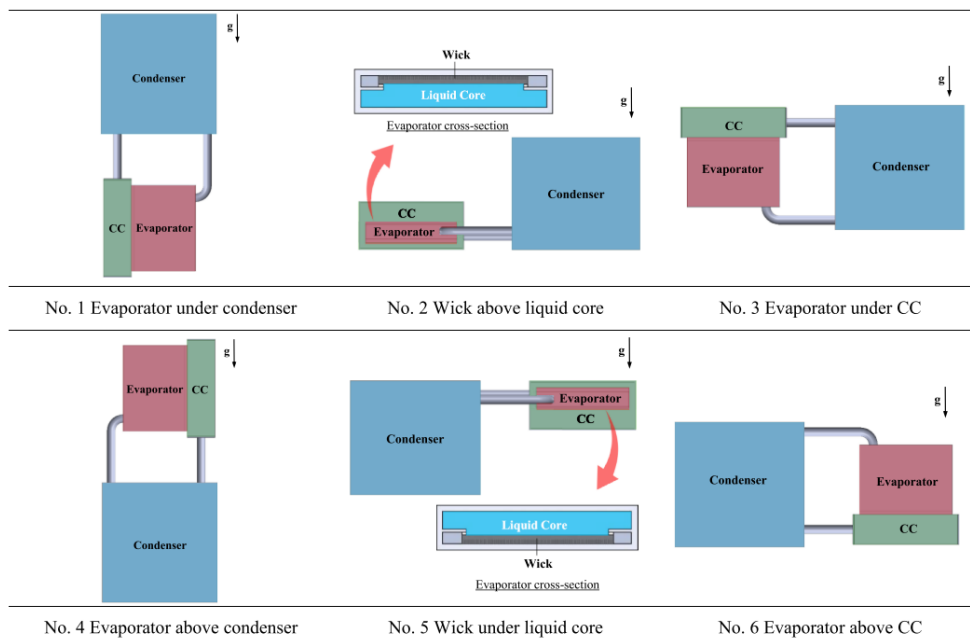


Figure 23 Six LHP orientations [42]

It was observed that for the six orientations tested, the LHP started up at 50W. The maximum heat transfer capacity was reached at 280 W for case No. 5. The lowest thermal resistance was observed in cases No.2 and No.5 with respectively 0.094 K/W and 0.064 K/W. The results in this paper show the importance of the location of the condenser, evaporator and compensation chamber (CC) on the heat transfer capacity of the LHP. It was also concluded

that the LHP was able to transfer a heat load when the evaporator section is above the condenser section.

The impact of the distance between the condenser and evaporator section of a loop heat pipe under anti-gravity conditions was studied by [43]

Grooved wick heat pipe

A grooved heat pipe is characterised by a series of axial grooves which allow the transport of the working fluid. These grooves are located in the inside of the heat pipe tube. The groove structure is made by broaching or extrusion which can be expensive as a mould needs to be made for the extrusion[44]. The shape of these structures can take different forms such as circular, trapezoidal, triangular or rectangular [45]. It can be noted that the capillary pressure is small compared to other wicked heat pipes such as sintered or screen heat pipes. The structure of the groove is rather simple compared to the other heat pipe wicks, the structure is composed of simple slots. Also, the size of the structure is larger than in other type of wicks [46].

The aim of these heat pipe structures is to work as gravity aided, horizontal and anti-gravity working conditions. The anti-gravity operating condition is limited to a 5-degree angle to horizontal. The best-case scenario for a grooved heat pipe is either vertical or horizontal [46]. Cross sections of a grooved wick heat pipe can be seen in Figure 24.

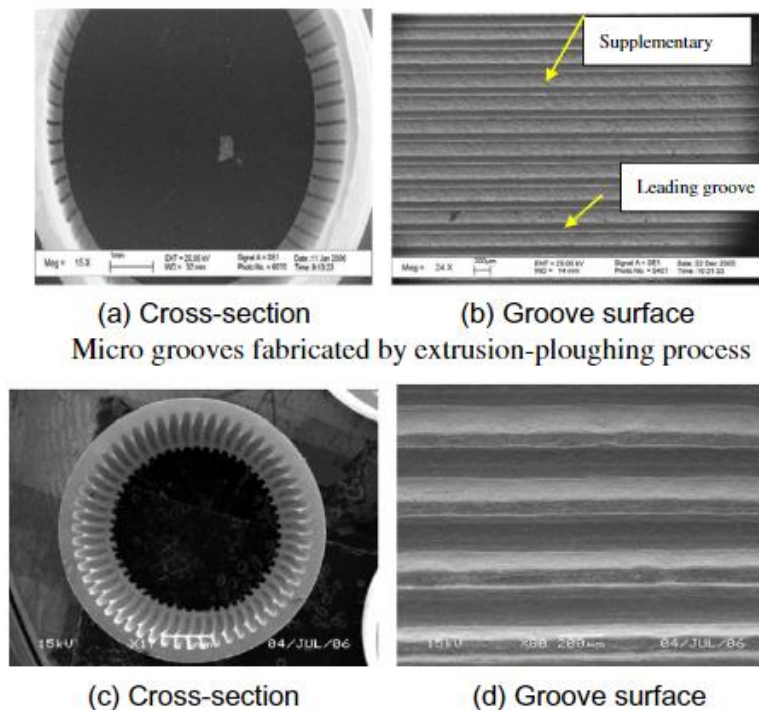


Figure 24 Cross section of a grooved heat pipe [44]

Sintered wick heat pipe

The heat pipe structure is made of a copper tube as a shell and a powder in the inner wall. The heat pipe is made using a mandrel that is inserted inside the copper tube during manufacture with a gap between the inner tube and the mandrel. Copper powder is inserted inside the void and vibrated in order to properly fill all the area [47]. The tube is then placed in a sintering oven that will heat up the copper powder in order to fix it on the heat pipe wall. The process will create a sponge like structure with micro air pockets in the entire structure. The mandrel is then removed leaving a large void area in which the vapour can travel.

The technique creates a heat pipe with a strong capillary force, much greater than for other types of structures. Therefore, this type of structure can be used for heat fluxes up to 300 W/cm^2 [48]. In addition, the heat pipe can also carry the working fluid in an anti-gravity vertical orientation. Thus, the heat pipe is mainly used for anti-gravity and space applications [49]. A cut of a sintered heat pipe can be seen in Figure 25.



Figure 25 Cut view sintered heat pipe

Screen mesh heat pipe

This type of structure is composed of a tube and a wire type copper mesh. This heat pipe is made by inserting the woven mesh inside the tube using a mandrel in order to leave a space in which the vapor can travel. The wick will be filled with the working fluid travelling back to the evaporator section. This heat pipe structure can work in vertical (gravity aided) and horizontal orientations. As with the grooved heat pipe, the heat pipe can work with a maximum angle of 5 degrees to the horizontal. This type of heat pipe is capable of transporting a maximum heat flux of 60 W/m^2 [49].

2.2.1.3 Heat pipe design

Working fluid

The selection of the working fluid in a heat pipe is directly linked to the properties of the fluids. The properties of the fluid will have a direct impact on the thermal behaviour and capacity of the heat pipe and the compatibility of the shell and the fluid at working temperatures. The fluid characteristics that will need to be considered for the selection of the fluid are:

- Compatibility with the wick and the wall material
- Good thermal stability
- High latent heat
- High thermal conductivity
- Low liquid and vapour viscosity
- High surface tension

Table 2 lists some of the common working fluids used for heat pipes depending on the application temperature.

Table 2 Working fluids and temperature ranges

Fluid	Symbol/ Formula	Melting Point, (°C)	Normal Temp (°C)	Boiling	Critical Temp (°C)	Critical Pressure, atm	Useful Range (°C)
Helium	He	-272.2	-268.9		-267.95	2.24	-271 to -269.1
Hydrogen	H	-259.14	-252.87		-239.95	12.8	-259 to -242
Neon	Ne	-248.6	-246.08		-228.75	27.2	-246 to -236
Nitrogen	N ₂	-210	-195.8		-146.9	33.5	-203 to -170
Oxygen	O ₂	-218.3	-182.9		-118.6	49.8	-200 to -154
Methane	CH ₄	-182.4	-161.7		-82.5	510.8	-182 to -113
Ethane	C ₂ H ₆	-183.2	-88.5		32.4	48.2	-123 to -33
Freon R22	CHClF ₂	-175.42	-159.15		96.1	49.1	-80 to 50
Freon R410a		-155	-48.5		72.8	48.85	-100 to 35
Propane	C ₃ H ₈	-187.69	-42		96.8	41.9	-85 to 57
Ammonia	NH ₃	-77.73	-33.34		132.4	111.3	-65 to 100
Freon R134a	CH ₂ FCF ₃	-103.3	-27		101	40.06	-75 to 50
Freon R408a		N/A	-44.4		83.3	43.65	-82 to 48
Acetone	C ₃ H ₆ O	-94.3	56.1		235	47.37	0 to 120
Methanol	CH ₃ OH	-97.6	64.7		240	78.5	10 to 130
Ethanol	C ₂ H ₆ O	-114.35	78.35		241	62.17	0 to 130
Water	H ₂ O	0	100		373.95	217.7	10 to 287
Toluene	C ₇ H ₈	-95	111		318.64	40.5	50 to 200
Dowtherm A		12	257.1		497	30.9	150 to 395
Caesium	Cs	28.44	671		1664.85	92.77	450 to 900
Potassium	K	63.38	759		1949.85	157.9	500 to 1000
Sodium	Na	97.72	883		2299.85	345.4	600 to 1200
Silver	Ag	961.78	2212		N/A	N/A	1800 to 2300

The other deciding factor for the selection of the working fluid is the merit number. The merit number is used to determine, for a maximum capillarity heat transport capability, the best fluid possible for the application temperature range. In order to calculate this number, it is assumed that vapour pressure and gravity can be neglected. The merit number for a wick heat pipe can be determined by (1)

$$\Phi_1 = \frac{\rho \sigma h_{fg}}{\mu_f} \quad (1)$$

where ρ is the density of the fluid (kg/m^3), h_{fg} is the latent heat of evaporation (J/kg), σ is the surface tension (N/m) and μ_f is the dynamic viscosity of the fluid (kg/m-s)

The results for commonly used working fluids in wicked heat pipes are presented in Figure 26

The figure of merit for gravity heat pipes (thermosyphons) is presented in Equation (2)

$$\Phi_2 = \left(\frac{L \lambda_l \rho_l}{\mu_l} \right)^{1/4} \quad (2)$$

where L is the specific latent heat of vaporisation (J/kg), λ_l is the thermal conductivity (W/mK), ρ_l is the density of the fluid (kg/m^3) and μ_l is the dynamic viscosity of the fluid (kg/m-s).

the results for common fluid used in thermosiphon can be seen in Figure 27.

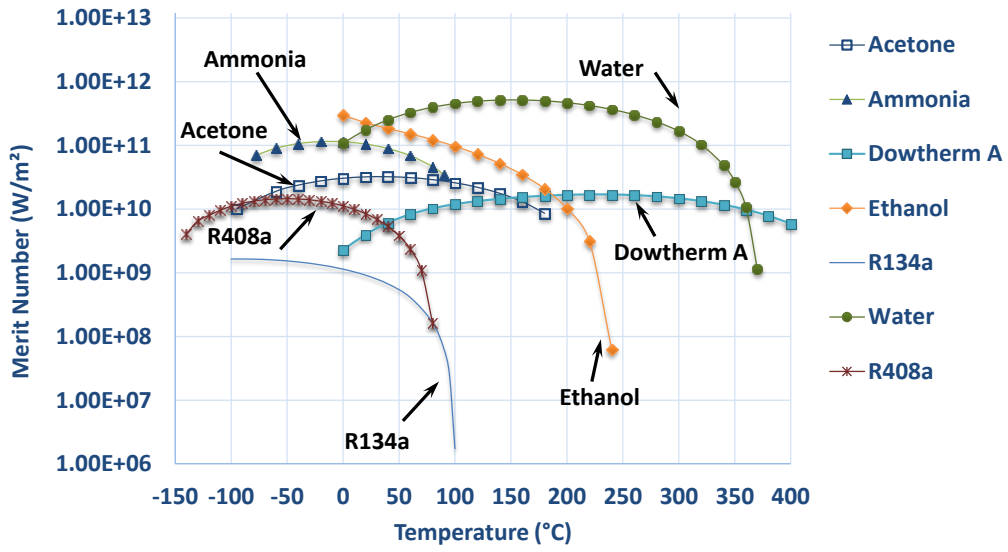


Figure 26 Figure of merit for common working fluids in wicked heat pipes

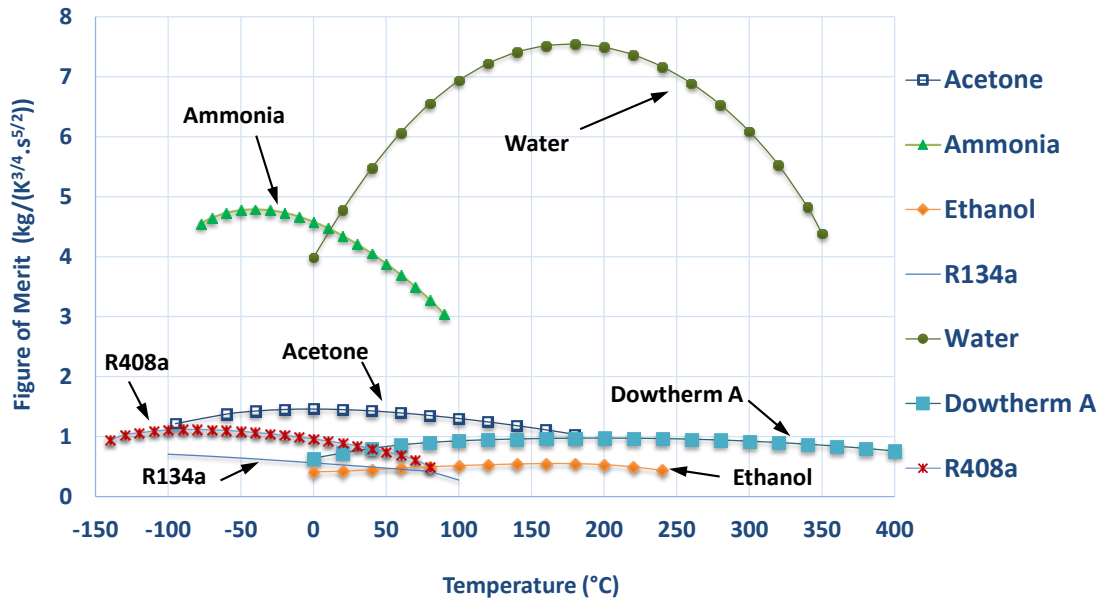


Figure 27 Figure of merit of common working fluids used in thermosyphons

Heat pipe shell

The compatibility between the shell and the working fluid will play an important role to reduce the generation of non-condensable in the heat pipe. A list of different compatibility between working fluids and shell material can be seen in Table 3.

Table 3 Compatibility between materials and working fluids

Working fluid	Compatible material	Incompatible material
Acetone (Pure)	Aluminium, Stainless Steel	
Methanol (Pure)	Stainless Steel, Copper	Aluminium, Titanium
Water	Copper, Monel, Nickel, Titanium, Stainless Steel, Carbon steel	Aluminium, Inconel
Dowtherm A	Aluminium, Stainless Steel, Titanium, Carbon steel	Copper, copper nickel

2.2.1.4 Heat pipe limitations

In order to choose a proper shell material and dimensions for the heat pipe it is important to consider the limitations of heat pipe technology. The limitations will be considered during the design phase of the heat pipe. Figure 28 illustrates the different limitations of the heat pipe using the axial heat flux and the temperature.

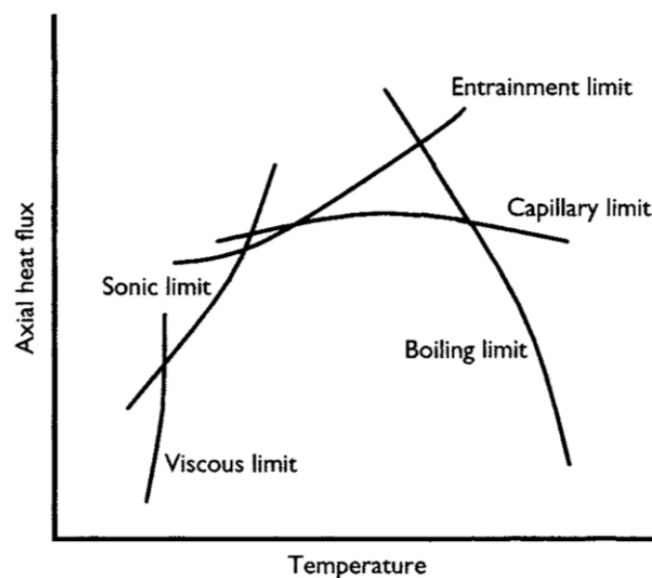


Figure 28 Operational limitations

Wickless heat pipe

Entrainment limit (flooding limit)

In a thermosyphon the entrainment limit is linked to the evaporator flooding limit. The flooding limit occurs when a high velocity of the vapour provokes an instability in the liquid fill by a high value of interfacial shear, preventing the condensate returning to the evaporator section. This will cause a dry out of the evaporator section, limiting the heat transfer capability of the heat pipe. Correlations have been developed by *Faghri et al* [50] to determine the maximum heat transfer

$$Q_{max} = Kh_{fg}A[q\sigma(\rho_l - \rho_v)]^{1/4}[\rho_v^{-1/4} + \rho_l^{-1/4}]^{-2} \quad (3)$$

where K is a dimensionless number (Kutateladze number)

$$K = R'tanh^2Bo^{1/4} \quad (4)$$

where Bo is the dimensionless Bond number

$$Bo = \left[\frac{\sigma}{g(\rho_l - \rho_v)} \right] \quad (5)$$

Boiling limit

At large filling ratios and high radial heat flux, the boiling limitation can occur. When the radial heat flux is high, the bubble generation will be high as well. If the radial heat flux is increased, more bubbles will be generated until a critical heat flux is reached. At the critical heat flux, the vapour bubbles generated prevent the contact of the liquid with the heat pipe wall. This phenomenon can be compared to film boiling which results in a rapid increase of the heat pipe wall temperature. *Imura et al.* [51] suggested correlations for the boiling limit

$$Q_{b,max} = Ku_{BL} \cdot \pi \cdot D_i \cdot l_e \cdot hf g \cdot \rho_v^{0.5} [g\sigma(\rho_l - \rho_v)]^{1/4} \quad (6)$$

where:

$$Ku_{BL} = 0.16 \left[1 - \exp \left\{ \left(-\frac{D_i}{l_e} \right) \left(\frac{\rho_l}{\rho_v} \right)^{0.13} \right\} \right] \quad (7)$$

Wicked heat pipe

Viscous limit

The viscosity of the fluid is an important fluid property for heat pipe using a wick to transport the fluid back to evaporator. At low heat inputs, the viscosity of the fluid will have a large impact on the heat pipe thermal performance. The viscosity will thus impact on the start-up of the heat pipe [52]. A higher fluid viscosity will lead to a lower fluid movement from the condenser to the evaporator due to higher shear forces, causing friction[53]. *Hua Han et al* [54]. investigated the behaviour of a PHP under different working fluids and it was shown that the dynamic

viscosity of the fluid was the main property to affect the heat transfer capability of the PHP [54]. In order to determine if the dynamic viscosity of the fluid reached the acceptable limit, Dunn and Reay [55] discussed the limit and suggested the following criterion

$$\frac{\Delta P_v}{p_v} < 0.1 \quad (8)$$

The maximum heat transfer under the vicious limit can be determined using the equation based on the Busse analysis [37,56]

$$Q_v = \frac{\pi r_v^4 h_{fg} \rho_v P_v}{16 \mu_v l_{eff}} \quad (9)$$

Where $\Delta P_{c,max}$ is the maximum capillary pressure equal to:

$$\Delta P_{c,max} = \frac{2\sigma}{r_{eff}} \quad (10)$$

The maximum heat transfer rate for the boiling limit can be expressed as

$$Q_{b,max} = \frac{4\pi l_{eff} k_{eff} \sigma T_v}{h_{fg} \rho_v \ln\left(\frac{r_i}{r_v}\right)} \left(\frac{1}{r_{nb}} - \frac{1}{r_{eff}} \right) \quad (11)$$

The nucleation radius r_{nb} is 10^{-7} m for conventional heat pipes [50].

Sonic limitation

The analogy between the sonic limit in a heat pipe and a converging-diverging nozzle can be made. The difference is that in a converging-diverging nozzle, the mass flow rate remains the same while the velocity increases. In a heat pipe the mass flow rate will depend on the rate of evaporation. A higher rate of evaporation will increase the mass flow rate of vapour in the same section as a low rate of evaporation thus increasing the velocity of the vapour. The vapour velocity in the heat pipe will vary depending on the heat input in the evaporator section. If the velocity of the steam reaches the sonic limit, any increase in the heat rejection rate in the condenser section will not reduce the temperature of the evaporator. It will only decrease the temperature of the condenser section. The maximum heat transfer under maximum velocity below sonic can be expressed as [57]

$$q_{s,m} = A_v \rho_v \lambda \left(\frac{\gamma_v R_v T_v}{2(\gamma_v + 1)} \right) \quad (12)$$

The entrainment limit

In a thermosyphon or wicked heat pipe, the fluid and the vapour are travelling in counter flow. When the vapour velocity is high, droplets of liquid can be picked up by the vapour which can

cause a dry out of the evaporator section. In order to avoid this phenomenon, a commonly cited criterion is the Weber number, defined as the ratio of the viscous shear force to the force resulting from the liquid surface tension,

$$We = \frac{2(r_{h,w})\rho_v V_v^2}{\sigma} \quad (13)$$

To prevent this entrainment of the droplet by the vapour, the Weber number must be below 1. The maximum transport capacity based on entrainment limitations can be determined by relating the vapour capacity and the heat transport capacity

$$V_v = \frac{q}{A_v \rho_v \lambda} \quad (14)$$

$$q_{e,m} = A_v \lambda \left(\frac{\sigma \rho_v}{2(R_{h,w})} \right)^{1/2} \quad (15)$$

Boiling limitation

For very high radial heat fluxes, the formation of nucleate boiling in the wick can occur, the bubble of vapour will then be trapped in the wick section of the heat pipe. The vapour bubble will block the liquid which can cause a dry out of the evaporator section. The boiling limit can be defined using the theory for nucleate boiling. Two phenomena occur during the nucleate boiling. The first is the bubble formation and the growth of the bubble. This phenomenon is governed by the size and the number of bubbles on a surface. The second is the collapse of the bubbles depending on the fluid temperature. In the case of the boiling limitation, the Clausius-Clapeyron equation can be used to determine the maximum heat flux

$$Q_{b,max} = \frac{2\pi l_{eff} k_{eff} T_v}{h_{fg} \rho_v \ln \left(\frac{r_i}{r_v} \right)} \left(\frac{2\sigma}{r_{nb}} - \Delta P_{c,max} \right) \quad (16)$$

Capillarity limit

A wicked heat pipe uses the capillarity effect to move the liquid and the vapour from the condenser and the evaporator. For a wick to sustain this process, the net capillarity pressure difference between the condenser and the evaporator sections has to be higher than the sum of all the pressure drops that will occur in the heat pipe. The pressures losses are presented in the following equation

$$\Delta P_{cap,max} \geq \Delta P_l + \Delta P_v + \Delta P_g \quad (17)$$

The difference of pressure generated by the wick structure can be expressed by the Laplace-Young equation

$$\Delta P_{cap} = \frac{2\sigma}{r_{eff}} \cos\theta \quad (18)$$

Where θ is the contact angle of the fluid-wick combination, when $\theta = 0^\circ$, then the surface is perfectly wet. r_{eff} is the effective pore radius of the wick.

The maximum capillarity heat transfer can be expressed by the following equation [50]

$$Q_{cap} = \frac{\sigma_l \rho_l l_v}{\mu_l} \frac{KA_{wk}}{l_{eff}} \left(\frac{2}{r_{eff}} - \frac{\rho_l g l_t \cos\varphi}{\sigma_l} \right) \quad (19)$$

Condenser limit

At steady state operation, the heat input in the evaporator is equal to the heat output from the condenser section. For high operating temperatures, the dominant heat transfer mode in the condenser section is radiation. The heat transfer from the condenser can be expressed as

$$Q_{c,radiation} = \pi D_o l_c \varepsilon_c \sigma_{Boltzman} (T_c^4 - T_\infty^4) \quad (20)$$

where ε is the emissivity of the condenser outer wall, l_c the length of the condenser section and D_o the outer pipe wall diameter.

For low temperatures, the heat transfer in the condenser section is dominated by convection. The condenser limit will be reached when the condenser is not able to extract the heat input.

2.2.2 Heat pipe applications

2.2.2.1 Heat pipes in heavy industrial applications

Heavy industrial applications such as metal casting and aluminium forging require robust and reliable equipment. The use of heat pipes within the metal industry have been investigated by [58]. A flat heat pipe heat exchanger was composed of rows of stainless-steel tubes interconnected by a collector and a shell and tube heat exchanger section. The heat pipe was installed on top of hot metal rods. A photo of the system installed can be seen in Figure 29.



Figure 29 Flat Heat Pipe on cooling line

The heat transferred through radiation to the heat pipe was then transferred to the heat sink. The water was then reused in the process. The system was able to recover up to 15.6 kW at a water flow rate of 0.28 kg/s. The heat source was hot rods at 450 °C. The maximum temperature of the surface of the heat pipe heat exchanger was 160 °C. The use of a radiantly heated heat pipe for waste heat recovery is a good way to extract heat in an efficient way. The currently developed heat pipe had a constant spacing between the tubes, which implies that the heat transfer surface was the same along the path of the hot rod. The modification of the spacing between the tubes could lead to a better control and tuning of the cooling rate and a more uniform and smooth cooling.

[59] investigated the potential of using a heat pipe heat exchanger to recover the hot air from the cooling stack of a roller hearth kiln. In this paper, a heat pipe heat exchanger installation was simulated. The system was composed of rows of thermosyphons with fins. The system was able to recover 863 MWh per year of thermal energy to use to heat up the hot stream of the dryers, thus saving about 110,600 Sm³ per year of natural gas, which represents a total saving of 22,000 euro.

Meena et al. [60] investigated the use of closed-loop oscillating heat pipes as air preheaters to reduce the relative humidity in the drying process. The heat pipe system was composed of copper tubes 3.58 m long with an internal diameter of 0.002 m. The evaporator section and

condenser section were 0.19 m long with an adiabatic section of 0.08 m. The working fluid used in the heat pipe was refrigerant R134a with a filling ratio of 50%. The flue gas air velocity tested was 0.5, 0.75, and 1.0 m/s at temperatures of 50, 60 and 70 °C with a relative humidity of 100%.

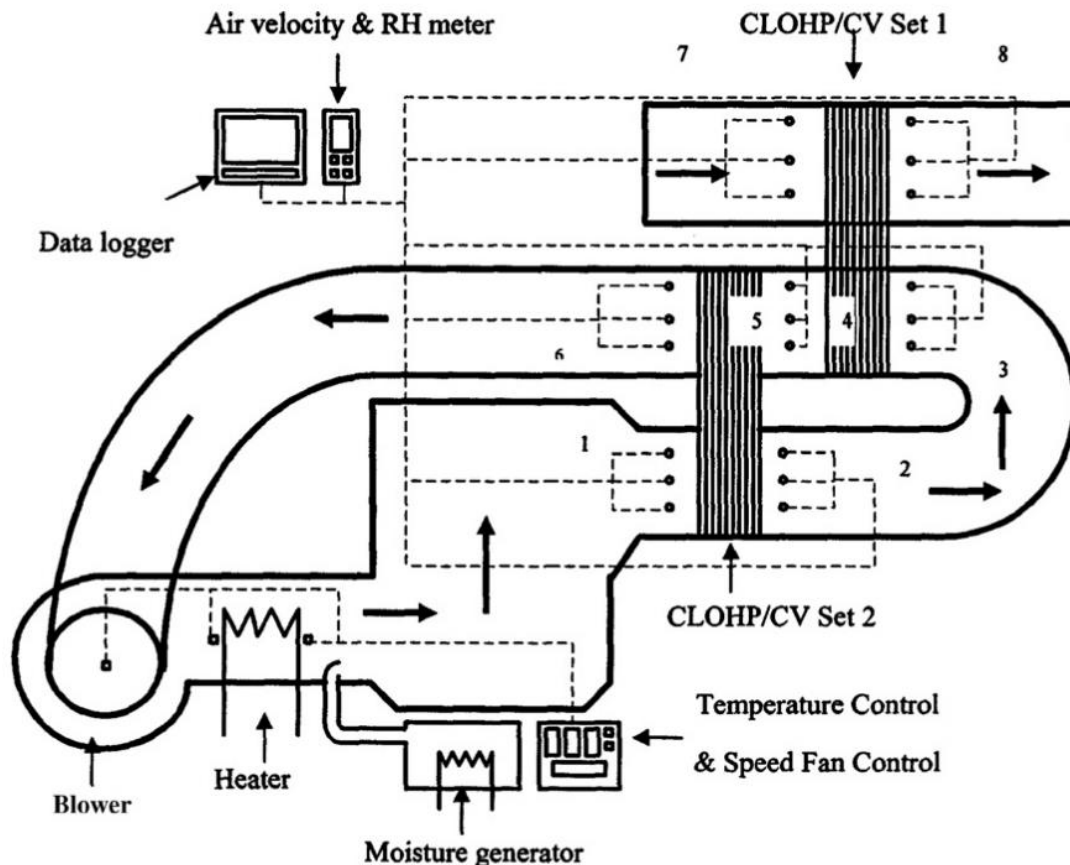


Figure 30 Test rig Closed-loop heat pipe

The results showed a reduction in the relative humidity after the heat pipe system from the range of 89 to 100% to 54 to 72%. The use of loop heat pipes in a dryer technology is effective but the cost of such heat pipes in large quantity will end up being too expensive to install on an industrial scale compared to thermosyphon systems. An illustration can be seen in Figure 30.

Lukitobudi et al. [61] used heat pipe technology to recover the waste heat from a bakery oven to generate hot air. The thermosyphon technology was used with water as a working fluid at 60% filling ratio of the evaporator length. The length of both the evaporator section and the condenser section were set at 300 mm with an adiabatic section of 150 mm. The thermosyphons were placed in a staggered arrangement to decrease the overall size of the system. The heat pipes tested were finned to increase the heat transfer area. The characteristics of the flue gas in this experiment were 300 °C to 350 °C for a velocity range of

1.5 to 5 m/s. It was observed that with finned copper tube, the effectiveness of the heat pipe heat exchanger ranged from 17.8 to 63%.

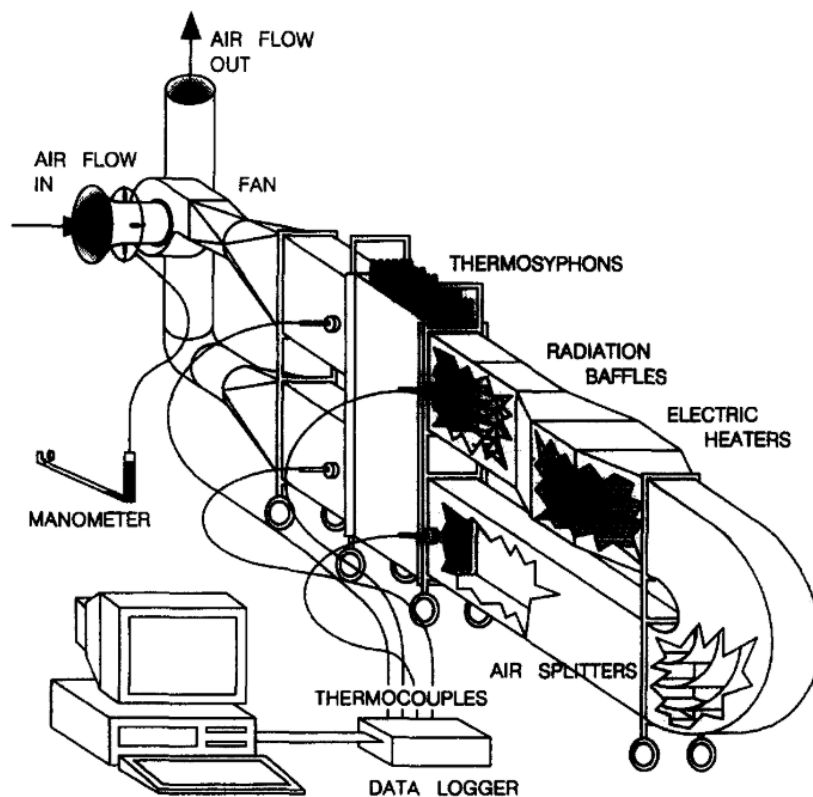


Figure 31 HPHE in bakery test rig

The heat pipe heat exchanger in this application is superior to regular heat exchanger systems in terms of effectiveness. The issue that was not investigated was fouling as the exhaust from a bakery can create a substantial number of particles that could reduce the heat pipe heat exchanger efficiency or block the flow by accumulation of particles in the fins. The test set up can be seen in Figure 31.

2.2.2.2 Heat pipes for solar application

Radiative heat pipe technology has also been applied by [62]. A novel flat heat pipe bonded to a PV panel was developed to generate both heat and electricity from solar radiation. The system was composed of a manifold, a wicked heat pipe and a PV panel. The results showed a thermal energy conversion of 64% with no PV and 50% with the PV bonded on top of the panel. The impact of cooling the PV panel with the heat pipe was investigated and highlighted a 15% increase in efficiency. The system has been installed in a full-scale house in Cardiff, UK [63].

Chapter 3: Experimental apparatus and equipment

3.1 Introduction

Different systems have been tested in order to validate the different theoretical models developed in this thesis. Tests have been carried out in an industrial size kiln in Italy to identify the temperatures of the tiles along the firing section and the cooling section of a roller earth kiln.

A lab scale system has been developed to test a horizontal radiative heat pipe with a vertical condenser. The system was then inserted into a kiln. Three modules have also been manufactured to investigate the impact of a different evaporator heat transfer area on ceramic tiles.

The first part of this chapter will describe the equipment and procedures used to measure the temperatures inside the industrial kiln. The aim of this testing was to measure the cooling profile of the tiles along the slow cooling section.

The second part of the chapter will present the single radiative heat pipe system investigated in laboratory scale. The aim of this test was to validate the theoretical models regarding the view factor correlation, the boiling and condensation regime, the impact of the filling ratio and the overall heat transfer of the system.

The third part of the chapter will describe the three different modules developed to investigate the impact of the heat transfer surface on the cooling profile of the tiles. Three modules with different distances between the tubes were developed. The experimental tests mainly focused on the heat transfer area, determination of the view factor, heat transfer coefficients on the condenser and evaporator sides, and an investigation of the impact of liquid film and tube bundle arrangements on the condensation heat transfer coefficient.

3.2 Data collection at tile manufacturing plant

A datalogging system was used to measure the temperature of the tile along a roller earth kiln. A roller earth kiln is composed of two sections in continuous process, the firing section and the cooling section. In order to measure the tile temperatures in the cooling section, the DATAPAQ system will need to cross the firing section first. The results of this test will be included in this section. Tests were also conducted on the air temperatures and the roller temperatures.

3.2.1 Datapaq instrument

The datalogging DATAPAQ® system consists of a thermal barrier to keep the data logger system and the thermocouple connections at acceptable working temperatures (Figure 32). The logger used in the datapaq was a Tpaq 21 high accuracy data logger. The Tpaq21 is used in the furnace industry to measure high temperatures in a safe way. The system can accommodate up to ten thermocouples, the data are stored inside the system during the test and the data are only accessible once the test is finished. The accuracy of the system is +/- 0.2°C. The system specifications are indicated in Table 4.



Figure 32 Tpaq 21 data logger

Table 4 Tpaq specifications

Operating Temperatures	Normal	High
-------------------------------	---------------	-------------

Model Number*	TP2086	TP2016	TP2186	TP2116
Number of Channels	8	10	8	10
Memory (data points)	130,000			
Maximum Operating	70 °C		110 °C	
Battery Type	NiMH rechargeable		VHT Lithium	
Maximum Battery Life**	340 hours between charges		250 hours	
Sampling Interval:				
No Telemetry	0.1 sec - 50 mins	0.2 sec - 50 mins	0.1 sec - 50 mins	0.1 sec - 50 mins
Hardwire	0.1 sec - 50 mins	0.1 sec - 50 mins	0.1 sec - 50 mins	0.1 sec - 50 mins
Telemetry			50 mins	
RF Telemetry	n/a	2 secs - 50 mins	n/a	3 secs - 50 mins
Maximum Operating Pressure at 20°C (68°F)	20 bar/290 psi			
Minimum Operating Pressure at 20°C (68°F)	10 ⁻⁵ Millibar			

*Model number shown is for type K thermocouples only, other types have different model numbers.

** Maximum battery life depends on sampling interval, operating temperature and use of RF telemetry.

The thermocouples used for this test are K type thermocouples in a carpet setting. In order to create this carpet of thermocouples, a special tile had to be prepared. The tile dimensions used for this test are as follows:

- Length 400 mm
- Width 500 mm
- Thickness 14 mm

Twelve tiles have been positioned on the conveyer in two rows of six to form a carpet of 2400 mm by 1000 mm as shown in Figure 33



Figure 33 "carpet" tile on the conveyer

The eight thermocouples have then been installed on the "carpet" as shown in Figure 34

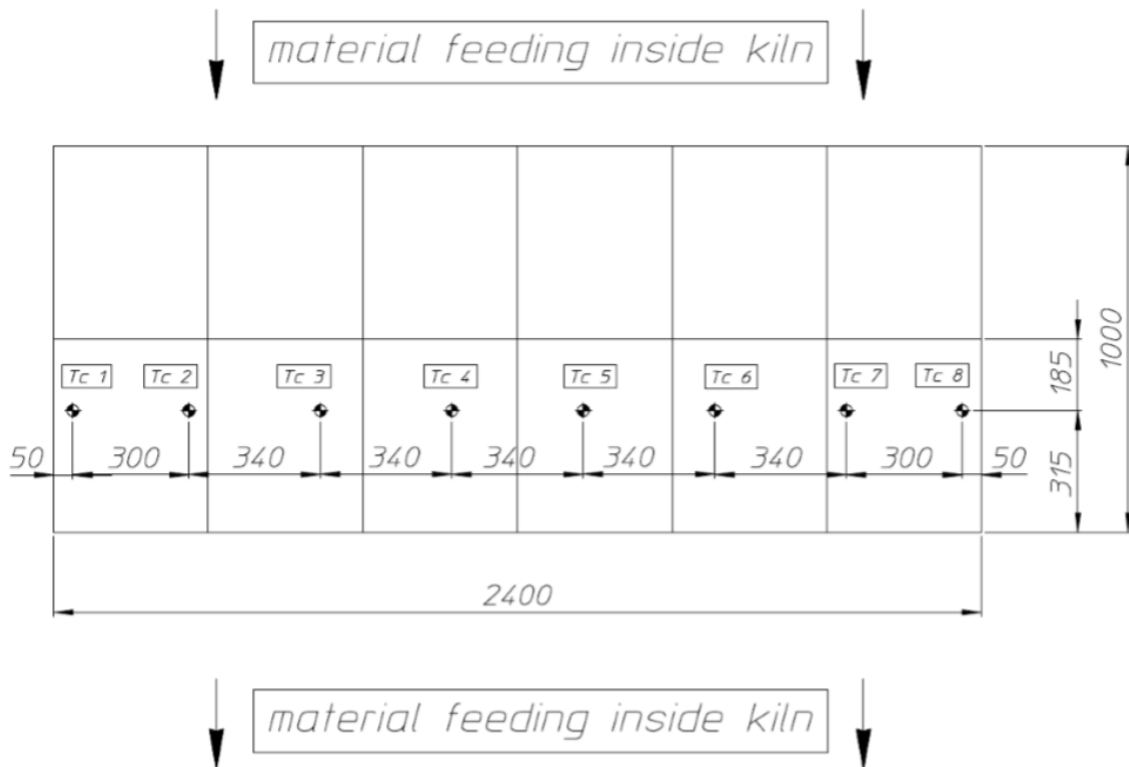


Figure 34 Thermocouple arrangement

Thermocouples number 1, 3, 4, 6 and 8 were placed inside the tiles at a depth of 7 mm as presented in Figure 35, the rest of the thermocouples were positioned in the air 13 mm above the tile surface as shown in Figure 36.



Figure 35 Thermocouple distance from the tile



Figure 36 Arrangement of the thermocouple on the tile

In order to protect the logging system during the tests, the system was filled with water as shown in Figure 37.



Figure 37 Data logger box

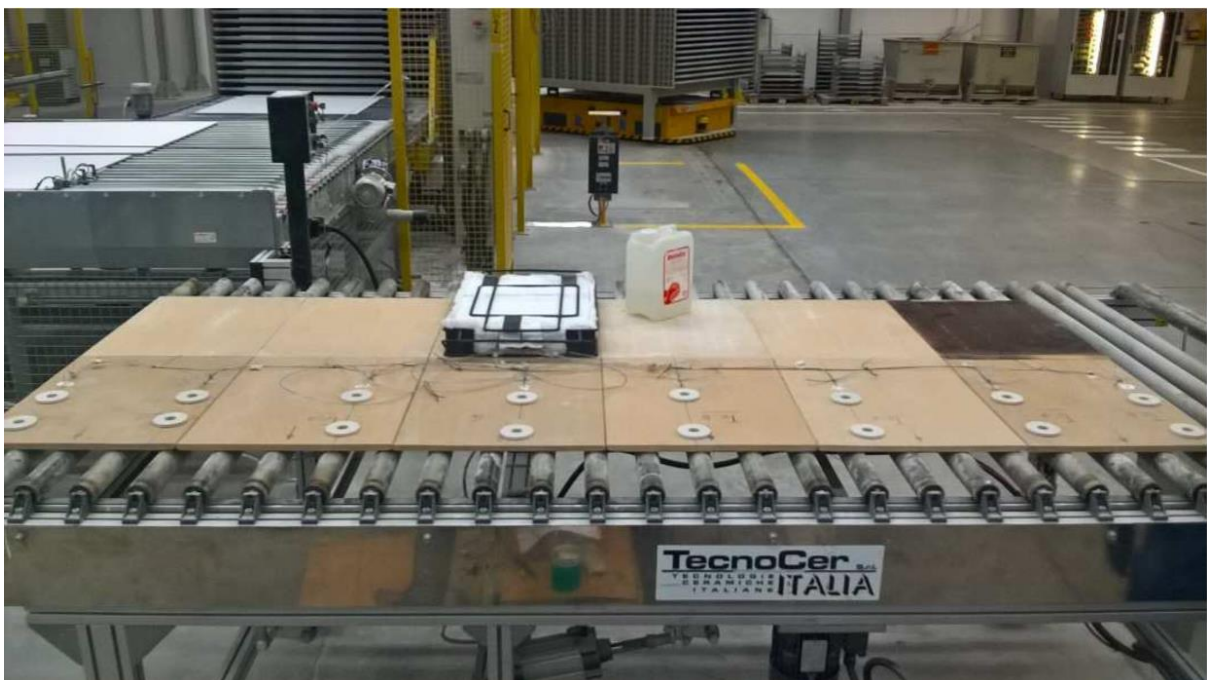


Figure 38 Full arrangement of the thermocouples on the tile

Once the system was installed as illustrated in Figure 38, it was sent into the kiln. After the test, the system was opened in order to check the integrity of the different components. The water protecting the system had evaporated leaving the system exposed to the heat inside

the kiln, leading to a rapid deterioration of the components, as can be seen in Figure 39. The data in the system were recovered but a second test was not possible.



Figure 39 State of the Datapaq after the test

The excessive damage to the system occurred in module 38, thus a limited amount of data was available for the indirect slow cooling section. The damage to the system can be seen in Figure 39. The needed area for the radiative heat pipe which correspond to the indirect cooling section was lacking as shown in Table 5.

3.2.2 Results

The results extracted by the data logger can be seen in Table 5.

Table 5 Results of the temperature measurement of the tile

MODULE N°		TEMPERATURE DETECTED WITH DATAPAQ®							
		TC 1	TC 2	TC3	TC 4	TC5	TC6	TC7	TC8
FIRING STAGE	1	76	94	29	31	42	30	74	28
	2	206	266	63	72	264	77	279	66
	3	228	276	92	102	277	107	291	98
	4	254	307	107	141	297	149	336	124
	5	290	345	164	189	326	194	365	173

6	324	390	206	236	386	236	385	213
7	381	428	256	287	442	287	453	265
8	437	478	306	330	488	338	502	314
9	504	547	368	409	549	410	542	378
10	575	621	437	475	597	475	610	446
11	651	673	505	543	690	543	686	517
12	710	795	594	625	753	624	787	601
13	771	846	674	701	815	700	851	683
14	832	894	746	769	867	770	896	751
15	885	951	818	837	934	839	956	815
16	938	992	880	898	979	904	997	875
17	982	1030	945	964	1020	966	1037	942
18	1026	1065	996	1014	1065	1014	1075	995
19	1071	1108	1048	1064	1122	1062	1120	1044
20	1112	1147	1096	1108	1157	1108	1163	1093
21	1144	1178	1140	1149	1191	1150	1195	1137
22	1171	1194	1176	1183	1215	1184	1213	1171
23	1197	1216	1203	1209	1232	1210	1229	1197
24	1211	1227	1216	1219	1231	1221	1232	1212
25	1231	1242	1236	1237	1251	1237	1244	1230
26	1226	1233	1235	1236	1238	1237	1239	1232
27	1217	1221	1231	1230	1232	1233	1229	1230
28	1203	1217	1216	1216	1206	1218	1207	1217
29	1173	1170	1194	1193	1171	1196	1172	1199
30	1128	1111	1158	1155	1106	1158	1097	1162

	31	1063	1024	1107	1100	1013	1104	1026	1111
	32	999	950	1047	1034	939	1039	939	1051
	33	924	870	975	960	852	967	846	979
DIRECT RAPID COOLING	34	796	720	881	861	734	865	716	874
	35	734	673	805	783	680	788	669	795
	36	669	615	740	717	626	725	614	731
	37	621	578	690	668	596	677	590	680
INDIRECT SLOW COOLING	38	587	553	651	629	576	639	568	641
	39	-	-	-	-	-	-	-	-
	40	-	-	-	-	-	-	-	-
	41	-	-	-	-	-	-	-	-
	42	-	-	-	-	-	-	-	-
	43	-	-	-	-	-	-	-	-
	44	-	-
	45	-	-	-	.
DIRECT FINAL COOLING	46
	47
	48
	49
	50
	51
	52
	53
	54
	55

Temperature detected by thermocouples with tolerances according to IEC58 4. 2 cl. 2 (± 2 K or $\pm 0.75\%$, the highest value applies)

A simulation using the data recovered during the firing and indirect cooling was used to predict the temperatures of the tiles in the relevant slow cooling section.

3.3 Single radiative heat pipe

3.3.1 Mechanical design

The single radiative heat pipe, 28 mm in diameter, consisted of a stainless-steel tube and a water jacket. The tube can be defined in three sections. The evaporator section was 430 mm long with an angle of inclination of 5 degrees. The tube was then connected to a bend in order to accommodate the condenser section. Water was running through the water jacket using the main water supply. The heat pipe system was mounted on a support system and installed inside the kiln. The condenser section was located outside the kiln while the evaporator section was exposed to radiation and natural convection heat transfer. The overall dimensions of the single radiative heat pipe can be seen in Figure 40.

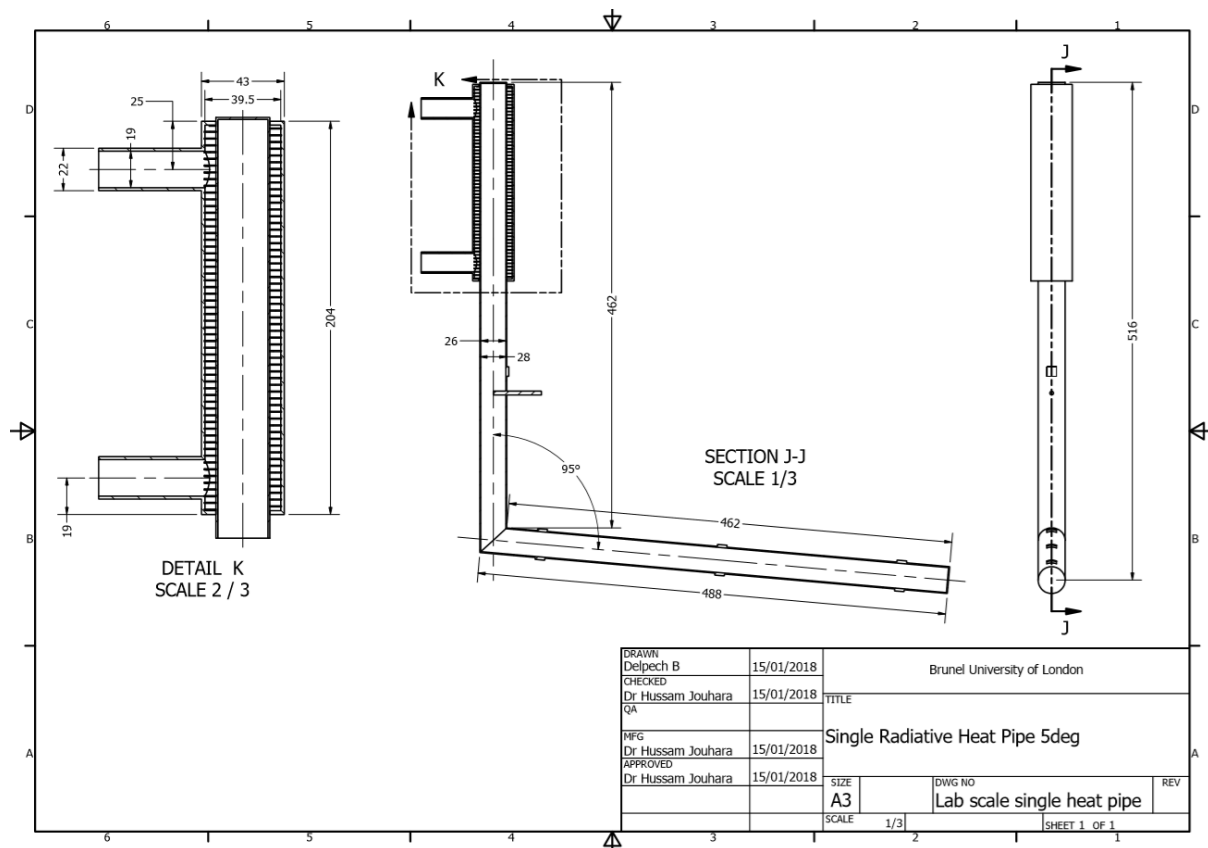


Figure 40 Single radiative heat pipe 5 degrees

The system was attached to a support to fix the distance between the evaporator section and the heating elements. The single heat pipe arrangement in the kiln is illustrated in Figure 41.

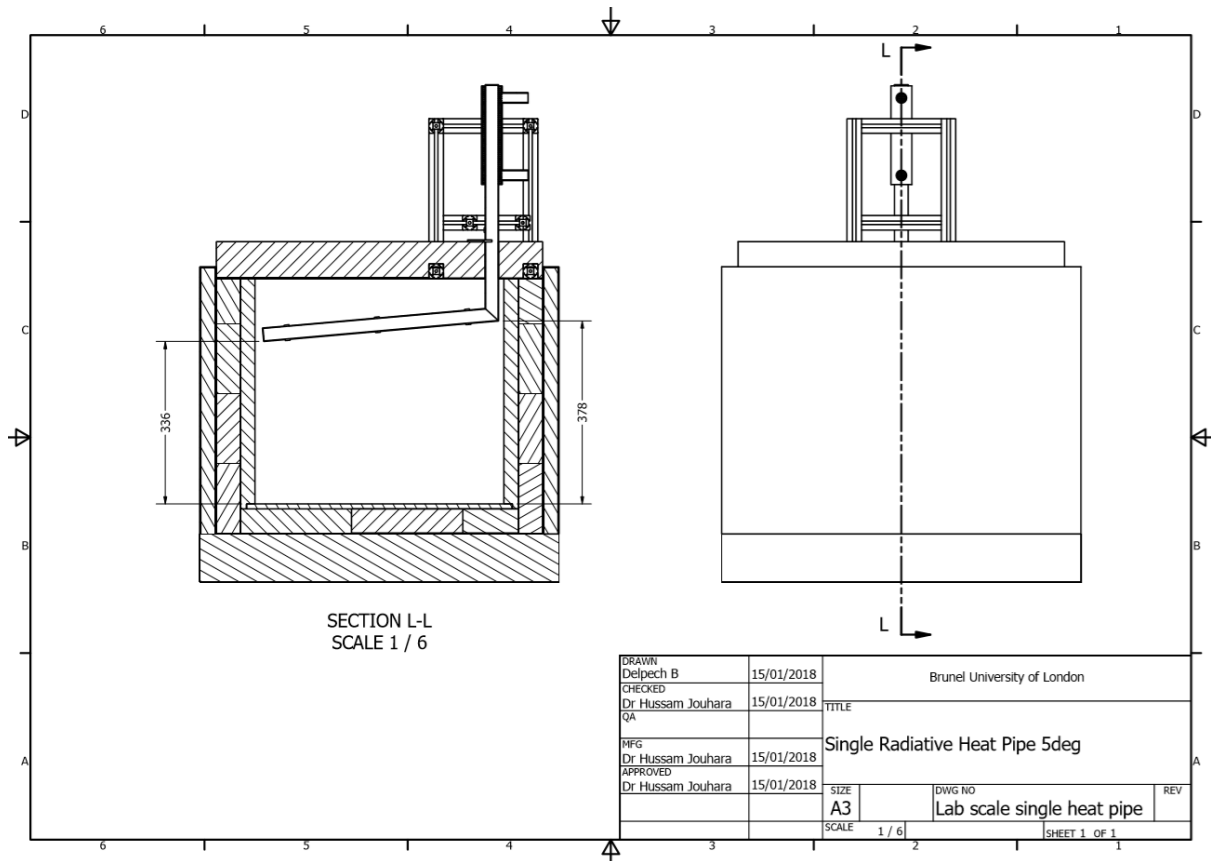


Figure 41 Single heat pipe in the kiln

A three-dimensional view of the system in the kiln is illustrated in Figure 42

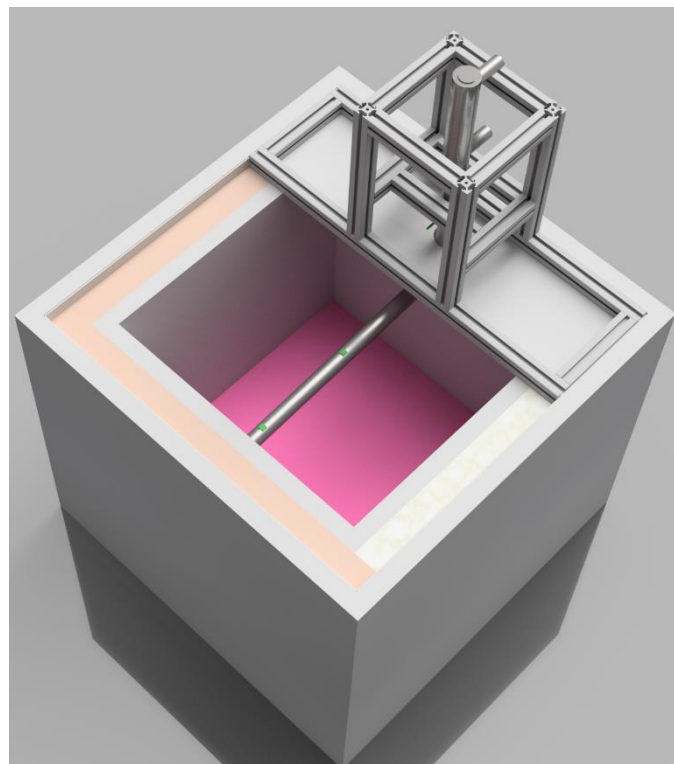


Figure 42 3D view of the Single Heat Pipe

3.3.2 Kiln set up

The kiln was composed of five fixed walls arranged in a cube. The side walls were composed of three layers, one layer of Calcium-magnesium silicate thermal insulation of 30 mm thickness with low thermal conductivity as shown in Table 6, one layer of fire brick of 30 mm with the specification listed in Table 7 and a second layer of calcium-magnesium silicate thermal insulation. On the bottom wall the insulation was 50 mm firebrick and 100 mm of calcium-magnesium insulation. The kiln was closed with a removable lid composed of 50 mm of calcium-magnesium silicate insulation. The dimensions of the kiln can be seen in Figure 43.

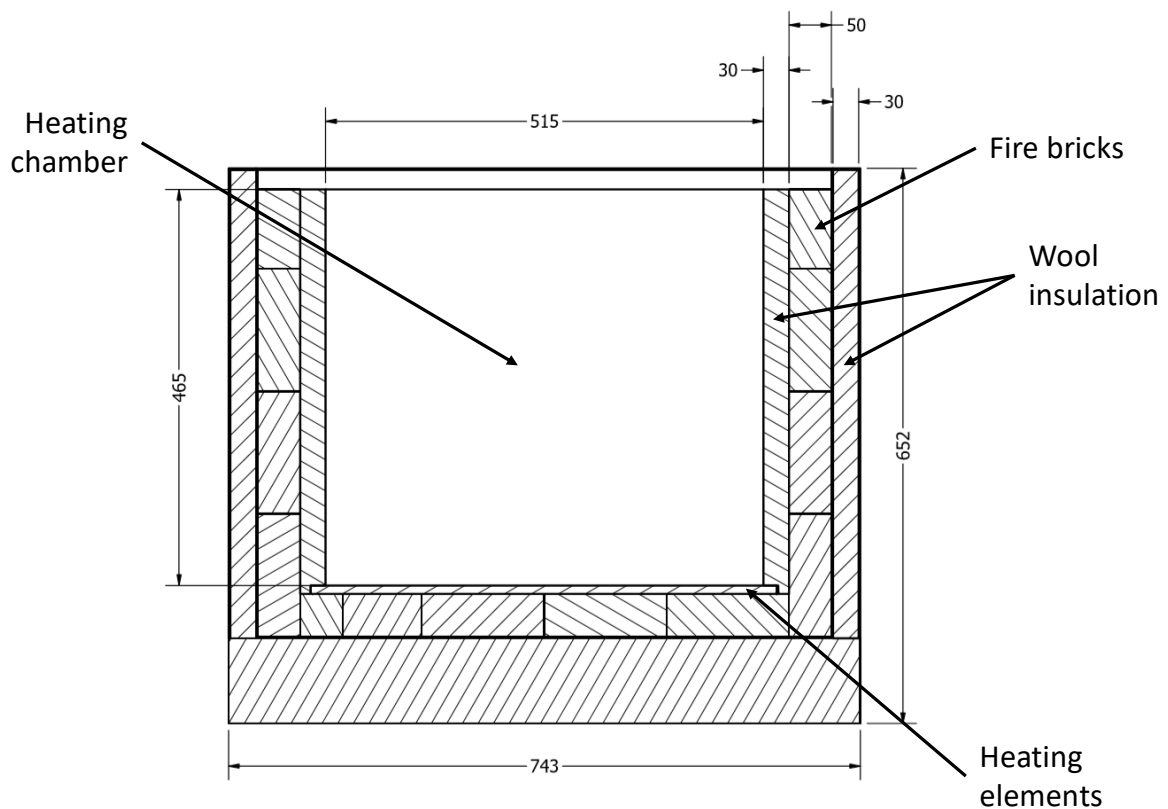


Figure 43 Kiln arrangement

Calcium-magnesium silicate thermal insulation specifications can be found in Table 6

Table 6 Insulation specifications

Type	Made from high temperature insulation wool	
Classification Temperature	13000C (ENV 1094-3)	
Continuous use Temperature:	11500CC the maximum continuous use temperature depends on the application	
Colour:	White	

Density:	kg/m ³	64, 96, 128, 160	
Tensile Strength (ENV 1094-7)	64 kg/m ³	30 kPa	
	96 kg/m ³	50 kPa	
	128 kg/m ³	75 kPa	
	160 kg/m ³	95 kPa	
Thermal conductivity (ASTM C-201) at mean temperature of			
2000°C	W/m.K	0.05	0.04
4000°C	W/m.K	0.1	0.08
6000°C	W/m.K	0.19	0.14
8000°C	W/m.K	0.32	0.23
10000°C	W/m.K	0.48	0.34
12000°C	W/m.K	0.69	0.48
Chemical composition			
SiO ₂	70-80%		
CaO + MgO	18-25%		
Others	<3%		

The fire brick layer specifications can be found in Table 7

Table 7 Brick specifications.

QUALITY	C-20	C-23	C-26	C-28	C-30	C-32
ASTM C155-97 Classification	20	23	26	28	30	32
ISO 2245 Classification		125-0.5-L	140-0.8-L	150-0.9-L	160-1.9-L	170-1.2-L
Classification Temperature °C	1093	1260	1430	1540	1650	1760
°F	2000	2300	2600	2800	3000	3200
Density Kg/m ³	480	520	810	880	1030	1250
ASTM C-134-95 Lbs/ft ³	30	32.5	50.6	55	64.3	78
Cold Crushing Strength MPa	1.1	1.2	1.6	2.1	2.5	3.5

ASTM C-93-84 Lbs/in2	160	170	230	300	360	510
Modulus of Rupture MPa	0.8	0.9	1.1	1.3	2.1	2.1
ASTM C-93-84 Lbs/in2	116	130	160	190	300	300
Permanent Linear Change, %	0	0.5	0.4	1	0.9	0.9
Reversible Thermal Expansion, %	0.45	0.5	0.7	0.8	0.9	1.1
Thermal Shock Resistance Cycles		30	30	30	30	30
Thermal Conductivity (W/m- k)						
200°C	0.15					
400°C	0.17	0.18	0.27	0.32	0.41	0.49
600°C	0.19	0.19	0.29	0.34	0.43	0.5
800°C	0.21	0.21	0.31	0.36	0.44	0.51
1000°C		0.23	0.33	0.38	0.45	0.53
1200°C			0.35	0.41	0.47	0.56
Al ₂ O ₃ , %	51	51	58	67	73	77
Fe ₂ O ₃ , %	1	0.7	0.7	0.6	0.5	0.4

3.3.3 Heating elements

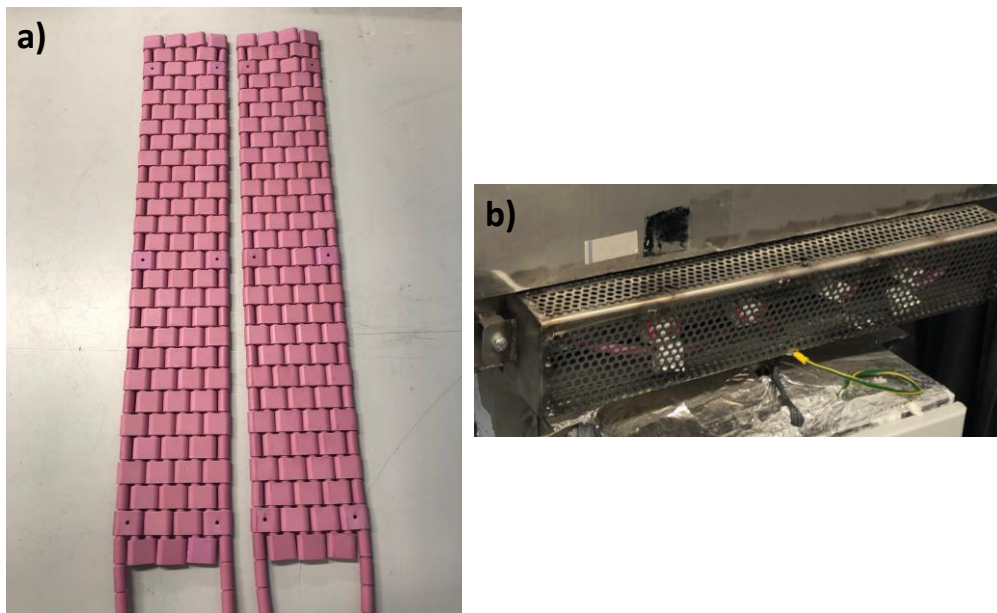


Figure 44 a) ceramic pad heater b) ceramic pad installed in the kiln

The heaters selected for this test were flexible ceramic pad heaters from Artechservices® as shown in Figure 44 a). The heater is composed of a ceramic envelope (aluminium oxide) and a low resistance wire going through the beads (high grade nickel chrome (NiCr) 80/20). The use of such a heater allows a good reliability of the test and the possibility of running the experiment at high temperature (maximum temperature 1050 °C). Also, the use of ceramic heaters will give results as close as possible to the real case study regarding emissivity. The technical specification of the heater can be found in Table 8. The heaters were mounted in series and provided with a 60 Volt, 58 Amp supply. The total energy input in the system was 7 kW. A photo of the heating elements can be seen in Figure 45.

Table 8 Specification of the heaters

Ceramic beads	
Density kg/dm ³	8.13
Specific heat at 20°C J/kg°C	419
Melting range	1380-1400°C
Electrical resistivity at 20°C microhm/cm	108
Mean co-efficient of resistance per °C	20 - 100°C = 0.00008 20 - 500°C = 0.00014
Colour	Pink/white
Density g/cm ³	3.6
Porosity	0°



Figure 45 Ceramic heater parts

3.3.4 Water supply

The water supply used in the tests was similar for all the experiments. The water circuit was composed of a flow meter, a gate valve to regulate the flow in the condenser section and two thermocouples, one at the inlet of the heat pipe condenser section and the second thermocouple at the outlet of the condenser section. The water was supplied by the main at a maximum flow rate of 30L/min and a maximum pressure of 3 bar. A schematic of the system is presented in Figure 46.

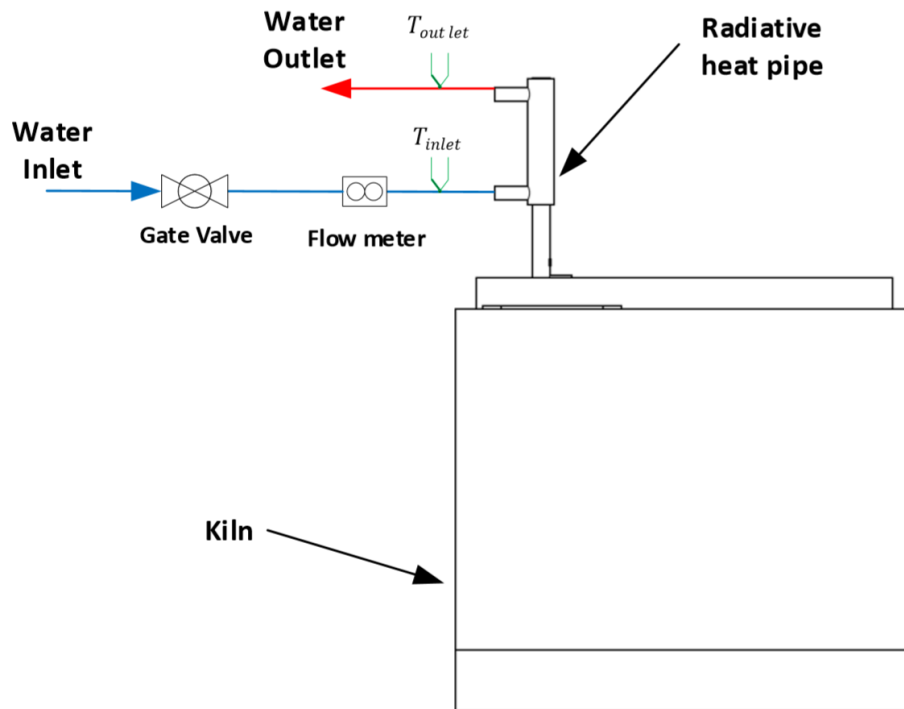


Figure 46 Water cooling system

3.3.5 Control system

The control system used in this test was a PID controller; a description of the control system can be seen in Figure 47. The main parameter to control during this test was the surface temperature of the ceramic heater. In order to control this temperature, a high temperature thermocouple was placed on top of the surface. The thermocouple signal was then sent to a proportional integral derivatives controller system. A PID device is a control loop feedback system used in industrial applications as a control system for the oven and firing kiln. The PID system uses the thermocouple signal to adjust the electrical input in the heater in order to match the target temperature set at the beginning of the test. When the ceramic heater temperature is below the target temperature, the PID will provide energy to the heater. Once the target temperature is reached, the PID will shut down the heater. It was noted that the inertia of the thermocouple feedback and the energy input in the system could not provide a steady temperature. Thus, the temperature variation during the test was $\pm 25\text{ }^{\circ}\text{C}$. A fail safe condition was also programmed into the PID. When there is a loss of thermocouple signal, no energy was input to the heater.

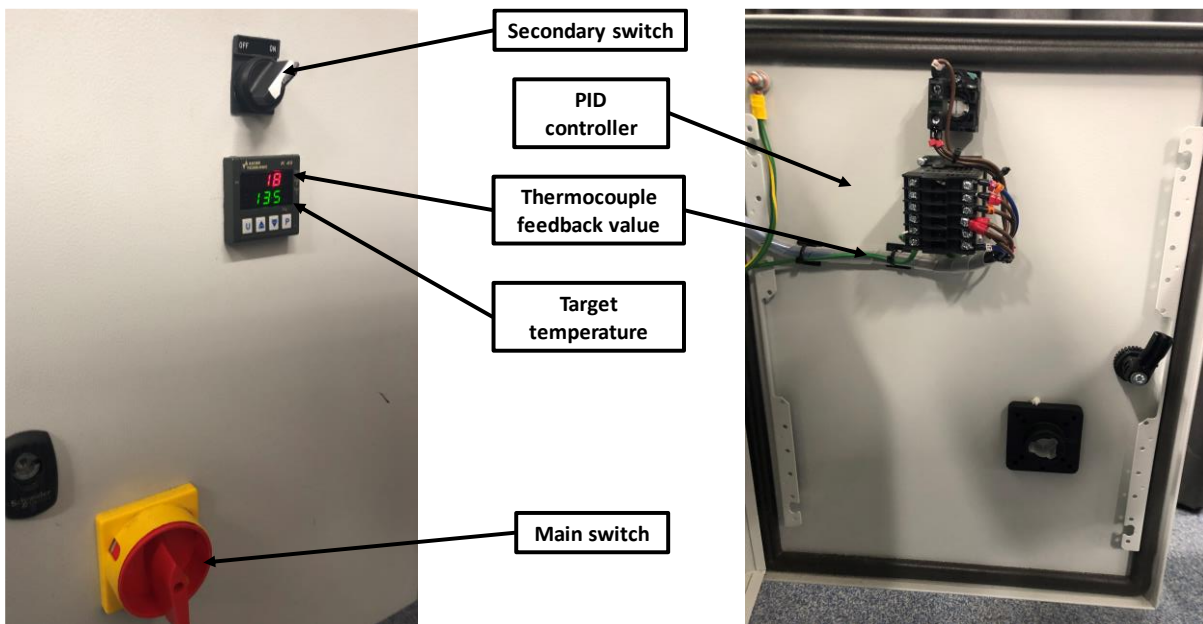
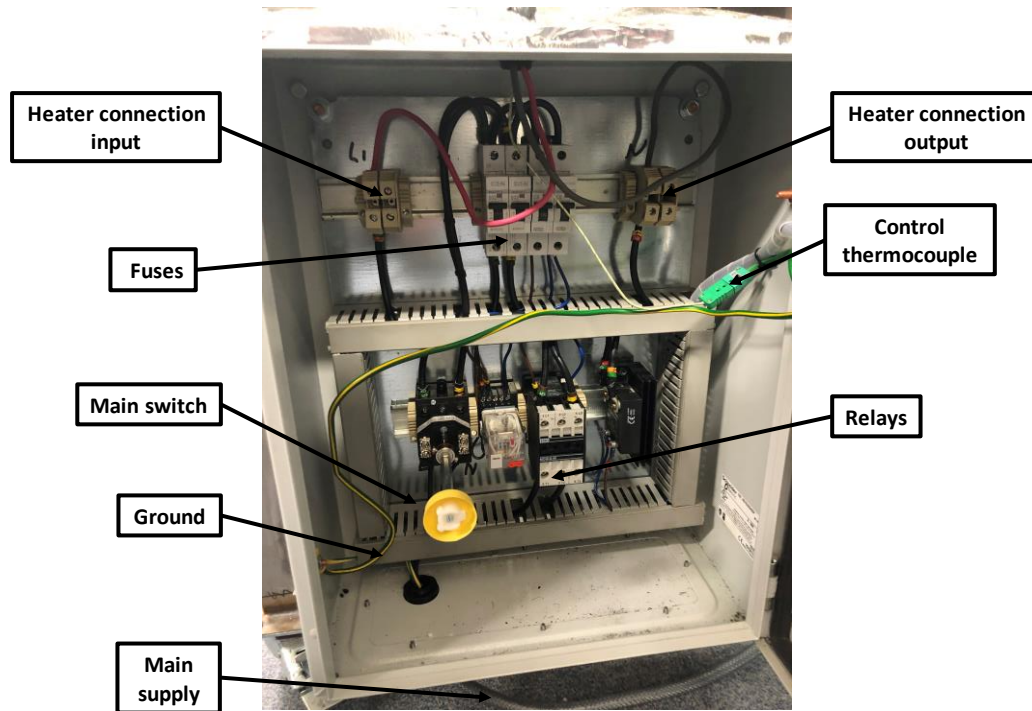


Figure 47 Electrical board

3.3.6 Instrumentation

The system used for all the tests was a multi-channel data logger from *National Instrument®*. The thermocouples were placed at different locations of the kiln and the heat pipe.

3.3.6.1 Thermocouples

Thermocouples on the kiln

K type shielded thermocouples were placed at different locations of the kiln. Five thermocouples were placed in the side wall and the bottom wall at approximately 25 mm

from the inner surface of the kiln. Four thermocouples were placed on the inner surface of the kiln below a small layer of insulation to avoid any disturbance due to radiation from the heating elements. One thermocouple was placed on the removable top panel of the kiln. The surface thermocouple was placed on the inner surface of the stainless-steel sheet. A thermocouple was placed below the heater that would monitor the temperature of the bricks and the heating elements. An industrial thermocouple was placed on the heater surface during the experiments to measure the surface temperature of the heater elements. Figure 48 and Figure 49 show the thermocouple locations in the kiln.

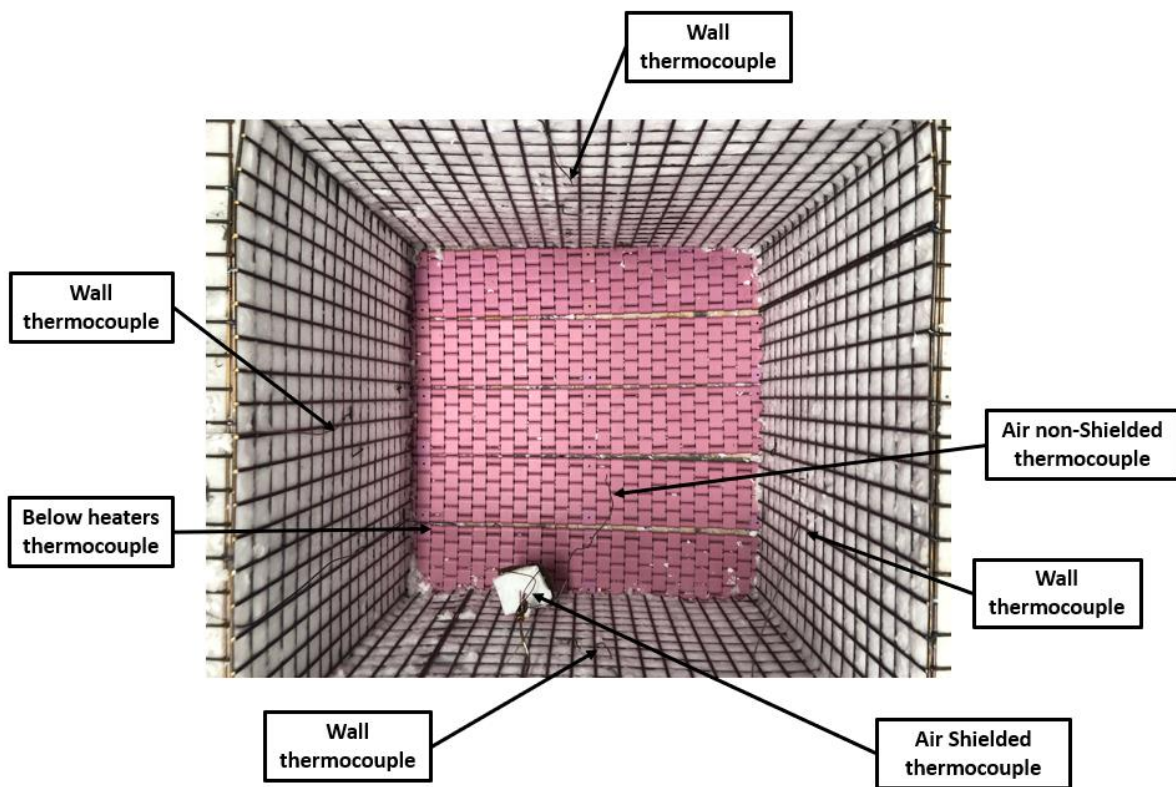


Figure 48 Thermocouples in the kiln

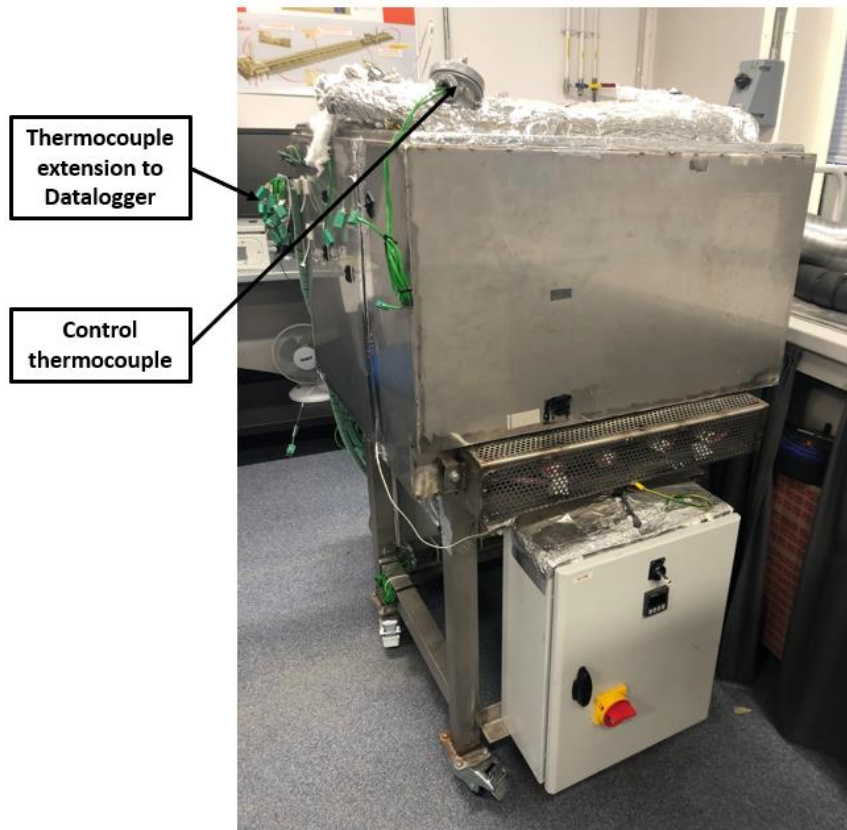


Figure 49 Thermocouples outside the kiln

Thermocouples on the single radiative heat pipe

In order to accurately measure the temperature of the outer wall of the heat pipe and investigate the effect on filling ratio on the localised temperature of the heat pipe, six thermocouples were placed on the evaporator section. The thermocouple positioning is shown in Figure 50. During the first test, jubilee clip thermocouples were used, but the impact of the air temperature on the thermocouples was too high, hence giving unrealistic results. In order to tackle this issue, thermocouples were brazed onto the outer skin of the evaporator section as shown in Figure 51. The element used for the brazing was nickel alloy. The filling material will create a thermal barrier between the hot air/radiation and the thermocouples. The stability and the reliability of this method increased the accuracy of the readings. In order to measure the saturated temperature of the working fluid, a thermocouple was inserted inside the tube and brazed in position. Because of the design of the condenser section, no thermocouples could be placed on the outer skin of the condenser section. In order to mitigate the loss of this information, a jubilee clip was placed above the condenser section.

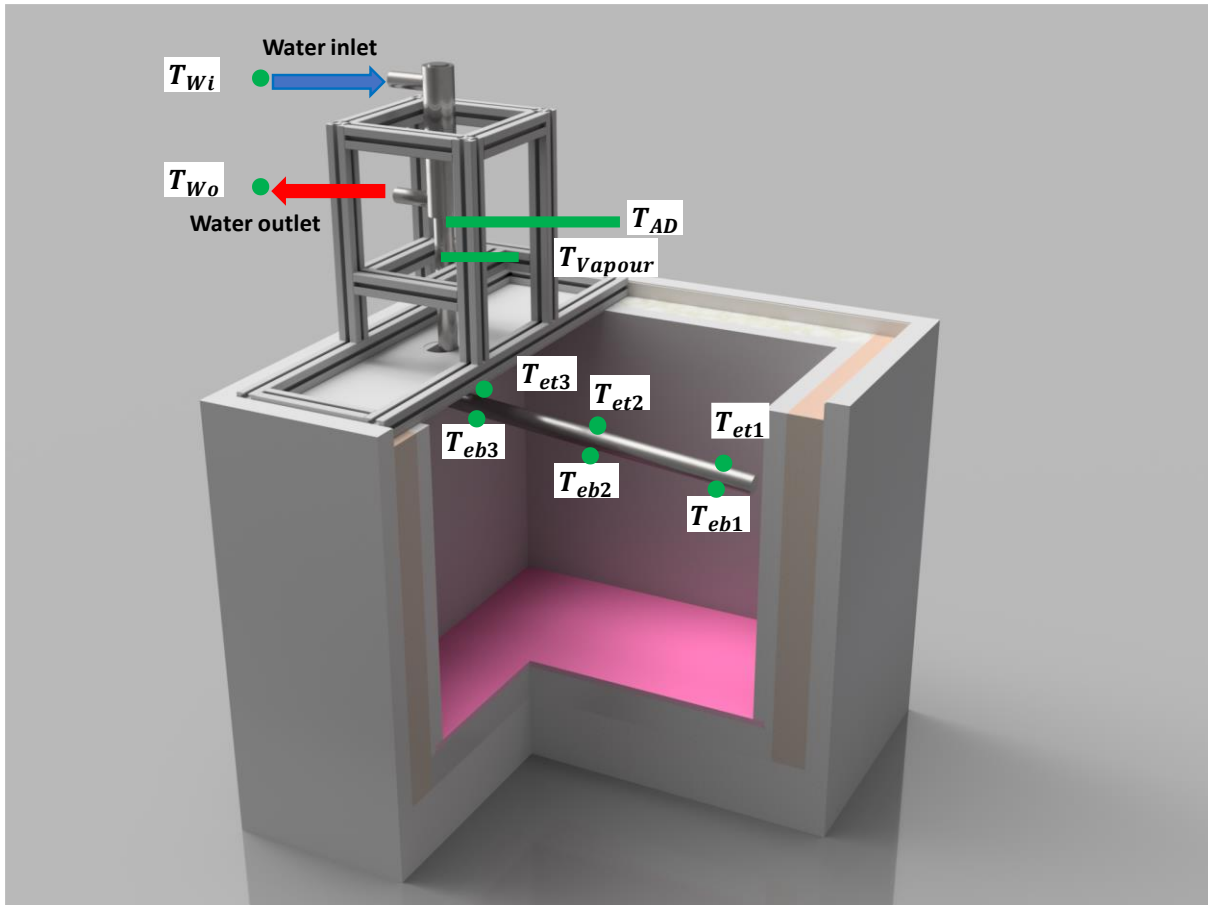


Figure 50 Thermocouple locations, single radiative heat pipe

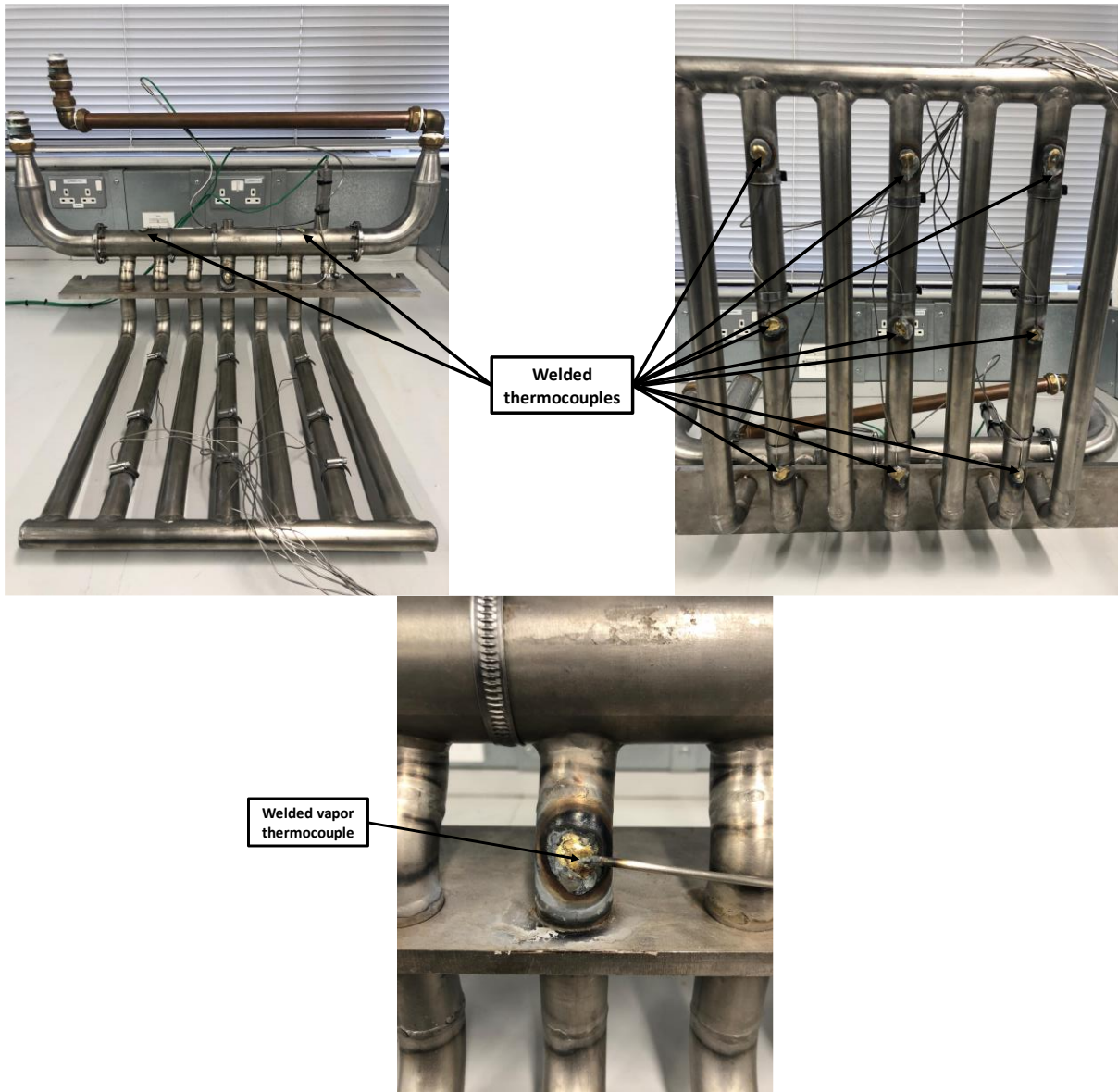


Figure 51 Welded thermocouples

Water section thermocouples

The measurement of the water temperature was made using two type K thermocouples fitted in the water flow. The first thermocouple was in the inlet tube of the water supply. The second thermocouple was located as close as possible from the outlet of the expansion part. Both thermocouples were in the middle of the tube cross section. The thermocouples were held in place using compression fittings.

3.3.6.2 Flow meter

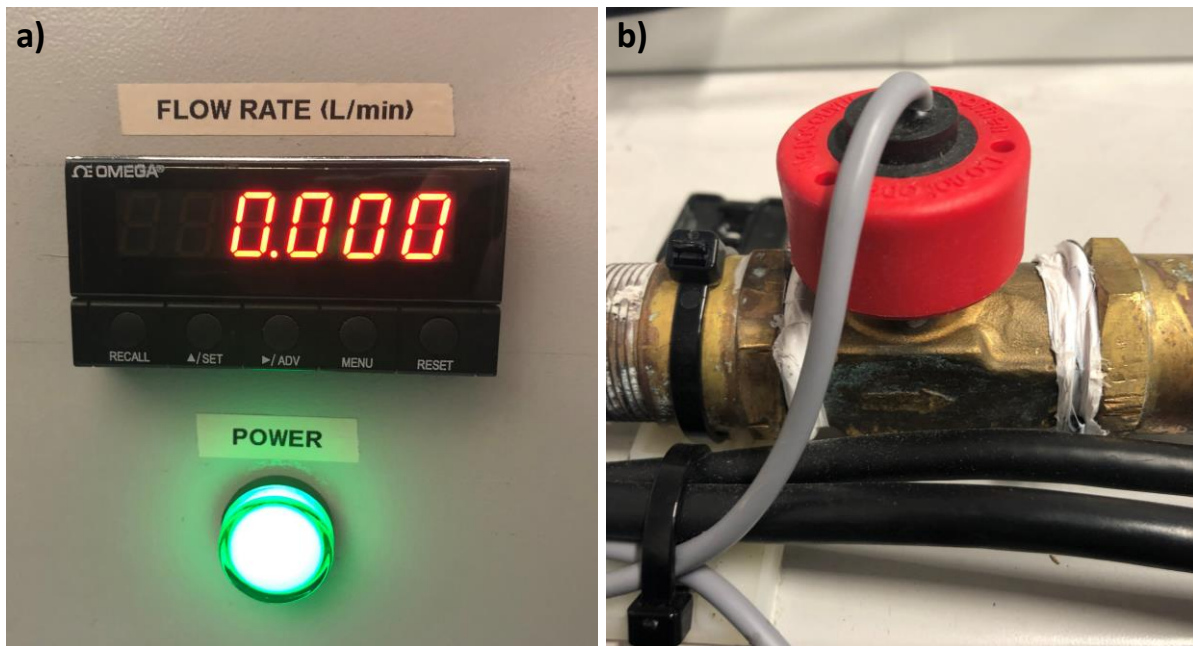


Figure 52 a) Flow meter display; b) flow meter

The flow measurement was made by an Omega® Turbine Flow Sensors FTB371-G, the flow meter was connected to a digital display as shown in Figure 52 a) Flow meter display; b) flow meter. The flow meter was a compact device with good accuracy. The turbine flow meter or axial turbine flow meter relies on a turbine rotating as the flow goes through the system, which activates a signal readable with a digital display. The accuracy of the FTB371-G was acceptable for these tests. The specifications of the flow meter are presented in Table 9

Table 9 Technical specifications - FTB371-G

Specifications			
Model Number	FTB371-G	FTB372-R	FTB373-R
Range	2 to 40 l/min. (Continuous 20 l/min max.)	4 to 160 l/min (Continuous 80 l/min max.)	0.4 to 25 m ³ /h (6.7 to 417 l/min)
Accuracy	±1 % of range	±5 % of reading	±7 % of reading <3 m ³ /h & ±5 % of reading >3 m ³ /h
Repeatability	±0.2 %	±0.5 %	±0.5 %
Signal Output	from 0.3 l/min	from 1 l/min	from 0.1 m ³ /h
Max. Fluid Temperature	85 °C		
Max. Pressure	10 bar		
Diameter	DN15	DN 25	DN 40
Length	80 mm	178 mm	270 mm
Process Connection	G¾A Male	R1 (1" BSPT) Male	R1½ (1½" BSPT) Male

Pulse Rate (K Factor)	855 pulses/litre	65 pulses/litre	26.6 pulses/litre
Output Resolution	1.2 ml/pulse	15 ml/pulse	37.6 ml/pulse
Signal Shape	Square Wave. NPN Open Collector		
Signal Current	10 mA max.	19 mA max.	19 mA max.
Electrical Connection	1.5 m Screened PVC Cable (70 °C max.)	2 m Screened PVC Cable (70 °C max.)	2 m Screened PVC Cable (70 °C max.)
Power Supply	4.5 to 24 Vdc	10 to 30 Vdc	10 to 30 Vdc
Protection Class	IP 54		
Max. Particle Size	0.5 mm	0.63 mm	0.63 mm
Wetted Parts			
Body	Brass: CuZn36Pb2 As CW602N		
Sensor Housing	PPO Noryl GFN3	PPO Noryl GFN 1630 V	PPO Noryl GFN 1630 V / POM Celcom
Turbine System	PEI ULTEM	PPO Noryl GFN 2 V/PPO Noryl GFN 3 V	PPO Noryl GFN 2 V/PPO Noryl GFN 3 V
O-Ring Seal	NBR	EPDM	EPDM

3.3.6.3 Data logging system

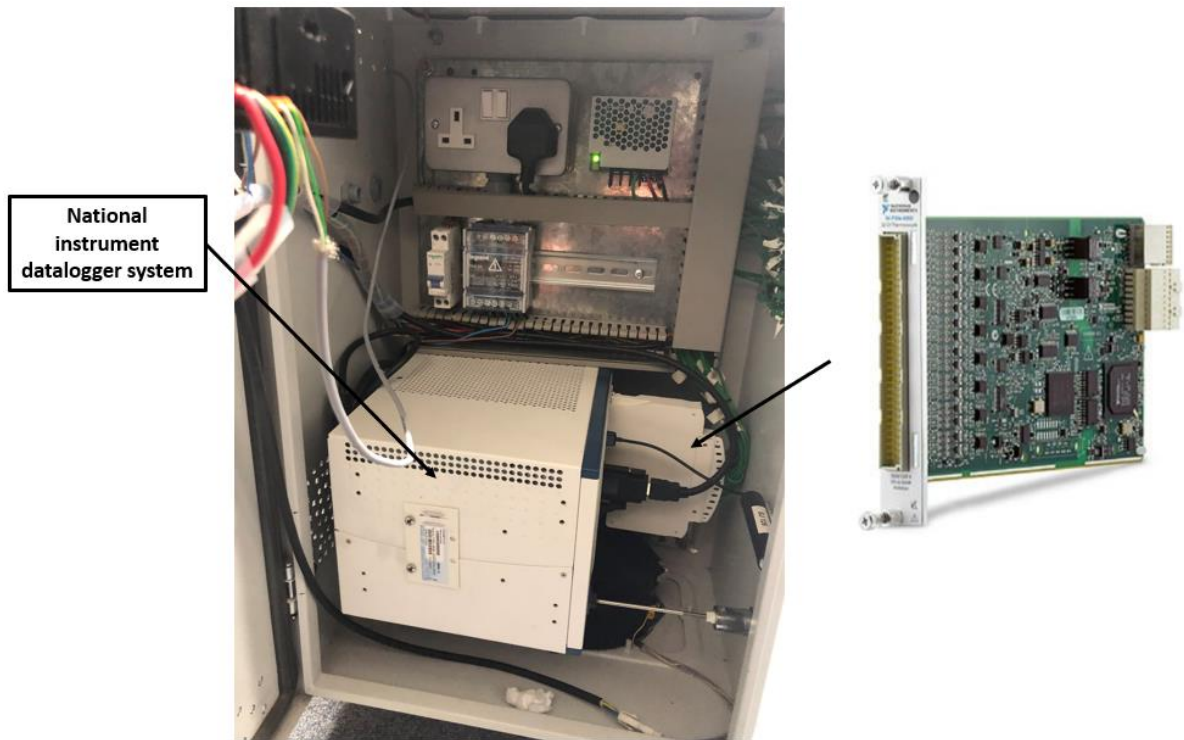


Figure 53 Data logging system

The logging system was composed of a PC PXIe-1071 and a data acquisition system NI PXIe-4353 from National Instrument. The system installed can be seen in Figure 53. The data acquisition system had 32 thermocouple channels with high speed (90 S/s per channel) and high accuracy (1S/s per channel) modes. The typical accuracy of this system was 0.30 °C. Table 10 below includes the error of the module and the terminal block.

Table 10 Thermocouple type K measurement accuracy (°C)

		- 100 °C	0°C	100 °C	300 °C	500 °C	700 °C	900 °C	1100 °C	1400 °C
High Resolution	Typical 23 °C ±5 °C	0.42	0.29	0.26	0.36	0.35	0.45	0.56	0.64	0.86
	Max 23 °C ±5 °C	0.70	0.49	0.46	0.58	0.59	0.70	0.85	0.97	1.26
	Max 0-55 °C	1.14	0.79	0.71	0.92	1.02	1.24	1.50	1.76	2.29
High Speed	Typical 23 °C ±5 °C	0.65	0.46	0.43	0.55	0.56	0.67	0.82	0.93	1.22
	Max 23 °C ±5 °C	0.98	0.70	0.66	0.80	0.82	0.96	1.14	1.30	1.66
	Max 0-55 °C	1.43	1.00	0.91	1.14	1.25	1.49	1.80	2.09	2.68

3.3.7 Experimental test plan

The aim of this system was to investigate the impact of the filling ratio on the average heat transfer coefficient of the heat pipe. The filling ratio also had an impact on the geyser boiling effect of the system. The heat pipe allowed the validation of the theoretical model and the approach developed for the view factor determination. In order to achieve those objectives, the experimental programme was designed to test and validate the hypotheses made in the theoretical model. The tests followed the table below:

Table 11 Experimental plan single radiative heat pipe

Filling ratio	25%	50%	75%	100%
200 °C	Test 1	Test 5	Test 9	Test 13
300 °C	Test 2	Test 6	Test 10	Test 14
400 °C	Test 3	Test 7	Test 11	Test 15
500 °C	Test 4	Test 8	Test 12	Test 16

The flow rates used during these tests were kept constant when possible. Due to the low heat flux at low temperature, geyser boiling was occurring. This phenomenon rendered difficult the collection of data at steady state. In order to obtain data at steady state, the flow rate was decreased in certain cases:

Table 12 Flow value used for the tests

Filling ratio	Temperatures of tile (°C)			
	200	300	400	500
25%	1.05 L/min	1.05 L/min	1.05 L/min	3.70 L/min
50%	0.90 L/min	3.70 L/min	3.70 L/min	3.70 L/min
75%	0.70 L/min	3.70 L/min	3.70 L/min	3.70 L/min

100%	0.70 L/min	3.70 L/min	3.70 L/min	3.70 L/min
------	------------	------------	------------	------------

All the data obtained were then used in an excel sheet for analysis

3.4 Modular radiative heat pipes

The same kiln, instrumentation, control system and heater were used in these experimental arrangements. The positioning of the thermocouples will be covered in this section for each module. In order to determine the heat transfer and the optimal flow rate for all the conditions discussed in the theoretical chapter, three test rigs were manufactured. Each test rig was characterised by a different spacing between the pipes in the evaporator section. The condenser section composed of a shell and tube was similar for each test rig. The modification of the spacing between the pipes resulted in a decrease in heat transfer, thus potentially a more uniform cooling on the ceramic tiles.

3.4.1 Module 15

3.4.1.1 Mechanical design

Module 15 was composed of ten stainless steel pipes of 28 mm diameter connected through a collector of 28mm diameter at the bottom and a shell and tube condenser section at the top. The distance between the pipes of the evaporator section was 15 mm. The shell and tube section was composed of nine pipes of 10 mm diameter, 1 mm thick stainless tube. The shell of the condenser was a 50 mm outer diameter stainless steel pipe with a thickness of 1 mm. The condenser was connected to an expansion piece. The connection to the expansion piece was a 28 mm diameter tube. The tube was connected to the water supply using a compression fitting. The assembly was welded, and pressure tested to ensure no leakage could occur at high working pressures and temperatures. The whole assembly was designed to handle a pressure of 80 bars, secured by a rupture disk located at the top of the system. The system was charged using water as a working fluid. Depending on the filling ratio required, the volume of water varied. The system was charged in a way that ensured no incondensable gases were generated in the heat pipe. Indeed, the presence of incondensable gases in the condenser section would reduce the overall heat transfer as a reduced area of tube bundle would be covered by the vapour in the condenser section.

The offset of the condenser is due to the design of the kiln and the accessibility of the condenser section once installed in the kiln. In order to have an easy access to the condenser flanges, the condenser had to be offset. For the working fluid and the vapour to flow properly between the condenser section and the evaporator section, the radiative heat pipes were inclined at 5 degrees.

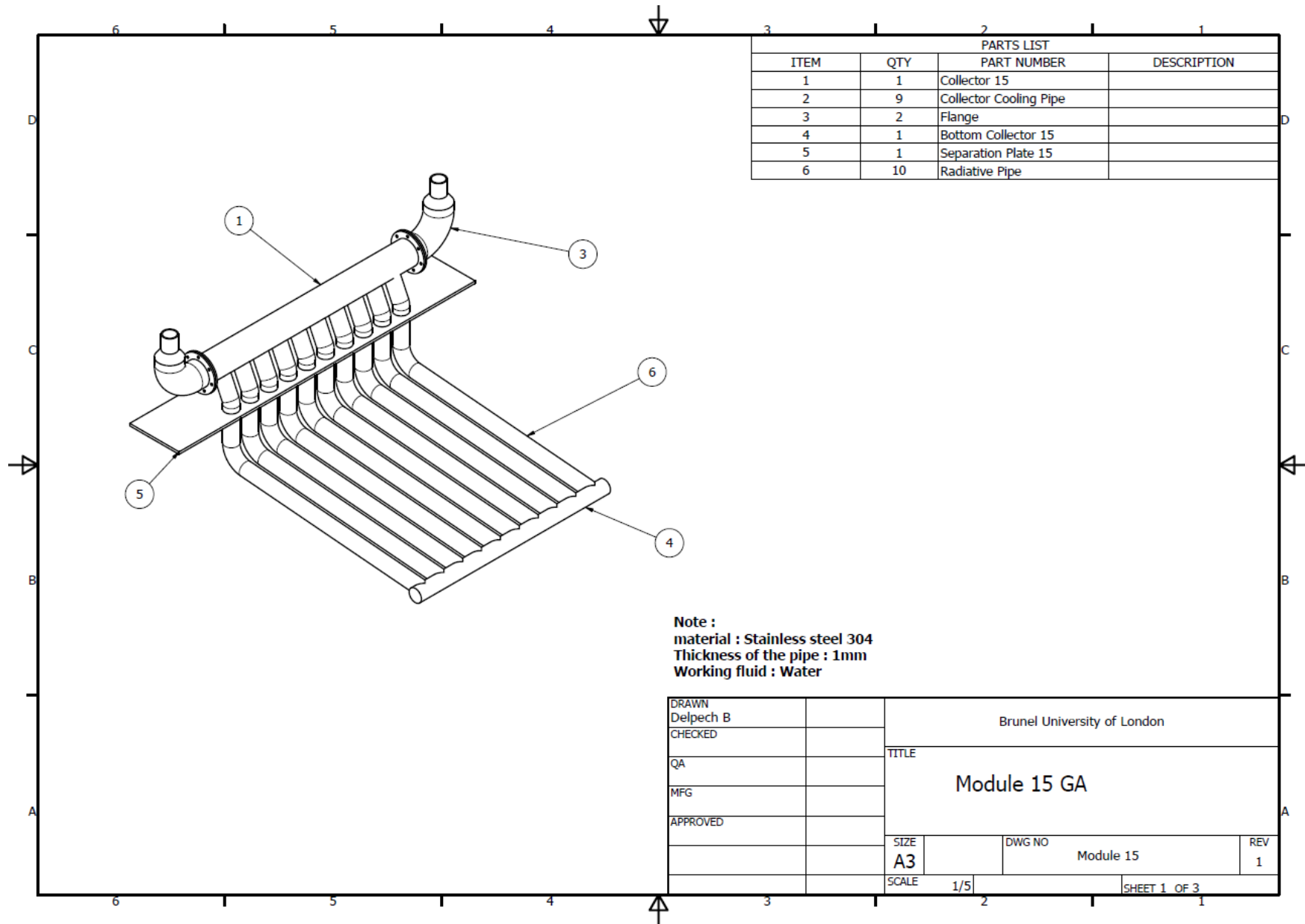


Figure 54 Module 15 GA

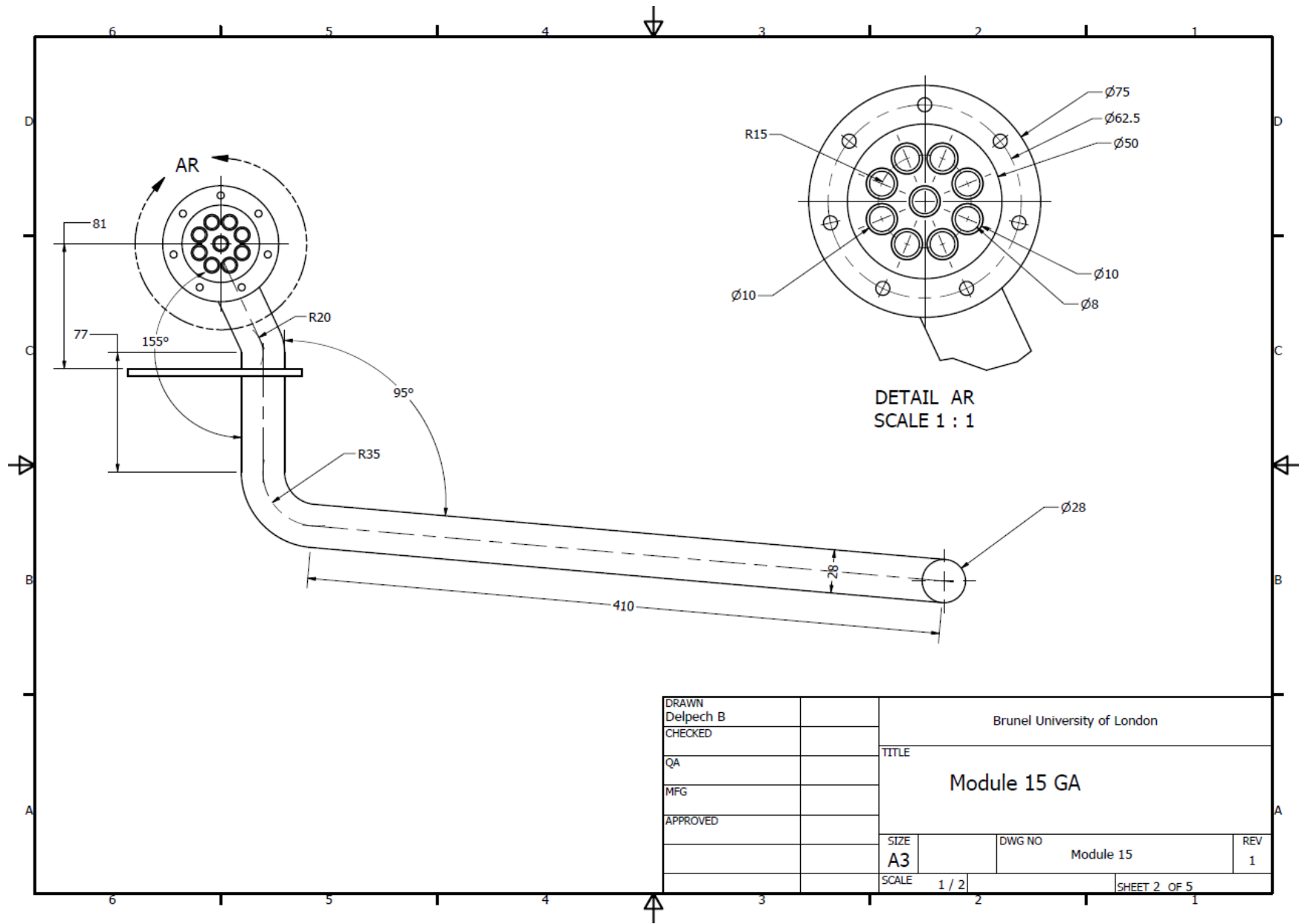


Figure 55 Module 15 condenser detail

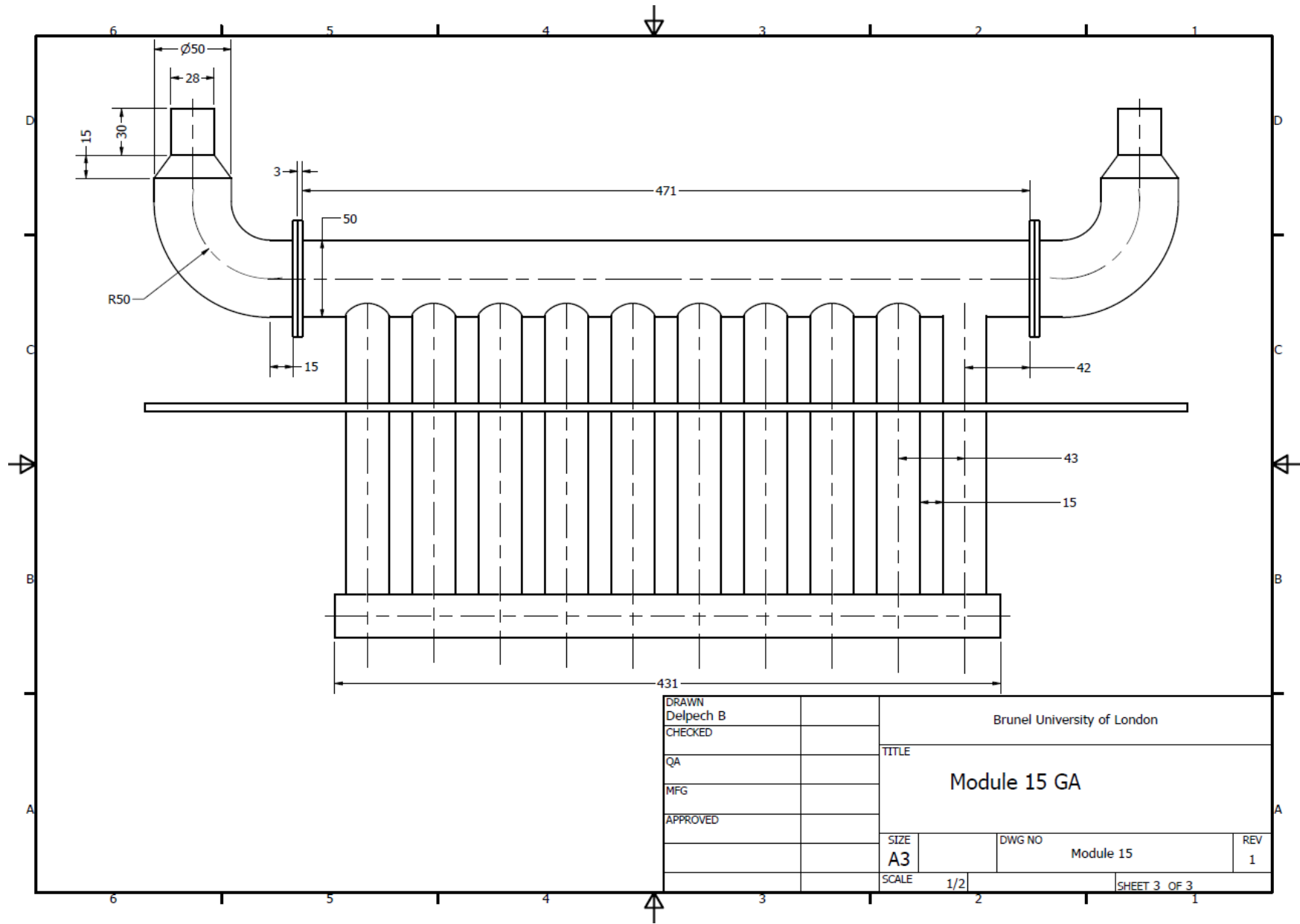


Figure 56 Module 15 detail: Front view

3.4.1.2 Thermocouple locations

In the same way as with the radiative heat pipe, the thermocouples were welded onto the surfaces of module 15. Nine thermocouples were placed on the evaporator/radiative section, one thermocouple was placed inside the heat pipe to measure the vapour temperature and two thermocouples were welded on top of the condenser section to measure the surface temperature of the cooling pipe and ensure that no incondensable gases were present in the heat pipe. The thermocouple positions are shown in Figure 58. All the thermocouples were connected to the data logger as illustrated in Figure 57.

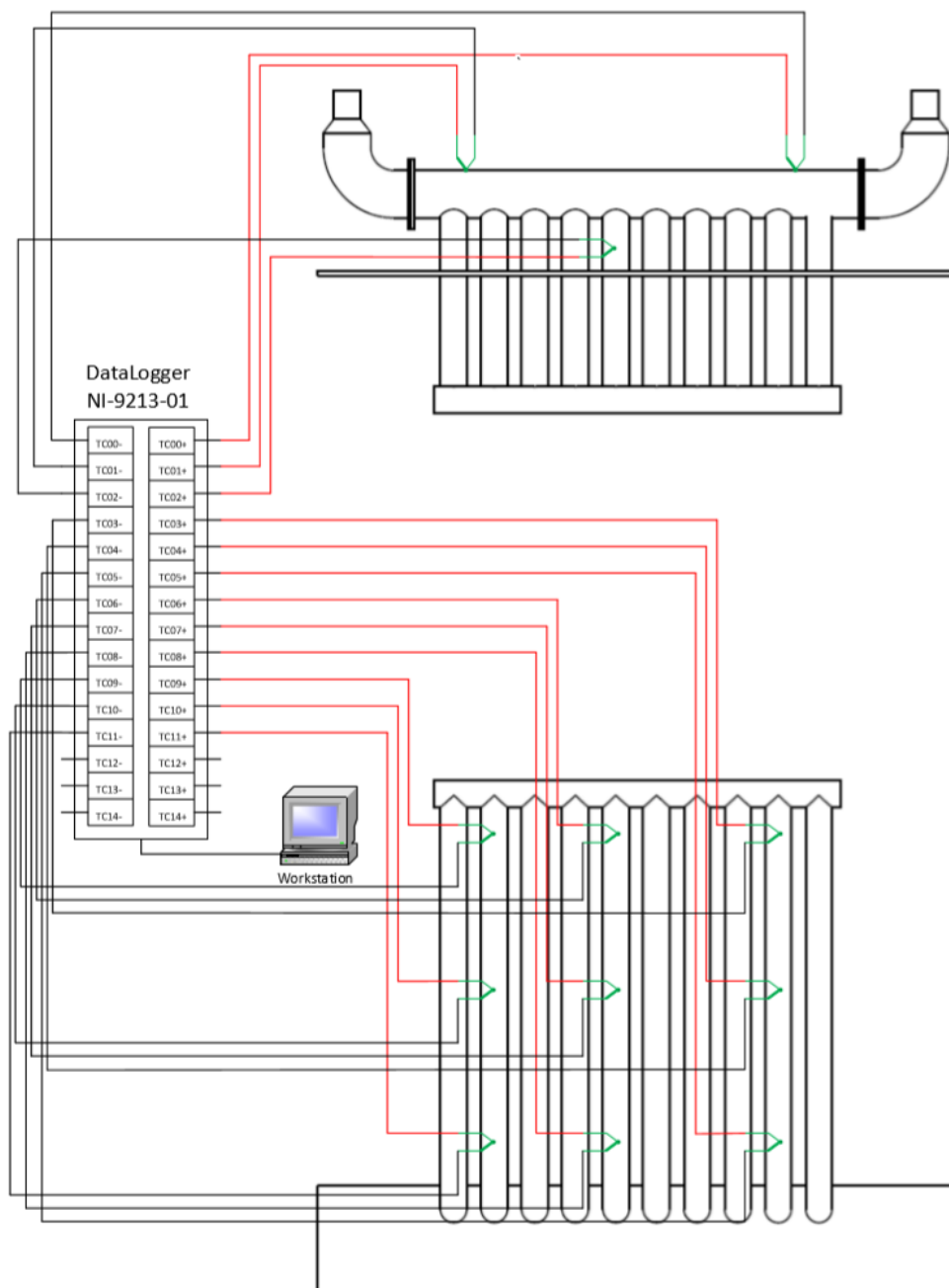


Figure 57 Thermocouple wiring, module 15

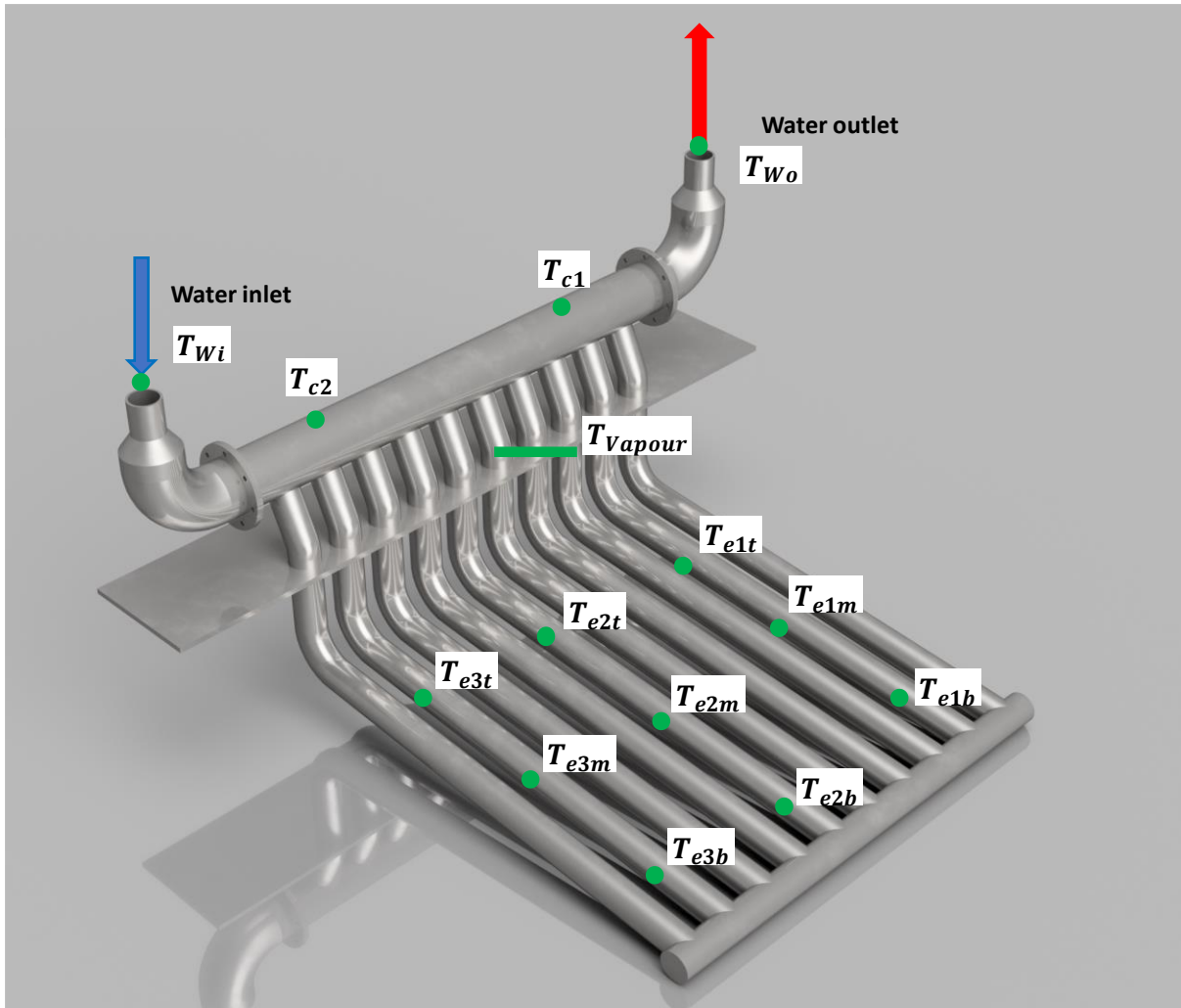


Figure 58 Thermocouple locations, Module 15

3.4.2 Module 25

3.4.2.1 Mechanical design

Module 25 was composed of eight stainless steel pipes of 28 mm diameter connected through a collector of 28mm diameter at the bottom and a shell and tube condenser section at the top. The shell and tube section, similar to module 15, consisted of nine pipes of 10 mm diameter each. The shell of the condenser was a 50 mm outer diameter stainless steel pipe with a thickness of 1 mm. The spacing between the pipes of the evaporator section was 25 mm.

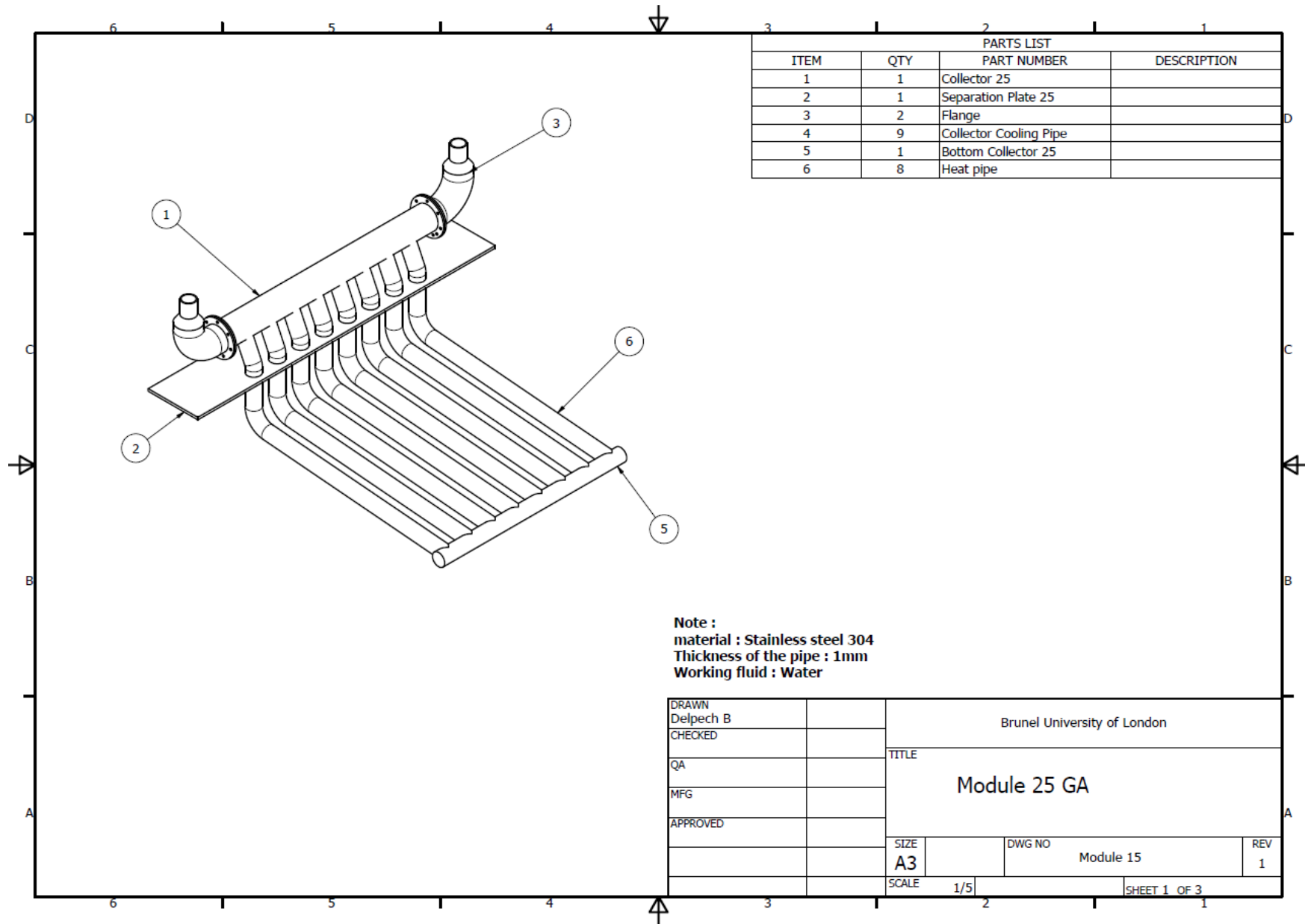


Figure 59 Module 25 GA

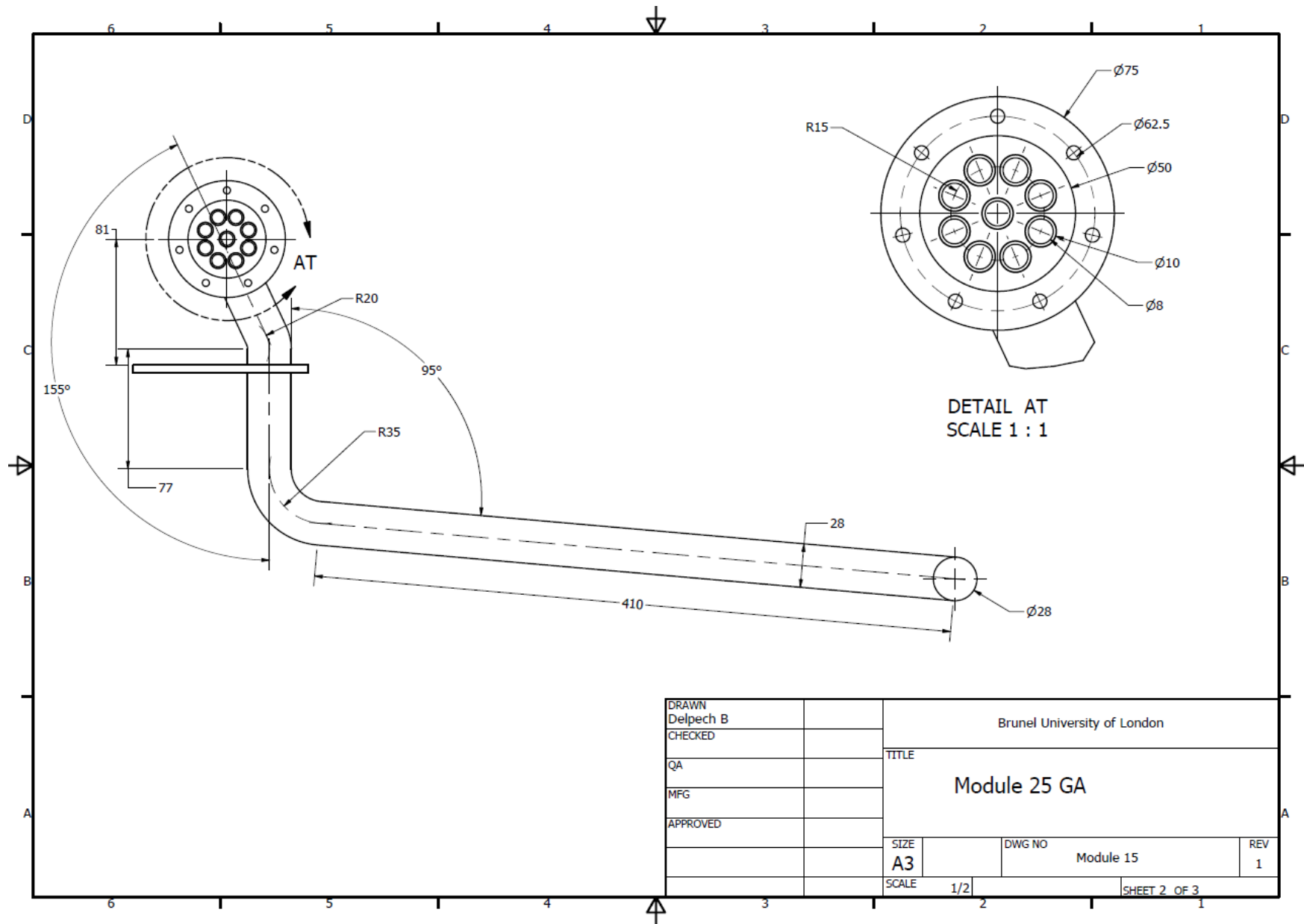


Figure 60 Module 25 Condenser details

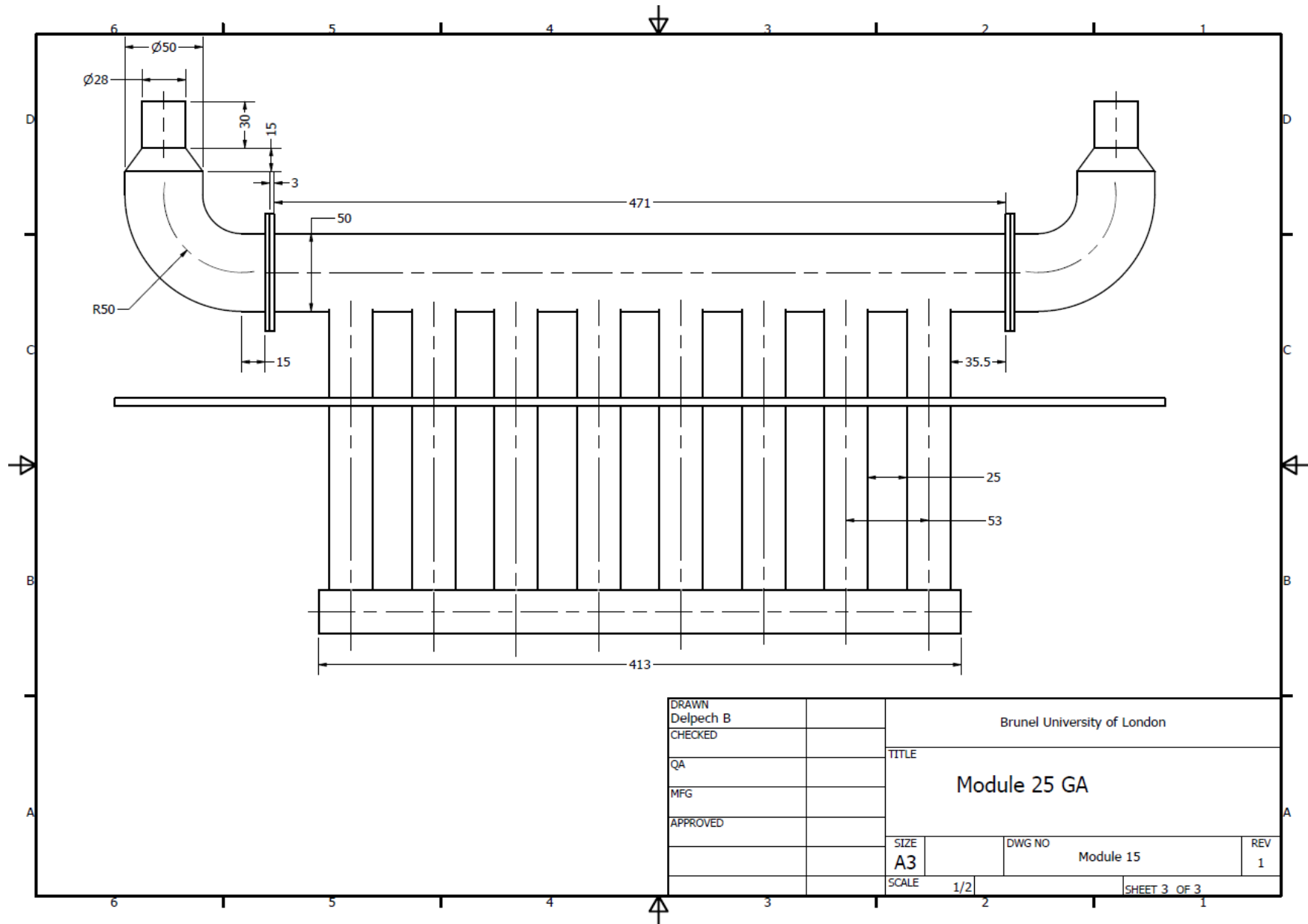


Figure 61 Module 25 front view

3.4.2.2 Thermocouple locations

Nine thermocouples were placed on the bottom of the evaporator section pipes. Similar to module 15, two thermocouples were welded on top of the condenser section and one thermocouple was placed in the vapour stream. The thermocouple positions are shown in Figure 63, the wiring diagram is illustrated in Figure 62

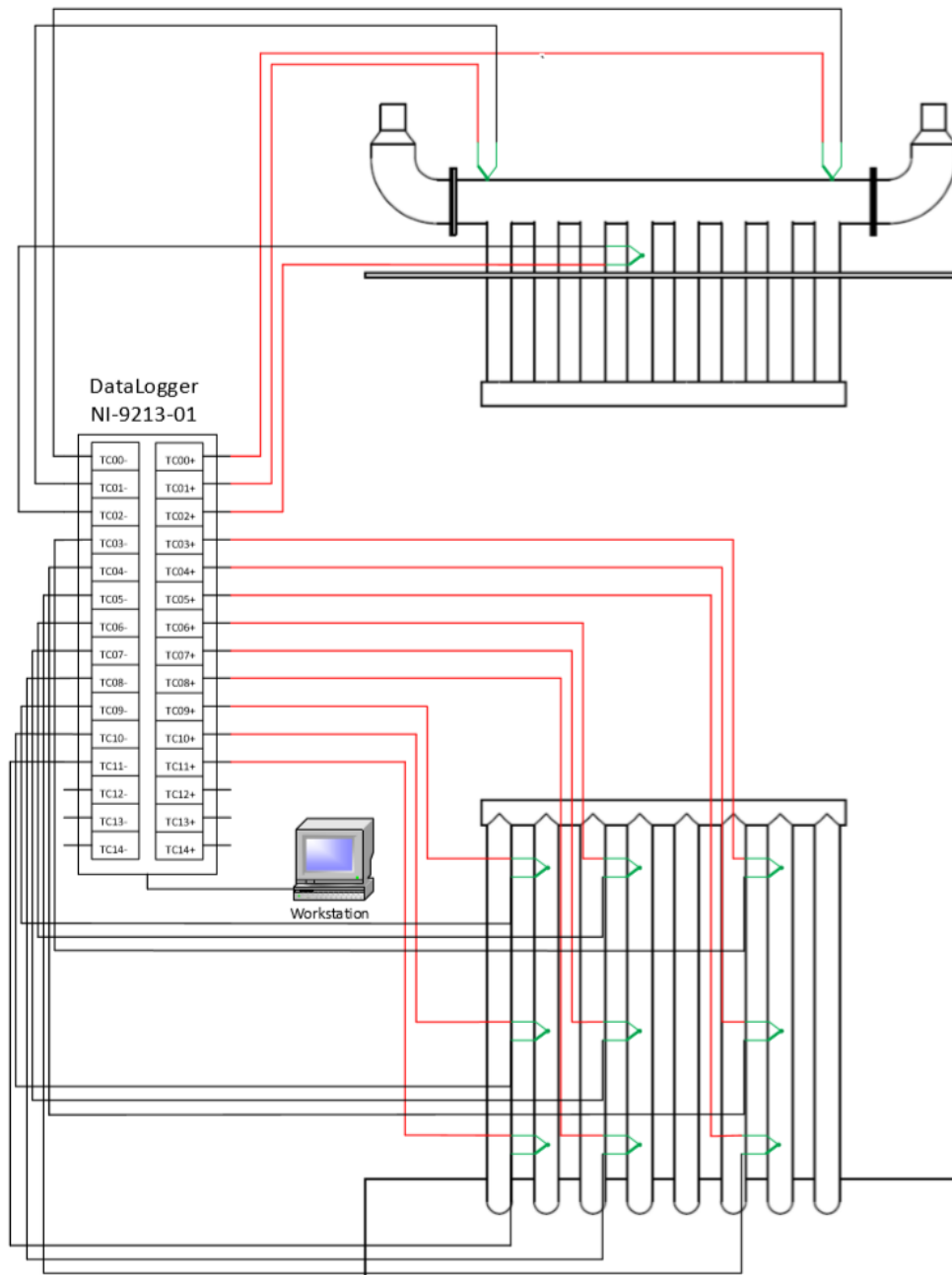


Figure 62 Thermocouples wiring Module 25

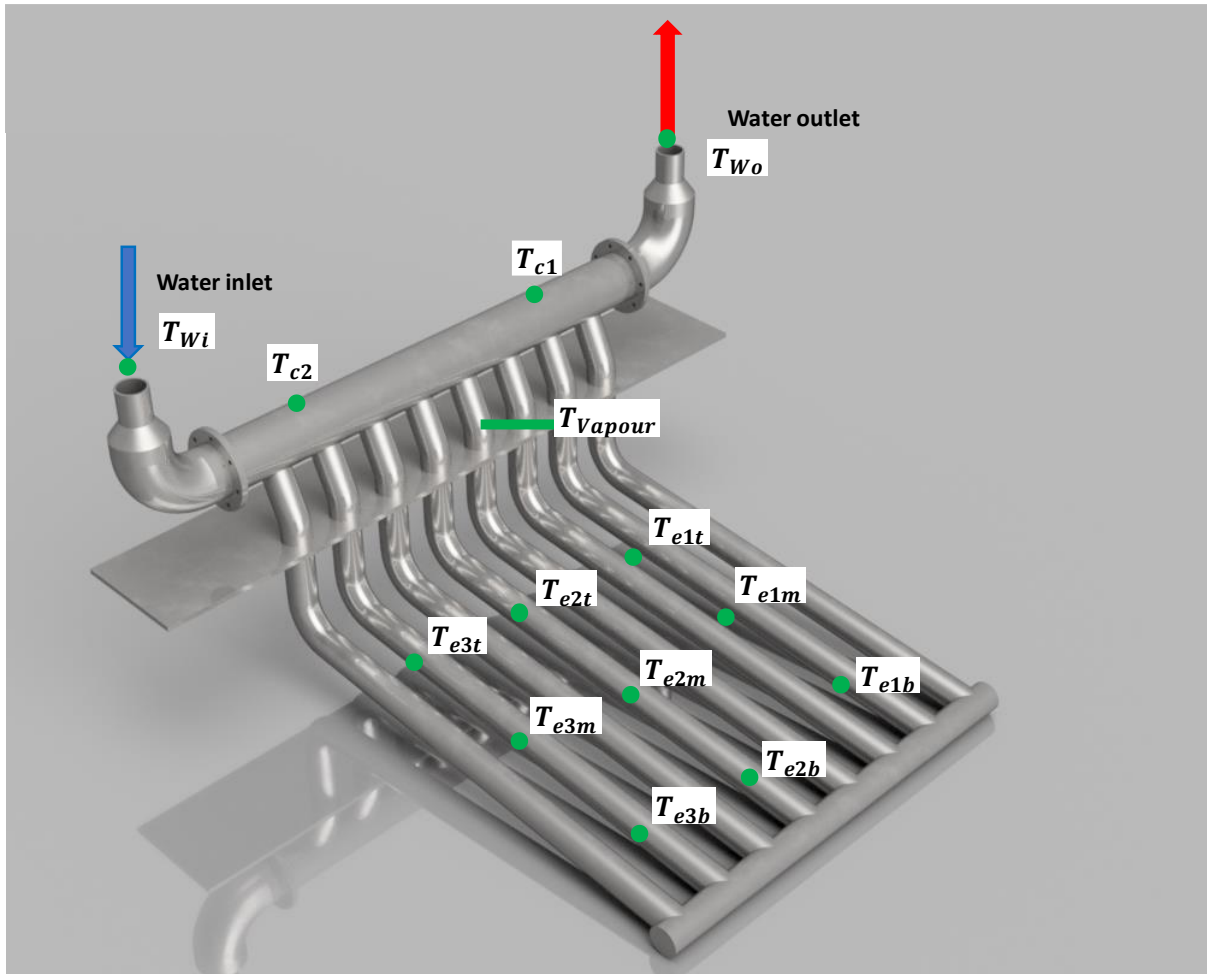


Figure 63 Thermocouple positions, module 25

3.4.3 Module 35

3.4.3.1 Mechanical design

Module 35 was composed of seven stainless steel pipes of 28 mm diameter connected through a collector of 28 mm diameter at the bottom and a shell and tube condenser section at the top. The shell and tube section similar to module 15, consisted of nine pipes each of 10 mm diameter as shown in Figure 64. The shell of the condenser was a 50 mm outer diameter stainless steel pipe with a thickness of 1 mm; a picture of the condenser section of the modules is presented in Figure 65. The spacing between the pipes of the evaporator section was 35mm.

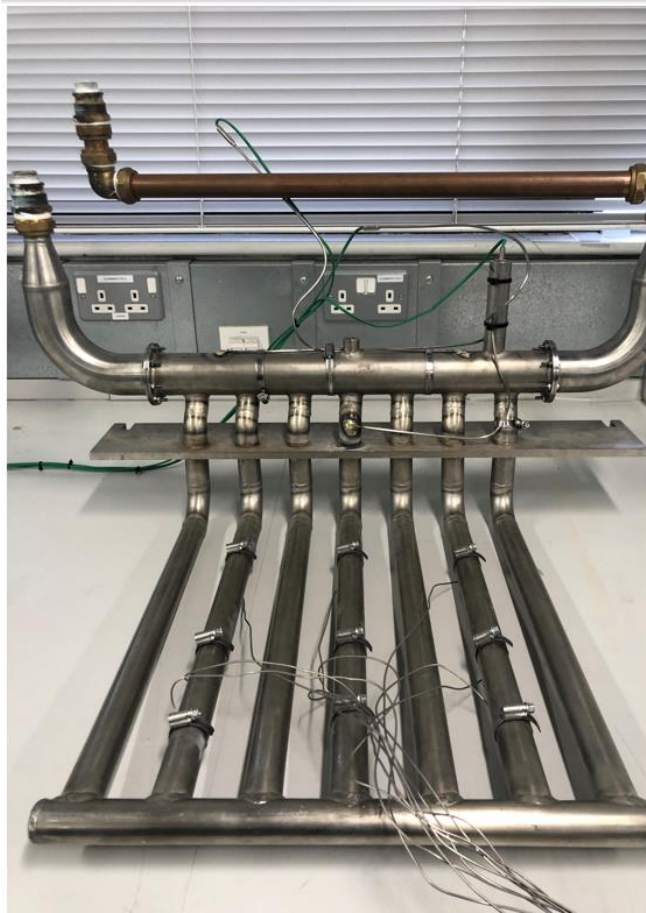


Figure 64 Module 35



Figure 65 Shell and tube condenser

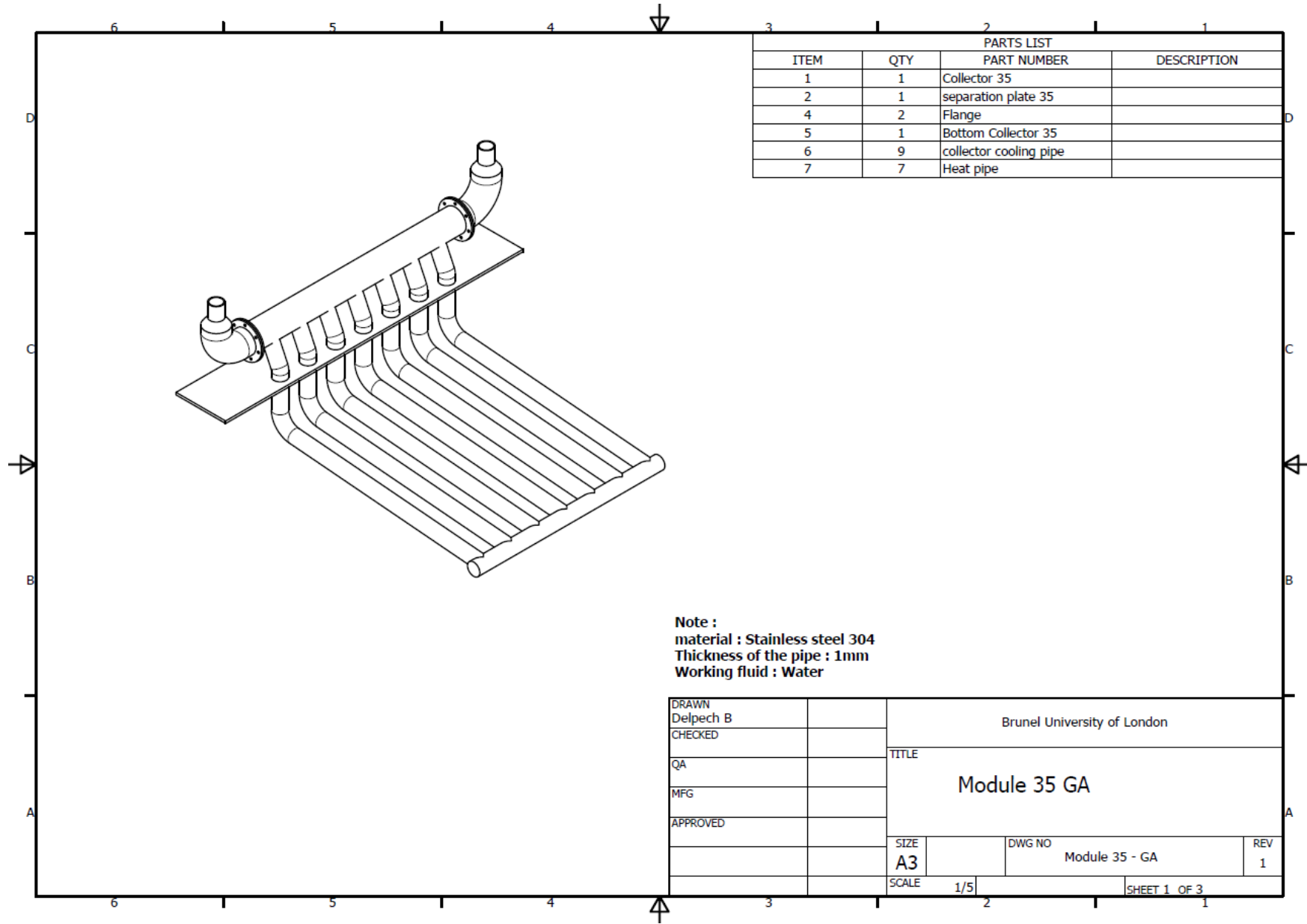


Figure 66 Module 35 GA

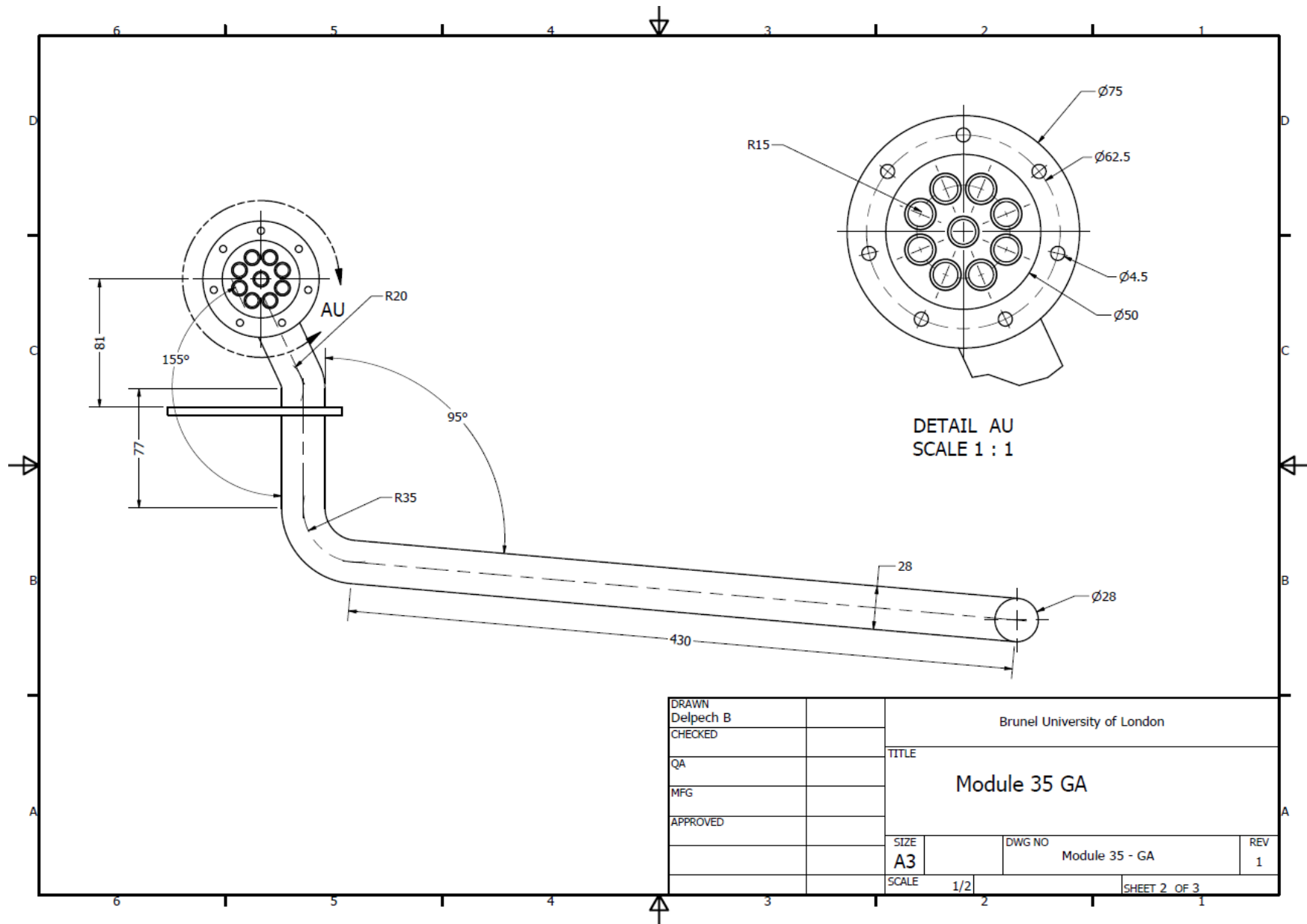


Figure 67 Module 35 condenser detail

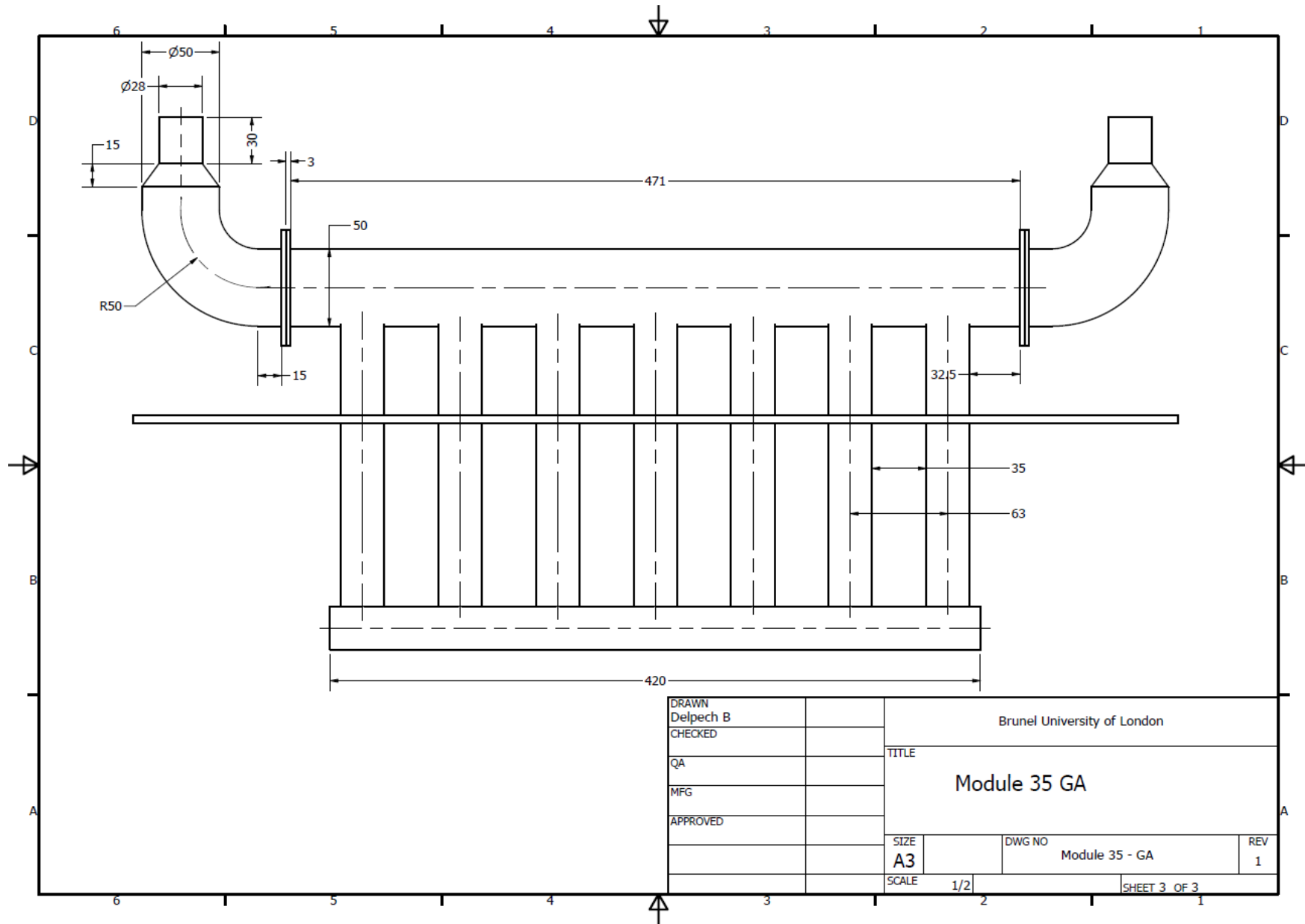


Figure 68 Module 25 front view

3.4.3.2 Thermocouple locations

Nine thermocouples were welded onto the bottom of three rows of tubes in the evaporator section at the bottom, facing the heating elements. Two thermocouples were placed on the condenser section and one thermocouple was in the vapour stream as shown in Figure 70. The thermocouples were then connected to the data logger as illustrated in Figure 69

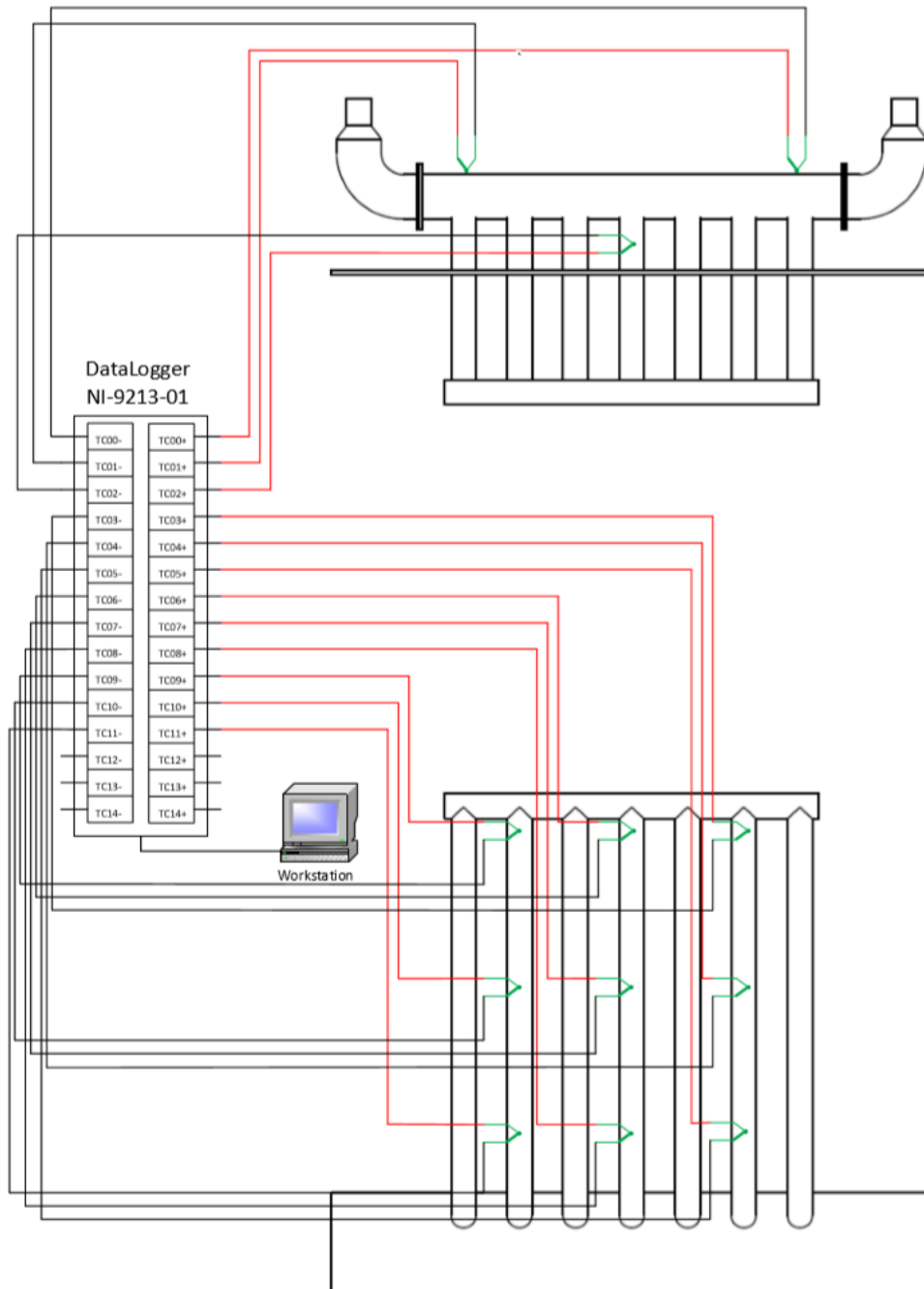


Figure 69 Thermocouples wiring, module 35

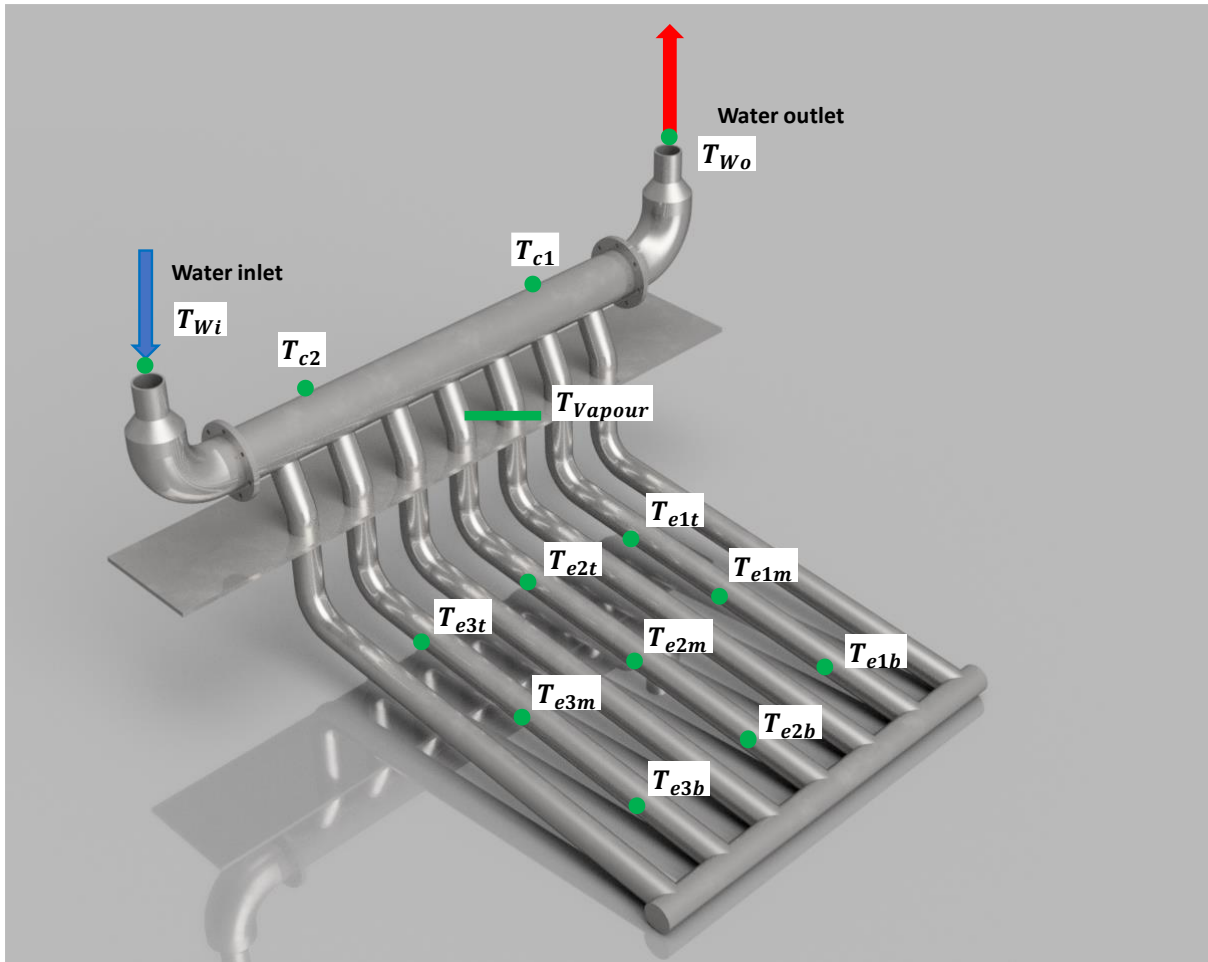


Figure 70 Thermocouples location, Module 35

3.4.4 Experimental plan

The aim with these systems was to validate the theoretical model developed in chapter 4 and to investigate the capacity of this innovative shape of heat pipe to recover heat. By using the experimental data, the heat transfer coefficient of this shape of heat pipe can be determined. The experiments were also used to investigate the phenomenon of geyser boiling at lower heat flux powers.

The difference between the three modules was the distance between the pipes. This distance has an impact on the heat flux going through the heat pipe due to a modification of the heat transfer area of the evaporator. The impact of changing this parameter resulted in a modification of the radial and axial heat fluxes in the heat pipe. The modification of the heat transfer area also has an impact on the overall view factor of the heat pipe, though decreasing the heat transfer through radiation.

Three tests were designed to verify the above objectives. All the heat pipes were charged at 75% filling ratio as it was determined using the single radiative heat pipe to be the best case regarding the heat transfer coefficient, evaporator dry out and geyser boiling. The modules were exposed to temperatures between 200 °C and 500° C for flow rates of 5 L/min to 20 L/min.

Table 13 Module 15 Test Plan

	Flow rate (L/min)			
Heat source (°C)	5	10	15	20
200	Test 1	Test 2	Test 3	Test 13
300	Test 4	Test 5	Test 6	Test 14
400	Test 7	Test 8	Test 9	Test 15
500	Test 10	Test 11	Test 12	Test 16

Table 14 Module 25 Test Plan

	Flow rate (L/min)			
Heat source (°C)	5	10	15	20
200	Test 16	Test 17	Test 18	Test 19
300	Test 20	Test 21	Test 22	Test 23
400	Test 24	Test 25	Test 26	Test 27
500	Test 28	Test 29	Test 30	Test 31

Table 15 Module 35 Test Plan

	Flow rate (L/min)

Heat source (°C)	5	10	15	20
200	Test 32	Test 33	Test 34	Test 35
300	Test 36	Test 37	Test 38	Test 39
400	Test 40	Test 41	Test 42	Test 43
500	Test 44	Test 45	Test 46	Test 47

Chapter 4: Theoretical modelling

4.1 Introduction

This chapter will develop the theoretical model used to create a full-scale model of a radiative heat pipe ceiling in a roller hearth ceramic kiln. The chapter will also cover the fundamentals of heat transfer using radiation, natural convection, forced convection and conduction as well as the heat pipe modelling. The chapter is separated in four sections. The first section will present the heat transfer background that will be used to design a thermal modelling tool, the second section the thermal modelling for a single radiative heat pipe. The third section will cover the modules 15, 25, 35. In the last section, the use of the radiative heat pipe for the full-scale model will be discussed and the modelling tools developed.

4.2 Heat transfer background

A wide variety of heat transfer principles are used in heat pipe heat exchanger. A heat pipe will rely on two phase heat transfer to transmit heat from the evaporator to the condenser section. The boiling and condensation regimes will be discussed in this section. In the kiln, the heat will be transferred to the heat pipe through radiation, external forced convection and natural convection. The heat will be transferred from the outer surface of the heat pipe to the inner surface by conduction. Internal forced convection will be used in the condenser to extract the heat from the heat pipe to the heat sink fluid.

4.2.1 Natural convection

Natural convection relies on low velocities and high temperatures to transfer heat from one surface to the other. The effect of the natural convection in a kiln is a large contributor to the heat transfer when no or low air velocity is applied. The heat transfer through natural convection is governed by the derivation of the equation of the fluid motion in a boundary layer under the effect of buoyancy.

A non-dimensional number called the Grashof number is introduced to quantify the ratio between the buoyancy force and the viscous force acting on the fluid. The Grashof number is as follows.

$$\text{Gr}_L = \frac{g\beta(T_s - T_\infty)L_c^3}{\nu^2} \quad (21)$$

where g is the gravitational acceleration (m/s^2), β is the coefficient of volume expansion ($1/\text{K}$) ($\beta = 1/T$ for ideal gases), T_s is the temperature of the surface ($^\circ\text{C}$), T_∞ is the temperature of the fluid sufficiently far from the surface ($^\circ\text{C}$), L_c characteristic length of the geometry (m), ν is the kinematic viscosity of the fluid (m^2/s)

The Grashof number, as the Reynolds number in forced convection, is the main criterion to determine if the fluid is laminar or turbulent in natural convection.

The natural convection over a surface depends on the orientation of the surface and the geometry. It will also involve the variation of temperature on the surface and the thermal properties of the fluid and material involved. Although the principal of natural convection is well understood, there is no equation that can be obtained through an analytical method. The determination of the natural convection heat transfer depends on an empirical approach. The determination of the Nusselt number using empirical correlations is determined as,

$$Nu = \frac{hL_c}{k} = C(Gr_L Pr)^n = CRa_L^n \quad (22)$$

where the Rayleigh number is the product of the Prandtl and Grashof numbers

$$Ra_L = Gr_L Pr = \frac{g\beta(T_s - T_\infty)L_c^3}{\nu^2} Pr \quad (23)$$

The values of the constants C and n depend on the geometry of the surface and the flow regime which is characterised by the Rayleigh number. The value of n is usually 1/4 for laminar flow and 1/3 for turbulent flow while the value of C is usually below 1. The value for the Nusselt number needs to be evaluated with fluid properties at the film temperature $T_f = \frac{1}{2}(T_s + T_\infty)$. If the Nusselt number for the convection is known, the rate of heat transfer from a material surface to the surrounding fluid can be expressed as,

$$Q_{N.convection} = hA_s(T_s - T_\infty) = \frac{(T_s - T_\infty)}{R_{N.convection}} \text{ (W)} \quad (24)$$

where $R_{N.convection} = 1/(hA_s)$ ($^{\circ}\text{C}/\text{W}$) is the thermal resistance of the fluid and the surface from the natural convection heat transfer. The thermal resistance will be used for the thermal resistance analogy.

As mentioned above, the heat transfer through natural convection will depend on the temperature, the shape and the inclination of the surface.

Al-Arabi and Salman [64] developed a correlation for natural convection of inclined cylinders at a constant heat flux,

$$\text{Al-Arabi and Salman: [64]} \quad Nu_D = 0.6 - 0.488(\sin \theta)^{1.03} (GR_D Pr)^{\frac{1}{4} + \frac{1}{12}} (\sin \theta)^{1.75} \quad (25)$$

where $Ra_D = 10^{5.5} - 10^9$, $0^\circ < \theta < 90^\circ$ from vertical.

Oosthuizen [65] developed a correlation for inclined cylinders

Oosthuizen: [65]

$$Nu_D = 0.42(Gr_D \cos \varphi)^{1/4} \left[1 + \left(\frac{1.31}{L^4} \right)^3 \right]^{1/2} \quad (26)$$

Rani et al. [66] proposed a new correlation for Nusselt number determination using the experimental data from [67]. Four proposed correlations were subjected to a nonlinear regression analysis method using two parameters a and b. The results were then compared to experimental values available in the literature in [65,67,68]. The selected correlation was as below.

Rani et al. [66]

$$Nu_D = 0.54 + 0.39 \left[\frac{PrGr}{\left\{ 1 + \left(\frac{0.559}{Pr} \right)^{16} \right\}^{16/9}} \right]^{0.1685} \quad (27)$$

where the characteristic length is calculated from Eq.(28):

Characteristic length

$$L_c = \left[\frac{LD}{\left(\frac{L}{D} \right) \cos \varphi + \left(\frac{D}{L} \right) \sin \varphi} \right]^{1/2} \quad (28)$$

Li and Tarasuk [69] developed a new correlation using two coefficients m and n . Those coefficients are determined by a least squares straight-line approximation of the logarithm of the average Nusselt number and Rayleigh number. The error from the correlation are given in Table 16. The correlation and experimental data were then compared with correlations developed by Salman [64], Morgan [70], and Oosthuizen [65]. The comparison with the other correlations highlighted a good agreement with the experimental data.

$$Nu_D = m(\varphi) Ra_D^{n(\varphi)} \quad (29)$$

where

$$m(\varphi) = 0.5925 + 0.2278 \times 10^{-2} \times (\varphi) - 0.1436 \times 10^{-3} \times (\varphi)^2 + 0.1877 \times 10^{-5} \times (\varphi)^3 + 0.986 \times 10^{-8} \times (\varphi)^4 \quad (30)$$

$$n(\varphi) = 0.2295 + 0.1553 \times 10^{-2} \times (\varphi) - 0.7396 \times 10^{-4} \times (\varphi)^2 + 0.1157 \times 10^{-5} \times (\varphi)^3 - 0.5783 \times 10^{-8} \times (\varphi)^4 \quad (31)$$

Table 16 Value and error associated with n , m and Nusselt number

Angle	m	n	Range of Ra_D	Error
0°	0.5925	0.2294	1.2×10^4 to 2.9×10^9	-6.4 to 6.3%
45°	0.5349	0.2313	1.1×10^4 to 3.3×10^9	-1.3 to 0.79%
60°	0.49	0.2313	1.2×10^4 to 2.5×10^9	-0.24 to 1.7%
75°	0.4375	0.2349	1.2×10^4 to 3.1×10^9	-4.6 to 2.9%
90°	0.3561	0.2339	1.4×10^4 to 3.1×10^9	-14.6 to 5.5%

Heo and Chung [71] investigated correlations on inclined cylinders for a Rayleigh number between 1.69×10^8 and 5.07×10^{10} at angles of inclination from 0° to 90° for a ratio L/D between 3.7 to 25.

$$\text{Laminar flow} \quad Nu_D = 0.3Ra_D^{0.25}(1 + 0.7 \cos \varphi) \quad (32)$$

$$\text{Turbulent flow} \quad Nu_D = 0.13Ra_D^{0.3}(1 + 0.6 \cos \varphi) \quad (33)$$

4.2.2 Radiation

Radiation heat transfer does not rely on any contact between the emitting surface and the receiving surface and reaches maximum efficiency in a vacuum. Radiation heat transfer occurs from solids, liquids and gases.

In 1864, James Clerk Maxwell demonstrated that electric and magnetic fields travel in space as waves. The electromagnetic waves are emitted energy by any object due to the change in atoms or molecule electronic configuration.

Radiation travels, in a vacuum, at the speed of light. This speed is equal to the product of the wavelength of the radiation and the frequency.

$$c = \lambda \nu \quad (34)$$

Thermal radiation corresponds to the electromagnetic radiation from a body due to the energy transition of its molecules as a function of the temperature. Thermal radiation from a body is continually emitted by the body when the temperature of the body is above absolute zero. The thermal radiation can be emitted by solids and liquids, the radiation will be transmitted through a vacuum, gases and some liquids and solids depending on the opacity. The range of thermal radiation is between 0.1 μm to 100 μm . The visible range of thermal radiation is from 0.4 to 0.7 μm . The electromagnetic spectrum and thermal radiation portion can be seen in Figure 71.

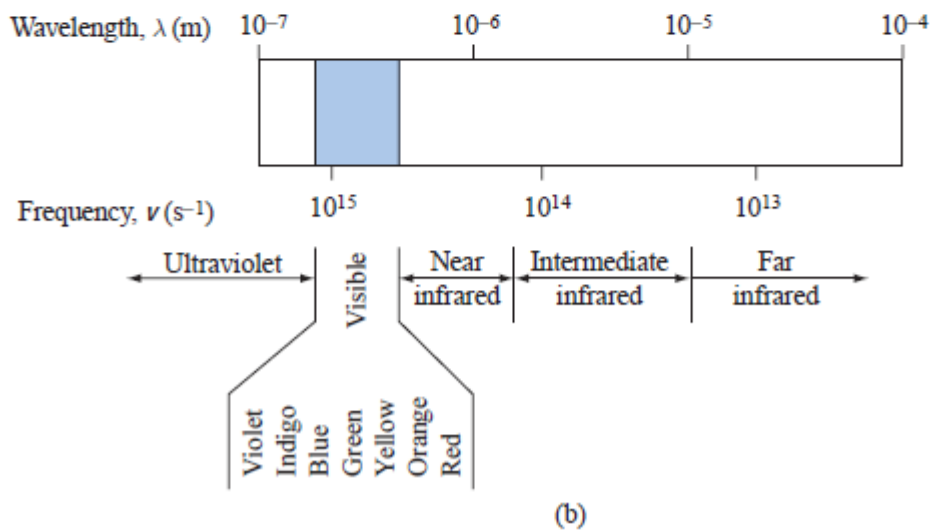
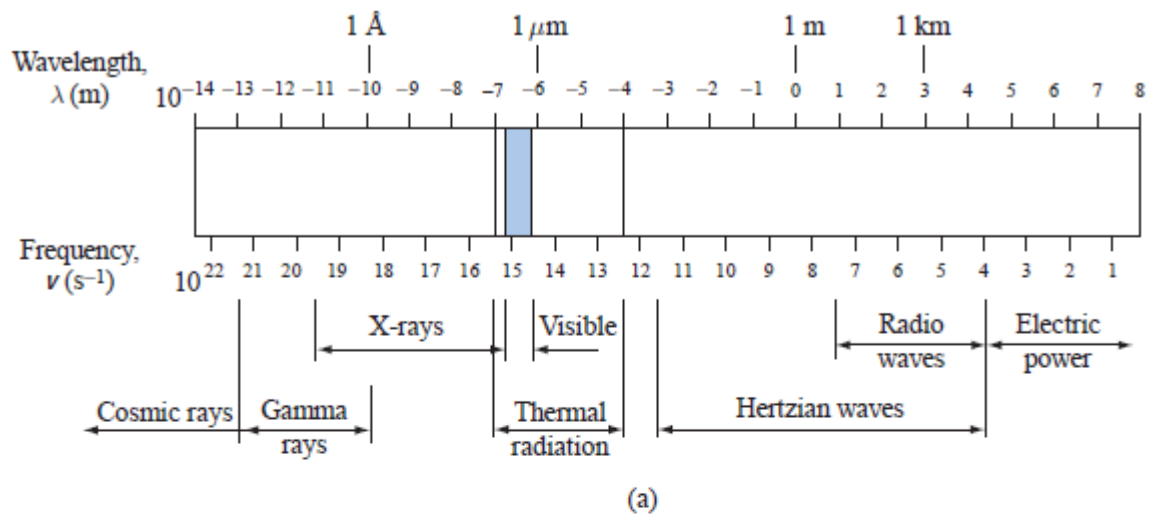


Figure 71 (a) Electromagnetic spectrum. (b) Thermal radiation portion of the electromagnetic spectrum. [72]

4.2.2.1 Blackbody radiation

A blackbody is considered to be an ideal body that can emit and absorb the maximum radiation energy possible at any wavelength for any temperature.

A black body can absorb any wavelength with any given incidence. Also, the energy emitted by the black body is uniform in all directions per unit area normal to the direction of emission. It is considered as a diffuse emitter. The correlation between the spectral radiant energy emission per unit of time and area was defined experimentally by Joseph Stefan in 1879 and Ludwig Boltzmann theoretically in 1884

$$E_b(T) = \sigma T^4 \quad (35)$$

A relationship between the emissive power of a blackbody and the wavelength distribution was derived by Max Planck in 1900 in his quantum theory,

$$E_{b\lambda}(T) = \frac{C_1}{\lambda^5 \left[\exp\left(\frac{C_2}{\lambda T}\right) - 1 \right]} \quad (36)$$

where $C_1 = 3.74177 \times 10^8 \text{ W} \cdot \frac{\mu\text{m}^4}{\text{m}^2}$, $C_2 = 1.43878 \times 10^4 \mu\text{m} \cdot \text{K}$

C_1 is the first radiative constant, C_2 is the second radiant constant, $E_{b\lambda}(T)$ is the monochromatic emissive power of a blackbody at temperature T , T is the absolute temperature of the surface, λ is the wavelength of the radiated emission.

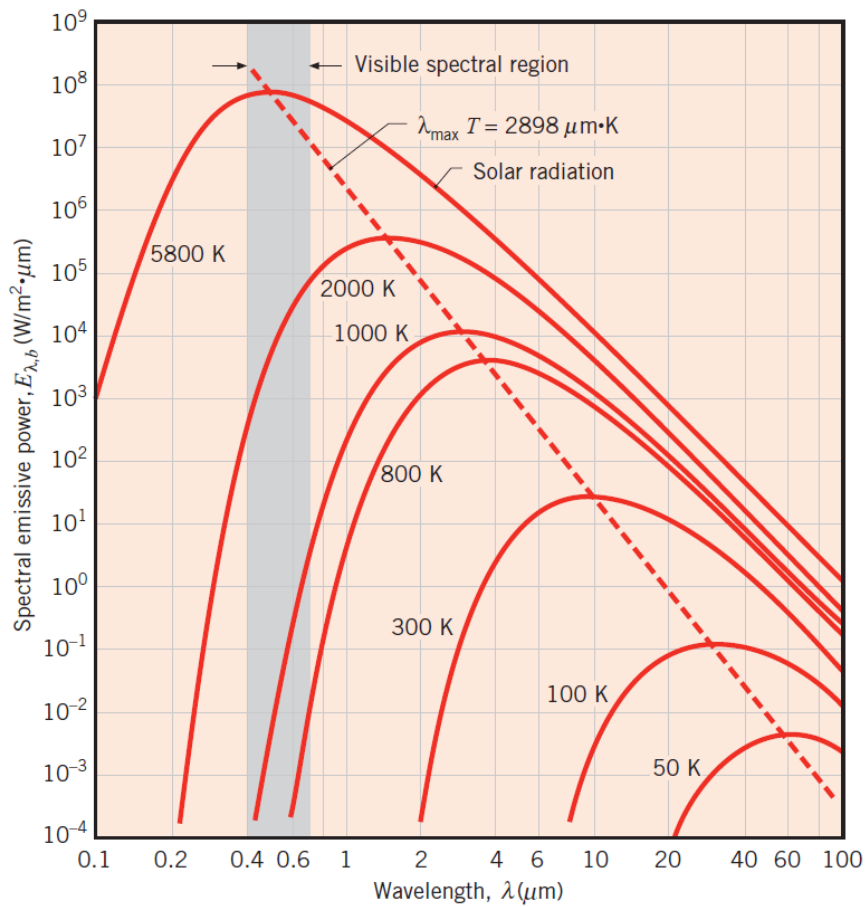


Figure 72 Spectral blackbody emissive power [73]

It can be noted from Figure 72 that the emitted radiation varies continuously with the wavelength, the emitted radiation increases with increasing temperature at any given wavelength. Also, most of the emitted radiation below 800K does not appear in the visible spectral region. The emitted radiation for each temperature reaches a peak and decreases as the wavelength increases up to the infrared wavelengths. In order to determine the emitted radiation peak for each temperature, the Wien Displacement Law is introduced,

$$\lambda_{\text{max power}} T = 2897.8 \mu\text{m} \cdot \text{K} \quad (37)$$

The integration of Planck's law of the spectral emissive power of a blackbody over the range of wavelength spectrum is the total blackbody emissive power E_b ,

$$E_b(T) = \int_0^{\infty} E_{b\lambda}(\lambda, T) d\lambda = \sigma T^4 \text{ (W/m}^2 \text{)} \quad (38)$$

where σ is Stephan-Boltzmann constant $\sigma = 5.67 \times 10^{-8} \text{ W/m}^2\text{K}^4$

4.2.2.2 Radiation intensity

Radiation can be propagated in every direction. In order to determine the net radiative heat transfer rate, it is important to understand how the radiation is propagated from or to a surface. By considering the directional distribution of radiation as a sphere above the radiative surface, the direction may be specified with a zenith angle θ and an azimuthal angle ϕ .

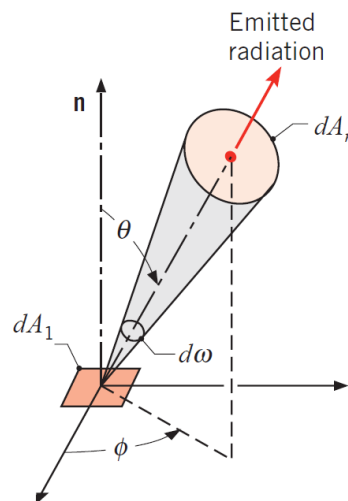


Figure 73 Emission of radiation from a differential area dA_1 into a solid angle $d\omega$ subtended by dA_n at a point on dA_1 [73]

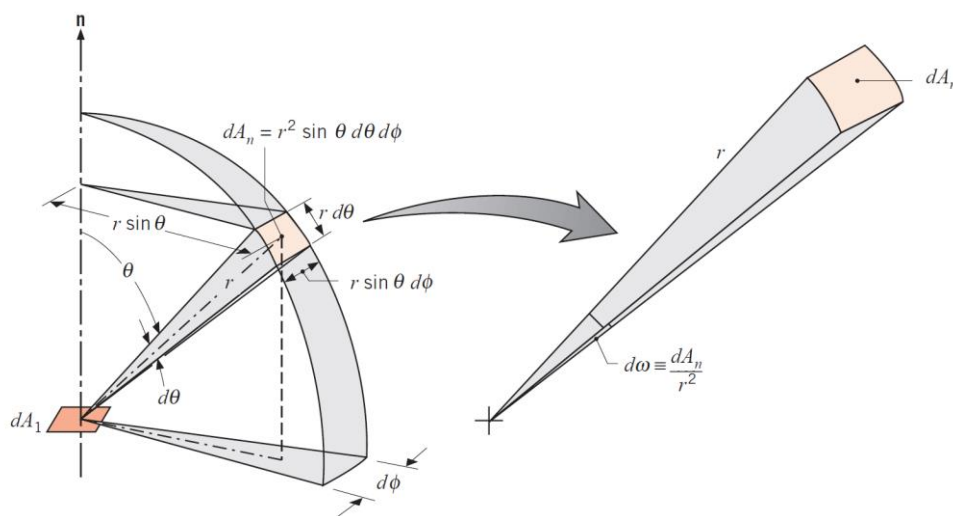


Figure 74 The solid angle subtended by dA_n at a point on dA_1 in the spherical coordinate [73]

The surface dA_n where the radiation passes, has a differential solid angle $d\omega$ when viewed from the point of dA_1 . $d\omega$ is expressed as,

$$d\omega = \sin \theta \, d\theta \, d\phi \quad (39)$$

If the surface dA_1 is considered opaque, the radiation will be emitted in any direction in a hemisphere above the surface. The solid angle associated with the hemisphere can be determined by integrating equation (39) over the limits $\theta = 0$ to $\theta = \pi/2$ and $\phi = 0$ to $\phi = 2\pi$

$$\int_h d\omega = \int_0^{2\pi} \int_0^{\pi/2} \sin \theta \, d\theta \, d\phi = 2\pi \int_0^{\pi/2} \sin \theta \, d\theta = 2\pi r \quad (40)$$

The rate at which the emission from dA_1 passes through dA_n is expressed as the spectral intensity $I_{\lambda,e}$. The spectral intensity can be defined as the rate at which radiant energy is emitted at the wavelength λ in the (θ, ϕ) direction, per unit area of emitting surface normal to this direction, per unit solid angle about this direction and per unit wavelength interval $d\lambda$ about λ .

$$I_e(\lambda, \theta, \phi) = \frac{dq}{dA_1 \cos \theta \, d\omega \, d\lambda} \quad (41)$$

where $\left(\frac{dq}{d\lambda}\right) \equiv dq_\lambda$ the rate at which radiation of wavelength λ passing through dA_n , leaving from dA_1 , (41) can be expressed as,

$$dq_\lambda = I_e(\lambda, \theta, \phi) dA_1 \cos \theta \, d\omega \quad (42)$$

If we express (42) per unit area of emitting surface and substituting (39), we obtain the spectral radiation flux associated with dA_1 ,

$$dq_\lambda = I_e(\theta, \phi) \cos \theta \sin \theta \, d\theta \, d\phi \, (W/m^2) \quad (43)$$

The spectral hemispherical emissive power E_λ can be determined by integrating (42), if $I_e(\lambda, \theta, \phi)$ is known. E_λ is defined as the rate at which radiation of wavelength λ is emitted in all directions from a surface per unit surface area. E_λ is the spectral heat flux associated with the emission in a hypothetical hemisphere above the surface dA_1 as shown in Figure 75.

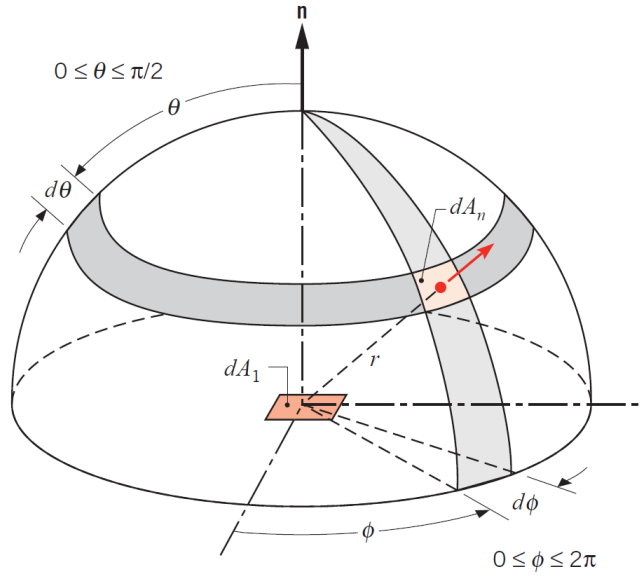


Figure 75 Emission from a differential surface dA_1 to a differential surface dA_n [73]

$$E = \int_{\phi=0}^{2\pi} \int_{\theta=0}^{\pi/2} I_e(\theta, \phi) \cos \theta \sin \theta d\theta d\phi \quad (\text{W/m}^2) \quad (44)$$

The total hemispherical emissive power E can be defined as,

$$E = \pi I_e \quad (\text{W/m}^2) \quad (45)$$

The surfaces do not only emit but also receive radiation emitted or reflected from other surfaces, the radiation incident on a surface from all direction is defined as irradiation G ,

$$G = \int_{\phi=0}^{2\pi} \int_{\theta=0}^{\pi/2} I_i(\theta, \phi) \cos \theta \sin \theta d\theta d\phi \quad (\text{W/m}^2) \quad (46)$$

Similar to (45), it can be determined that

$$G = \pi I_i \quad (\text{W/m}^2) \quad (47)$$

4.2.2.3 Radiation properties

Emissivity

The blackbody is a perfect element that will emit and receive all the energy available in its surroundings. The emissivity is used to describe a real surface. A real radiative surface will not be able to act as a blackbody. The emissivity is defined as the ratio of the radiation energy emitted by a surface at a given temperature to the radiation of a black body at the same temperature. The emissivity is within the range of $0 \leq \varepsilon \leq 1$. The emissivity will vary depending on the orientation of the emitted radiation at a given temperature and wavelength.

$$\varepsilon_{\lambda, \theta}(\lambda, \theta, \phi, T) = \frac{I_{\lambda, e}(\lambda, \theta, \phi, T)}{I_{\lambda, b}(\lambda, T)} \quad (48)$$

To simplify equation (48), the direction of θ and ϕ can be averaged.

$$\varepsilon_\lambda(\lambda, T) = \frac{E_\lambda(\lambda, T)}{E_{b\lambda}(\lambda, T)} \quad (49)$$

The emissivity is then a function of the wavelength and the temperature of the surface. The emissivity can be also defined as the average for all wavelengths from the surface, defined as the total hemispherical emissivity or average emissivity:

$$\varepsilon(T) = \frac{E(T)}{E_b(T)} \quad (50)$$

Absorption, reflection and transmission

Various types of heat fluxes are defined in the radiation theory of shown in Figure 76. The Emissive Power of the surfaces correspond to the rate at which radiation is emitted from a surface per unit area. When the body is considered as a black body, only emissive power and irradiation play a role. In the case of a real semi-transparent body, new heat fluxes need to be introduced, the absorption by the solid of the irradiation, the transmission of the irradiation through the solid and the reflection of the irradiation.

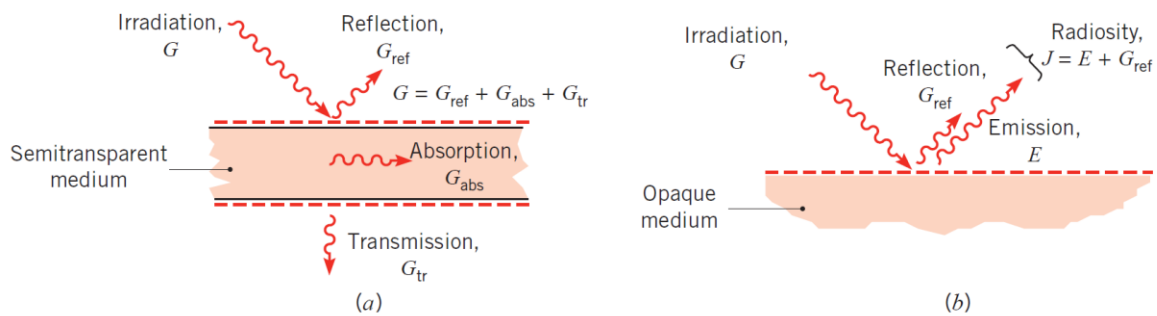


Figure 76 Radiation at a surface. (a) Reflection, absorption, and transmission of irradiation for a semi-transparent medium. (b) The radiosity for an opaque medium.[73]

Table 17 Radiative fluxes[73]

Flux (W/m ²)	Description
Emissive power, E	Rate at which radiation is emitted from a surface per unit area
Irradiation, G	Rate at which radiation is incident upon a surface per unit area
Radiosity, J	Rate at which radiation leaves a surface per unit area

Net radiative flux,

Net rate of radiation leaving a surface per unit area

$$q''_{rad} = J - G$$

Absorptivity α can be defined as the fraction of irradiation absorbed by the solid, the reflectivity ρ as the fraction of irradiation reflected and the transmissivity τ as the fraction of the irradiation that is transmitted, as all the irradiation must be reflected, transmitted or absorbed,

$$\alpha + \rho + \tau = 1 \quad (51)$$

An opaque medium will have a transmissivity of 0

$$\alpha + \rho = 1 \quad (52)$$

Using the equation above, two additional heat fluxes can be defined, the radiosity of the surface which accounts for all the radiant energy leaving the surface. In the case of an opaque medium, it includes the reflection of the irradiation and the emitted radiation from the medium, therefore,

$$J = E + \rho G \quad (53)$$

The net radiation leaving an opaque surface can be then defined as,

$$q''_{rad} = \epsilon \sigma T_s^4 - \alpha G$$

Kirchhoff's law

Kirchhoff's law was introduced by Gustav Kirchhoff. By considering a large blackbody enclosure at a temperature T_s , with two small solid bodies 1 and 2 within the enclosure, the impact of the small body can be considered negligible. Thus, the incident radiation on the small body is equal to the emitted radiation by the large black body at equilibrium at the same temperature T_s ,

$$G = E_b(T_s) = \sigma T_s^4 \quad (54)$$

At equilibrium, the temperature of the blackbody surface and the temperature of the solid are equal, thus, the net heat transfer between the enclosure and the solid must be zero. Applying this to the body 1,

$$\alpha_1 G A_1 - E_1(T_s) A_1 = 0 \quad (55)$$

From Equation (54),

$$\frac{E_1(T_s)}{\alpha_1} = E_b(T_s) \quad (56)$$

The same method can be applied for all the bodies in the enclosure,

$$\frac{E_1(T_s)}{\alpha_1} = \frac{E_2(T_s)}{\alpha_2} = \dots = E_b(T_s) \quad (57)$$

Equation (57) is known as the Kirchhoff's law. An alternative equation of the Kirchhoff's law based on the definition of the total hemispherical emissivity is introduced,

$$\frac{\varepsilon_1}{\alpha_1} = \frac{\varepsilon_2}{\alpha_2} = \dots = 1 \quad (58)$$

Hence, for any surface in an enclosure,

$$\varepsilon = \alpha \quad (59)$$

The total hemispherical absorptivity of a surface is equal to the total emissivity if the surface is considered isothermal and there is no net radiation heat transfer between other surfaces.

4.2.2.4 Real surfaces

Radiation from real surfaces is different from radiation in black bodies. Any real surfaces will have variable emissive power depending on the characteristic or the geometry of the surface. It can be considered that the real emissive power of a real surfaces is a fraction of the total emissive power of a blackbody,

$$E_{real}(T_s) = \varepsilon \sigma T^4 \quad (60)$$

4.2.2.5 View factor

In order to define the heat transfer rate between two surfaces, the view factor needs to be introduced. The view factor is described as the fraction of radiation leaving the surface i reaching the surface j . To develop a general expression illustrating F_{ij} , two surfaces A_i and A_j are considered. These two surfaces are differential surfaces dA_i and dA_j . The distance between these two surfaces is R . two polar angles are introduced as θ_i and θ_j form an angle with respectively n_i and n_j . The solid angle can be determined as,

$$d\omega_{12} = \cos \theta_2 \frac{dA_2}{r^2} \quad (61)$$

From the definition of radiation intensity, the rate of radiation leaving the surface dA_i intercepted by dA_j can be expressed as,

$$dQ_{ij} = I_i \cos \theta_i dA_i d\omega_{ij} \quad (62)$$

The radiosity of the surface dA_i ,

$$J_i = \pi I_i \quad (63)$$

thus,

$$dQ_{ij} = J_i \left(\frac{\cos \theta_i \cos \theta_j}{\pi r^2} \right) dA_i dA_j \quad (64)$$

The radiation leaving the surface A_i intercepted by A_j can be expressed as

$$Q_{ij} = J_i \int_{A_i} \int_{A_j} \left(\frac{\cos \theta_i \cos \theta_j}{\pi r^2} dA_i dA_j \right) \quad (65)$$

where it is assumed that the radiosity J_i is uniform over the surface A_i .

The view factor is a fraction of the radiation leaving A_i and reaching A_j , thus

$$F_{ij} = \frac{Q_{ij}}{A_i J_i} \quad (66)$$

It follows that,

$$F_{ij} = \frac{1}{A_j} \int_{A_j} \int_{A_i} \left(\frac{\cos \theta_i \cos \theta_j}{\pi r^2} \right) dA_i dA_j \quad (67)$$

View factor relations

View factor relations are used to simplify the analytical approach of the calculation of the view factor.

Reciprocity rule

The reciprocity is useful to determine view factor when more than two surfaces are present in the system,

$$A_1 F_{1,2} = A_2 F_{2,1} \quad (68)$$

Summation rule

The summation rule state that the sum of all the view factors of surfaces in an enclosure must be equal to 1,

$$\sum_{j=1}^N F_{ij} = 1 \quad (69)$$

The superposition rule

The superposition rule is expressed as the view factor from a surface 1 to a surface (2,3) is equal to the sum of the view factors from surface 1 to 2 and the surface 1 to 3 as shown in Figure 77.

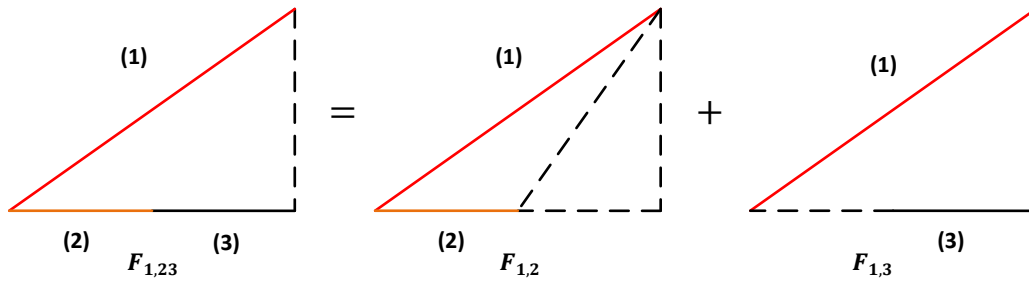


Figure 77 Illustration of superposition rule

Hence,

$$F_{1 \rightarrow (2,3)} = F_{12} + F_{13} \quad (70)$$

The symmetry rule

To simplify the view factor determination in any shape, symmetry must be identified and used to reduce the complexity of the view factor. The symmetry rule can be expressed as follows: two or more surfaces that possess the same geometry with a third surface will have an identical view factor value. The symmetry rule can be expressed as,

$$F_{12} = F_{13} \quad (71)$$

hence

$$F_{21} = F_{23} \quad (72)$$

An illustration of the symmetry rule can be seen in Figure 78.

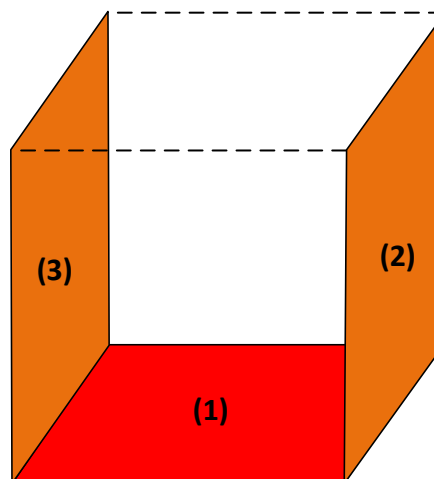


Figure 78 Illustration of summation rule

Literature review on view factor

Views factors for common geometries have been developed, investigated and tested. A catalogue of view factors for different geometries has been developed by Howell [74]. The

view factors are determined through analytical, mathematical and numerical calculation. Most common view factors used for pipes and enclosures are reported below.

For two infinite planes with a common edge at an angle of 90° from each other, the view factor was reported by [75,76]. An illustration can be seen in Figure 79.

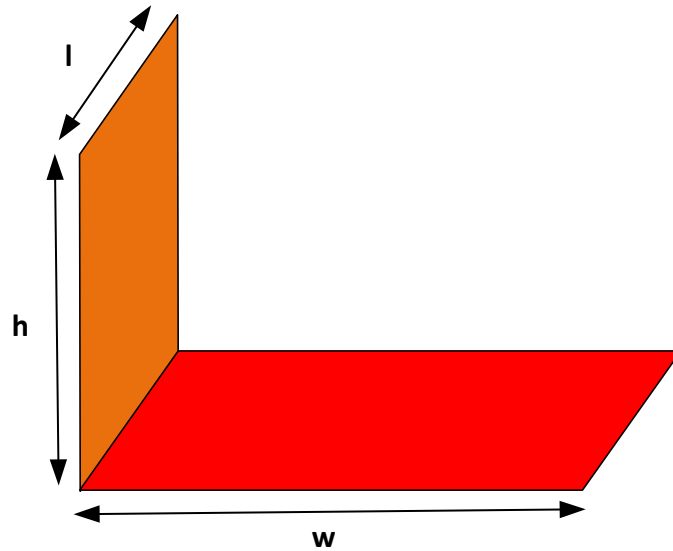


Figure 79 Schematic of two infinite planes with a common edge at an angle of 90° from each other

$$F_{1-2} = \frac{1}{W\pi} \left(W \tan^{-1} \frac{1}{W} + H \tan^{-1} \frac{1}{H} - \sqrt{H^2 + W^2} \tan^{-1} \sqrt{\frac{1}{H^2 + W^2}} \right. \\ \left. + \frac{1}{4} \ln \left\{ \frac{(1 + W^2)(1 + H^2)}{1 + W^2 + H^2} \left[\frac{W^2(1 + W^2 + H^2)}{(1 + W^2)(W^2 + H^2)} \right]^{W^2} \left[\frac{H^2(1 + H^2 + W^2)}{(1 + H^2)(H^2 + W^2)} \right]^{H^2} \right\} \right) \quad (73)$$

where $H = h/l, W = w/l$.

The view factor for two parallel rectangles of different size as shown in Figure 80 was studied and reported by [77] and validated by Gross *et al.* [78], Boeke and Wall [79], and Chkhovskii [80]. An illustration can be seen in Figure 80.

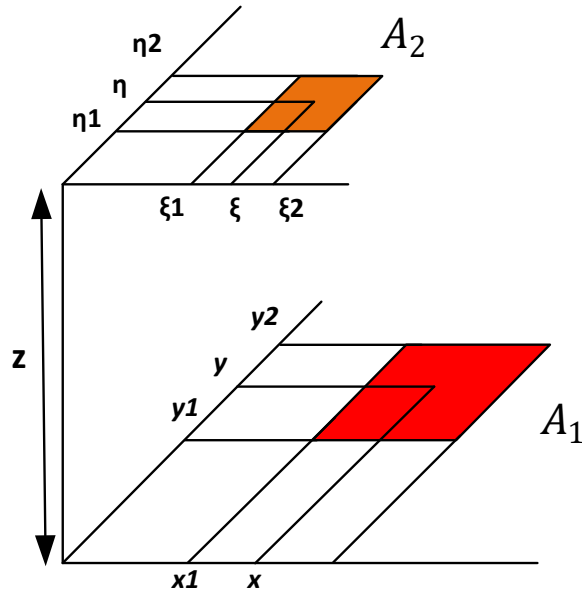


Figure 80 Schematic of the geometry of two rectangles in a parallel plane

$$F_{1-2} = \frac{1}{(x_2 - x_1)(y_2 - y_1)} \sum_{i=1}^2 \sum_{k=1}^2 \sum_{j=1}^2 \sum_{l=1}^2 (-1)^{(i+j+k+l)} G(x_i, y_j, \eta_k, \xi_l) \quad (74)$$

$$G = \frac{1}{2\pi} \left(\begin{aligned} & (y - \eta)[(x - \xi)^2 + z^2]^{1/2} \tan^{-1} \left\{ \frac{y - \eta}{[(x - \xi)^2 + z^2]^{1/2}} \right\} \\ & + (x - \xi)[(y - \eta)^2 + z^2]^{1/2} \tan^{-1} \left\{ \frac{x - \xi}{[(y - \eta)^2 + z^2]^{1/2}} \right\} \\ & - \frac{z^2}{2} \ln[(x - \xi)^2 + (y - \eta)^2 + z^2] \end{aligned} \right) \quad (75)$$

An equation was also developed by [77] and validated by Gross *et al.* [78], Boeke and Wall [79], and Chkhovskii [80] for a view factor between two surfaces of different sizes perpendicular to each other. An illustration can be seen in Figure 81.

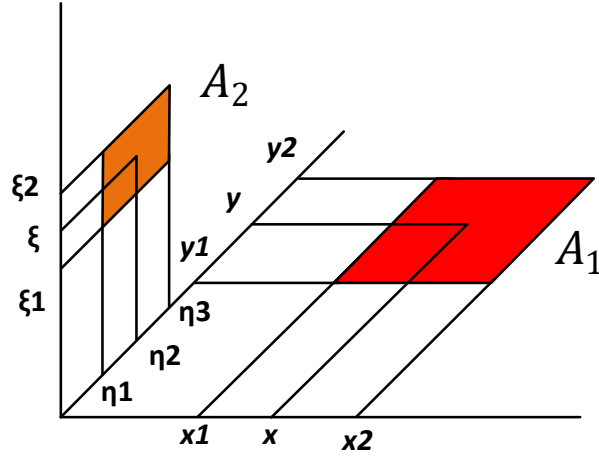


Figure 81 Schematic of the geometry of two rectangles in a perpendicular plane

$$F_{1-2} = \frac{1}{(x_2 - x_1)(y_2 - y_1)} \sum_{l=1}^2 \sum_{k=1}^2 \sum_{j=1}^2 \sum_{i=1}^2 [(-1)^{(i+j+k+l)} G(x_i, y_j, \eta_k, \xi_l)] \quad (76)$$

$$G = \frac{1}{2\pi} \left\{ \begin{aligned} & (y - \eta)(x^2 + \xi^2)^{\frac{1}{2}} \tan^{-1}(K) \\ & - \frac{1}{4} \left[(x^2 + \xi^2) \ln(1 + K^2) - (y - \eta)^2 \ln \left(1 + \frac{1}{K^2} \right) \right] \end{aligned} \right\} \quad (77)$$

where:

$$K \equiv (y - \eta) / (x^2 + \xi^2)^{1/2} \quad (78)$$

The view factor from a strip to a cylinder is calculated using the equation below

$$F_{12} = \frac{1}{2\pi} (\tan^{-1} B_1 - \tan^{-1} B_2) \quad (79)$$

where

$$B_1 = \frac{b_1}{a}, B_2 = \frac{b_2}{a} \quad (80)$$

An illustration can be seen in Figure 82

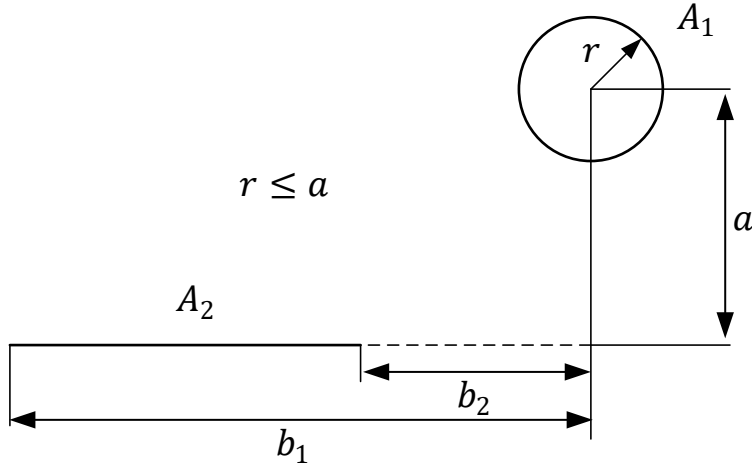


Figure 82 Illustration of the view factor between a cylinder and a strip

4.2.2.6 Net radiation in three surface enclosure

As previously said, any surfaces that have a temperature above absolute zero will emit heat in any given direction. When the surface receives an incident radiation, the total radiation leaving the receiving surface will be composed of the emission and the reflection. The sum of these two heat fluxes is the radiosity.

For a grey and opaque surface i ($\varepsilon_i = \alpha_i$ and $\rho_i + \alpha_i = 1$), the radiosity is expressed as,

$$J_i = (\text{Radiation emitted surface } i) + (\text{Radiation reflected surface } i) \quad (81)$$

$$J_i = \varepsilon_i E_{bi} + \rho_i G_i \quad (82)$$

$$J_i = \varepsilon_i E_{bi} + (1 - \varepsilon_i) G_i \quad (83)$$

By considering a surface that will gain energy by absorbing emitted radiation and losing energy by emitting radiation, a surface will have a net gain or loss of energy. The net heat transfer from a surface i of area A_i is expressed as,

$$Q_i = \left(\begin{array}{c} \text{Radiation leaving} \\ \text{entire surface } i \end{array} \right) - \left(\begin{array}{c} \text{Radiation incident} \\ \text{on entire surface } i \end{array} \right) \quad (84)$$

$$Q_i = A_i (J_i - G_i) \quad (85)$$

hence

$$Q_i = A_i \left(J_i - \frac{J_i - \varepsilon_i E_{bi}}{1 - \varepsilon_i} \right) = \frac{A_i \varepsilon_i}{1 - \varepsilon_i} (E_{bi} - J_i) \quad (W) \quad (86)$$

By applying the electrical analogy to (86) the following can be obtained

$$Q_i = \frac{E_{bi} - J_i}{R_i} \quad (W) \quad (87)$$

$$R_i = \frac{1 - \varepsilon_i}{A_i \varepsilon_i} \quad (88)$$

where R_i is the surface resistance of the surface, Q_i is the net radiation and $E_{bi} - J_i$ represent the potential difference. An illustration can be seen in Figure 83.

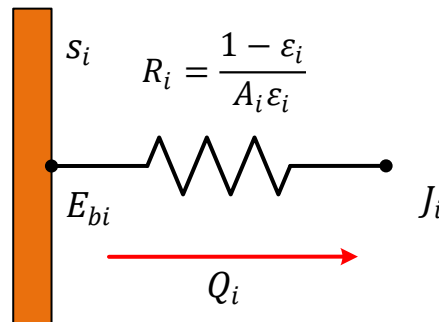


Figure 83 Schematic of the resistance approach of radiation leaving a surface i

The net radiation between two grey surfaces can be expressed as follows,

$$Q_{ij} = \left(\begin{array}{l} \text{Radiation leaving} \\ \text{the entire surface } i \\ \text{and striking surface } j \end{array} \right) - \left(\begin{array}{l} \text{Radiation leaving} \\ \text{the entire surface } j \\ \text{and striking surface } i \end{array} \right) \quad (89)$$

thus

$$Q_{ij} = A_i F_{ij} J_i - A_j F_{ji} J_j \quad (90)$$

Applying the reciprocity rule the following can be obtained,

$$Q_{ij} = A_i F_{ij} (J_i - J_j) = \frac{J_i - J_j}{R_{ij}} \quad (\text{W}) \quad (91)$$

where R_{ij} correspond to the space resistance to radiation,

$$R_{ij} = \frac{1}{A_i F_{ij}} \quad (92)$$

The use of the radiation resistance approach was developed to simplify radiation problems. Each node corresponds to the radiosity of each surface. The method allows a good visualisation of the radiative problem. An illustration can be seen in Figure 84.

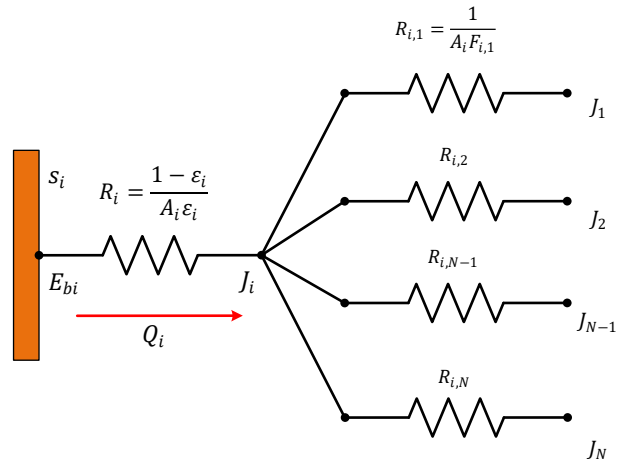


Figure 84 Schematic of the radiation resistance approach for receiving surfaces.

The net radiation leaving the surface i and reaching the surfaces $1, 2 \dots (N - 1), N$ can be expressed as,

$$Q_i = \sum_{j=1}^N Q_{ij} = \sum_{j=1}^N A_i F_{ij} (J_i - J_j) = \sum_{j=1}^N \frac{(J_i - J_j)}{R_{ij}} \text{ (W)} \quad (93)$$

or

$$\frac{E_{bi} - J_i}{R_i} = \sum_{j=1}^N \frac{(J_i - J_j)}{R_{ij}} \text{ (W)} \quad (94)$$

The radiation resistance approach for an enclosure with two surfaces is expressed as,

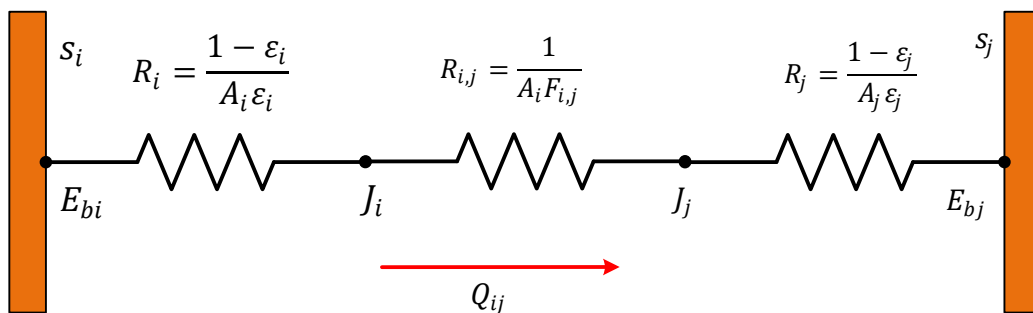


Figure 85 Schematic of the radiation resistance approach for an enclosure with two surfaces.

$$Q_{12} = \frac{E_{b1} - E_{b2}}{R_1 + R_{12} + R_2} \text{ (W)} \quad (95)$$

or

$$Q_{12} = \frac{\sigma(T_1^4 - T_2^4)}{\frac{1 - \epsilon_1}{A_1 \epsilon_1} + \frac{1}{A_1 F_{12}} + \frac{1 - \epsilon_2}{A_2 \epsilon_2}} \text{ (W)} \quad (96)$$

An illustration can be seen in Figure 85.

4.2.3 Two phase heat transfer

4.2.3.1 Boiling heat transfer

Overview of boiling heat transfer

The boiling heat transfer occurs when a liquid reaches a particular temperature that will change the phase of the liquid to vapour. In this case, the latent heat of the liquid will allow large amounts of energy to be transferred from a hot surface to a liquid/vapour phase. The boiling heat transfer is mainly used for applications where the heat flux is substantial. Apart from the latent heat, the surface tension at the liquid vapour interface and the density difference between the two phases will be important factors to take into account. This difference will induce a buoyancy force.

The boiling heat transfer can be identified in four regimes: free convection boiling, nucleate boiling, transition boiling and film boiling. Each of the modes can be applied in different situations and are illustrated in Figure 86. The temperature of the surface can be identified as T_s and the saturation temperature of the liquid as T_{sat} . The excess temperature ΔT_e can be calculated as

$$\Delta T_e = T_s - T_{sat} \quad (97)$$

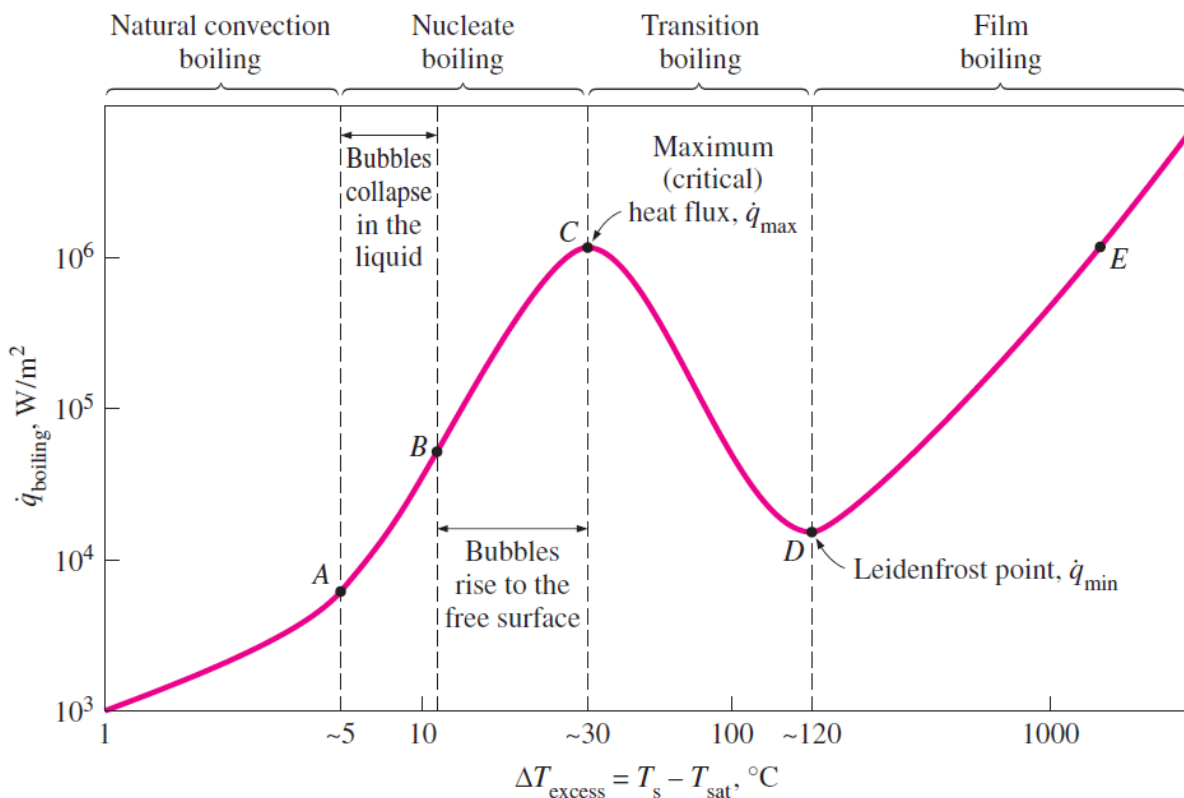


Figure 86 Boiling curve for water at 1 atm [81]

The free convection boiling occurs when $\Delta T_e \leq \Delta T_{e,A}$, where $\Delta T_{e,A} \approx 5^\circ\text{C}$. The temperature difference between the surface and the saturation temperature is not enough to allow the generation of bubbles. Hence, the heat transfer in this range mainly occurs through free convection between the solid and the liquid phase.

Nucleate boiling will appear when $\Delta T_{e,A} \leq \Delta T_e \leq \Delta T_{e,C}$, for $\Delta T_{e,C} \approx 30^\circ\text{C}$. In this range, two regimes can be identified. For ΔT_e close to $\Delta T_{e,A}$, isolated bubbles will form around the nucleation site on the hot surface. The bubbles will allow the liquid to move over the plate, thus increasing the heat transfer coefficient and the heat flux at the interface. In this case, most of the heat transfer relies on forced convection over the hot plate. The second regime occurs when ΔT_e is close to $\Delta T_{e,C}$, in this case, the vapour bubble generation increases. The size of the bubbles can be identified from columns of vapour leaving the heated surface and merging into slugs. When ΔT_e is closer to $\Delta T_{e,C}$, the heat flux is increasing slowly to reach the critical heat flux point when $\Delta T_e = \Delta T_{e,C}$. For water at atmospheric pressure the critical heat flux $q''_C = q''_{max} = 1\text{MW}/\text{m}^2$. After this point a considerable amount of vapour is generated. The liquid will struggle to reach the surface.

Transition boiling occur when $\Delta T_{e,C} \leq \Delta T_e \leq \Delta T_{e,D}$. In this transition regime, the vapour generation is so high that a vapour film or vapour blanket is forming on the surface, blocking the liquid from reaching the hot surface. At this regime the film is not stable and can disappear at points of the hot surface. As the thermal conductivity of vapour is significantly lower than the liquid, the heat flux and the heat transfer coefficient will decrease.

Film boiling exist when $\Delta T_{e,D} \leq \Delta T_e$. The point D is referred as the Leidenfrost effect. This effect occurs when the difference in temperature between a surface and the liquid is so high that a vapour blanket forms between the two bodies. This blanket can act as an insulator hence decreasing the heat flux. When ΔT_e is higher, the main heat transfer mode between the surface will be radiation. Thus, the heat flux between the surface and the liquid will increase to reach a maximum when the temperature of the surface is above the melting temperature. Film boiling is a regime that can be dangerous to maintain as the melting temperature of the solid can be reached, hence the potential failure of the system. Therefore, Point C is considered as the burnout point for boiling.

The rate of heat transfer for boiling can be expressed as

$$Q_{boiling} = h_b A_s (T_s - T_v) \quad (98)$$

where $Q_{boiling}$ is the rate of heat transfer (W), h_b is the heat transfer coefficient ($\text{W}/\text{m}^2 \cdot \text{K}$), A_s is the surface area (m^2), T_s is the temperature of the surface and T_v is the temperature of the vapour phase (K).

The electrical analogy can be applied in a similar way as for radiation heat transfer,

An illustration can be seen in Figure 87.

$$Q_{boiling} = \frac{T_s - T_v}{R_{boiling}} \quad (99)$$

where

$$R_{boiling} = \frac{1}{h_b A_s} \quad (100)$$

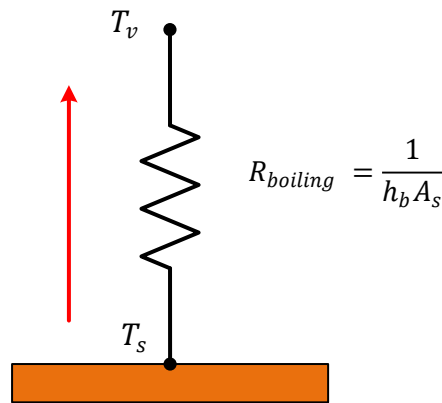


Figure 87 Schematic of the boiling heat transfer

Common correlations for boiling in heat pipes

Correlations for heat pipe have been developed and tested. The boiling in a heat pipe occurs in two distinct regions. The first region is the boiling in the evaporator section where the liquid is boiled in a pool. The second region is on the falling film of condensate liquid coming back from the condenser section of the heat pipe.

Correlations for boiling related to the pool of liquid are listed in Table 18

Table 18 List of correlations for boiling in the evaporator liquid pool

Author	Equation	Eq.	Conditions
Rohsenow [82]	$q_{ei} = \mu_l \cdot h_{fg} \left[\frac{g \cdot (\rho_l - \rho_v)}{\sigma} \right]^{1/2} \cdot \left[\frac{c_p \cdot (T_{ei} - T_v)}{(C_{sf} \cdot h_{fg} \cdot Pr_l^n)} \right]^3$ <p>where:</p> $q_{ei} = h_{ei} \cdot (T_{ei} - T_v)$	(101)	n=1 for water and n=1.7 for other liquids

Cooper [83]	$h_{ei} = 55p_r^{0.12-0.4343\ln R_p} (-\log_{10} p_r)^{-0.55} M^{-0.5} q_{ei}^{0.67}$	(102)	$p_r = \frac{P}{P_{crit}}$
Gorenflo[84]	$F_{PF} = 1.73p_r^{0.27} + \left(6.1 + \frac{0.68}{1 - p_r}\right) p_r^2$	(103)	For water and helium only where these are for water $P_{critical} = 220.6$ (bar) $M = 18.02$ $h_0 = 5600$ W/m ² .°C
McNelly[85]	$h_{ei} = 0.225 \left(\frac{qC_p}{h_{fg}}\right)^{0.69} \left(\frac{Pk_l}{\sigma}\right)^{0.31} \left(\frac{\rho_l}{\rho_v} - 1\right)^{0.31}$	(104)	
Forster And Zuber[86]	$q_{ei} = 0.00122 \left(\frac{k_l^{0.79} C_p^{0.45} \rho_l^{0.49}}{\sigma^{0.5} \mu_l^{0.29} h_{fg}^{0.24} \rho_v^{0.24}}\right) \Delta T_v^{1.24} \Delta p_v^{0.75}$ Where: $\Delta T_v = (T_{ei} - T_v)$, $\Delta p_v = P_{ei} - P_v$ and $q_{ei} = h_{ei} \cdot \Delta T_v$	(105)	Δp_v is the difference between the vapor pressures at the heating surface and liquid temperatures
Mostinski[87]	$h_{ei} = 3.7 \times 10^{-5} P_{crit}^{0.69} q_{ei}^{0.7} \left[1.8 \left(\frac{P}{P_{crit}}\right)^{0.17} + 4 \left(\frac{P}{P_{crit}}\right)^{1.2} + 10 \left(\frac{P}{P_{crit}}\right)^{10} \right]$	(106)	
Stephan and Abdelsalam[88]	$Nu = \frac{h_{ei} D_d}{k_l} = 0.24 \times 10^7 X_1^{0.67} X_4^{-1.58} X_3^{1.62} X_8^{5.22}$ $X_1 = \left(\frac{q_{ei} D_d}{k_l T_v}\right), \quad X_3 = \left(\frac{C_p T_v D_d^2}{\alpha^2}\right), \quad X_4 = \left(\frac{h_{fg} D_d^2}{\alpha^2}\right), \quad X_8 = \left(\frac{\rho_l - \rho_v}{\rho_l}\right)$ $D_d = 0.0208 \times \theta \left[\frac{\sigma}{g(\rho_l - \rho_v)}\right]^{\frac{1}{2}}, \quad \alpha = \frac{k_l}{\rho_l C_p}$	(107)	$10^{-4} < \frac{P}{P_{crit}} < 0.88$ $\theta = 45^\circ$
Imura [89]	$h_{ei} = 0.32 \left(\frac{\rho_l^{0.65} k_l^{0.3} C_p^{0.7} g^{0.2}}{\rho_l^{0.25} \mu_l^{0.4} \mu_l^{0.1}}\right) \left(\frac{P_v}{P_{atm}}\right)^{0.3} q_{nb}^{0.4}$		

Labunstov [90]	$h_{ei} = 0.075 \left[1 + 10 \left(\frac{\rho_v}{\rho_l - \rho_v} \right)^{0.67} \right] \left(\frac{\rho_l k_l^2}{\mu_l \sigma T_{sat}} \right)^{0.33} q''_{nb}{}^{0.67}$		
Kiatiroat [91]	<p>Where,</p> $L_b = \left[\frac{\sigma}{g(\rho_l - \rho_v)} \right]^{1/2}$ $\begin{cases} C = 18.688 \text{ for water} \\ C = 17.625 \text{ for ethanol} \\ C = 20.565 \text{ for triethylene glycol (TEG)} \end{cases}$ $\begin{cases} n = 0.3572 \text{ for water} \\ n = 0.3300 \text{ for ethanol} \\ n = 0.3662 \text{ for triethylene glycol (TEG)} \end{cases}$		
Shiraishi [92]	$h_{ei} = 0.32 \left(\frac{\rho_l^{0.65} k_l^{0.3} C_{p,l}^{0.7} g^{0.2}}{\rho_l^{0.25} h_{fg}^{0.4} \mu_l^{0.1}} \right) \left(\frac{P_v}{P_{atm}} \right)^{0.23} q''_{nb}{}^{0.4}$		

Correlations for boiling in the falling film are listed in Table 19

Table 19 List of correlations for falling film boiling

Author	Correlation	Eq.
Kopchikov [93]	$h^* = 0.1 \left(\frac{k_l i_{lv} \rho_v}{\sigma T_{sat}} q''_{fb} \right) \frac{1}{k_l} \left(\frac{\mu_l^2}{\rho_l^2 g} \right)^{1/3}$	(108)
El-Genk and Saber [94]	$h^* = \left(\frac{4}{3} \right)^{1/3} Re_f^{-1/3} (h_x^3 + h_{f,boiling}^3)^{1/3}$ $h_x = \left(\frac{4}{3} \right)^{1/3} Re_f^{-1/3} \left(\frac{k_l}{L_f} \right)$ $h_{f,boiling} = 1.155 \times 10^{-3} \left(\frac{k_l}{L_b} \right) N_\mu^{0.33} Pr_l^{0.35} \left(\frac{q''_{f,boiling} L_b \rho_l}{\rho_v i_{lv} \mu_l} \right)^{0.7} \left(\frac{PL_b}{\sigma} \right)^{0.7}$ <p>where,</p> $L_f = \left(\frac{\mu_l^2}{g \rho_l (\rho_l - \rho_v)} \right)^{1/3} : \text{Liquid film thickness scale}$	(109)

	$L_b = [\sigma/g(\rho_l - \rho_v)]^{1/2}$: Bubble length scale $N_\mu = \frac{\mu_l}{(\sigma\rho_l L_b)^{0.5}}$: Viscosity number	
Gogonin [95]	$h^* = 0.01 \left(\frac{\mu_l^2}{\rho_l^2 g} \right)^{1/3} L_b^{-1} Re_{fb}^{0.8} Pr_l^{1/3} b K_t^{0.4} \bar{R}_z^{-0.2} \left(\frac{k_l c_{p,l} \rho_l}{k_w c_{p,w} \rho_w} \right)^{-0.2}$	(110)
	$b = \left[1 + 10 \left(\frac{\rho_v}{\rho_l - \rho_v} \right)^{2/3} \right]$ $K_t = \frac{(i_{lv} \rho_v)^2 L_b}{c_{p,l} T_{sat} \rho_l \sigma}$ $\bar{R}_z = R_z / L_f$	
Chun and Seban [96]	$h^* = 0.606 (Re_f / 4)^{-1/3}$	(111)
	$Re_f \leq 2.44 Ka^{-1/11}$ $0.3 \times 10^5 \leq q_{fb} \leq 0.7 \times 10^5 \text{ W.m}^{-2}$	

4.2.3.2 Condensation heat transfer

Overview of condensation heat transfer

Condensation heat transfer occurs when the temperature of a surface is lower than the dew point of the surrounding vapour. The condensation on the surface can occur in two ways. If the surface is wetted by the condensate, then a film will build up on the surface. This phenomenon is referred as film wise condensation. If the condensate does not wet the surface, then droplets will form on the surface. Once the droplets reach a critical size, they will slide down from the surface creating a new condensate droplet, the phenomenon is referred as dropwise condensation. Dropwise condensation heat transfer is preferable for heat transfer applications. However, to achieve this, the surface needs to be coated. Thus, the lifespan of the dropwise condensation is limited by the coating.

Film condensation heat transfer was investigated by Nusselt [97] in 1926. Nusselt studied the condensation of liquid on a vertical plate and proposed a theory on the condensate film thickness. The thickness of the condensate flow on the plate will increase as the condensate travels down the plate. The latent heat for the condensation will then be transferred through the film and not onto the plate directly.

Heat transfer by condensation is expressed as

$$Q_{condensation} = h_{condensation} \cdot A_s (T_{sat} - T_s) \quad (112)$$

Applying the thermal resistance analogy

$$R_{condensation} = \frac{1}{h_{condensation}A_s} \quad (113)$$

An illustration can be seen in Figure 88.

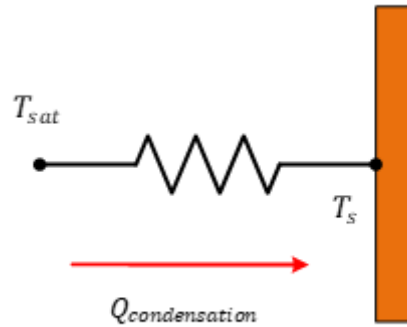


Figure 88 Schematic of the condensation heat transfer

Common correlations for condensation heat transfer

Common correlations for condensation heat transfer are reported in Table 20.

Table 20 Common correlations for condensation heat transfer coefficient

Author	Equation	Eq.	State
Nusselt [97,98]	$h_{ci} = 0.943 \left[\frac{\rho_l(\rho_l - \rho_v)gh_{fg}^*k_f^3}{l_c\mu_l(T_v - T_{ei})} \right]^{\frac{1}{4}}$	(114)	Laminar vertical
	Rohsenow modifications $h_{fg}^* = h_{fg} + 0.68C_p(T_v - T_{ei})$	(115)	
Nusselt [97]	$Re = \frac{4\dot{Q}_{ci}}{P\mu_l h_{fg}^*} = \frac{4A_s h_{ci}(T_v - T_{ei})}{P\mu_l h_{fg}^*}$	(116)	Laminar- vertical

	$h_{ci} \cong 1.47 k_l Re^{-\left(\frac{1}{3}\right)} \left(\frac{g \rho_l^2}{\mu_l^2}\right)^{\frac{1}{3}}$	(117)	
<i>Kutateladze [99]</i>	$h_{ci,wavy} = \frac{Re k_l}{1.08 Re^{1.22} - 5.2} \left(\frac{g \rho_l^2}{\mu_l^2}\right)^{\frac{1}{3}}$	(118)	
	$Re_{ver,wavy} = \left[4.81 + \frac{3.7 l_c k_l (T_v - T_{ei})}{\mu_l h_{fg}^*} \left(\frac{g \rho_l^2}{\mu_l^2}\right)^{\frac{1}{3}}\right]^{0.82}$	(119)	
<i>Nusselt [97]</i>	$h_{ci} = 0.943 \left[\frac{\rho_l(\rho_l - \rho_v) g h_{fg}^* k_l^3 \cos \theta}{l_c \mu_l (T_v - T_{ei})}\right]^{\frac{1}{4}}$	(120)	Inclined
<i>Nusselt [97]</i>	$h_{ci} = 0.725 \left[\frac{\rho_l(\rho_l - \rho_v) g h_{fg}^* k_l^3}{D \mu_l (T_v - T_{ei})}\right]^{\frac{1}{4}}$	(121)	Horizontal
<i>Chen [100][97][97][97]</i> <i>[97]</i>	$h_{ci} = 0.728[1 + 0.2(N - 1)Ja] \left[\frac{\rho_l(\rho_l - \rho_v) g h_{fg}^* k_l^3}{ND \mu_l (T_v - T_{ei})}\right]^{\frac{1}{4}}$	(122)	Horizontal - N rows
	Provided that: $[(N - 1)Ja] < 2$		
	Where $Ja = C_p(T_v - T_{ei})/h_{fg}$	(123)	
<i>Nusselt [97]</i>	$h_{ci} = 0.725 \left[\frac{\rho_l(\rho_l - \rho_v) g h_{fg}^* k_l^3}{ND \mu_l (T_v - T_{ei})}\right]^{\frac{1}{4}}$	(124)	Horizontal tube bank with N rows

<p><i>Rohsenow [98]</i></p>	$h_{ci} = 1.51 \left(\frac{P_v}{P_{crit}} \right)^{0.14} \times 0.943 \left\{ \frac{\rho_l(\rho_l - \rho_v)gk_l^3}{\mu_l L_c (T_v - T_{ci})} [h_{fg} + 3/8 c_{pl}(T_v - T_{ci})] \right\}^{1/4}$ <p>where the fluid properties should be evaluated at a temperature:</p> $T_f = T_{ci} + 0.31(T_{sat} - T_{ci})$		
<p><i>Jouhara et al [27]</i></p>	$h_{ci} = 0.85 Re_f^{0.1} \exp\left(0.000067 \frac{\rho_l}{\rho_v} - 0.14\right) \times 0.943 \left[\frac{\rho_l(\rho_l - \rho_v)gh_{fg}^* k_l^3}{l_c \mu_l (T_v - T_{ei})} \right]^{1/4}$ <p>where</p> $Re = \frac{4\dot{Q}_{ci}}{\pi D \mu_l h_{fg}^*}$	<p>(125)</p> <p>(126)</p>	<p>Wavy laminar and turbulent</p>

Heat transfer coefficient for condensation on a tube bundle

In order to define the heat transfer coefficient for condensation on a tube bundle, condensation on a single tube need to be introduced. The laminar film free convection of condensate on a smooth isothermal tube can be expressed as,

$$Nu_m = \frac{h_m d_0}{k_l} = 0.728 \left\{ \frac{\rho_l(\rho_l - \rho_g)g l_g d_0^3}{\mu_l (T_s - T_{wo})k_l} \right\}^{1/4} \quad (127)$$

An illustration can be seen in Figure 89.

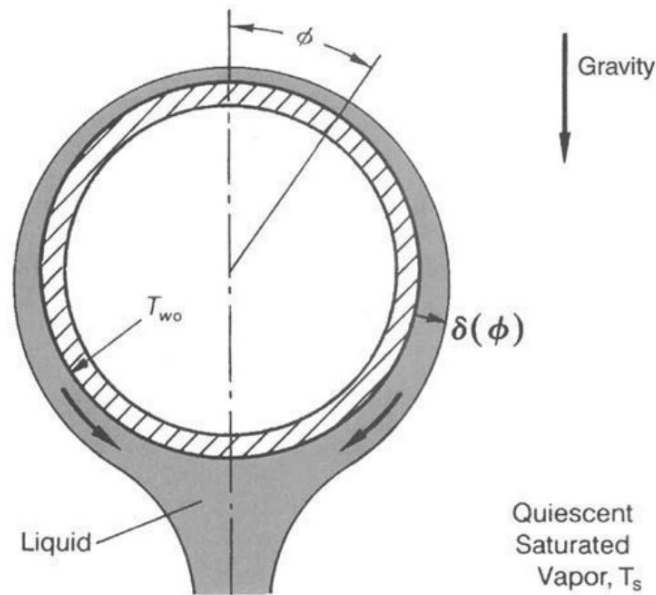


Figure 89 Laminar flow on an horizontal tube [57]

A laminar forced convection approach was developed by [101]. Indeed, the vapour surrounding the tube is moving, two effects have an impact on the overall heat transfer coefficient. The surface shear stress between the liquid phase and the vapour will influence the film thickness and the vapour distribution around the tube that will disturb the flow of condensate. The correlation developed by [101] is expressed as,

$$Nu_m \bar{Re}_d^{-1/2} = \frac{0.9 + 0.728 F_d^{1/2}}{(1 + 3.44 F_d^2 + F_d)^{1/4}} \quad (128)$$

where,

$$Nu_m = \frac{h_m d_o}{k_l} \quad \bar{Re}_d = \rho_l V_\infty d_o / \mu_l \quad F_d = \frac{\mu_l i_{lg} g d_o}{k_l \Delta T V_\infty^2} \quad (129)$$

A more conservative relationship was developed by [102],

$$Nu_m \bar{Re}_d^{-1/2} = 0.416 [1 + (1 + 9.47 F_d)^{1/2}]^{1/2} \quad (130)$$

The condensation on the tube in a tube bundle will be disturbed by the neighbouring tubes in the bundles. The condensate created by the tube located at the top of the tube bundle will flow downward to the tube below by gravity or vapour shear stress. The effect of the local vapour velocity and the inundation of the pipe need therefore to be taken into account in the calculation of the heat transfer.

The effect of the vapour shear stress on the local heat transfer coefficient was investigated by [103] and a correlation was proposed,

$$Nu_m \widetilde{Re}_d^{-1/2} = 9.47 F_d^{1/5} \quad (131)$$

for $0.03 < F_d < 600$

When the vapour in the condenser is considered stable, no vapour shear effect will occur. The condensate on the tube will then flow downwards by gravity to the tube below. This will increase the thickness of the condensate film in the tube below, thus impacting the heat transfer coefficient.

[100] developed a correlation by analysing the boundary layer of the film and included the momentum of the film dropping on the tube below and the condensation accruing on the subcooled fluid between the pipes. The following correlations was proposed

$$\frac{h_{mN}}{h_{m1}} \cdot N^{1/4} = [1 + 0.2(N - 1)Pr_l J_l] \left\{ \frac{1 + 0.68Pr_l J_l + 0.02Pr_l J_l^2}{1 + 0.95J_l - 0.15Pr_l J_l^2} \right\}^{1/4} \quad (132)$$

In a tube bundle, the vapour shear and the inundation effect will both occur. [104] developed a methodology to calculate the heat transfer by coupling the two effects and treated shell side condensation as two-phase forced convection.

$$h_N = (h_{sh}^2 + h_{gr}^2)^{1/2} \quad (133)$$

where h_{gr} is given by (127) and multiplied by C_N

$$h_{gr} = \frac{0.728k_l C_N \left\{ \frac{\rho_l(\rho_l - \rho_g)g l_l d_o^3}{\mu_l(T_s - T_{wo})k_l} \right\}^{1/4}}{d_o} \quad (134)$$

for

$$C_N = N^{5/6} - (1 - N)^{5/6} \quad (135)$$

h_{sh} , the shear stress condensation heat transfer is given as,

$$h_{sh} = a \left[\frac{1}{X_{tt}} \right]^b h_l \quad (136)$$

X_{tt} corresponds to the Lockhart-Martinelli parameter defined as,

$$X_{tt} = \left(\frac{1-x}{x}\right)^{0.9} \left(\frac{\rho_g}{\rho_l}\right)^{0.5} \left(\frac{\mu_l}{\mu_g}\right)^{0.1} \quad (137)$$

h_l is the heat transfer coefficient for the single phase forced convection across a tube bank, if the flow is covering the entirety of the tubes.

$$h_l = C \frac{k_l}{d_o} Re_l^m Pr_l^n \quad (138)$$

where C , m and n are coefficients that will depend on the flow conditions across the tube bank.

4.2.4 Conduction heat transfer

The heat transfer through conduction in a one-dimensional, steady state condition wall can be determined using the electrical analogy.

$$Q_{cond} = \frac{T_{s,1} - T_{s,2}}{R_{cond}} \quad (139)$$

for

$$R_{cond,c} = \frac{L}{Ak_s} \quad (140)$$

where L is the wall thickness, A is the heat transfer area and k_s is the thermal conductivity depending on the wall material.

When the solid is a tube, the heat transfer can be determined by

$$Q_{cond,e} = \frac{T_{eo} - T_{ei}}{R_{cond,e}} \quad (141)$$

The thermal resistance can be obtained from

$$R_{cond,e} = \frac{\ln\left(\frac{D_{eo}}{D_{ei}}\right)}{2\pi l_e k_s} \quad (142)$$

4.2.5 Internal forced convection heat transfer

In order to calculate heat transfer for an internal flow in a section, the flow condition needs to be assessed. The Reynolds number can be used to determine if the flow is laminar or turbulent. The Reynolds number for a flow in a circular tube can be defined as,

$$Re = \frac{\rho u_m D}{\mu} \quad (143)$$

where u_m is the mean velocity over the cross section, D is the tube diameter, ρ is the density and μ is viscosity of the fluid. For $Re \leq 2300$, the flow is considered laminar. For $2300 < Re \leq 10000$, the flow is in a transition regime, if $Re > 10000$, the flow is considered turbulent.

As the flow in the tube varies depending on the distance from the wall of the tube, the velocity needs to be determined using the fluid density ρ , the mass flow rate through the tube \dot{m} and the area of the tube cross section A ,

$$\dot{m} = \rho u_m A \quad (144)$$

For a constant temperature of the heat transfer surface, the heat transfer can be calculated by,

$$Q_{F.convection} = h_{F.convection} A_s LMTD \quad (145)$$

where $h_{F.convection}$ is the heat transfer coefficient via forced convection, $LMTD$ is the logarithmic mean temperature and A_s is heat transfer surface area. $LMTD$ is given by,

$$LMTD = \frac{(T_s - T_{in}) - (T_s - T_{out})}{\ln\left(\frac{(T_s - T_{in})}{(T_s - T_{out})}\right)} \quad (146)$$

where T_s is the temperature of the surface, T_{in} is the inlet temperature of the fluid and T_{out} the outlet temperature of the flow.

The heat transfer coefficient is determined by

$$h = \frac{Nu \cdot k}{D} \quad (147)$$

where Nu is the Nusselt number that can be calculated using the correlations in Table 21

Table 21 Nusselt number correlations for forced convection in a tube

Reference	Equation	Eq.	conditions
Hausen [105]	$Nu = 3.66 + \frac{0.0668 Re Pr D_{ci}/L_c}{1 + 0.04(Re Pr D_{ci}/L_c)^{2/3}} \left(\frac{\mu_b}{\mu_{ci}}\right)^{0.14}$	(148)	$Re < 2300$
Hausen [105]	$Nu = 0.116(Re^{0.66} - 125)Pr^{0.3} \left(\frac{\mu}{\mu_{ci}}\right)^{0.14} \left[1 + \left(\frac{D_{ci}}{L_c}\right)^{0.66}\right]$	(149)	$2300 < Re < 10000$
Petukhov [106]	$Nu = \frac{(f/8)RePr}{1.07 + 12.7(f/8)^{1/2}(Pr^{2/3} - 1)} \left(\frac{\mu_b}{\mu_{ci}}\right)^n$ where $f = (1.82 \log_{10} Re - 1.64)^{-2}$	(150)	$0.5 < Pr < 2000$ $10^4 < Re < 5 \times 10^6$ $0.8 < \mu_b/\mu_{ci} < 40$

			$n = 0.11$ for $T_{ci} > T_b$ and $n = 0.25$ $T_{ci} < T_b$, $n = 0$ for gases Properties evaluated at $T_f = (T_{ci} + T_b)/2$ $T_b = \frac{T_{cold,in} + T_{cold,out}}{2}$
Sieder–Tate [107,108]	$Nu = \frac{hD_{ci}}{k} = 1.86(Re \cdot Pr \cdot D_{ci}/L_c)^{1/3} \cdot \left(\frac{\mu}{\mu_{ci}}\right)^{0.14}$	(151)	$Re < 2300$ $RePrD_{ci}/L_c > 10$ fluid properties are evaluated at the mean bulk temperature of the fluid $T_b = \frac{T_{cold,in} + T_{cold,out}}{2}$
Petukhov-Gienlinski modification [109]	$Nu = \frac{(f/8)(Re - 1000)Pr}{1 + 12.7(f/8)^{1/2}(Pr^{2/3} - 1)}$	(152)	$2300 < Re < 5 \times 10^6$ $0.5 \leq Pr \leq 10^6$
Gnielinski [109]	$Nu = 0.0214(Re^{0.8} - 100)Pr^{0.4}$	(153)	$10^4 < Re < 5 \times 10^6$ $0.5 < Pr < 1.5$
Gnielinski [109]	$Nu = 0.012(Re^{0.87} - 280)Pr^{0.4}$	(154)	$3000 < Re < 10^6$ $1.5 < Pr < 500$
Sleicher and Rouse [110]	$Nu = 5 + 0.015Re^m \cdot Pr_{ci}^n$ $m = 0.88 - \frac{0.24}{Pr_{ci}+4}, n = \frac{1}{3} + 0.5e^{-0.6 \cdot Pr_{ci}}$	(155)	$10^4 \leq Re \leq 10^6$ $0.1 < Pr < 10^5$
Petukhov-Popov [106]	$Nu = \frac{(f/8)RePr}{k_1 + k_2(f/8)^{1/2}(Pr^{2/3} - 1)}$ where f is the friction factor: $f = (1.82 \log_{10} Re_D - 1.64)^{-2}$ $k_1 = 1 + 3.4f$ and $k_2 = 11.7 + \frac{1.8}{Pr^{1/3}}$	(156)	$10^4 < Re < 5 \times 10^6$ $0.5 < Pr < 2000$
Gnielinski [109]	$Nu = \frac{(f/8)(Re - 1000)Pr}{1 + 12.7(f/8)^{1/2}(Pr^{2/3} - 1)} [1 + (D_{ci}/L_c)^{2/3}] \Phi$ $\Phi = \left(\frac{Pr}{Pr_{ci}}\right)^{0.11}$ for liquids $\Phi = \left(\frac{T_b}{T_{ci}}\right)^{0.45}$ for gases	(157)	$2300 < Re < 5 \times 10^6$ $0.5 < Pr < 200$

4.2.6 External forced convection heat transfer

The heat transfer of external forced convection over a plate can be calculated as,

$$Q = \frac{T_s - T_f}{R_{F,Conv,p}} \quad (158)$$

where

$$R_{F,Conv,p} = \frac{1}{h_{F,Conv,p} A_p} \quad (159)$$

The heat transfer coefficient for forced convection over a plate can be calculated as

$$h_{F,Conv,p} = \frac{Nu \cdot k}{L} \quad (160)$$

where L is the longitudinal length at the forced convection section and k is the thermal conductivity of the fluid.

Then Nusselt number can be calculated as,

$$\text{Laminar} \quad Nu = 0.664 Re_L^{0.5} Pr^{1/3} \quad Re_L < 5 \times 10^5 \quad (161)$$

$$\text{Turbulent} \quad Nu = 0.037 Re_L^{0.8} Pr^{1/3} \quad \begin{matrix} 0.6 \leq Pr \leq 60 \\ 5 \times 10^5 \leq Re_L \leq 10^7 \end{matrix} \quad (162)$$

The heat transfer of external forced convection over a row of n tubes.

$$Q = n \times \frac{T_s - T_f}{R_{F,Conv,tb}} \quad (163)$$

where

$$R_{F,Conv,p} = \frac{1}{h_{F,Conv,tb} A_{tb}} \quad (164)$$

The heat transfer coefficient for external forced convection for a row of n tubes.

$$h_{F,Conv,p} = \frac{Nu}{k \cdot D} \quad (165)$$

where

$$Nu_{Cyl,n} = 0.3 + \frac{0.62 Re^{1/2} Pr^{1/3}}{[1 + (0.4/Pr)^{2/3}]^{1/4}} \left[1 + \left(\frac{Re}{282,000} \right)^{5/8} \right]^{4/5} \quad (166)$$

For $Re Pr > 0.2$

4.3 Theoretical modelling of the single heat pipe

The single pipe radiative heat pipe was tested in a kiln; the heat transfer principles considered are shown in Figure 90 and are as follows. The heater will emit heat to the surroundings, the

heat will be absorbed by the heat pipe evaporator section and the wall. In addition, natural convection will occur between the heater and the air in the kiln. It will also occur between the hot air in the kiln and the heat pipe. The kiln walls reradiate all the heat to the surroundings as they are insulated, the heat travelling through the wall to the outside is neglected.

The heat absorbed by the heat pipe through natural convection and radiation is transferred to the internal wall of the heat pipe through conduction. Thus, the working fluid in the evaporator section will start boiling and evaporate. The vapour will carry the heat to the condenser section where it will release the latent heat to the condenser wall, condensing the working fluid that will flow back to the condenser. The heat is then transferred from the inner wall to the outer wall of the condenser section. The heat will be released to the water through forced convection.

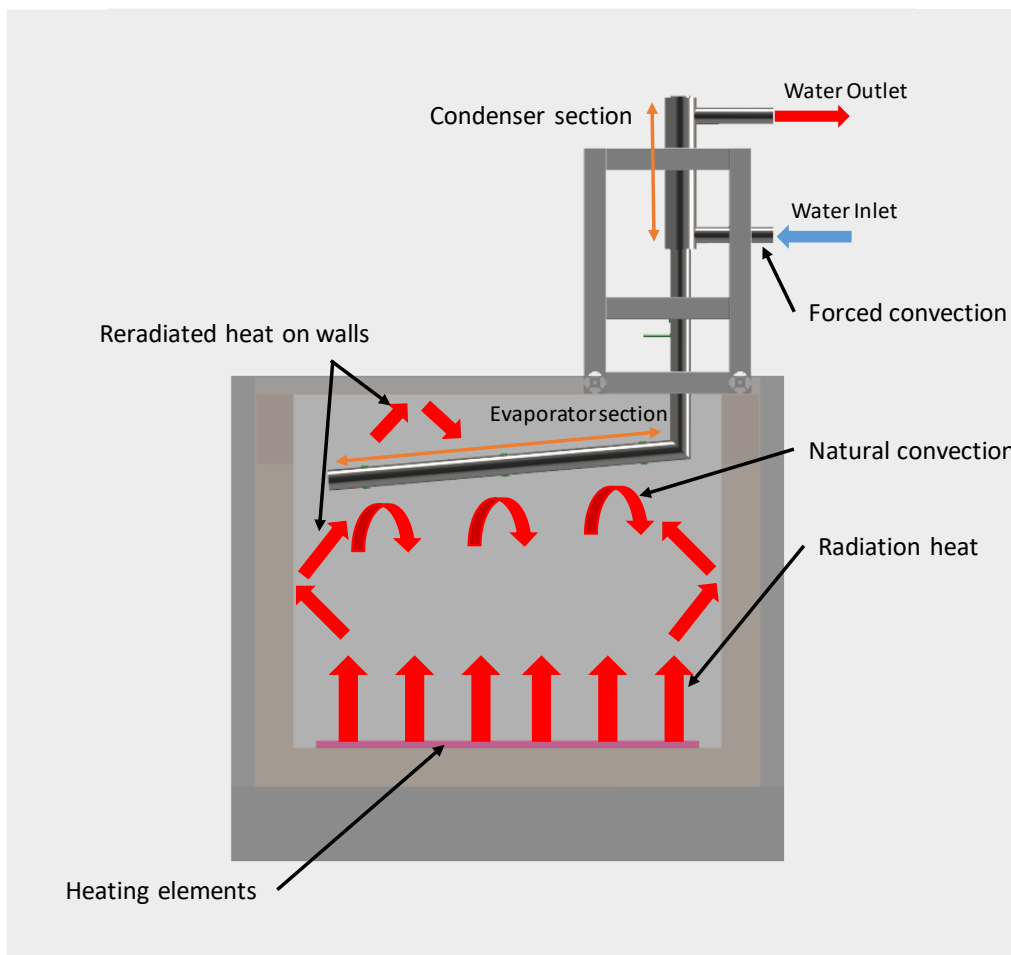


Figure 90 Schematic of the heat transfer principles in the test rig

4.3.1 Thermal network approach

The thermal network approach was used to simplify the thermal modelling of the heat pipe. The thermal network model is developed by applying the electrical resistance analogy approach to heat transfer modelling. Each thermal resistance will be analysed.

A schematic of the thermal resistance analogy is presented in Figure 91

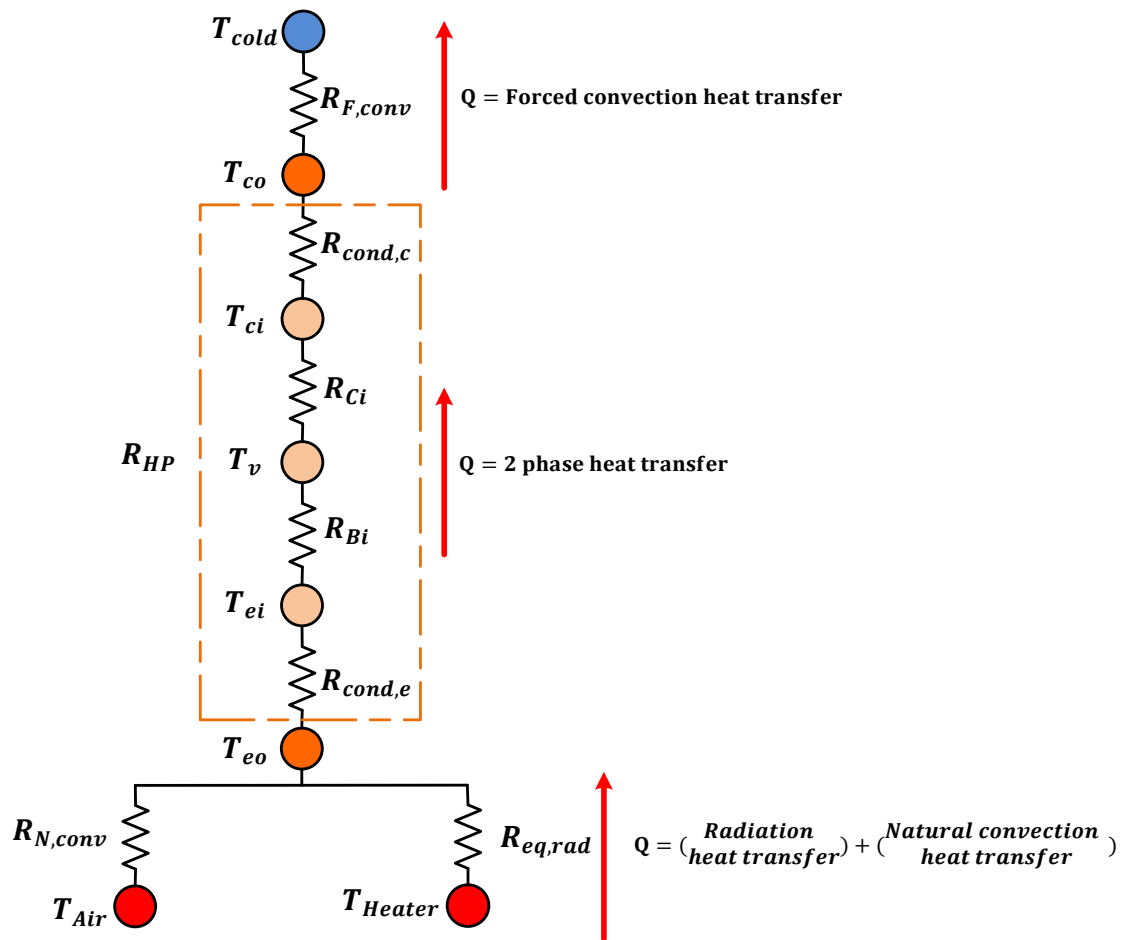


Figure 91 Model of the electrical resistance analogy for the radiative heat pipe

$R_{eq,rad}$: Radiation heat transfer resistance (K/W)

$R_{N,conv}$: Natural convection heat transfer thermal resistance (K/W)

$R_{cond,e}$: Conduction thermal resistance of the evaporator wall (K/W)

R_{Bi} : Boiling thermal resistance (K/W)

R_{Ci} : Condensation thermal resistance (K/W)

$R_{cond,c}$: Conduction thermal resistance of the condenser wall (K/W)

$R_{F,conv}$: forced Convection thermal resistance of condenser section (K/W)

T_{Heater} : Heater temperature (K).

T_{eo} : Outer wall evaporator temperature (K).

T_{ei} : Inner wall evaporator temperature (K).

T_v : Heat pipe working fluid vapour temperature (K).

T_{ci} : Inner wall condenser temperature (K).

T_{co} : Outer wall condenser temperature (K).

T_{cold} : Water coolant temperature (K).

R_{HP} : Heat pipe equivalent thermal resistance where

$$R_{HP} = R_{Con,e} + R_{Bi} + R_{Ci} + R_{Cond,c} \text{ (K/W)} \quad (167)$$

4.3.2 Natural convection

The natural convection resistance is calculated using the following equation,

$$R_{N.convection} = \frac{1}{h_{N.convection} A_{eo}} \quad (168)$$

where $h_{N.convection}$ is calculated using the correlations (25)-(33)

4.3.3 Radiation

The radiation resistance is calculated from two components, the direct radiation from the heater to the heat pipe and the radiation from the walls to the heat pipe. In order to calculate the radiation resistance, assumptions need to be made to simplify the model.

- All surfaces are considered opaque, diffuse and grey.
- The surfaces of the walls are well insulated; they can be considered as reradiating surfaces as the natural convection on the walls is not considered.
- The system is considered to be at steady state.
- The radiosity and emitted heat is constant and uniform over the surfaces.

The thermal resistance analogy was applied to the radiation resistance calculation. The system is composed of four side walls, the heat pipe wall, the heater and the top wall. An illustration of the thermal resistance analogy with the seven parts is shown in Figure 92.

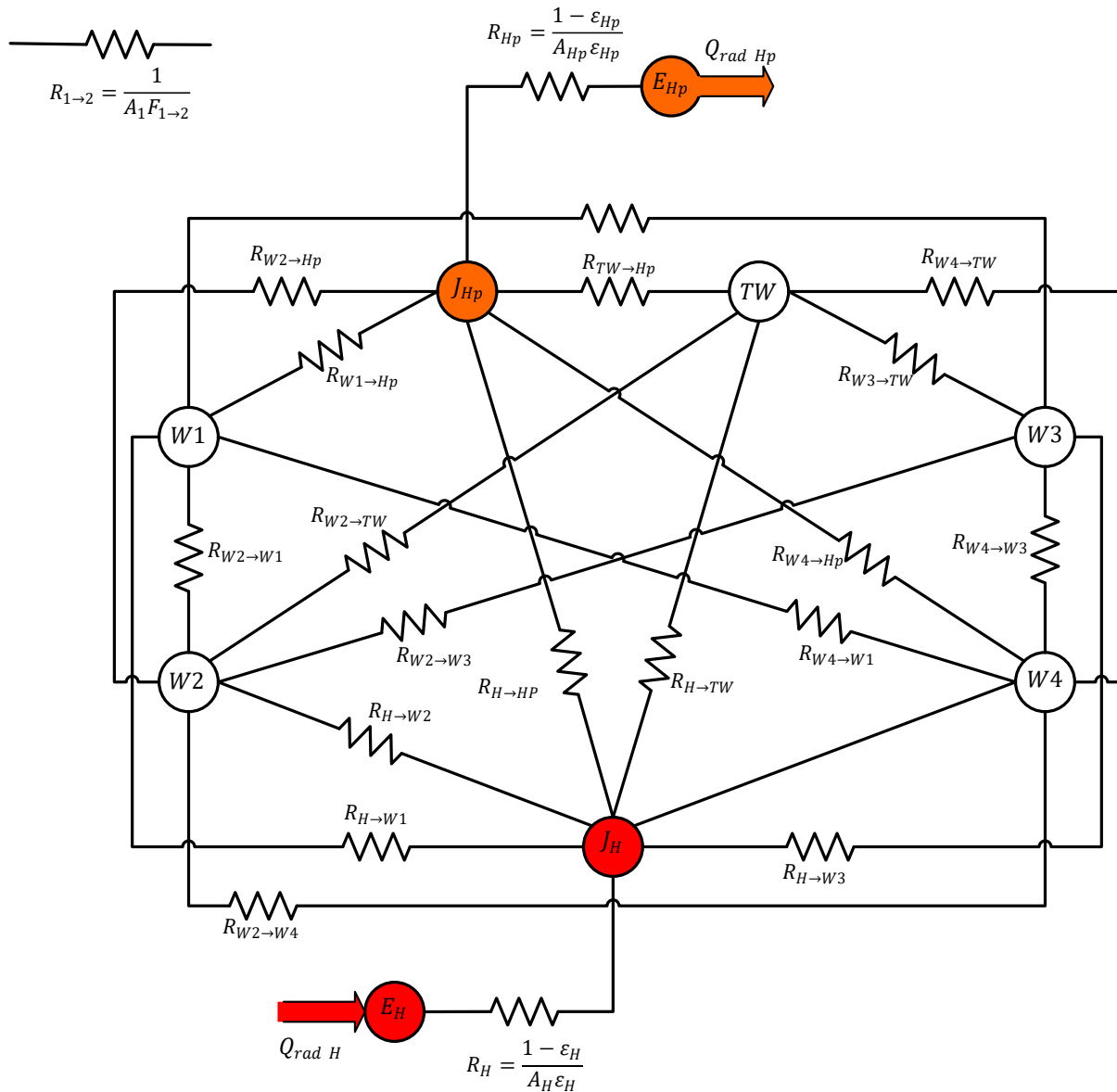


Figure 92 Model of the electrical resistance analogy applied to the radiation heat transfer for the radiative heat pipe

The representation of the radiation thermal analogy was used to simplify the description of the radiation problem. The heat injected into the system through the heater is represented as $Q_{rad H}$. The emitted heat by the heater is represented as E_h . The surface resistance to radiation of the heater is calculated using the emissivity of the ceramic beads. The emissivity of ceramic will change depending on the temperature. The radiosity J_H will radiate the heat to the walls of the kiln and the heat pipe, the space resistances $R_{H \rightarrow HP}$ depend mainly on the view factor of the heater to the heat pipe, similarly for the other space resistances, each view factor will need to be calculated. The top wall and the side walls are considered to be re-radiative, no heat is absorbed at steady state through the wall. The radiosity associated with the heat pipe, J_{HP} , is then transferred to the surface of the heat pipe through the surface

resistance. As for the heater, the emissivity of the heat pipe will change over the temperature range. Depending on the temperature range of the heater and the heat pipe, the variation of the emissivity can be neglected.

Solving this type of radiation resistance network is very complex. In order to simplify the resistance diagram, the four walls and the top wall can be considered as one entity, part of a cavity. The model can then be simplified to the following

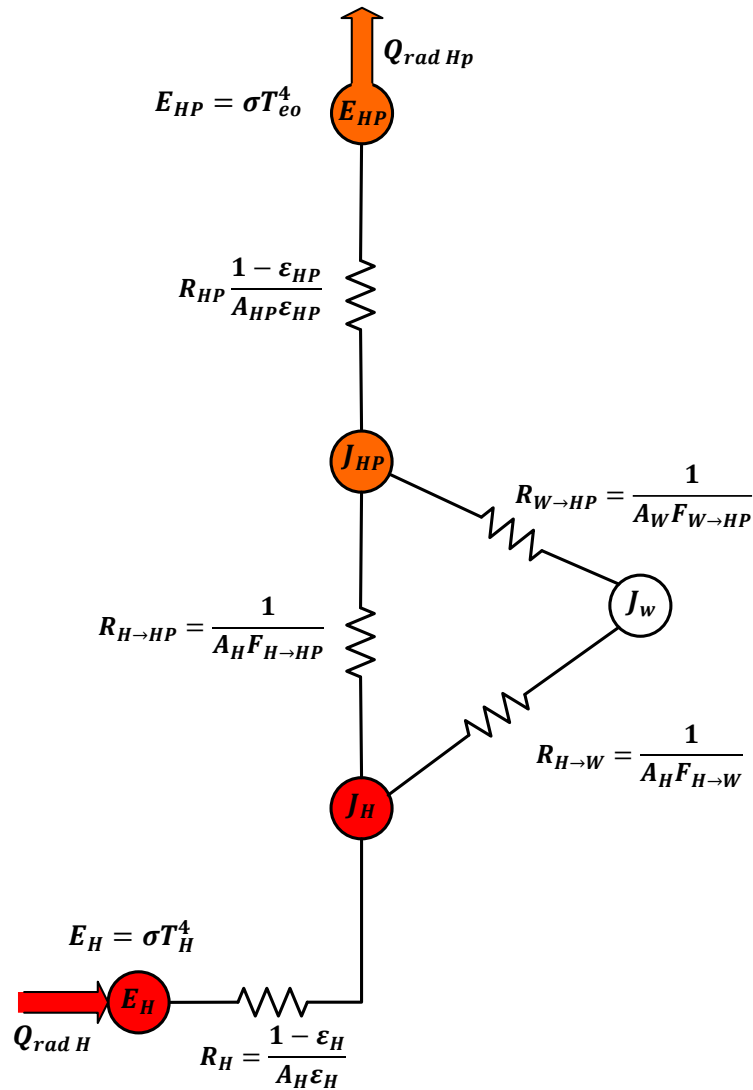


Figure 93 Simplified radiation model

The symbols shown in Figure 93 are as follows,

T_{eo} : Outer evaporator surface temperature (K)

T_{wall} : Inner wall temperature (K)

T_{Heater} : Heater temperature (K)

E_H : Emitted heat from the heater surface (W/m²)

E_{HP} : Emitted heat from the evaporator of the single heat pipe surface (W/m²)

J_H : Radiosity of the heater surface (W/m²)

J_{HP} : Radiosity of the single heat pipe evaporator surface (W/m²)

J_W : Wall radiosity (W/m²)

R_{E_H,J_H} : Heater surface radiation resistance (m²)

$R_{H,HP}$: Radiation space resistance between the heaters and the single heat pipe (m²)

$R_{H,W}$: Radiation space resistance between the heaters and the walls (m²)

$R_{W,HP}$: Radiation space resistance between the walls and the single heat pipe (m²)

$R_{E_{HP},J_{HP}}$: Evaporator radiation surface resistance (m²)

The walls are considered to be fully insulated and thus reradiating all the heat to the wall, $J_W = E_W$. It can be considered that the wall temperature and emissivity do not have any impact on the radiation heat transfer. It can also be seen in Figure 93 that $R_{H,W}$ and $R_{W,HP}$ are linked in series. $R_{H,W}$ and $R_{W,HP}$ are linked in parallel with $R_{H,HP}$.

The equivalent radiation resistance can be expressed as:

$$R_{rad,eq} = \frac{1 - \varepsilon_H}{\varepsilon_H A_H} + \frac{1}{A_H F_{H-HP} + \left[\frac{1}{A_H F_{H,W}} + \frac{1}{A_W F_{W,HP}} \right]^{-1}} + \frac{1 - \varepsilon_{HP}}{\varepsilon_{HP} A_{HP}} \quad (169)$$

The net heat transfer by radiation is determined by,

$$Q_{rad} = \frac{E_H - E_{HP}}{R_{rad,eq}} \quad (170)$$

(170) can be rearranged as,

$$Q_{rad} = \frac{\sigma(T_H^4 - T_{HP}^4)}{\frac{1 - \varepsilon_H}{\varepsilon_H A_H} + \frac{1}{A_H F_{H \rightarrow HP} + \left[\frac{1}{A_H F_{H \rightarrow W}} + \frac{1}{A_W F_{W \rightarrow HP}} \right]^{-1}} + \frac{1 - \varepsilon_{HP}}{\varepsilon_{HP} A_{HP}}} \quad (171)$$

The view factor for the system modelling need to be determined. From the summation rule,

$$F_{H \rightarrow H} + F_{H \rightarrow W} + F_{H \rightarrow HP} = 1 \quad (172)$$

where $F_{H,H} = 0$

$F_{H \rightarrow HP}$ can be determined using (74) and (75), it was assumed that the evaporator section is horizontal. The pipe was also considered to be a flat surface with a width equal to the diameter of the heat pipe. No data for inclined pipes with finite dimensions over a plane with finite dimensions are available in the literature. Those assumptions did not have an impact on the view factor as the ratio between the diameter of the pipe and the surface of the heater is small.

4.3.4 Conduction

Conduction heat transfer occurs between the outer and inner wall of the heat pipe for the evaporator and the condenser section.

The heat transfer by conduction for the evaporator section can be calculated as,

$$Q_{cond,e} = \frac{T_{eo} - T_{ei}}{R_{cond,e}} \quad (173)$$

The thermal resistance can be obtained from,

$$R_{cond,e} = \frac{\ln\left(\frac{D_{eo}}{D_{ei}}\right)}{2\pi l_e k_s} \quad (174)$$

where k_s is the thermal conductivity depending on the shell case material of the heat pipe.

The heat transfer for the condenser section is calculated by,

$$Q_{cond,c} = \frac{T_{co} - T_{ci}}{R_{cond,c}} \quad (175)$$

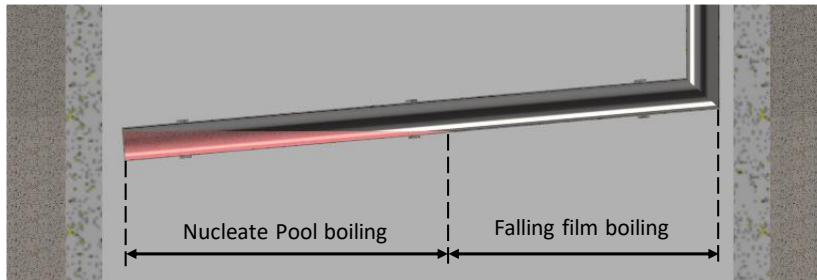
The thermal resistance can be obtained from,

$$R_{cond,c} = \frac{\ln\left(\frac{D_{co}}{D_{ci}}\right)}{2\pi l_c k_s} \quad (176)$$

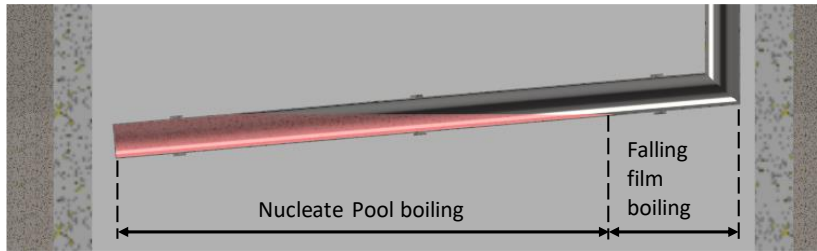
4.3.5 Boiling

As the filling ratio is modified during the testing in order to investigate the best-case scenario, different types of boiling will occur in the different case studies. An illustration of the two different types of boiling can be seen in Figure 94.

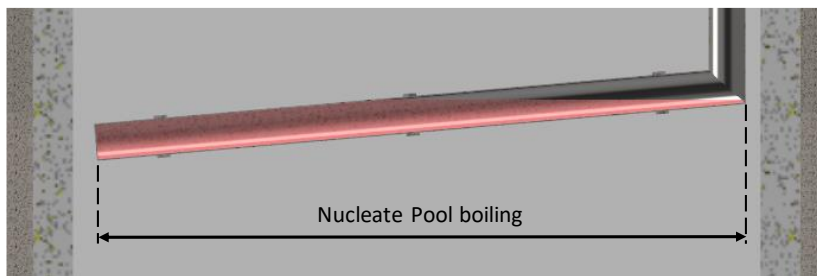
25% Filling ratio



50% Filling ratio



75% Filling ratio



100% Filling ratio

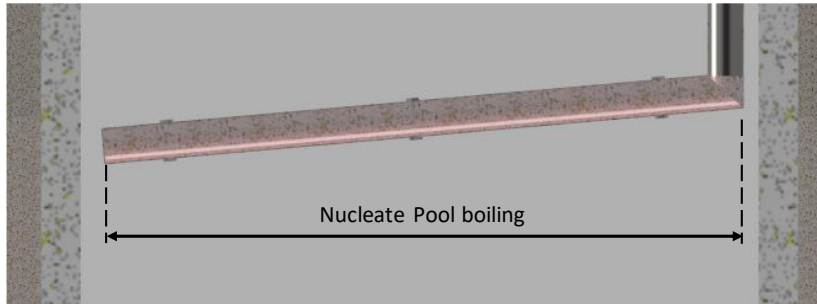


Figure 94 Different boiling regime under various filling ratio

The boiling heat transfer for the filling ratios of 25% and 50% is composed of two boiling heat transfer regimes. The first section of the evaporator from the bottom to the liquid level is considered to be nucleate pool boiling. The heat transfer above the liquid limit to the top of the evaporator section is nucleate falling film boiling. For the filling ratio from 75% to 100%, the heat transfer regime is considered to be nucleate pool boiling.

The sum of the boiling heat transfer can be expressed as,

$$Q_{cond,c} = Q_{boil,Nucleate} + Q_{boil,Film} \quad (177)$$

The heat transfer for the nucleate pool boiling can be expressed as,

$$Q_{boil,Nucleate} = \frac{T_{ei} - T_v}{R_{Bi,nucleate}} \quad (178)$$

where,

$$R_{Bi,nucleate} = \frac{1}{h_{ei,nucleate} A_{ei,nucleate}} \quad (179)$$

The heat transfer coefficient for nucleate pool boiling can be determined using Table 18

The heat transfer by falling film pool boiling can be determined by

$$Q_{boil,Film} = \frac{T_{ei} - T_v}{R_{Bi,film}} \quad (180)$$

where

$$R_{Bi,film} = \frac{1}{h_{ei,film} A_{ei,film}} \quad (181)$$

The nucleate falling film pool boiling heat transfer coefficient $h_{ei,nucleate}$ can be calculated using the correlations in Table 19.

When the filling ratio is covering the entire boiling surface area, it can be assumed that $Q_{boil,Film} = 0$.

Thus,

$$Q_{cond,c} = Q_{boil,Nucleate} \quad (182)$$

The length of the nucleate pool boiling heat transfer area can be calculated as

$$L_{Boil,Nucleate} = L_{evaporator} \cdot \text{filling ratio} \quad (183)$$

The internal surface temperature of the heat pipe will be different at the two boiling regimes for the same vapour temperature. The thermal network model needs to be modified as shown in Figure 95.

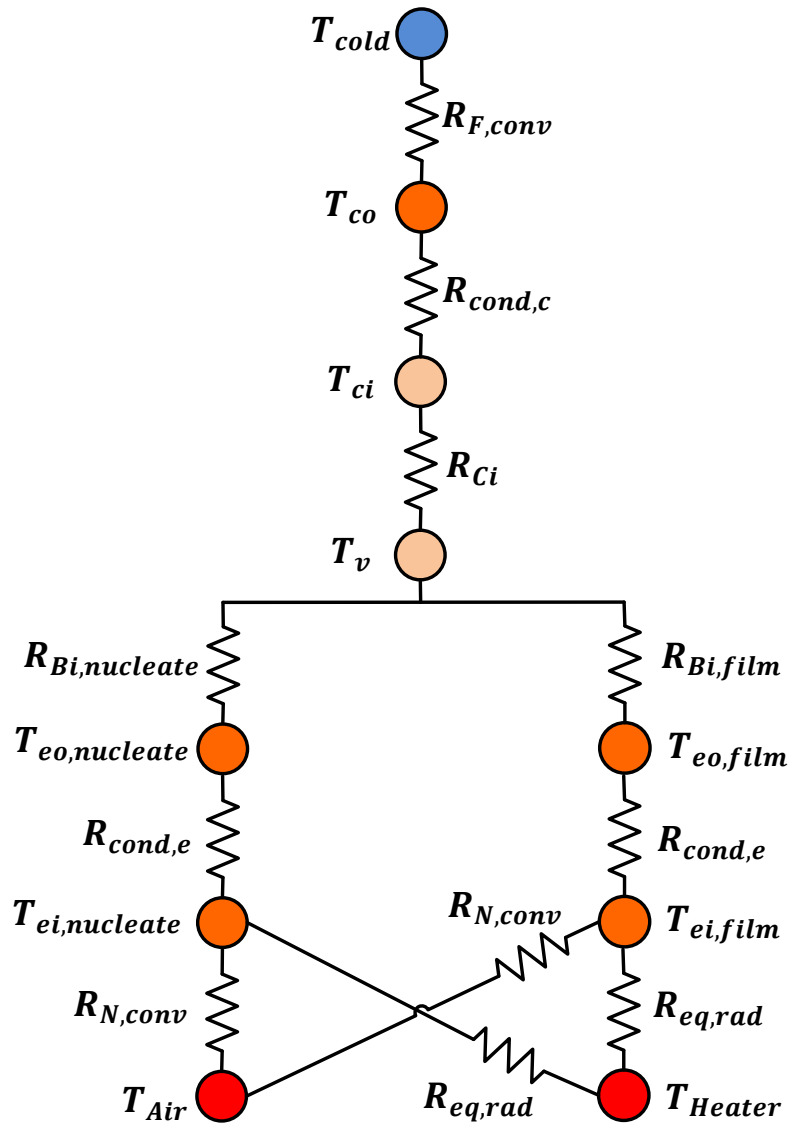


Figure 95 Thermal network schematic including the two boiling regimes

4.3.6 Condensation

The heat transfer rate via condensation can be expressed as,

$$Q_{cond} = \frac{(T_v - T_{ci})}{R_{Ci}} \quad (184)$$

The thermal resistance for condensation can be obtained by,

$$R_{Ci} = \frac{1}{h_{ci}A_{ci}} \quad (185)$$

The heat transfer coefficient for the condensation can be calculated using Table 20.

4.3.7 Forced convection

The heat transfer by forced convection in the condenser section can be determined by,

$$Q_{F.convection} = h_{F.convection} \cdot A_{con,total} \cdot \frac{[(T_v - T_{in}) - (T_v - T_{out})]}{\ln\left(\frac{(T_v - T_{in})}{(T_v - T_{out})}\right)} \quad (186)$$

Thus, the following equation can be obtained,

$$Q_{F.convection} = h_{F.convection} \cdot A_{con,total} \cdot \frac{(T_{out} - T_{in})}{\ln\left(\frac{(T_v - T_{in})}{(T_v - T_{out})}\right)} \quad (187)$$

where $h_{F.convection}$ is the heat transfer coefficient by forced convection, the heat transfer coefficient can be calculated using the correlations in Table 21, $A_{co,total}$ is the total heat transfer surface in the condenser including the fins. As the fins will not have the same temperature as the wall in direct contact with the inner wall of the condenser, a coefficient of efficiency was introduced,

$$A_{con,total} = A_{con} + \eta A_{con,fin} \quad (188)$$

A detailed drawing of the condenser section is presented in Figure 96,

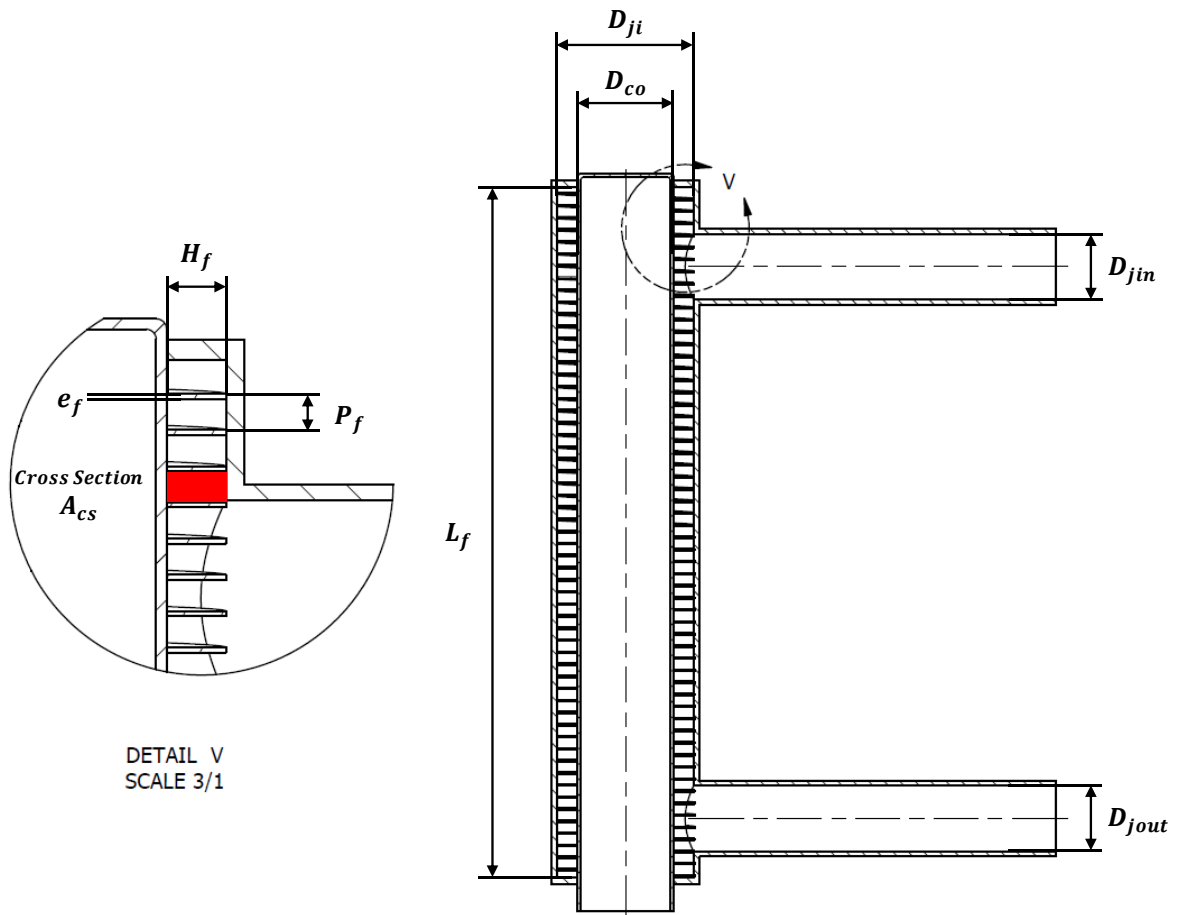


Figure 96 Detailed drawing of the single heat pipe condenser section

where H_f is the height of the fins, P_f is the pitch of the helical, A_{cs} is the cross section area of the flow and e_f is the fin thickness.

The efficiency of the surface can be calculated using

$$\eta_{fins} = \frac{\tanh(m \cdot H_f)}{m \cdot H_f} \quad (189)$$

where m is:

$$m = \sqrt{\frac{2h_{F.convection}}{k_f e_f}} \quad (190)$$

The heat transfer area corresponding to the fins surface $A_{con,fin}$ is calculated from,

$$A_{con,fin} = H_f L_{helical} \quad (191)$$

$L_{helical}$ is the average length of the helical,

$$L_{helical} = \left[\pi^2 \left(\frac{D_{ji} + D_{co}}{2} \right)^2 + P_f^2 \right]^{0.5} \frac{L_c}{P_{fin}} \quad (192)$$

where L_c/P_f represents the number of turns of the helical path in the condenser cooling jacket.

4.4 Theoretical modelling of the radiative modules

The theoretical modelling of the modular radiative heat pipe is similar to that for the single heat pipe theoretical model. Heat is generated by the heater. The heat is then transferred through radiation and natural convection to the outer surface of the heat pipe evaporator. The heat is then transferred to the inner surface of the evaporator section through conduction heat transfer. The heated evaporator inner surface will transfer the heat to the working fluid through nucleate pool boiling. The vapour generated will travel to the condenser section. The condenser section is made of a tube bundle where the heat is transferred to the liquid by condensation on the tube surface. The heat is then transferred to the liquid via conduction and internal forced convection in tubes.

A schematic of the different heat transfer regimes is presented in Figure 97 and Figure 98.

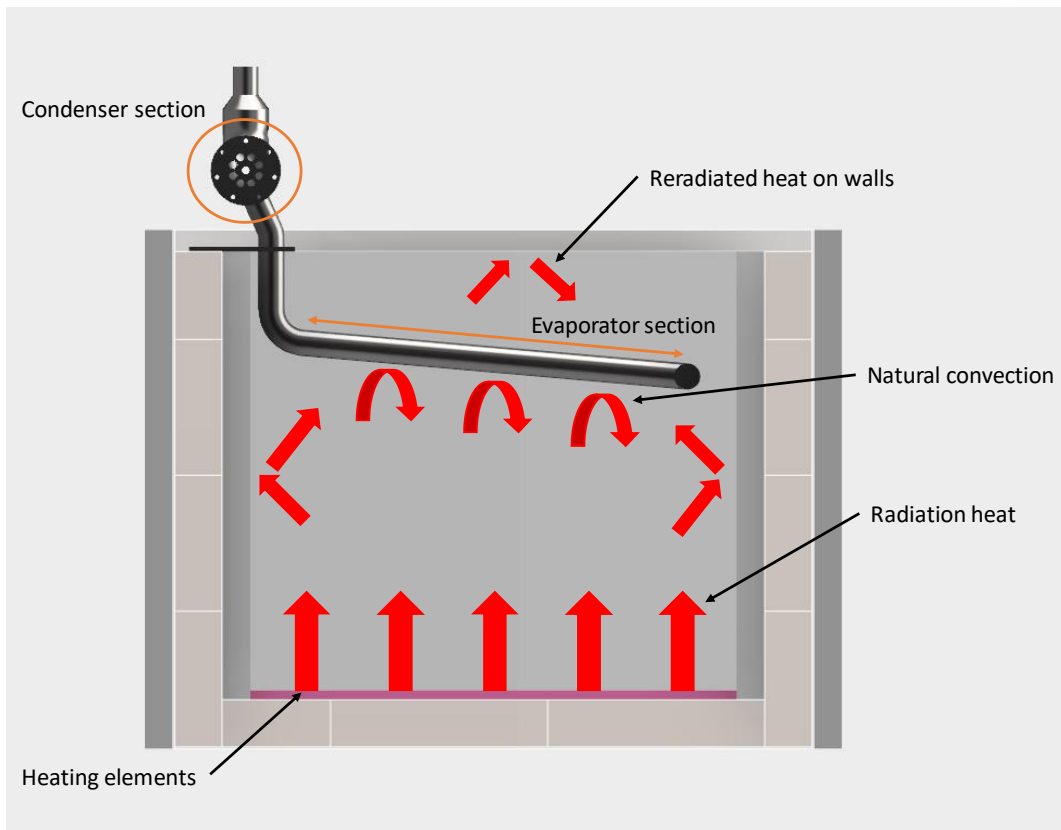


Figure 97 Heat transfer regime in radiative module 1

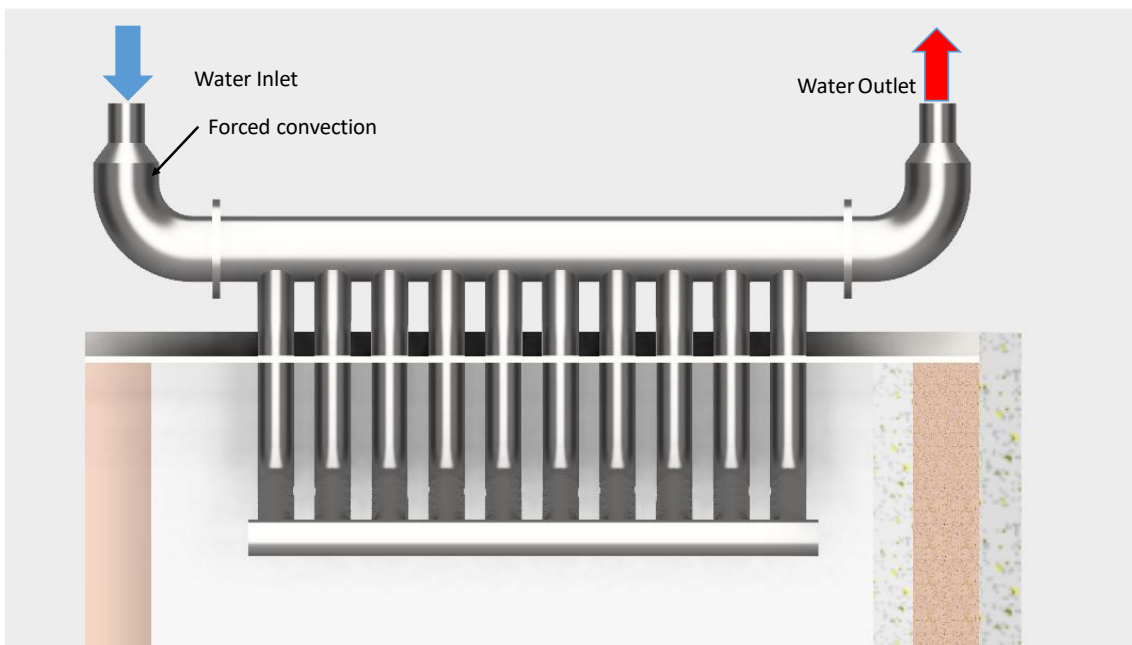


Figure 98 Heat transfer regime in radiative module 2

The approach for the module radiative ceiling is similar to the single radiative heat pipe. The thermal network model approach will be similar. The change of design in the evaporator

section will mainly impact the view factor, evaporator heat transfer area and the boiling regime. The condenser section was also modified to decrease the pressure drop induced by the water jacket tested in the single radiative heat pipe. The correlations used in the single heat pipe for condensation will have to be modified to consider the falling film on the tube bundle and the inundation of the tube bundle.

4.4.1 Thermal network model for radiative modules

The thermal network approach is similar to the single radiative heat pipe, a schematic of the network is presented in Figure 99.

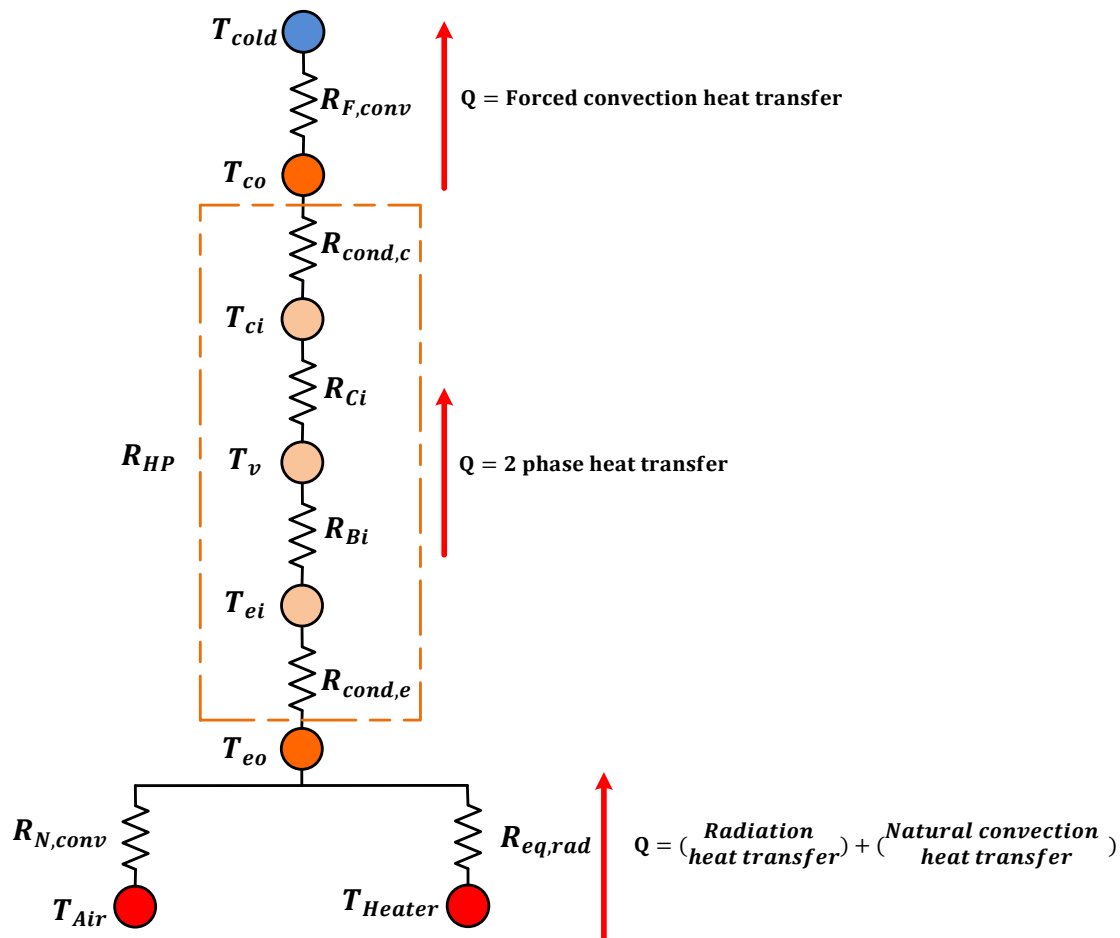


Figure 99 Thermal network modelling of radiative heat pipe modules

$R_{eq,rad}$: Radiation heat transfer resistance (K/W)

$R_{N,conv}$: Natural convection heat transfer thermal resistance (K/W)

$R_{cond,e}$: Conduction thermal resistance of the evaporator wall (K/W)

R_{Bi} : Boiling thermal resistance (K/W)

R_{Ci} : Condensation thermal resistance (K/W)

$R_{cond,c}$: Conduction thermal resistance of the condenser wall (K/W)

$R_{F,conv}$: Convection thermal resistance of condenser section (K/W)

T_{Heater} : Heater temperature (K).

T_{eo} : Outer wall evaporator temperature (K).

T_{ei} : Inner wall evaporator temperature (K).

T_v : Heat pipe working fluid vapour temperature (K).

T_{ci} : Inner wall condenser temperature (K).

T_{co} : Outer wall condenser temperature (K).

T_{cold} : Water coolant temperature (K).

R_{HP} : Heat pipe equivalent thermal resistance where,

$$R_{HP} = R_{Con,e} + R_{Bi} + R_{Ci} + R_{Cond,c} \text{ (K/W)} \quad (193)$$

4.4.2 Natural convection

Natural convection resistance is calculated using the following equation,

$$R_{N.convection} = \frac{1}{h_{N.convection} A_{eo}} \quad (194)$$

where $h_{N.convection}$ is calculated using the correlations (25)-(33).

4.4.3 Conduction

The conduction heat transfer occurs between the outer and inner wall of the heat pipe for the evaporator and the condenser section.

The heat transfer by conduction for the evaporator section can be calculated as,

$$Q_{cond,e} = \frac{T_{eo} - T_{ei}}{R_{cond,e}} \quad (195)$$

The thermal resistance can be obtained from,

$$R_{cond,e} = \frac{\ln\left(\frac{D_{eo}}{D_{ei}}\right)}{2\pi l_e k_s} \quad (196)$$

where k_s is the thermal conductivity depending on the shell case material of the heat pipe.

The heat transfer for the condenser section is calculated by,

$$Q_{cond,c} = \frac{T_{co} - T_{ci}}{R_{cond,c}} \quad (197)$$

The thermal resistance can be obtained from,

$$R_{cond,c} = \frac{\ln\left(\frac{D_{co}}{D_{ci}}\right)}{2\pi l_c k_s} \quad (198)$$

4.4.4 Radiation

4.4.4.1 Radiation heat transfer

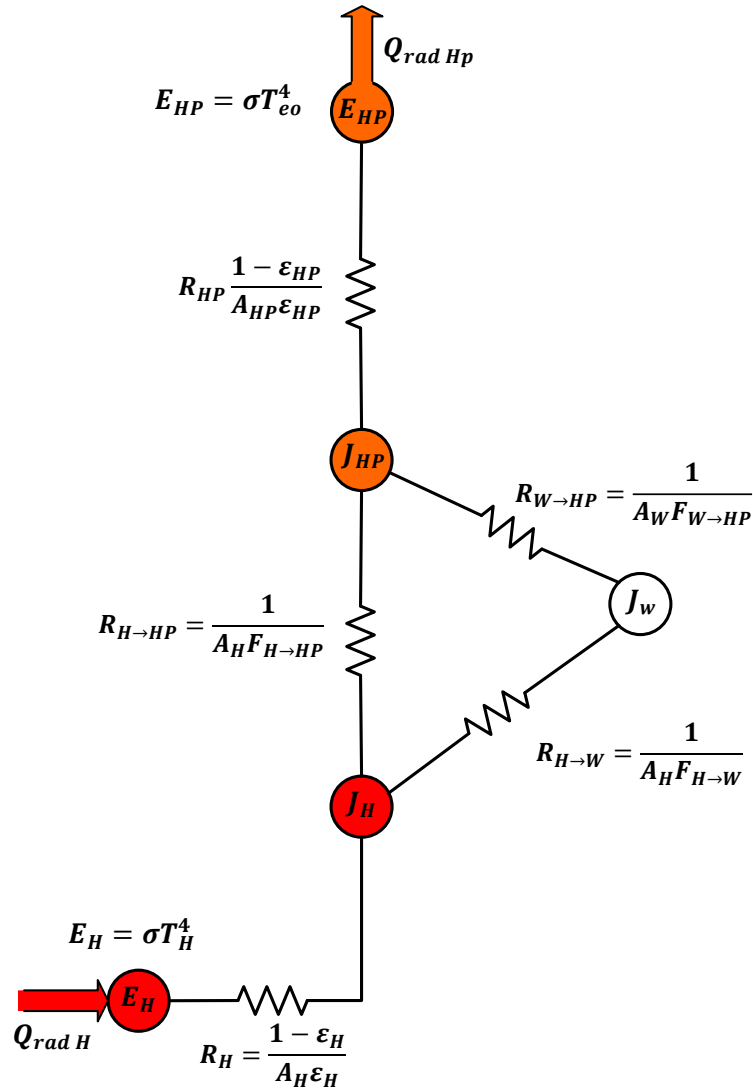


Figure 100 Thermal radiation network

The symbols shown in Figure 100 are as follows,

T_{eo} : Outer evaporator surface temperature (K)

T_{wall} : Inner wall temperature (K)

T_{Heater} : Heater temperature (K)

E_H : Emitted heat from the heater surface (W/m²)

E_{HP} : Emitted heat from the evaporator of the heat pipe module surface (W/m²)

J_H : Radiosity of the heater surface (W/m²)

J_{HP} : Radiosity of the heat pipe module evaporator surface (W/m²)

J_W : Wall radiosity (W/m²)

R_{E_H, J_H} : Heater surface radiation resistance (m²)

$R_{H, HP}$: Radiation space resistance between the heaters and the Heat Pipe Module (m²)

$R_{H, W}$: Radiation space resistance between the heaters and the walls (m²)

$R_{W, HP}$: Radiation space resistance between the walls and the heat pipe module (m²)

$R_{E_{HP}, J_{HP}}$: Evaporator radiation surface resistance (m²)

The equivalent radiation resistance can be expressed as,

$$R_{rad,eq} = \frac{1 - \varepsilon_H}{\varepsilon_H A_H} + \frac{1}{A_H F_{H \rightarrow HP} + \left[\frac{1}{A_H F_{H,W}} + \frac{1}{A_W F_{W,HP}} \right]^{-1}} + \frac{1 - \varepsilon_{HP}}{\varepsilon_{HP} A_{HP}} \quad (199)$$

The net heat transfer by radiation is determined by,

$$Q_{rad} = \frac{E_H - E_{HP}}{R_{rad,eq}} \quad (200)$$

(170) can be rearranged as,

$$Q_{rad} = \frac{\sigma(T_H^4 - T_{HP}^4)}{\frac{1 - \varepsilon_H}{\varepsilon_H A_H} + \frac{1}{A_H F_{H \rightarrow HP} + \left[\frac{1}{A_H F_{H \rightarrow W}} + \frac{1}{A_W F_{W \rightarrow HP}} \right]^{-1}} + \frac{1 - \varepsilon_{HP}}{\varepsilon_{HP} A_{HP}}} \quad (201)$$

4.4.4.2 View factor correlation

The view factor for the different modules can be determined as,

$$F_{H \rightarrow H} + F_{H \rightarrow W} + F_{H \rightarrow HP} = 1 \quad (202)$$

for

$$n F_{H \rightarrow HP \text{ leg}} + F_{H \rightarrow HP \text{ col}} = F_{H \rightarrow HP} \quad (203)$$

where n is the number of pipes exposed to the radiation, $F_{H \rightarrow HP \text{ leg}}$ is the view factor associated to one leg of the radiative heat pipe modules and $F_{H \rightarrow HP \text{ col}}$ is the view factor associated to the bottom collector of the radiative heat pipe. There is no correlation for n tubes above a finite plane surface. In order to determine $F_{H \rightarrow HP \text{ col}}$ and $F_{H \rightarrow HP \text{ leg}}$, the tubes were considered as a

flat surface with a width equal to the diameter of the tube. The view factor for the heat pipe is calculated using (74) and (75). A schematic of the view factor is presented in Figure 101

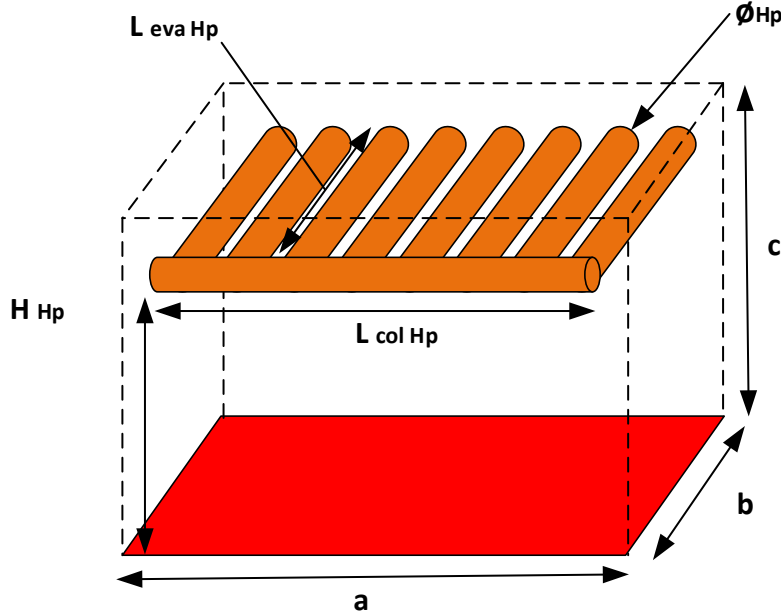


Figure 101 Schematic of view factor from the heater to the tube bundle

4.4.5 Boiling

The heat transfer for the nucleate pool boiling can be expressed as,

$$Q_{boil,Nucleate} = \frac{T_{ei} - T_v}{R_{Bi,nucleate}} \quad (204)$$

where

$$R_{Bi,nucleate} = \frac{1}{h_{Bi,nucleate} A_{ei,nucleate}} \quad (205)$$

The heat transfer coefficient for nucleate pool boiling can be determined using Table 18.

4.4.6 Condensation over tube bundle

The condenser section in the radiative heat pipe model differs from that in the single radiative heat pipe. The condenser is composed of a tube bundle with water running inside the tube. The condensation of the vapour will occur on the outer surfaces of the cooling tubes.

The heat transfer rate by condensation is represented as follows,

$$Q_{co} = \frac{(T_v - T_{co})}{R_{co}} \quad (206)$$

where

T_v : Vapour temperature (K)

T_{co} : Temperature of outer surface of the inner tubes

R_{co} : Thermal resistance of heat transfer by condensation

$$R_{co} = \frac{1}{h_{co} \cdot A_{co}}$$

A_{co} : Heat pipe condenser area which represents the overall external surface area of the horizontal tubes in the condenser section (m²).

$$A_{co} = \pi \times D_{co} \times L_c \times N_{water\ tube} \quad (207)$$

D_{co} : Condenser outer diameter (m)

L_c : Condenser length (m)

$N_{water\ tube}$: Number of water tubes

h_{co} : Condensation heat transfer coefficient (W/m².K)

The condensate from the top of the tube bundle will have an impact on the rows of tubes below as gravity will drive the liquid down onto the other pipes. The condensate film located on the bottom tube of the tube bundle will be larger, impacting the local condensation heat transfer coefficient. The inundation of the tubes and the shear stress induced by the vapour need to be taken into account when calculating the overall heat transfer coefficient by condensation in tube bundles.

Two heat transfer regimes can be identified for condensation of vapour over a tube bundle, the shear heat transfer coefficient and the heat transfer coefficient for the single phase forced convection across a tubes bank.

The condensation heat transfer coefficient in a tube bundle can be defined as,

$$h_N = (h_{sh}^2 + h_{gr}^2)^{1/2} \quad (208)$$

where the shear heat transfer coefficient is calculated using,

$$h_{sh} = a \left[\frac{1}{X_{tt}} \right]^b h_l \quad (209)$$

h_l is the heat transfer coefficient for the single phase forced convection in a tube bundle assuming that the flow is covering the entirety of the tube bank,

$$h_l = C \frac{k_l}{D_{co}} Re_l^m Pr_l^n \quad (210)$$

h_{gr} can be determined by,

$$h_{gr} = \frac{0.728 k_l C_N \left\{ \frac{\rho_l (\rho_l - \rho_g) g i_{lg} D_{co}^3}{\mu_l (T_s - T_{wo}) k_l} \right\}^{1/4}}{D_{co}} \quad (211)$$

A schematic of the condenser section is presented in Figure 102,

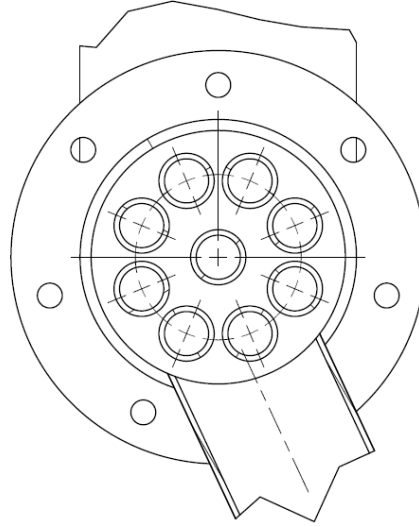


Figure 102 Schematic of condenser section

4.4.7 Forced convection in tubes

The heat transfer by forced convection in the condenser section can be determined by,

$$Q_{F.convection} = h_{F.convection} \cdot A_{con,total} \cdot \frac{[(T_v - T_{in}) - (T_v - T_{out})]}{\ln \left(\frac{(T_v - T_{in})}{(T_v - T_{out})} \right)} \quad (212)$$

Thus, the following can be obtained,

$$Q_{F.convection} = h_{F.convection} \cdot A_{con,total} \cdot \frac{(T_{out} - T_{in})}{\ln \left(\frac{(T_v - T_{in})}{(T_v - T_{out})} \right)} \quad (213)$$

4.5 Theoretical modelling of a full-scale system.

4.5.1 Thermal network model for radiative modules

In order to establish a theoretical model of the multi module radiative heat pipe, the sections of the kiln need to be separated in six distinct regions: the region on the side of the kiln, close

to the wall, the intermediate regions and the two central regions where most of the heat transfer is located. An illustration can be seen in Figure 103.

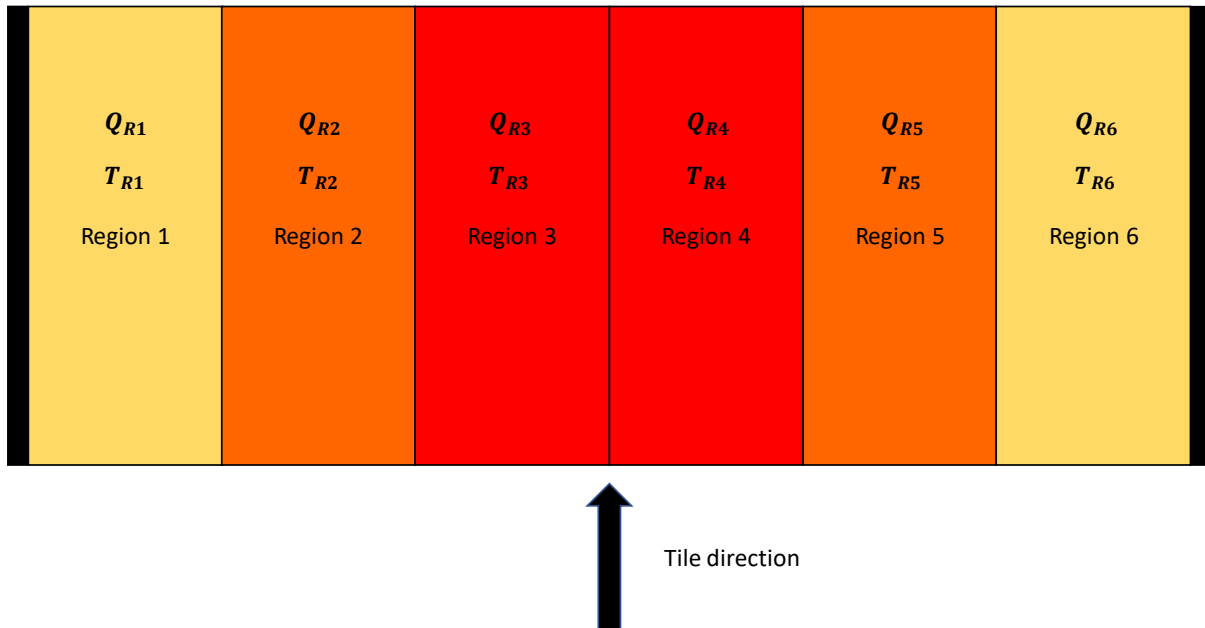


Figure 103 Temperature distribution in the kiln

Testing on the tiles demonstrated that the temperature between the side of the tiles and the middle varies. In order to achieve a uniform temperature, the multi module heat pipe can be applied.

Each region of the kiln cross section needs to be separated in order to determine the heat transfer that needs to be extracted. Using the current set up, the temperatures of the tiles vary from the side to the middle with a constant heat flux. The aim of the model is to have a constant temperature with a heat flux varying in the kiln cross section. In order to achieve this uniform cooling, a conceptual heat pipe system using the modules investigated above was designed. The concept is presented in Figure 104.

The theoretical model developed and validated with the laboratory tests can then be applied in all the regions of the system.

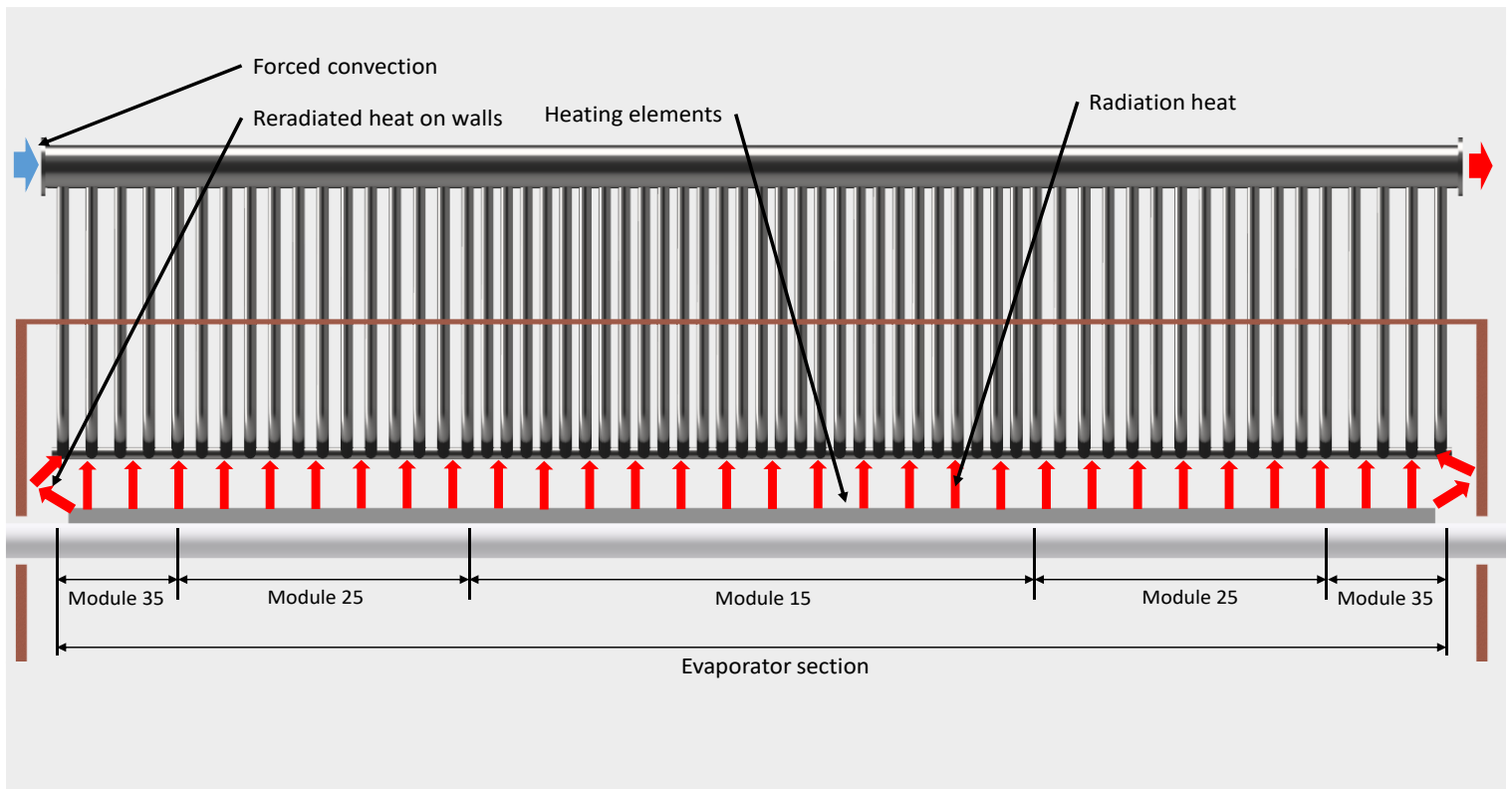


Figure 104 Heat transfer in the radiative hot pipe ceiling

The tiles will radiate heat onto the heat pipe ceiling. The fine tuning of the spacing between the pipes will modify the local view factor and the local heat transfer area above the different regions of the tiles. The heat from the tiles will also be received by the side wall. This heat will then be radiated from the top and sides walls to the radiative heat pipe. The heat generated by the tiles and the reradiation from the side walls of the kiln will be absorbed by the heat pipe ceiling through radiation. Air is used to cool down the tiles at a later stage in the process. This air will also go through the pipes of the heat pipe ceiling. This air will be cooled down by the heat pipe evaporator section by external forced convection. As the heat pipe is composed of a vertical and a horizontal region, the heat transfer regimes for the forced convection heat transfer have to be separated. The forced convection over a plate will be used on the horizontal section of the heat pipe ceiling and forced convection over a cylinder will be used for the vertical section. The total heat absorbed from the heat pipe will then be transferred through the wall by conduction. The heat will be transferred to the liquid. The liquid will then be vaporized and travel to the top section of the heat pipe ceiling. The latent heat of vaporization will be released to the condensing tube through conduction heat transfer. The heat will then be transferred through the tube wall by conduction. The heat will be removed by forced convection in the tubes to the heat sink fluid. This approach was used to develop the theoretical model for the full-scale heat pipe ceiling. A schematic of the approach is shown in Figure 105.

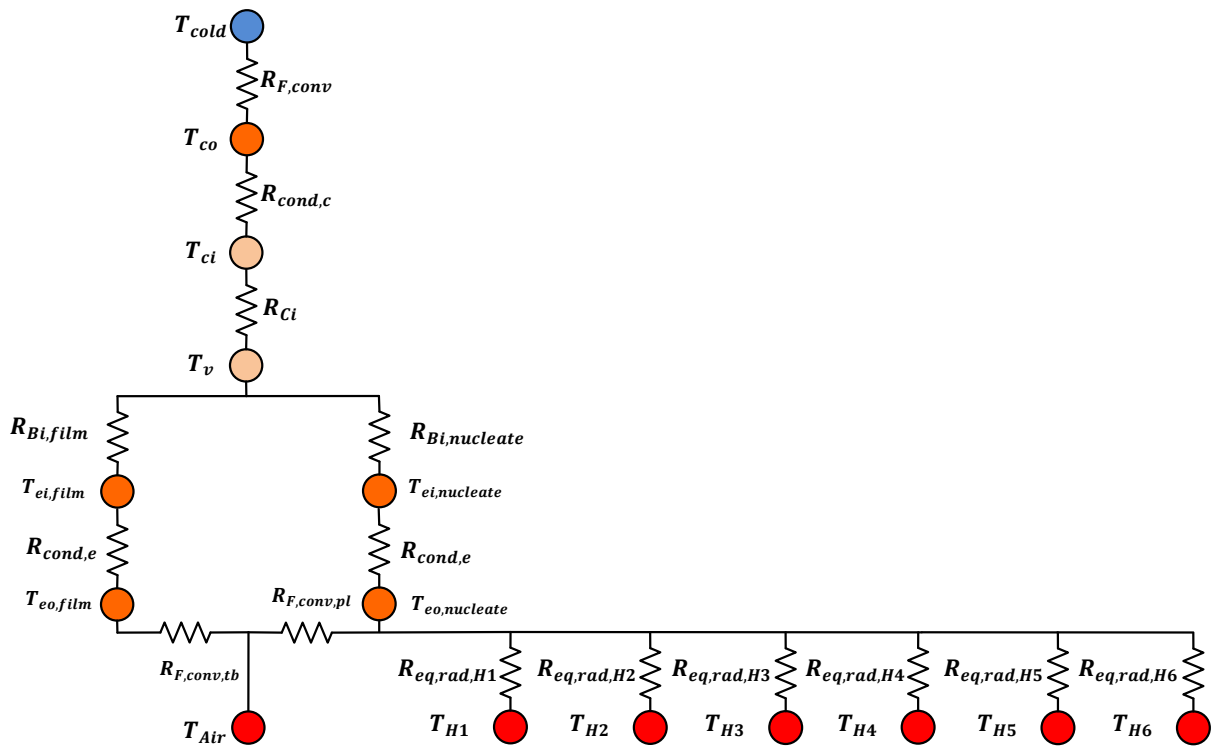


Figure 105 Schematic thermal model heat pipe ceiling

$R_{eq,rad}$: Radiation heat transfer resistance (K/W)

$R_{F,conv,tb}$: External forced convection heat transfer thermal resistance over tubes (K/W)

$R_{F,conv,pl}$: External forced convection heat transfer thermal resistance over a plate (K/W)

$R_{F,conv}$: Internal forced convection heat transfer thermal resistance (K/W)

$R_{cond,e}$: Conduction thermal resistance of the evaporator wall (K/W)

$R_{Bi,nucleate}$: Boiling thermal resistance for nucleate boiling (K/W)

$R_{Bi,film}$: Boiling thermal resistance for film boiling (K/W)

R_{Ci} : Condensation thermal resistance (K/W)

$R_{cond,c}$: Conduction thermal resistance of the condenser wall (K/W)

T_H : Heated tiles temperature (K).

$T_{eo,film}$: Outer wall evaporator temperature for film boiling (K).

$T_{eo,nucleate}$: Outer wall evaporator temperature for nucleate boiling (K).

$T_{ei,nucleate}$: Inner wall evaporator temperature for nucleate boiling (K).

$T_{ei,film}$: Inner wall evaporator temperature for film boiling (K).

T_v : Heat pipe working fluid vapour temperature (K).

T_{ci} : Inner wall condenser temperature (K).

T_{co} : Outer wall condenser temperature (K).

T_{cold} : Water coolant temperature (K).

4.5.2 Radiation heat transfer

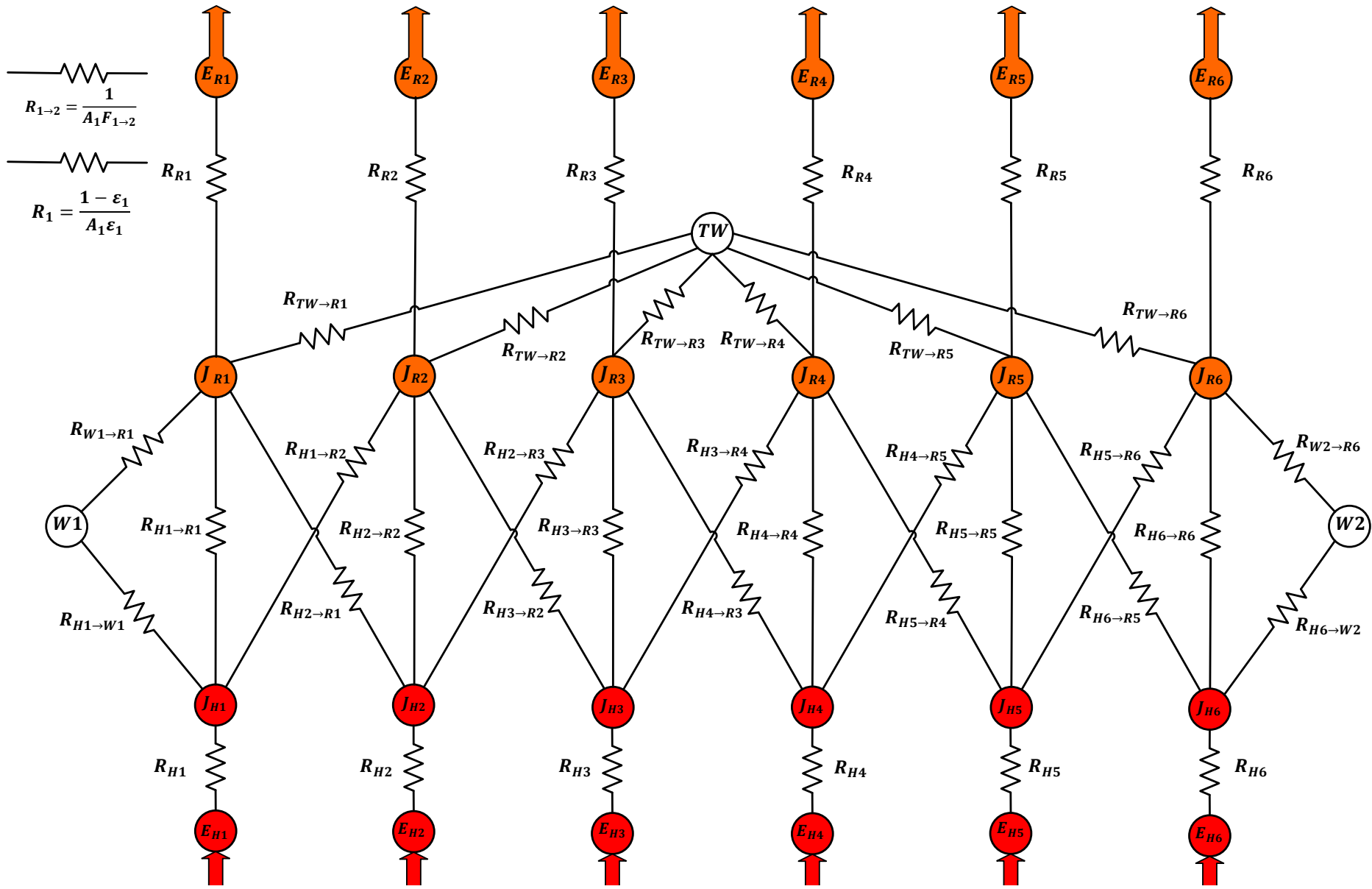


Figure 106 Radiation heat transfer schematic

The radiation from the region n will have an impact on the heat pipe region $n - 1$ and $n + 1$, the rest of the heat pipe region can be neglected as shown on Figure 106.

The heat pipe is considered to be isothermal as all the pipes in the evaporator section are connected together with a bottom collector and the condenser section. Thus, it can be assumed that the temperature of the heat pipe above each region of the tiles will be the same.

As the distance between the regions two to five is large, the impact of the radiation from the side wall was neglected. The schematic was simplified to obtain Figure 107.

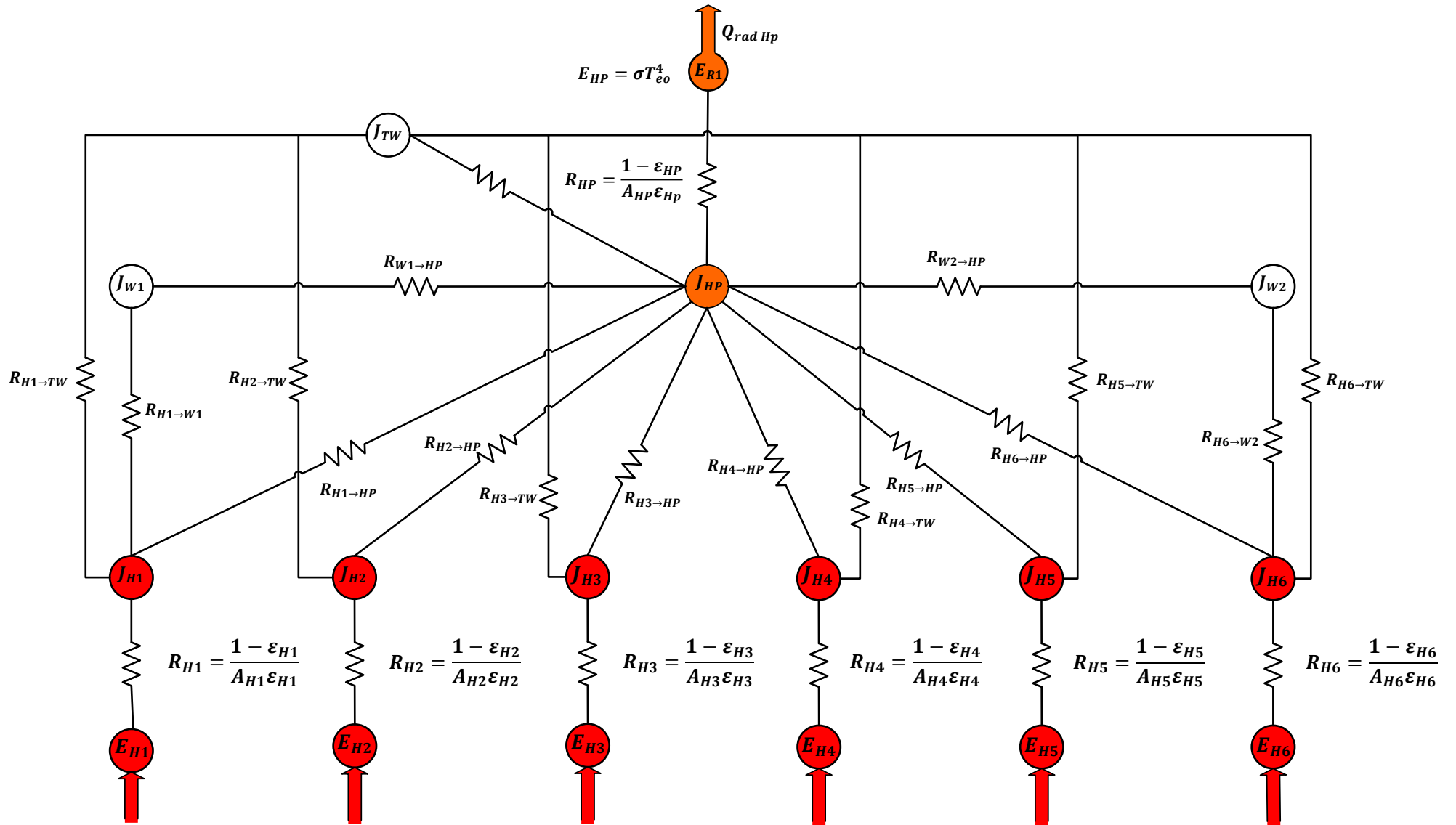


Figure 107 Simplified radiation network schematic

where,

E_{Hn} : Heat emitted from the region n (W/m^2)

J_{Hn} : Radiosity of the n region surface which is the overall radiation leaving the surface (W/m^2)

J_{Wn} : Radiosity of the n wall surface which is the overall radiation leaving the surface (W/m^2)

J_{Top} : Radiosity of the top wall surface which is the overall radiation leaving the surface (W/m^2)

J_{HP} : Radiosity of the heat pipe ceiling surface which is the overall radiation leaving the surface (W/m^2)

E_{HP} : Heat emitted from the heat pipe ceiling surface (W/m^2)

R_{Hn} : n regions resistance to radiation (m^{-2})

$R_{Hn \rightarrow HP}$: Space resistance to radiation for n regions to the heat pipe ceiling (m^{-2})

R_{HP} : Heat pipe ceiling resistance to radiation (m^{-2})

The net heat transfer by radiation received by the heat pipe ceiling is determined by,

$$Q_{rad} = \frac{E_{H1} - E_{HP}}{R_{rad,eq,H1}} + \frac{E_{H2} - E_{HP}}{R_{rad,eq,H2}} + \frac{E_{H3} - E_{HP}}{R_{rad,eq,H3}} + \frac{E_{H4} - E_{HP}}{R_{rad,eq,H4}} + \frac{E_{H5} - E_{HP}}{R_{rad,eq,H5}} + \frac{E_{H5} - E_{HP}}{R_{rad,eq,H5}} \quad (214)$$

$R_{rad,eq,H1}$ can be calculated as,

$$R_{rad,eq,H1} = \frac{1 - \varepsilon_{H1}}{\varepsilon_{H1}A_{H1}} + \frac{1}{A_{H1}F_{H1-HP} + \left[\frac{1}{A_{H1}F_{H1,W1}} + \frac{1}{A_{W1}F_{W1,HP}} \right]^{-1} + \left[\frac{1}{A_{H1}F_{H1,TW}} + \frac{1}{A_{TW}F_{TW,HP}} \right]^{-1}} + \frac{1 - \varepsilon_{HP}}{\varepsilon_{HP}A_{HP}} \quad (215)$$

$R_{rad,eq,H2}$ can be calculated as,

$$R_{rad,eq,H2} = \frac{1 - \varepsilon_{H2}}{\varepsilon_{H2}A_{H2}} + \frac{1}{A_{H2}F_{H2,HP} + \left[\frac{1}{A_{H2}F_{H2,TW}} + \frac{1}{A_{TW}F_{TW,HP}} \right]^{-1}} + \frac{1 - \varepsilon_{HP}}{\varepsilon_{HP}A_{HP}} \quad (216)$$

Using (215) and (216), (214) can be rearranged as,

$$\begin{aligned}
Q_{rad} &= \frac{E_{H1} - E_{HP}}{\frac{1 - \varepsilon_{H1}}{\varepsilon_{H1} A_{H1}} + \frac{1}{A_{H1} F_{H1,HP}} + \left[\frac{1}{A_{H1} F_{H1,W1}} + \frac{1}{A_{W1} F_{W1,HP}} \right]^{-1} + \left[\frac{1}{A_{H1} F_{H1,TW}} + \frac{1}{A_{TW} F_{TW,HP}} \right]^{-1} + \frac{1 - \varepsilon_{HP}}{\varepsilon_{HP} A_{HP}}} \\
&+ \frac{E_{H2} - E_{HP}}{\frac{1 - \varepsilon_{H2}}{\varepsilon_{H2} A_{H2}} + \frac{1}{A_{H2} F_{H2,HP}} + \left[\frac{1}{A_{H2} F_{H2,TW}} + \frac{1}{A_{TW} F_{TW,HP}} \right]^{-1} + \frac{1 - \varepsilon_{HP}}{\varepsilon_{HP} A_{HP}}} \\
&+ \frac{E_{H3} - E_{HP}}{\frac{1 - \varepsilon_{H3}}{\varepsilon_{H3} A_{H3}} + \frac{1}{A_{H3} F_{H3,HP}} + \left[\frac{1}{A_{H3} F_{H3,TW}} + \frac{1}{A_{TW} F_{TW,HP}} \right]^{-1} + \frac{1 - \varepsilon_{HP}}{\varepsilon_{HP} A_{HP}}} \\
&+ \frac{E_{H4} - E_{HP}}{\frac{1 - \varepsilon_{H4}}{\varepsilon_{H4} A_{H4}} + \frac{1}{A_{H4} F_{H4,HP}} \left[\frac{1}{A_{H4} F_{H4,TW}} + \frac{1}{A_{TW} F_{TW,HP}} \right]^{-1} + \frac{1 - \varepsilon_{HP}}{\varepsilon_{HP} A_{HP}}} \\
&+ \frac{E_{H5} - E_{HP}}{\frac{1 - \varepsilon_{H5}}{\varepsilon_{H5} A_{H5}} + \frac{1}{A_{H5} F_{H5,HP}} + \left[\frac{1}{A_{H5} F_{H5,TW}} + \frac{1}{A_{TW} F_{TW,HP}} \right]^{-1} + \frac{1 - \varepsilon_{HP}}{\varepsilon_{HP} A_{HP}}} \\
&+ \frac{E_{H6} - E_{HP}}{\frac{1 - \varepsilon_{H6}}{\varepsilon_{H6} A_{H6}} + \frac{1}{A_{H6} F_{H6,HP}} + \left[\frac{1}{A_{H6} F_{H6,W2}} + \frac{1}{A_{W2} F_{W2,HP}} \right]^{-1} + \left[\frac{1}{A_{H6} F_{H6,TW}} + \frac{1}{A_{TW} F_{TW,HP}} \right]^{-1} + \frac{1 - \varepsilon_{HP}}{\varepsilon_{HP} A_{HP}}}
\end{aligned} \tag{217}$$

The view factors for the modelling need to be determined. From the summation rule:

$$\begin{aligned}
F_{H1 \rightarrow H1} + F_{H1 \rightarrow H2} + F_{H1 \rightarrow H3} + F_{H1 \rightarrow H4} + F_{H1 \rightarrow H5} + F_{H1 \rightarrow H6} + F_{H1 \rightarrow w1} + F_{H1 \rightarrow w2} \\
+ F_{H1 \rightarrow tw} + F_{H1 \rightarrow HP} = 1
\end{aligned} \tag{218}$$

where $F_{H1 \rightarrow H1} = F_{H1 \rightarrow H2} = F_{H1 \rightarrow H3} = F_{H1 \rightarrow H4} = F_{H1 \rightarrow H5} = F_{H1 \rightarrow H6} = 0$

It can also be considered that $F_{H1 \rightarrow w2} = 0$ as the distance between region 1 and the opposite side wall is large compared to the dimensions of the region.

Then,

$$F_{H1 \rightarrow w1} + F_{H1 \rightarrow tw} + F_{H1 \rightarrow HP} = 1 \tag{219}$$

$$F_{H6 \rightarrow w2} + F_{H6 \rightarrow tw} + F_{H1 \rightarrow HP} = 1 \tag{220}$$

The views factor from the central regions of the kiln can be expressed as

$$\begin{aligned}
F_{H3 \rightarrow H1} + F_{H3 \rightarrow H2} + F_{H3 \rightarrow H3} + F_{H3 \rightarrow H4} + F_{H3 \rightarrow H5} + F_{H3 \rightarrow H6} + F_{H3 \rightarrow w1} + F_{H3 \rightarrow w2} \\
+ F_{H3 \rightarrow tw} + F_{H3 \rightarrow HP} = 1
\end{aligned} \tag{221}$$

where $F_{H3 \rightarrow H1} = F_{H3 \rightarrow H2} = F_{H3 \rightarrow H3} = F_{H3 \rightarrow H4} = F_{H3 \rightarrow H5} = F_{H3 \rightarrow H6} = 0$

The impacts of the side walls on the central regions are neglected as the distance from the regions to the side wall is large compare to the position and the dimensions of the regions.

$$F_{H3 \rightarrow tw} + F_{H4 \rightarrow HP} = 1 \quad (222)$$

$$F_{H4 \rightarrow tw} + F_{H4 \rightarrow HP} = 1 \quad (223)$$

$$F_{H5 \rightarrow tw} + F_{H5 \rightarrow HP} = 1 \quad (224)$$

$$F_{H6 \rightarrow tw} + F_{H6 \rightarrow HP} = 1 \quad (225)$$

$F_{Hn \rightarrow HP}$, where n is the region number can be determined using (74) and (75). No correlations for the view factor using a tube with an angle exist in the literature. It was assumed that the tube was horizontal. As used in the single and multi-module section, the surface of the pipe was considered to be a flat surface with finite dimensions over a finite plate. The view factor was calculated tube by tube as the heat pipe ceiling has a varying tube spacing distance.

4.5.3 Conduction heat transfer

Conduction heat transfer occurs between the outer and inner walls of the heat pipe for the evaporator and the condenser sections.

The heat transfer by conduction for the evaporator section can be calculated as,

$$Q_{cond,e} = \frac{T_{eo} - T_{ei}}{R_{cond,e}} \quad (226)$$

The thermal resistance can be obtained from,

$$R_{cond,e} = \frac{\ln\left(\frac{D_{eo}}{D_{ei}}\right)}{2\pi l_e k_s} \quad (227)$$

where k_s is the thermal conductivity depending on the shell case material of the heat pipe.

The heat transfer for the condenser section is calculated by,

$$Q_{cond,c} = \frac{T_{co} - T_{ci}}{R_{cond,c}} \quad (228)$$

The thermal resistance can be obtained from,

$$R_{cond,c} = \frac{\ln\left(\frac{D_{co}}{D_{ci}}\right)}{2\pi l_c k_s} \quad (229)$$

4.5.4 Natural convection

The natural convection resistance is calculated using the following equation,

$$R_{N.convection} = \frac{1}{h_{N.convection} A_{eo}} \quad (230)$$

where $h_{N.convection}$ is calculated using the correlations (25)-(33),

The impact of the natural convection on the heat pipe ceiling can be neglected as the contribution of radiation and forced convection will be larger.

4.5.5 External forced convection

A hot air flow was applied in the kiln to cool down the tiles. The impact of the forced convection on the tube must be included in the thermal model. The forced convection is represented in Figure 108

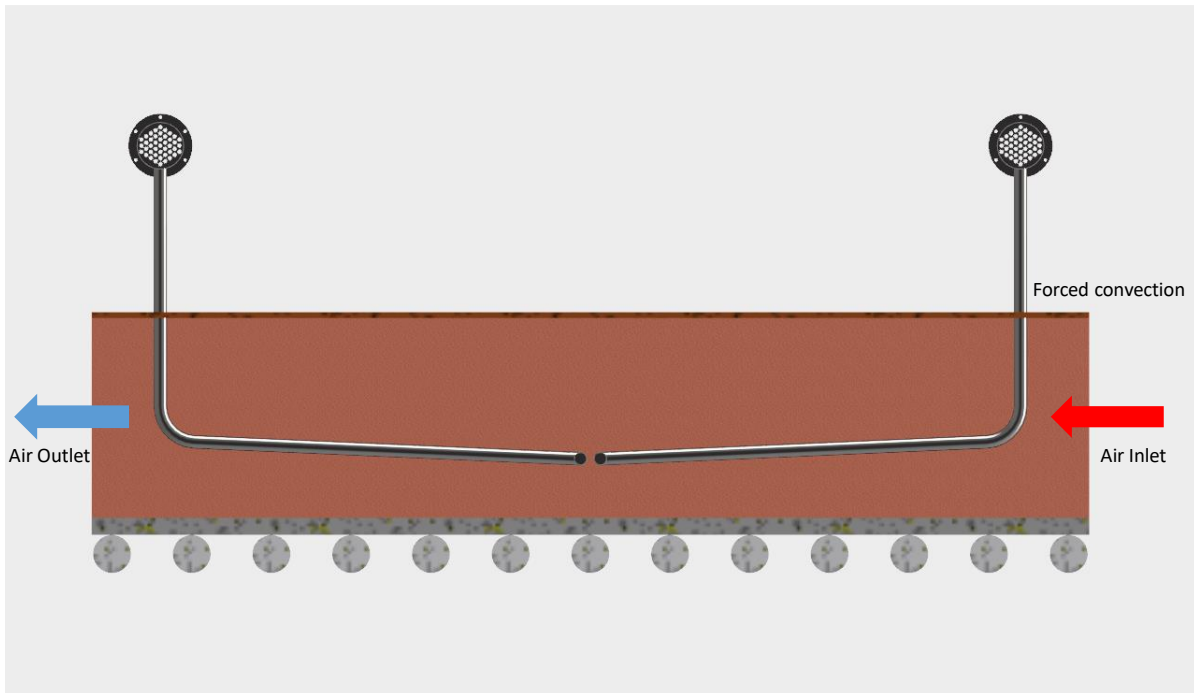


Figure 108 External forced convection

The external forced convection can be considered in two distinct regions. Region 1 is considered to be external forced convection over a plate as the air direction and the tubes are parallel. In the second region, the air direction and the tube are perpendicular. In this region, different correlations to determine the heat transfer coefficient will be used.

4.5.5.1 Forced convection over a plate.

The heat transfer of external forced convection over a plate can be calculated as,

$$Q_{F,conv,p} = \frac{T_s - T_f}{R_{F,Conv,p}} \quad (231)$$

where,

$$R_{F,Conv,p} = \frac{1}{h_{F,Conv,p} A_e} \quad (232)$$

The heat transfer coefficient for forced convection over a plate can be calculated as,

$$h_{F,Conv,p} = \frac{Nu \cdot k}{L} \quad (233)$$

where L is the longitudinal length of the forced convection section and k is the thermal conductivity of the fluid. The Nusselt number can be calculated using (161) and (162).

4.5.5.2 Forced convection across tubes row

The heat transfer of external forced convection of a row of n tubes.

$$Q_{F,conv,tr} = n \times \frac{T_{air} - T_{eo}}{R_{F,Conv,tr}} \quad (234)$$

where

$$R_{F,Conv,tr} = \frac{1}{h_{F,Conv,tr} A_{tr}} \quad (235)$$

The heat transfer coefficient for external forced convection of a row of n tubes.

$$h_{F,Conv,tr} = \frac{Nu}{k \cdot D} \quad (236)$$

where D is the diameter of the cylinder and k is the thermal conductivity of the fluid. The Nusselt number can be calculated using (166).

4.5.6 Boiling heat transfer

The heat transfer for the nucleate pool boiling can be expressed as,

$$Q_{boil,Nucleate} = \frac{T_{ei} - T_v}{R_{bi,nucleate}} \quad (237)$$

where,

$$R_{Bi,nucleate} = \frac{1}{h_{Bi,nucleate} A_{ei,nucleate}} \quad (238)$$

The heat transfer coefficient for nucleate pool boiling can be determined using Table 18,

4.5.7 Condensation heat transfer

The heat transfer rate by condensation is represented as follows,

$$Q_{co} = \frac{(T_v - T_{co})}{R_{co}} \quad (239)$$

where,

T_v : Vapour temperature (K)

T_{co} : Temperature of outer surface of the inner tubes

R_{co} : Thermal resistance of heat transfer by condensation

$$R_{co} = \frac{1}{h_{co} \cdot A_{co}}$$

A_{co} : Heat pipe condenser area which represents the overall external surface area of the horizontal tubes in the condenser section (m²).

$$A_{co} = \pi \times D_{co} \times L_c \times N_{water\ tube} \quad (240)$$

D_{co} : Condenser outer diameter (m)

L_c : Condenser length (m)

$N_{water\ tube}$: Number of water tubes

h_{co} : Condensation heat transfer coefficient (W/m².K)

The heat transfer coefficient for condensation can be calculated using correlations (208) to (211).

Internal forced convection

The heat transfer by forced convection in the condenser section can be determined by,

$$Q_{F.convection} = h_{F.convection} \cdot A_{con,total} \cdot \frac{[(T_v - T_{in}) - (T_v - T_{out})]}{\ln\left(\frac{(T_v - T_{in})}{(T_v - T_{out})}\right)} \quad (241)$$

Thus, the following can be obtained,

$$Q_{F.convection} = h_{F.convection} \cdot A_{con,total} \cdot \frac{(T_{out} - T_{in})}{\ln\left(\frac{(T_v - T_{in})}{(T_v - T_{out})}\right)} \quad (242)$$

The heat transfer coefficient of forced convection can be calculated using the correlations in Table 21.

4.6 Theoretical modelling tool

In order to simulate and predict the behaviour of the radiative heat pipe ceiling, a theoretical model was developed using VBA coding. A program was designed using correlations selected from experimental analysis, the correlations were then used in iteration and loop processes until an energy balance is achieved between the heat absorbed by the heat pipe and the heat transferred to the heat sink fluid. As the temperature changes in the loops and iterations, the properties of the fluids such as density, specific heat, will change. In order to simplify the design of the modelling tool, the values were calculated at the working fluid temperature and the average temperature of the heat sink fluid. The tool was used in the single radiative heat

pipe, the modules heat pipe and the full-scale system. The Flow chart is presented in Figure 109.

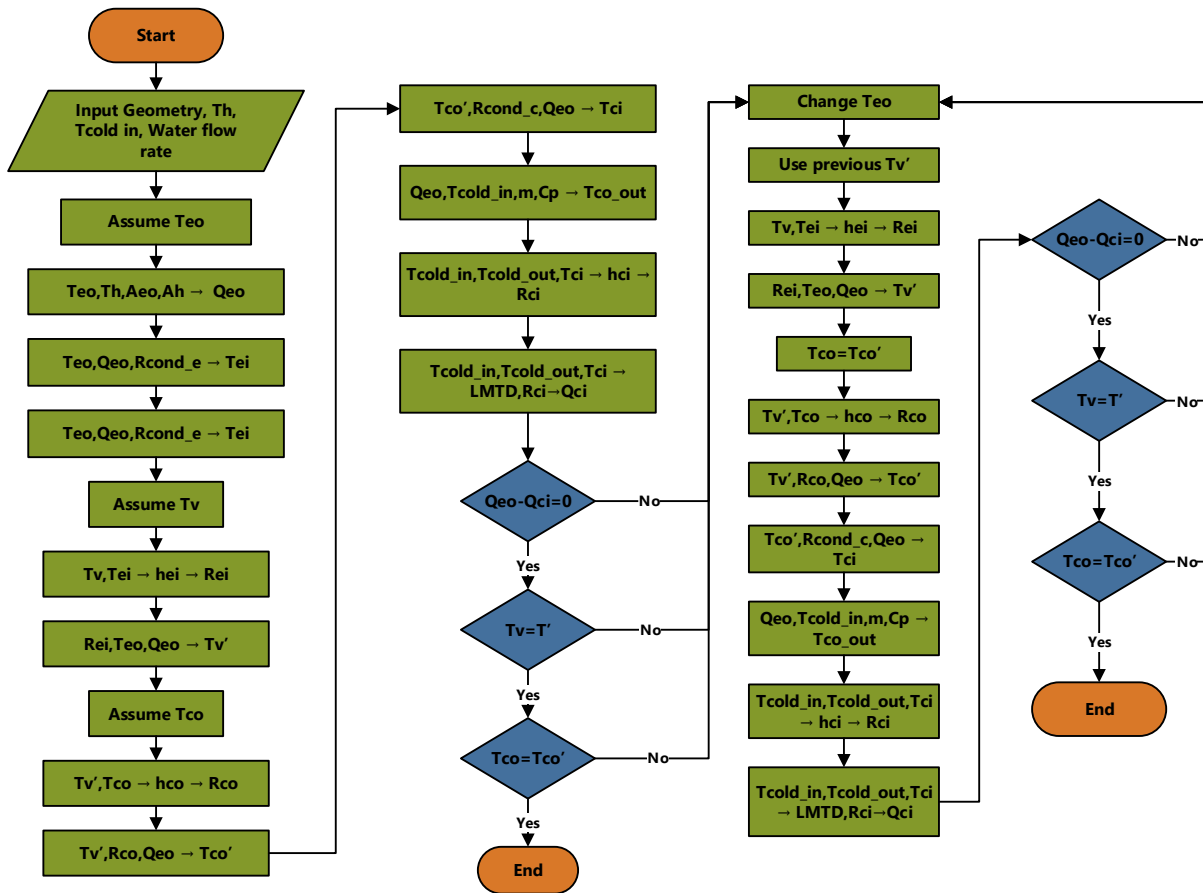


Figure 109 Heat pipe theoretical model tool

The correlations used in the thermal design tools were selected after a comparison in accuracy between the experimental and theoretical calculations at different conditions. In order to achieve an accurate thermal design modelling, an extensive analysis of the correlations had to be carried out. The selected correlations can then be used in the modelling tool and theoretical results compared with experimental results.

Chapter 5: Data reduction

5.1 Introduction

Data extracted from logging system need to be reduced in order to be suitable for a deep results analysis of the different tests. Comparing data to theoretical results can be extensive, in order to achieve an accurate comparison between experimental and theoretical results, a data reduction to the thermal resistance of boiling, condensation, conduction, forced convection and radiation was carried out. This reduction will simplify the results exploitation. The data relative to the testing was collected and sorted to reflect a steady state for all the testing conditions. In some cases, the steady state for the heat pipe was difficult to identify due to instability in the logging and the occurrence of geyser boiling for low heat transfer coefficient cases. To use data as close as possible for the results section, a data reduction study was carried out. The aim of the data reduction is to reduce the data to thermal resistance. This data will then be used to compare the potential of different correlation that could be used in the modelling tool and their respective errors.

5.2 Power input

The power input for the steady state was measured using a voltmeter and an amp meter using the following equation:

$$P = V.I \quad (243)$$

The heating source was not constant as the PID system was switching on and off to match the target temperatures. The heat input can only be determined by identifying the amount of time the heater was off or on and use the ratio to calculate an approximate value of heat input in the system.

5.3 Heat transfer rate

The heat transfer rate was measured using the reading of the flow and the temperature at the inlet and outlet of the condenser section.

$$Q_{recovery} = m_{water}C_{p,water}(T_{w,out} - T_{w,in}) \quad (244)$$

5.4 Equivalent radiation thermal resistance

The equivalent radiation thermal resistance will depend on the surface's temperature and the view factor between the different surfaces of the enclosure. The wall are considered to be well insulated, it is assume that no heat loss to the ambient occur and the walls does not interact with the air in the kiln, the thermal radiation will depend on the temperature of the heater and the heat pipe and on the view factor between the two surfaces. The equivalent thermal radiation resistance can be determined by

$$R_{rad,eq} = \frac{T_H - T_{eo}}{Q_{rad}} \quad (245)$$

Where Q_{rad} is calculated from the overall heat pipe heat transfer rate at the coolant and the natural convection heat transfer rate.

$$Q_{rad} = Q_{recovery} - Q_{N.convection} \quad (246)$$

Where the heat transfer rate by natural convection is calculated using A_{eo} the external evaporator surface area, T_{air} the temperature of the air, T_{eo} average temperature of the heat pipe evaporator section and a heat transfer coefficient calculated through correlations available in the literature.

$$Q_{N.convection} = h_{N.convection} \cdot A_{eo} (T_{air} - T_{eo}) \quad (247)$$

5.5 Radiation space resistance.

The radiation space resistance was calculated experimentally by determining the radiation heat transfer rate and the emissivity of the heat pipe and the heater.

$$R_{space,eq} = \frac{\sigma(T_H^4 - T_{eo}^4)}{Q_{rad}} - \frac{1 - \varepsilon_{HP}}{\varepsilon_{HP} A_{HP}} - \frac{1 - \varepsilon_H}{\varepsilon_H A_H} \quad (248)$$

5.6 Conduction thermal resistance at the evaporator section

The conduction thermal resistance at the evaporator section can be expressed as:

$$R_{cond,e} = \frac{\ln\left(\frac{D_{eo}}{D_{ei}}\right)}{2\pi l_e k_s} \quad (249)$$

Where l_e is the length of the evaporator section, as the evaporator section changed with the different filling ratios, the length of the evaporator need to be modified for each test to reflect the actual length of the evaporator section.

5.7 Conduction thermal resistance at the condenser section

The conduction thermal resistance at the evaporator section was calculated using:

$$R_{cond,c} = \frac{\ln\left(\frac{D_{co}}{D_{ci}}\right)}{2\pi l_c k_s} \quad (250)$$

5.8 Overall conductance of the condenser

The overall conductance of the condenser section heat exchanger was determined by the UA value using the measured heat transfer rate, the temperature at the inlet and outlet of the condenser heat exchanger and the vapour temperature. The UA value can be expressed as:

$$UA = \frac{\left(\frac{(T_v - T_{cold,in}) - (T_v - T_{cold,out})}{\ln \left(\frac{T_v - T_{cold,out}}{T_v - T_{cold,in}} \right)} \right)}{Q_{recovery}} \quad (251)$$

5.9 Average evaporator temperature

The average temperature at the evaporator section was determined by the arithmetic average of the thermocouples located at the evaporator pool. As the filling ratio changed over the tests, the number of thermocouples included in the average evaporator average temperature will change. The average evaporator temperature can be calculated by:

$$T_{eo} = \frac{T_{e1} + \dots + T_{en}}{n} \quad (252)$$

where n is the number of thermocouples located at pool level.

5.10 Two phase thermal resistances.

5.10.1 Boiling thermal resistance

The boiling thermal resistance can be determined using the following equation:

$$R_{ei,average} = \frac{T_{ei} - T_v}{Q_{recovery}} \quad (253)$$

Where T_{ei} is determined by the external average evaporator temperature, the conduction thermal resistance at the evaporator section and the heat transfer rate.

5.10.2 Condensation thermal resistance

The condensation thermal resistance is calculated from the following equation:

$$R_{condensation} = \frac{T_v - T_{ci}}{Q_{recovery}} \quad (254)$$

As no thermocouple could be place on the condensation surface, T_{ci} was calculated from the following equation:

$$T_{ci} = T_{co} + Q_{recovery} \cdot R_{cond,c} \quad (255)$$

Where T_{co} was determined by

$$T_{co} = \frac{T_{out,water} - T_{in,water} \cdot e^{\left(\frac{T_{out,water} - T_{in,water}}{Q_{recovery} R_{co}} \right)}}{1 - e^{\left(\frac{T_{out,water} - T_{in,water}}{Q_{recovery} R_{co}} \right)}} \quad (256)$$

For R_{co} as the forced convection thermal resistance at the outer wall of the condenser section

5.11 Forced convection thermal resistance

The forced convection thermal resistance of the condenser was determined by:

$$R_{co} = \frac{1}{h_{co}A_{co,total}} \quad (257)$$

h_{co} is the heat transfer coefficient for forced convection (W/m²) and A_{co} is the overall surface area of the finned water jacket:

$$A_{co,total} = A_{co} + \eta A_{co, fins} \quad (258)$$

The heat transfer coefficient was determined using Hausen [105].

5.12 Boiling Heat flux

The experimental boiling heat flux was calculated using

$$q''_{Bi} = \frac{Q_{recovery}}{A_{evaporator}} \quad (259)$$

where $Q_{recovery}$ is the heat transfer rate at the coolant and $A_{evaporator}$ is the interface surface area between the pool and the internal evaporator surface, depending on the filling ratio of the Heat pipe.

Chapter 6: Results and discussion

6.1 Introduction

The data gathered during the testing of the different modules and the single heat pipe were compared with the thermal model developed in the chapter 4. The validation of the modelling was necessary to develop a model that could be used in the industrial application.

The first part of this section will be dedicated to the testing of the single heat pipe in a kiln at steady state. The different phenomena such as geyser boiling, evaporator dry out, filling ratio and impact of the view factor on the heat recovery will also be discussed. The thermal resistances were also determined and plotted against the different heat fluxes. Correlations available in the literature were used to predict the different thermal resistances and plotted to determine the accuracy for different heat fluxes and filling ratios. The radiation resistance was also assessed to validate the view factor used in the modelling tool.

The second part of the chapter will focus on the tests carried out for the radiative heat pipe module configuration with different evaporator section sizes. The heat transfer rate for three evaporator surface areas will be discussed. The impact of the evaporator section on the thermal resistances will also be determined. The correlations used in the single heat pipe will be used to predict the boiling thermal resistance at the evaporator section. The impact of the heat pipe filling ratio on the boiling thermal resistance will also be discussed. As the design of the condenser section changed, different correlations available in the literature and developed during this thesis will be used to predict the condenser thermal resistance. The impact of the heat pipe filling ratio on the boiling thermal resistance will also be discussed.

The last section of the chapter will focus on the development of the full-scale model using the conclusions of the previous sections. A theoretical model will be designed and applied to the current kiln section to prove the use of a modular heat pipe evaporator section to provide a uniform tile temperature during the cooling process.

6.2 Single heat pipe results and discussion

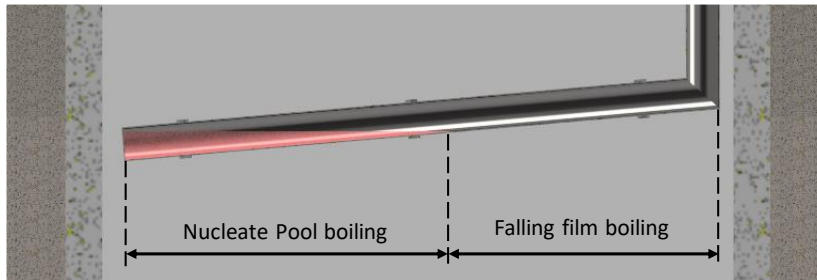
This section will cover the results from the testing of the single heat pipe for a temperature ranging from 200 °C to 500 °C at various flow rates. The geometry of the system and the overall set up of the experiment did not change between the different test sessions. Many phenomena occurred during the testing of the system as the arrangement and the design of the system was not optimal. Tests were carried out to define the impact of the filling ratio on a near horizontal evaporator section.

6.2.1 Single pipe experimental results

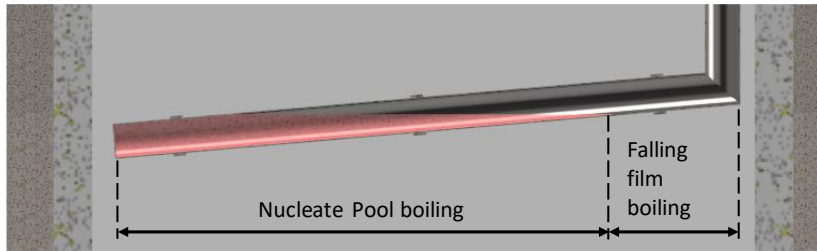
Filling ratio is defined as the percentage of working fluid in the overall volume of the evaporator section. The filling ratio will impact on the type of boiling occurring at the evaporator section, thus, the boiling heat transfer coefficient. If the filling ratio is too low in the evaporator section, dry out will occur and block the heat pipe. On the contrary, if the filling ratio is too high, the vapour generated by the evaporator section will struggle to reach the condenser section.

The single radiative heat pipe was tested for four filling ratios, 25%, 50%, 75% and 100 %, and exposed to temperatures ranging from 200 °C to 500 °C. A schematic of the filling ratios for the four different conditions can be seen in Figure 110.

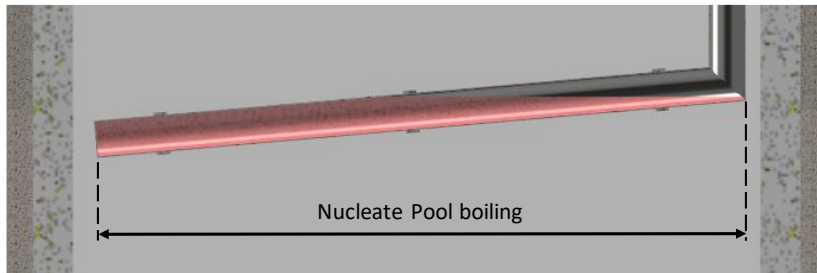
25% Filling ratio



50% Filling ratio



75% Filling ratio



100% Filling ratio

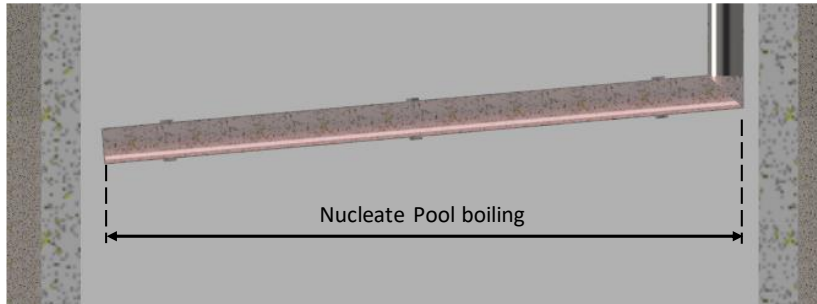


Figure 110 Filling ratio in single heat pipe

6.2.1.1 Impact of the filling ratio on the single heat pipe temperature

The tests carried out on the single heat pipe system highlighted the impact of the filling ratio on the heat pipe temperatures and the variation of the temperatures across the heat pipe. The temperature of the heat pipe was measured at four evaporator heat fluxes. The results can be seen in Figure 111.

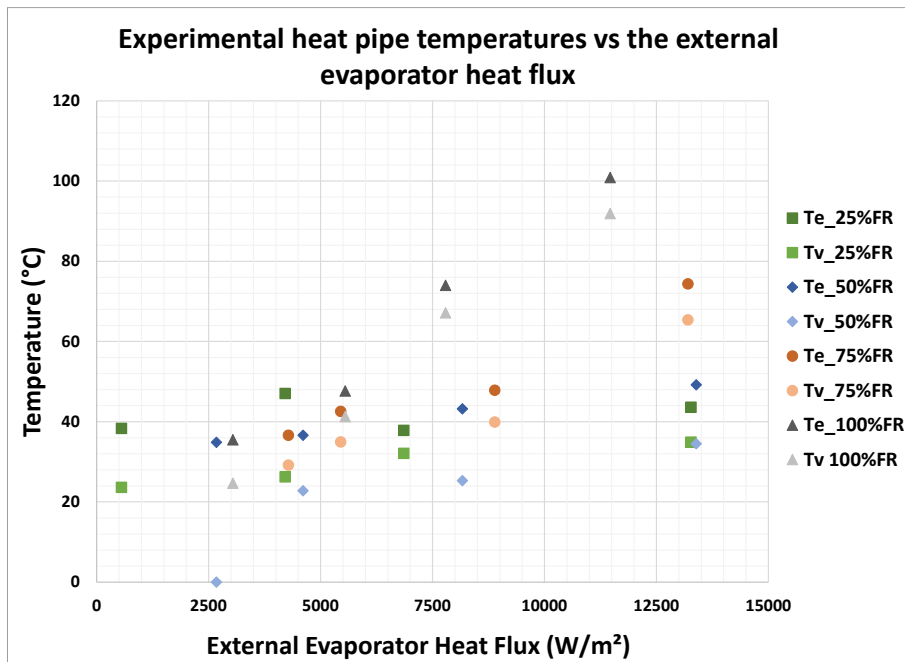


Figure 111 Experimental Evaporator temperature of the single heat pipe against the external evaporator heat flux

The temperature at the evaporator section exposed to the heat source increases as the heat flux at the evaporator section increases. It can be noted that the temperature of the evaporator for a filling ratio of 25% remains stable. In the case of a filling ratio of 50%, the evaporator temperature increased from a minimum of 34.9 °C at a heat flux of 2.7 kW/m². The increase in the evaporator temperature can be seen for a filling ratio of 100%, the minimum evaporator temperature is observed at a heat flux of 3 kW/m² for a temperature of 35.5 °C, the maximum temperature is reached at 100.9 °C for a heat flux of 11.5 kW/m².

The evaporator temperature is calculated using the average of all the thermocouples placed on the outer surface. However, the temperature distribution is not uniform for all the tests.

It can be noticed from Figure 112 that the temperatures of the heat pipe evaporator section at 25%FR was varying from 27.2 °C to a maximum of 46.7 °C for a heat flux of 0.55 kW/m². In the case of a filling ratio from 50% to 100%, the difference between the maximum and minimum temperatures was lower; for 50%, the temperatures in the evaporator section was varying from 27 °C to a maximum of 37.8 °C for a heat flux of 2.6 kW/m², for 75% the maximum evaporator temperature was 39.3°C with a minimum of 33.2 °C for a heat flux of 4.3 kW/m², for 100%, the maximum temperature for the evaporator was 38.8 °C with a minimum of 31.0 °C for a heat flux of 3.3 kW/m².

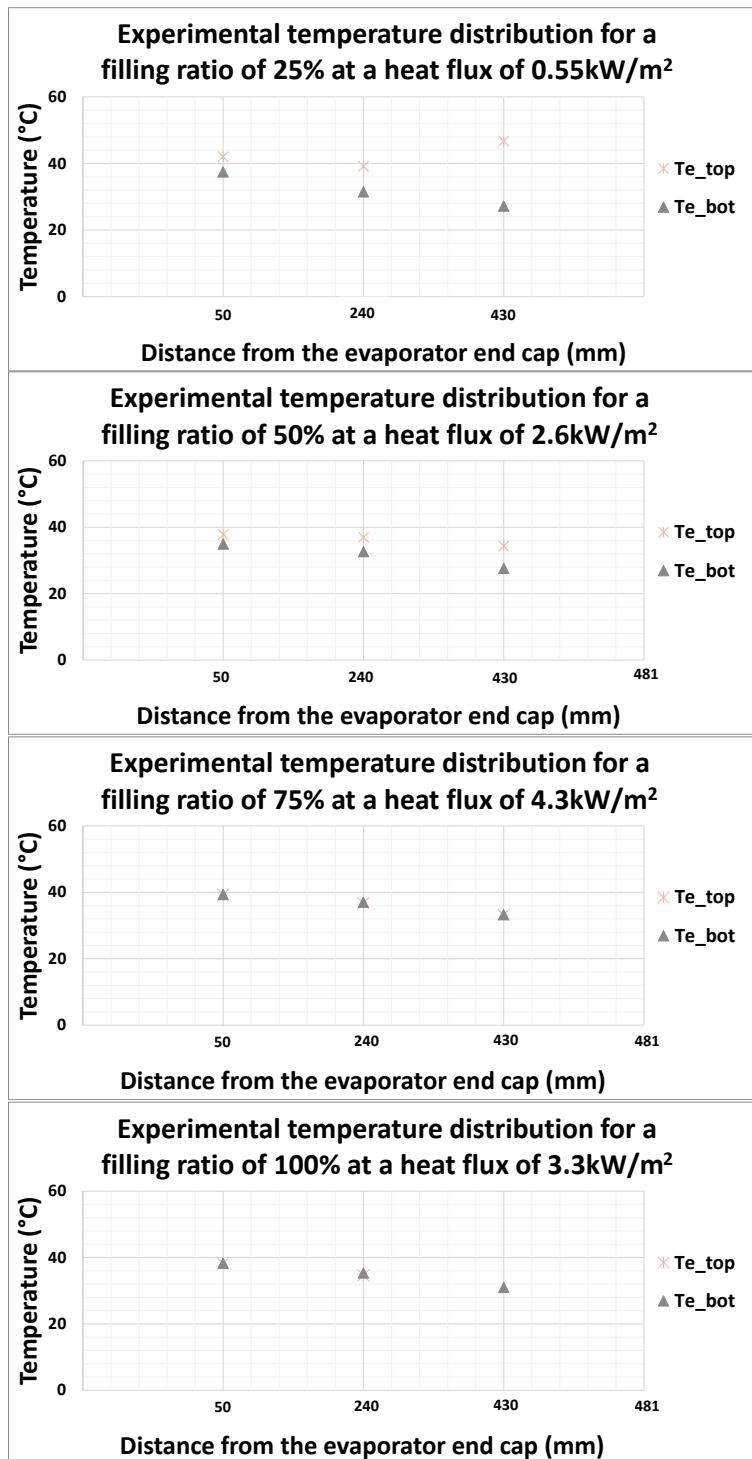


Figure 112 Temperature distribution at the evaporator section for low heat flux $< 4.5 \text{ W/m}^2$

It can be noted from the results that the temperature difference in the evaporator is larger in the case of a low filling ratio than for filling ratios higher than 50%. The variation in the evaporator section at low temperature can be explained by the geyser boiling phenomenon occurring in the heat pipe. Geyser boiling occurs when the heat input in the system is not sufficient to have steady nucleate boiling at the evaporator section. The temperatures of the working fluid in the evaporator section will increase in temperature and a vapour bubble will

be generated at some point of the evaporator section. As the bubble grows, its dimension will reach the diameter of the pipe. The vapour in the evaporator section will then propel the liquid in the evaporator section to the condenser end cap. Once the liquid reaches the end cap of the condenser, the vapour bubble will collapse. The liquid will then fall back to the evaporator, being subcooled by the condenser section. The liquid is then superheated again and the geyser boiling phenomenon starts again. This phenomenon can be observed in Figure 113.

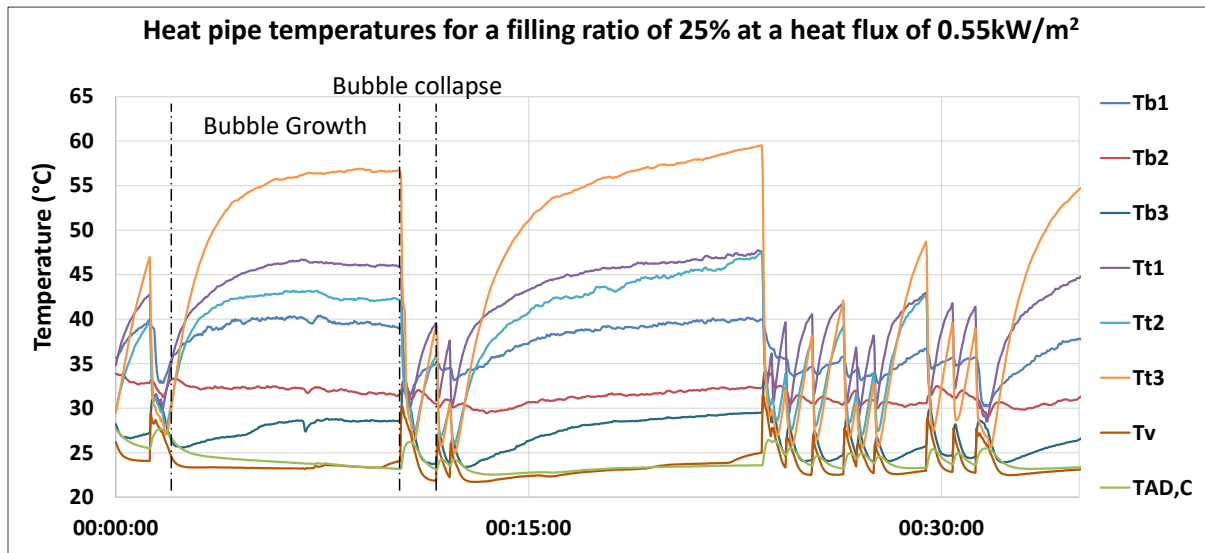


Figure 113 Geyser Boiling at 25% FR and 200°C heat source

The heat flux applied to the evaporator section was 0.55 kW/m² with a filling ratio of 25%. The temperature of the heat pipe evaporator increases as the bubble grows in the pipe. When the critical size of the bubble is reached, the bubble will travel to the condenser with the working fluid. T_v will increase while the temperature of the evaporator section will drop.

A similar test was conducted at a higher heater temperature.

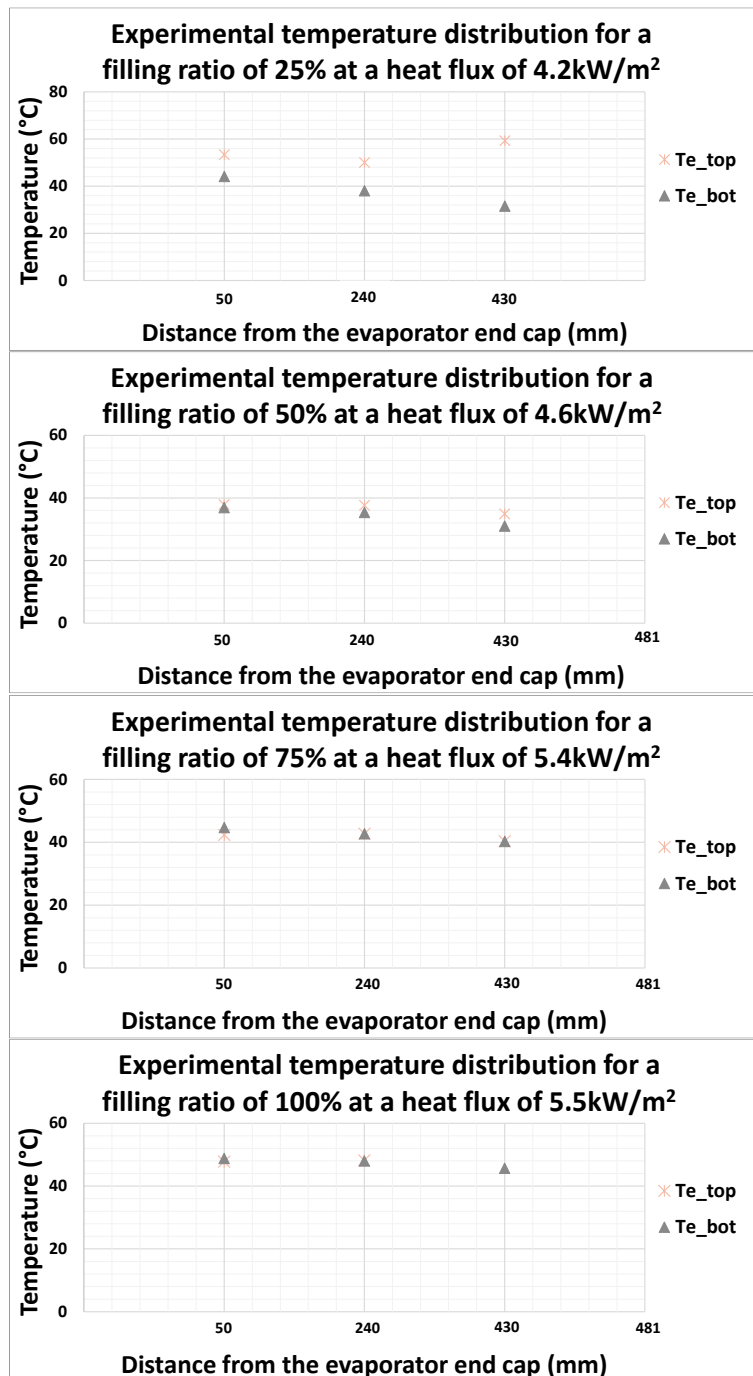


Figure 114 Experimental temperatures of the single heat pipe for heat flux between 4.2 kW/m² and 5.5 kW/m²

The results of the tests demonstrated in Figure 114 present four different sets of data. For a filling ratio above 50% of the evaporator volume, the geyser boiling is limited. The temperature of the heat pipe at 25% FR varied between 53.4 °C to 27.8 °C for a heat flux of 4.2 kW/m², for 50% FR the temperature varied from 37.6 °C to 31.0 °C for a heat flux of 4.6 kW/m², for 75% FR the temperature varied from 44.7 °C to 40.2 °C for a heat flux of 5.4 kW/m² and for 100% FR, the temperature of the heat pipe evaporator section varied from 48.8 °C to 45.7 °C for a heat flux of 5.5 kW/m². It can be determined from this test that the geyser boiling tends to

disappear as the filling ratio in the evaporator section and the heat flux increase. *Khazaei et al* [111] investigated the behaviour of geyser boiling under different conditions: the filling ratio, the heat load on the evaporator, the aspect ratio, and the coolant flow rate. In this study, the impact of the filling ratio on a vertical heat pipe was discussed, the geyser boiling tends to disappear when the filling ratio becomes less than 30% of the evaporator volume. This contradicts the results obtained during the test of the single heat pipe. The impact on geyser boiling of the amount of working fluid in a near horizontal heat pipe is not following the current state of the art on geyser boiling for a vertical heat pipe. In a near horizontal configuration, the behaviour of the bubble will differ from those in the vertical set up. The applied heat on the single heat pipe will uniformly heat the entirety of the heat pipe evaporator section. At low filling ratio, the superheated area is larger than at higher filling ratio. thus, the concentration of the heat flux on a small area will speed the generation of vapour. The bubble growth will be quicker and cover the entirety of the heat pipe cross section, thus resulting in geyser boiling. At higher filling ratio, the bubble generation along the pipe will be more uniform at similar heat flux. The geyser boiling will be limited. Comparing to the experimental investigation done by *Khazaei et al*, the

The behaviour of the bubble growth was investigated by *Jouhara et al* [112] as shown in Figure 115. Experimental tests were done using a glass heat pipe and compared to a three-dimensional simulation. The growth of the bubble can be clearly defined by the study. In the case of a vertical heat pipe, the bubble will have to cover only the diameter of the pipe.

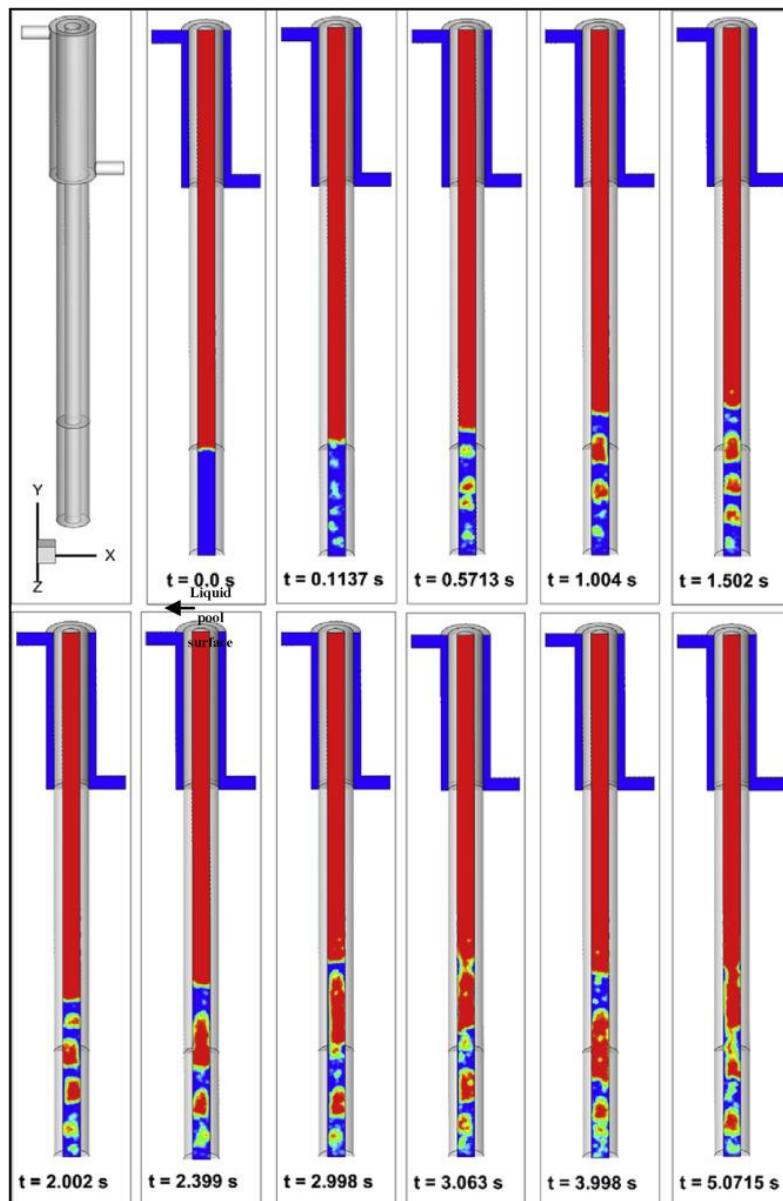


Figure 115 Geyser boiling occurrence in a heat pipe [112]

In the case of a near horizontal heat pipe, the vapour bubble will have to cover more area to block the flow of working fluid in the evaporator section. The temperature distribution across the evaporator will then differ from that in a vertical heat pipe. *Alammar et al* [112] experimentally investigated the influence of the geyser boiling phenomenon on the thermal performance of a thermosiphon for varying filling ratios, angles, and heat loads. It was observed that the temperature distribution across the evaporator section shows a large difference with a filling ratio of 25%. This is due to the location of the liquid pool in the evaporator section and the falling film from the condensed working fluid. As the filling ratio increases, there is a clear reduction in the temperature difference in the evaporator section for low heat flux. For a high heat flux, the temperature at the upper section of the evaporator will be higher than at the bottom due to the presence of falling film boiling. In the case of an

inclination angle of 10° , the difference in temperature will be lower as the pool of liquid is covering more surface, thus reducing the impact of the falling film on the evaporator temperature. The test was limited by the location of the thermocouples as only one thermocouple was placed at each level. The thermocouples for the single heat pipe were placed at the top and the bottom of the evaporator section at three levels. It can be seen from Figure 114 that the temperature at the thermocouple placed at the upper section of the single heat pipe during geyser boiling tends to be higher than at the bottom thermocouple due to the wall being superheated at the upper section of the heat pipe not exposed to the liquid pool. In the case of a filling ratio of 25%, the temperatures of the heat pipe clearly show the behaviour of the heat pipe with a near horizontal configuration. The temperature at thermocouple Tb3 located at the pool level below the heat pipe is higher than that for the thermocouple on top of the heat pipe at the same level, also located in the pool. The difference in temperature can be explained by the direction of the radiative heat toward the evaporator. As the heater is located below the heat pipe, the heat flux at the bottom section of the heat pipe will be higher than at the top. At mid-level, Tb2 will be at a lower temperature than Tt2 as the thermocouple is in the falling film, Tt2 is mainly exposed to vapour generated by the liquid pool, and the steam is also superheated by the heat pipe wall not exposed to any working fluid. At the highest level of the heat pipe, the steam will still be superheated by the wall. Tb1 is directly exposed to the subcooled liquid from the condenser section. It can be noted that the temperature of Tb1 is lower than Tb2. As the pool surface is below the location of Tb2, the area is subjected to film boiling.

Similarly, Figure 116 shows a good temperature uniformity at the evaporator section, the overall temperature of the heat pipe is also higher for higher filling ratios. Heat pipes using water as a working fluid can be limited in their applications for high temperatures. As the temperature in the heat pipe increases, the pressure in the vessel will also increase, reaching a critical limit where the shell cannot contain the pressure. In order to reduce this risk, the temperature of the water heat pipe should not reach a high temperature. It can be seen for this test that the higher the filling ratio is, the higher the temperature. It can be a limiting factor for the design of the module. For a filling ratio of 100%, the maximum temperature of the evaporator was 102.0°C and a minimum of 99.1°C at a heat flux of 11.5 kW/m^2 . For a filling ratio of 75% the temperature was lower with a maximum of 75.5°C and a minimum of 71.0°C at a heat flux of 13.2 kW/m^2 . In the case of a filling ratio at 50% the minimum and the maximum temperatures were respectively 43.7°C and 50.1°C at a heat flux of 13.4 kW/m^2 . At a filling ratio of 25% the evaporator minimum temperature was 38.5°C and a maximum of 46.1°C at a heat flux of 13.7 kW/m^2 .

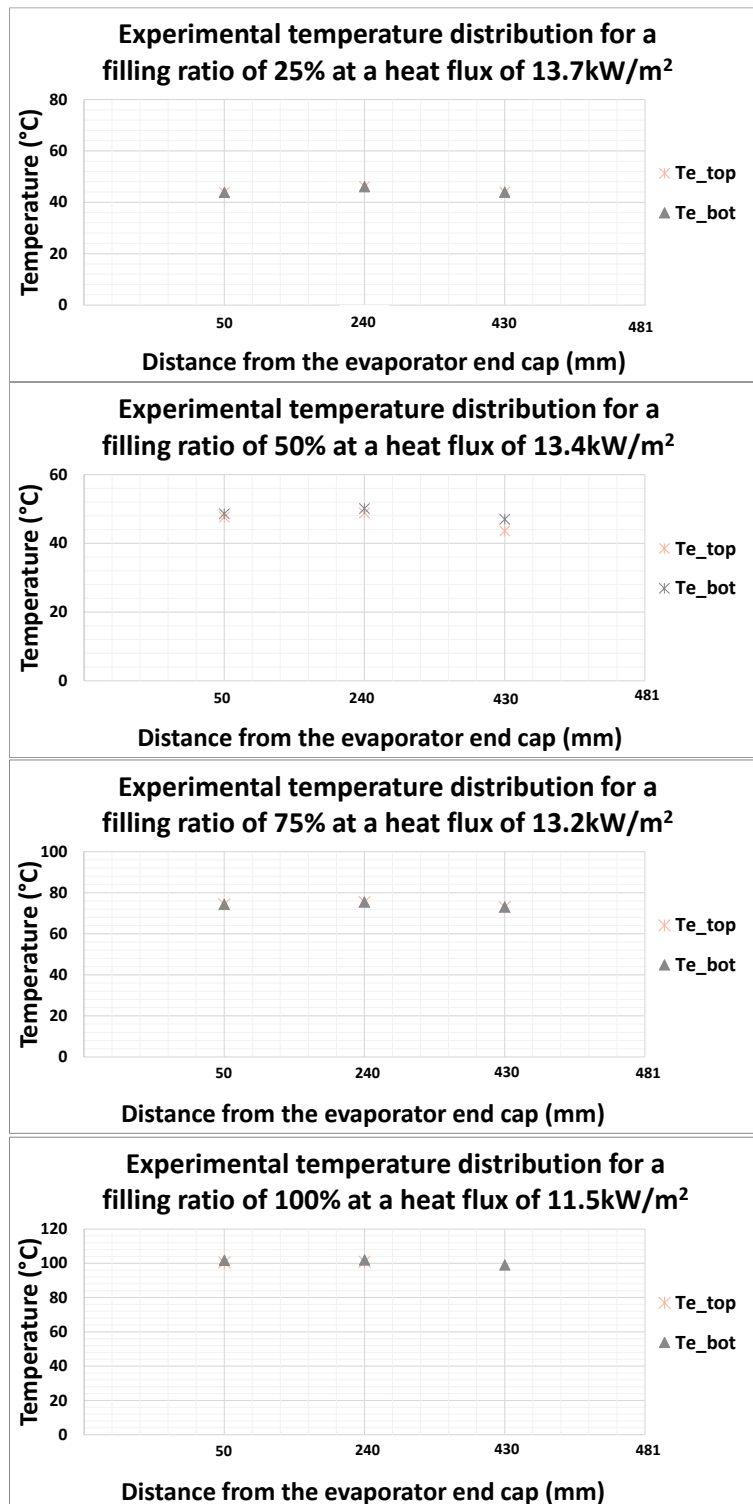


Figure 116 Experimental temperatures of the single heat pipe at heat flux > 11 kW/m²

The temperature distribution, the impact of geyser boiling, and the temperature of the heat pipe will have a major impact on the overall thermal performance of the heat pipe in a full-scale setting. It can be concluded from the results above that for a near horizontal heat pipe evaporator section, the best case of filling ratio regarding the geyser boiling is for a filling ratio of 75% and above. At low heat flux, geyser boiling will still occur, but it is limited when

compared to filling ratios lower than 75%. The temperature distribution can also be concluded to be better for filling ratios of 75% and above. This is mainly due to the occurrence of geyser boiling for low filling ratios. The temperature of the heat pipe will also be a major limiting factor in the potential application of the system for higher heat fluxes. It can be noted that the filling ratio of 100% is not suitable as it tends to significantly increase the temperature of the heat pipe. The best-case scenario for minimising temperatures in the heat pipe evaporator section was for a heat pipe filling ratio of 50% and below. The filling ratio of 75%, in regard to the heat pipe temperatures uniformity and to avoid occurrence of geyser boiling was the best-case scenario.

In the boiling regime, the temperature difference between the internal surface of the heat pipe and the vapour needs to be determined as it is considered a function of the heat flux. The temperature difference is usually referred as the excess temperature. To investigate the excess temperature, it will need to be evaluated at the boiling heat flux. The boiling heat flux corresponds to the local heat flux at the interface between the internal wall of the heat pipe and the pool. As the filling ratio changes over the different tests, the surface area considered for the boiling heat flux will also change. The surface area considered for each test point was calculated. The excess temperature against the heat flux for each filling ratio is plotted in Figure 117.

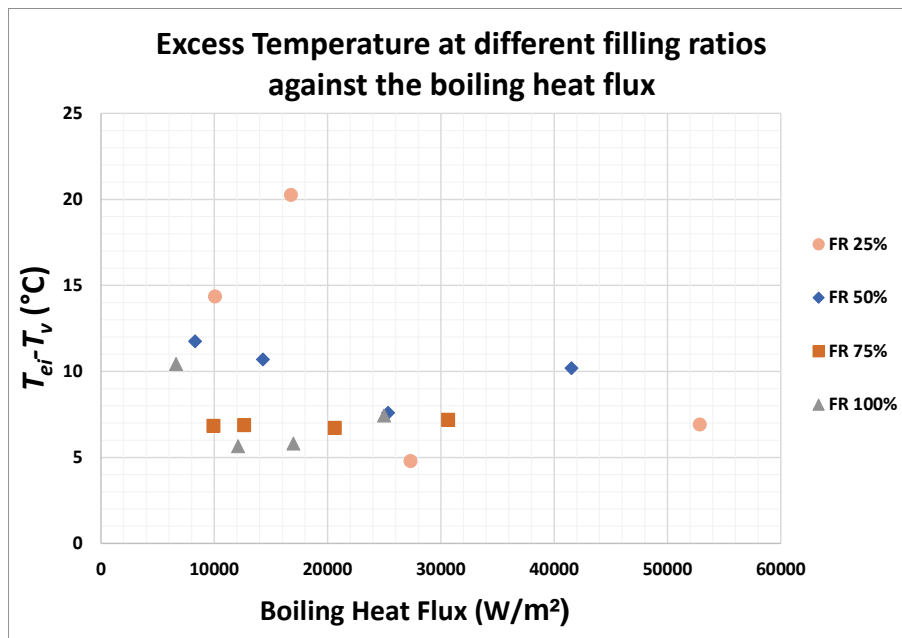


Figure 117 Excess temperature for various filling ratios

It can be seen that for heat fluxes below 20 kW/m² that the excess temperature is above 10 °C for a filling ratio of 50% and 25%. This is mainly due to the geyser boiling occurring at lower heat fluxes and low filling ratios. It can also be noted that for a filling ratio of 100%, if the heat

flux is lower than 10 kW/m^2 , the excess temperature is also above $10 \text{ }^\circ\text{C}$ due to the limitation in the bubble growth at high filling ratio. In the case of a filling ratio of 75%, the excess temperature did not exceed the value of $7 \text{ }^\circ\text{C}$. It can be concluded that for heat fluxes below 20 kW/m^2 , the excess temperature was higher apart from the case of a filling ratio of 75% where the excess heat is not strongly impacted by the boiling heat flux.

6.2.1.2 Influence of the filling ratio on the heat pipe thermal resistances

Boiling thermal resistance

The thermal resistances will have an impact on the heat pipe temperature and the heat recovered by the system. Heat pipe systems are usually considered as super conductors as the thermal resistances of those systems are usually lower than for other heat transfer devices. To achieve the best thermal performance possible, the overall thermal resistances need to be as low as possible. Thermal resistances for boiling and condensation were calculated based on the tests carried out for the different filling ratios.

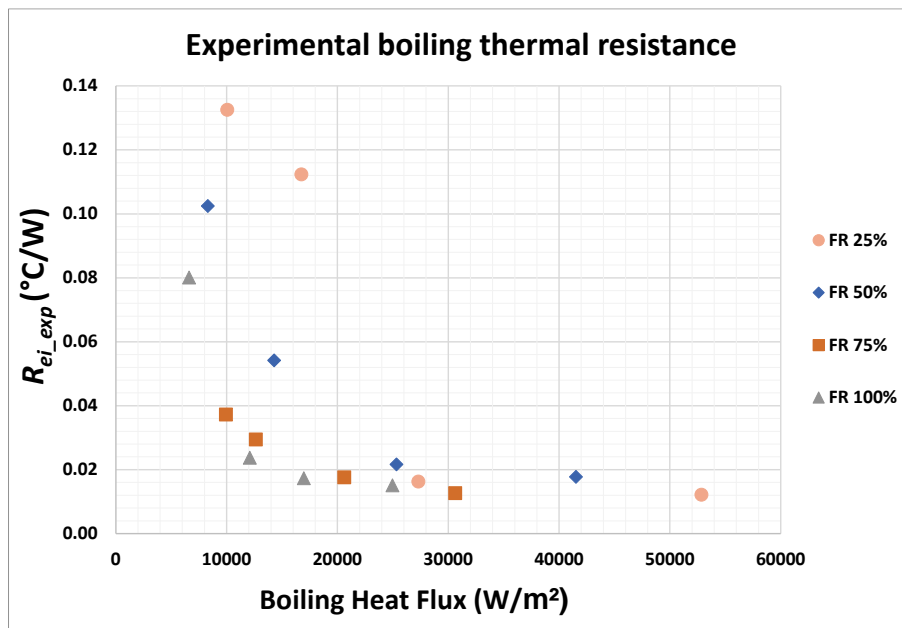


Figure 118 Experimental boiling thermal resistance versus heat flux under various filling ratios

Figure 118 presents the boiling resistance for the single radiative heat pipe at different boiling heat fluxes. It can be seen that geyser boiling has a major impact on the boiling thermal resistance at low heater temperatures. The intensity of the geyser boiling impact on the boiling thermal resistance decreased as the heat flux increased. For heat fluxes higher than 20 kW/m^2 geyser boiling disappears, and the thermal resistance decreases. The maximum boiling thermal resistance at 25% filling ratio is achieved for low heat flux at a value of $0.114 \text{ }^\circ\text{C/W}$. For a filling ratio of 50%, the maximum thermal boiling resistance is also achieved at heat fluxes below 10 kW/m^2 at $0.077 \text{ }^\circ\text{C/W}$, the thermal boiling resistance then decreases as the

filling ratio in the heat pipe increases. For heat fluxes above 30 kW/m^2 , the boiling thermal resistance does not exceed the value of $0.017 \text{ }^\circ\text{C/W}$. The filling ratio does not have a major impact on the boiling thermal resistance when the boiling heat fluxes are above 30 kW/m^2 . It can be deduced from Figure 118 that the best filling ratio in terms of boiling thermal resistance is for a filling ratio of 75% and 100%.

Condenser thermal resistance

Due to the design of the heat pipe, no thermocouple could be placed on the internal wall of the condenser section nor on the condenser external surface. Thus, the overall condenser resistance was calculated using the vapour temperature, the LMTD and the flow rate at the condenser. The overall condenser resistance obtained for the experimental tests at varying filling ratio is plotted in Figure 119. It can be seen that the behaviour of the thermal resistance changes with varying filling ratio. The thermal resistance for a heat flux higher than 15 kW/m^2 drastically increased for the FR of 75% and 100%. In the cases of a filling ratio of 25% and 50%, the heat pipe overall condenser resistance remains stable at heat fluxes higher than 10 kW/m^2 . The flooding of the heat pipe condenser section occurs for heat pipes with a large filling ratio, when the ratio between the evaporator surface and the condenser surface is high regardless of the radial heat flux. The vapour velocities induced by the high heat flux will force the subcooled liquid to remain in the condenser section, thus increasing the temperature of the wall at the evaporator section and increasing the vapour temperature. The flooding of the heat pipe will also occur as the vapour will push the liquid located at the evaporator section towards the condenser section. It can be seen that for high heat flux and high filling ratio, the condenser thermal resistance drastically increases due to the flooding of the condenser section, resulting in a higher film thickness at the condenser. The overall condenser resistance is obtained by calculating the UA value of the condenser section.

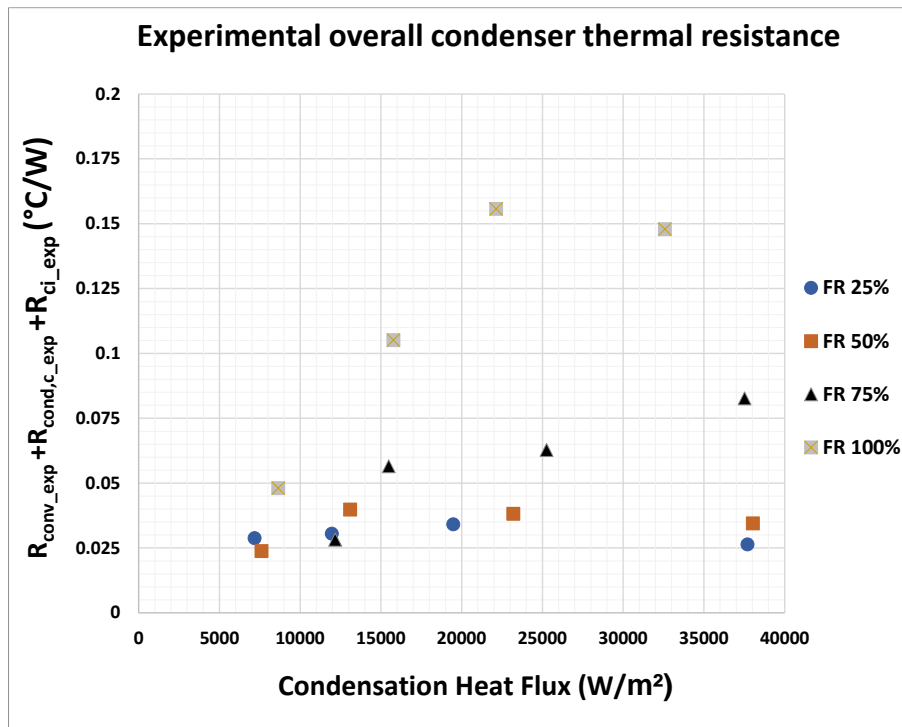


Figure 119 Experimental overall condenser thermal resistance

It can be concluded that a high ratio between condenser and evaporator areas will limit the operational range of the heat pipe. This phenomenon can be suppressed by increasing the heat transfer area at the condenser. The condensation thermal resistance was the main contributor in the variation of the overall condenser thermal resistance. The condenser resistance was determined by calculating the forced convection resistance at the manifold and the conduction resistance of the heat pipe wall. The condensation resistance of the heat pipe is plotted in Figure 120. A similar trend in the condensation resistance as the overall condensation resistance can be seen.

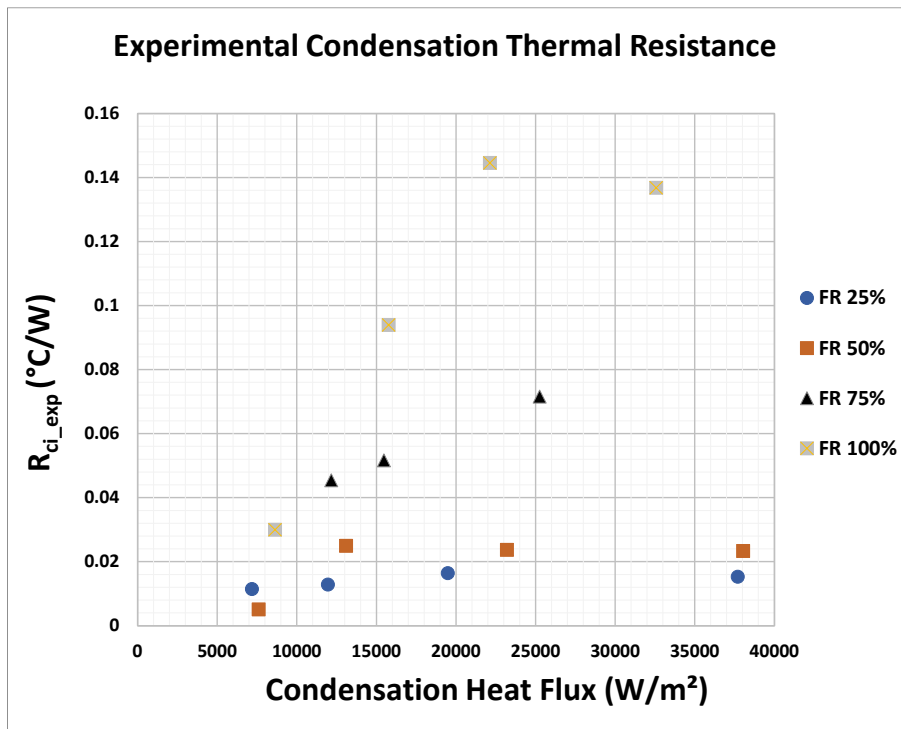


Figure 120 Experimental condenser thermal resistance

6.2.1.3 Impact of the filling ratio on the heat recovery

The heat recovery is impacted by the temperature of the heat pipe and the occurrence of geyser boiling. It can be seen from Figure 121 that, as the heater temperature increases, the heat recovery increases accordingly. It can be also seen that for a filling ratio of 100%, the heat recovered tends to be lower than at other filling ratios. At 500 °C, the heat recovery for a filling ratio of 100% is 491 W while the highest heat recovered is achieved by a filling ratio of 50% with 573 W. For a filling ratio of 75%, the heat transfer rate obtained is higher for the range of 200 °C to 400 °C than other filling ratios.

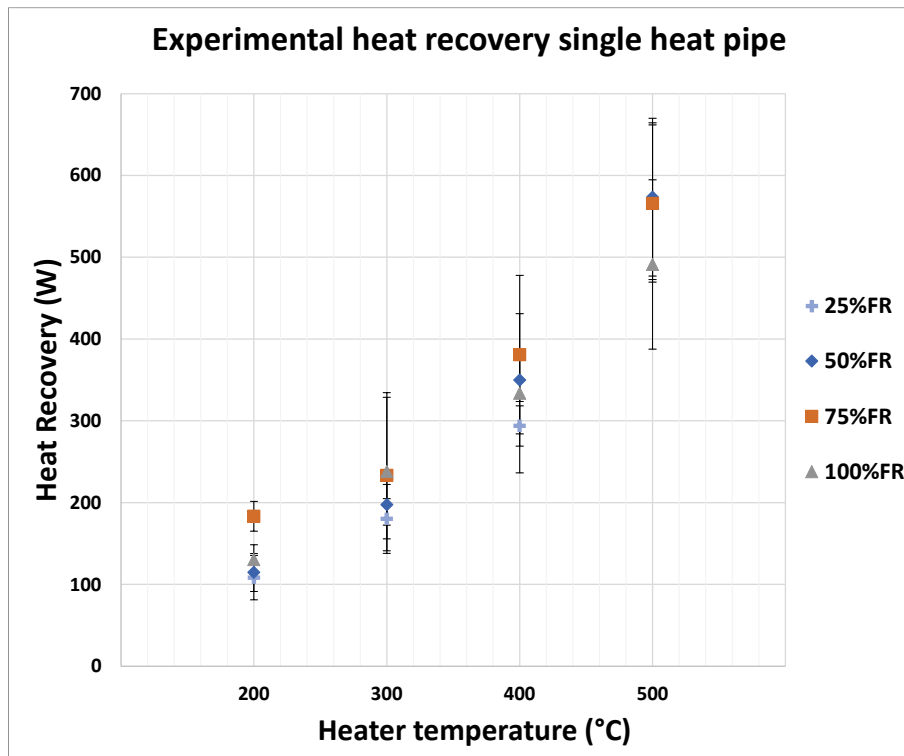


Figure 121 Impact of the filling ratio on the evaporator ΔT

By comparing the impact of the filling ratio on the condenser at different set up temperatures from 200 °C to 500 °C, it can be noticed that below a 50% filling ratio, uniformity of temperature in the evaporator section is not achieved. Above 50%, the heat pipe is uniform within the error of the thermocouples. The heat recovery when geyser boiling occurs is difficult to measure as it will fluctuate during the test. The impact of the geyser boiling on the heat recovery can be seen in Figure 122.

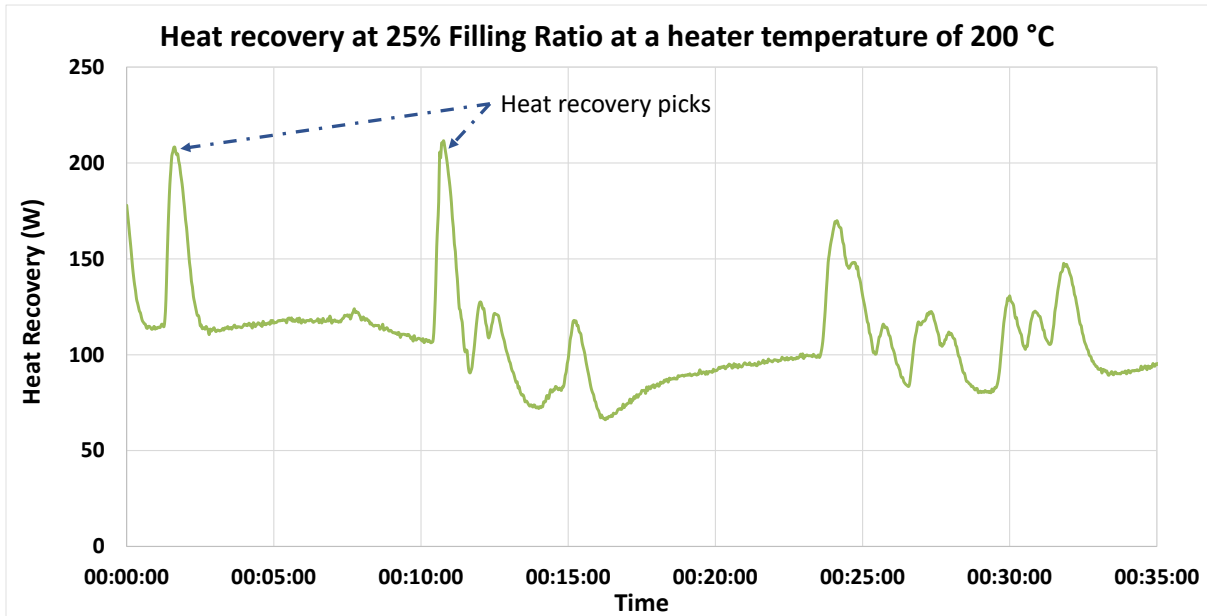


Figure 122 Fluctuation of the heat recovery during geyser boiling

During geyser boiling the superheated liquid and vapour pushed by the vapour bubble will significantly increase the temperature at the condenser section, thus increasing the outer wall temperature. The temperature at the outlet of the condenser will increase, thus increasing the heat transfer. In order to measure an accurate value of the heat recovered, the heat recovery at steady state is calculated between a defined numbers of peaks.

It can be concluded that to obtain a steady heat recovery output for the heat pipe, geyser boiling needs to be avoided. As most of the geyser boiling occurs at a filling ratio of 25% and 50%, the best-case scenario in terms of heat recovery for the single radiative heat pipe is for a filling ratio of 75%.

6.2.1.4 Influence of natural convection on the overall heat transfer rate

The heat transfer rate by natural convection was calculated from the experimental temperatures of the kiln and the heat pipe. The natural convection was determined using Rani [66] by taking into account the temperature of the air and the temperature of the heat pipe. The calculated values are plotted in Figure 123. It can be noticed that the natural convection heat transfer rate increased linearly as the temperature of the heater increased. It can be noted that the value for filling ratios between 25% and 50% is higher than for filling ratios at 50% and 100% for a heater temperature above 300 °C. The temperature of the evaporator section at high temperature is significantly higher for a high filling ratio, thus the heat recovered by natural convection will be lower as the heat transfer rate is dependent on the surface temperature.

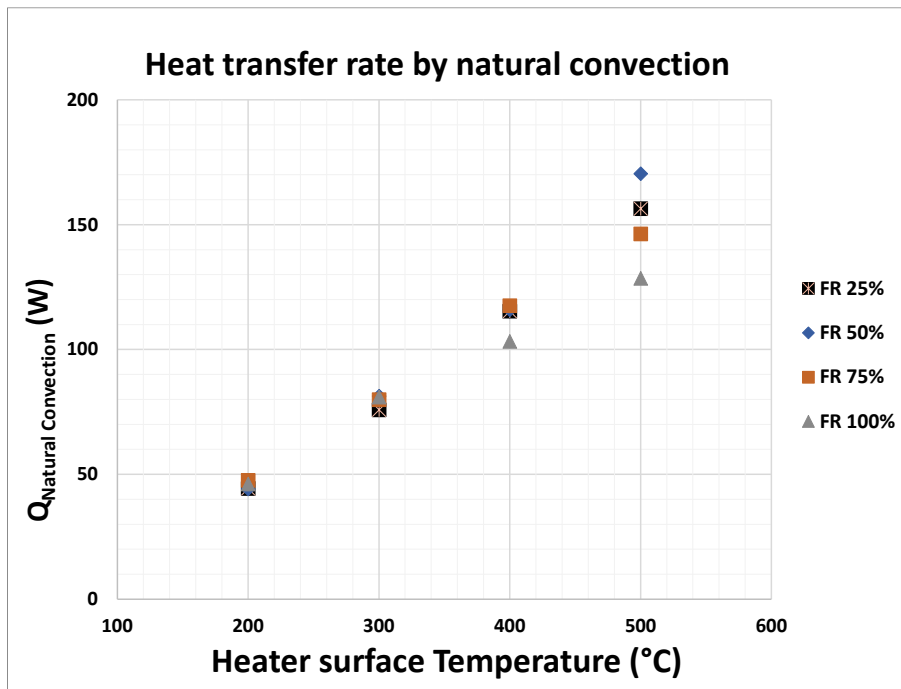


Figure 123 Heat transfer rate by natural convection

The influence of the natural convection on the overall heat transfer rate is presented in Figure 124. The natural convection is largely contributing to the heat transfer rate at low temperature. For a filling ratio of 25%, at 200 °C, the natural convection heat transfer rate contributes 41% of the overall heat transfer rate. The contribution to the overall heat transfer rate diminishes as the heater temperature increases to reach 27.5% for a filling ratio of 25% at a heater temperature of 500 °C. A similar trend can be seen for higher filling ratios. As mentioned above, for a filling ratio higher than 50%, the natural convection contribution to the overall heat transfer rate will be lower as the heat pipe temperature is higher. The natural convection will contribute 35.4% for a filling ratio of 100% and a heater temperature of 200°C.

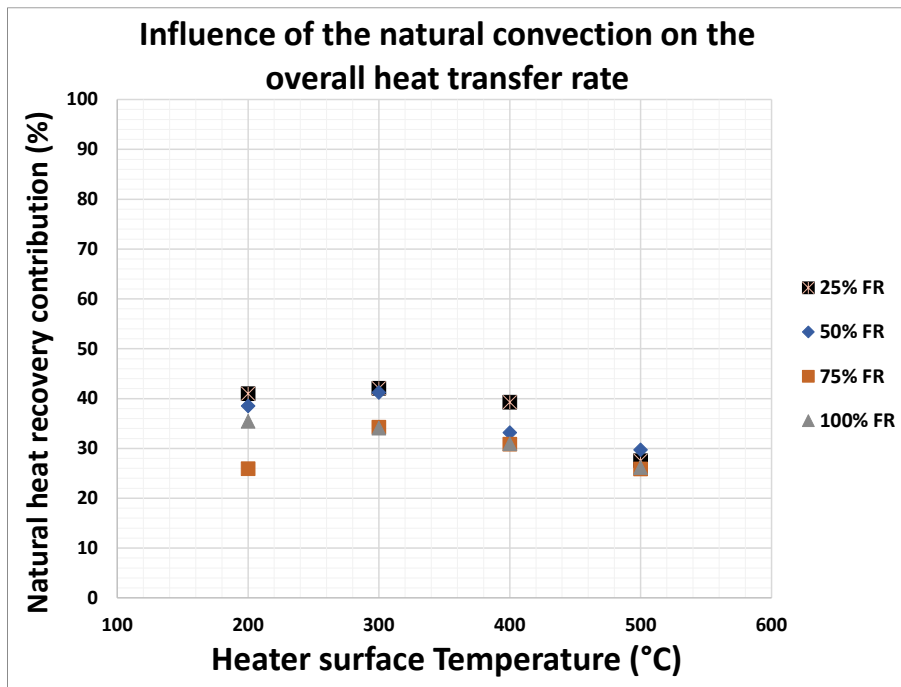


Figure 124 Influence of natural convection on the overall heat transfer rate

6.2.1.5 Experimental radiation heat transfer rate

The radiation heat transfer rate was obtained by subtracting the natural convection heat transfer from the overall heat transfer rate. Figure 125 shows a similar trend to the natural convection heat transfer rate. The heat transfer rate by radiation increase as the temperature of the heater increases. It can be noted that for a value of heater temperature higher than 400 °C, the radiation heat transfer rate doubles. For a heater temperature of 200 °C, the radiation heat transfer rate varied between 44.1 W and 47.5 W. The maximum heat transfer rate is achieved for a heater temperature of 500 °C and varied between 419 W and 363 W.

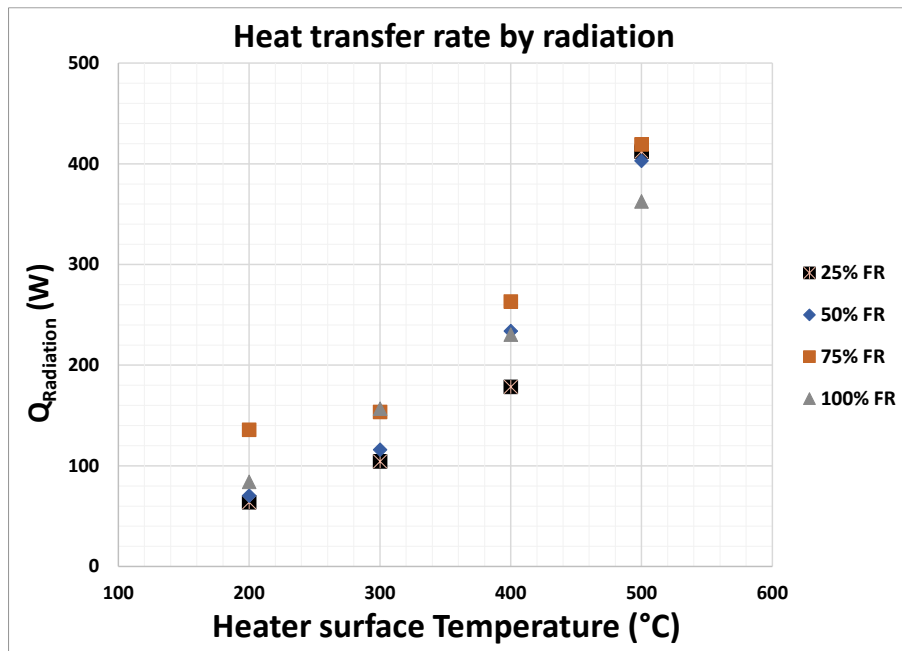


Figure 125 Heat transfer rate by radiation

6.2.2 Experimental versus theoretical boiling thermal resistance.

The heat flux and the boiling resistance will be strongly affected by the exotic design of the single heat pipe. The variation of the filling ratio will have a strong impact on the heat flux at the evaporator section. The heat flux at the evaporator section could not be measured at the internal surface of the evaporator nor at the outer section of the evaporator. In order to determine the local boiling heat flux, the heat transfer at the coolant was used. The error associated with the heat transfer and the coolant was $\pm 20\%$ when no geyser boiling occurs. If the heat pipe is subjected to geyser boiling, then the error on the heat transfer rate becomes too high for it to be used in any data analysis. In this regard, the data points that will be considered are for a boiling heat flux value equal or higher than 20 kW/m^2 . Also, as the filling ratio changes, the heat transfer area associated with the boiling heat flux will also change. The area of the pool/surface interface will also be reduced by the volume occupied by the vapour. As the vapour is generated in the evaporator section, the top section of the pipe will be covered by the vapour, thus reducing the active area of the pool as shown in Figure 126.

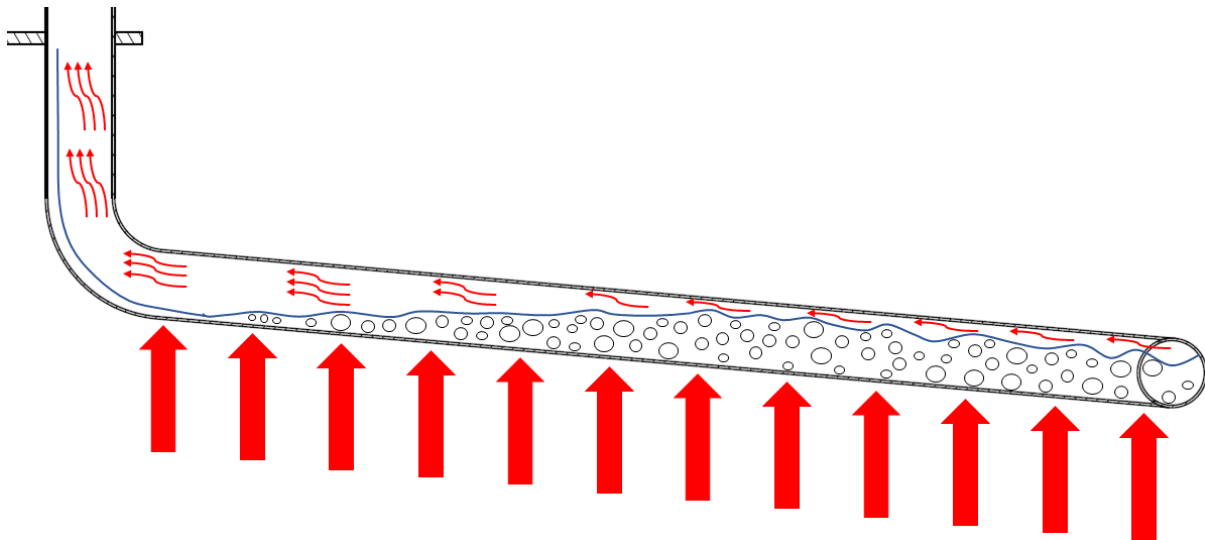


Figure 126 Surface area occupied by the pool at a filling ratio of 75%

The area used for each filling ratio was determined using AutoCAD Inventor for a liquid pool equal to the percentage of filling of the evaporator section. The experimental thermal boiling resistance was compared to general correlations used for boiling, using the heat flux at the test conditions. The value of the theoretical thermal resistance for a heat flux lower than 20 kW/m² is much lower than the experimental thermal resistance for a filling ratio of 25% and 50%. For a filling ratio of 100%, the predicted boiling resistance is much lower for a heat flux below 10 kW/m² while for a filling ratio of 75%, some correlations are in good agreement regardless of the boiling heat flux.

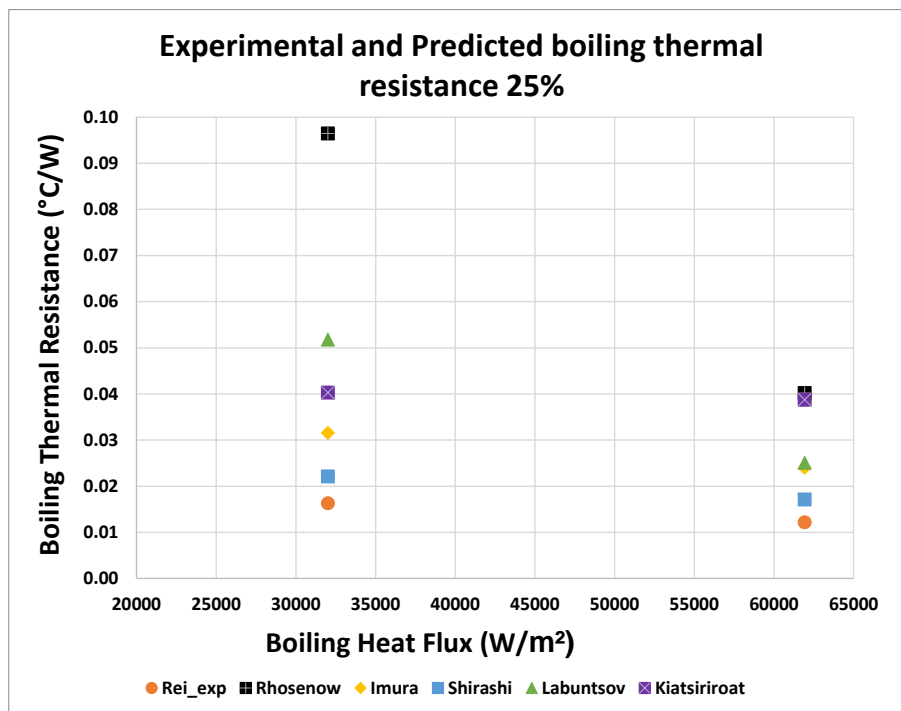


Figure 127 Experimental and predicted boiling thermal resistance FR25%

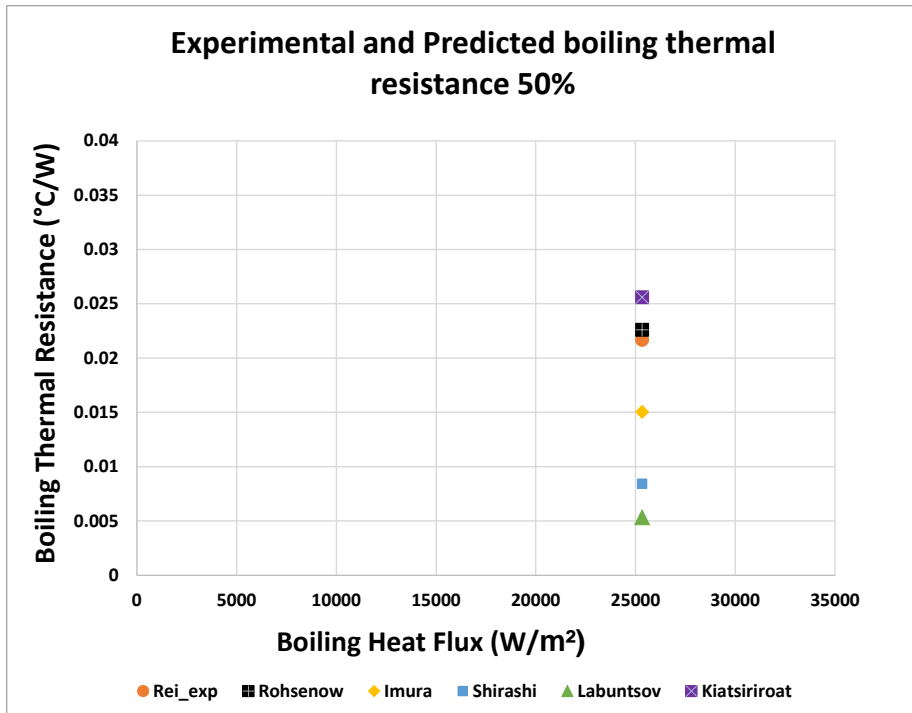


Figure 128 Experimental and predicted boiling thermal resistance FR50%

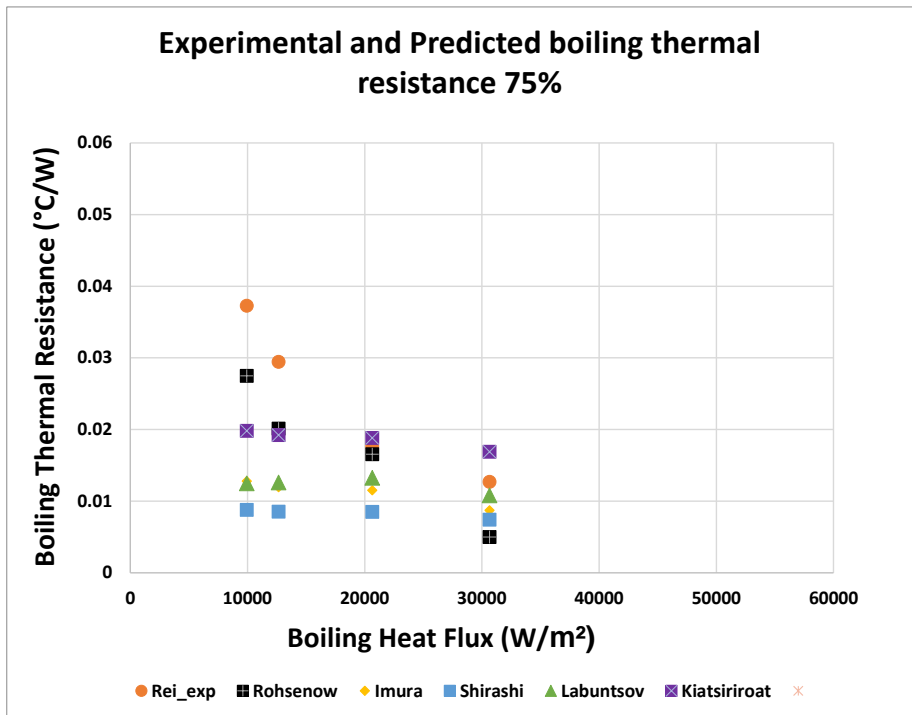


Figure 129 Experimental and predicted boiling thermal resistance FR75%

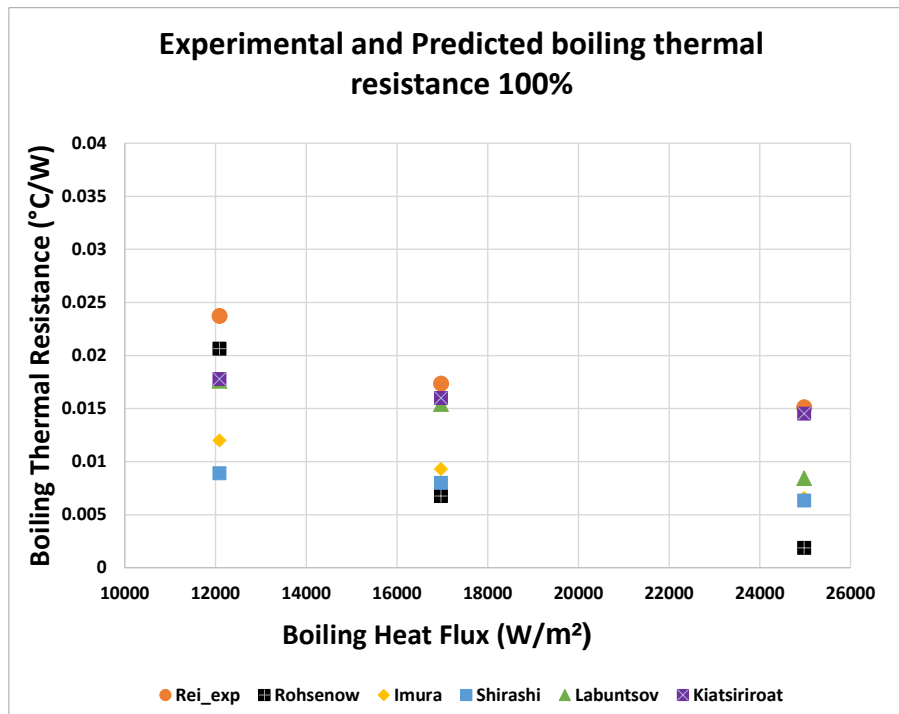


Figure 130 Experimental and predicted boiling thermal resistance FR100%

Figure 127 to Figure 130 show the different predictions for the boiling thermal resistance for the four filling ratios. The experimental boiling resistance is compared to predictions when geyser boiling was not occurring. Depending on the filling ratio, the minimum heat flux was 10 kW/m² for FR at 25%, 15 kW/m² for a FR of 50% and 10 kW/m² for a filling ratio of 100%. As no geyser boiling occurred for a FR of 75%, no restriction was taken. The uniformity of temperature at the evaporator pool was also considered, the variation of temperature at the evaporator did not exceed 7 °C. The excess temperature at the evaporator section for the selected data did not exceed 9 °C. It can be seen that *Rohsenow* [82] is in good agreement for most of the cases apart from a heat flux lower than 35 kW/m² and a FR of 25%. It can be noted that for a FR of 75%, the prediction using *Rohsenow* is close to the experimental value. *Imura* showed an excellent agreement for a heat flux higher than 20 kW/m² at a FR of 75%. For a FR of 100% *Imura* [89] was predicting lower thermal resistances than the experimental results, similarly for a FR of 50 %. For a FR of 25%, the prediction using *Imura* overpredicted the boiling resistance. *Shirashi* [92] was lower for the filling ratio above 25%. For a filling ratio of 75%, *Shirashi* was much lower. Similarly, *Labuntsov* [90] tended to predict a boiling resistance lower than the experimental boiling resistance. *Kiatsiriroat* [91] was able to predict a close value to the experimental boiling resistance in most of the cases for heat fluxes higher than 15 kW/m² apart from a filling ratio of 25%.

The predicted thermal resistance versus the experimental boiling resistance for each filling ratio is plotted in Figure 131 to Figure 134. It can be seen that for a filling ratio of 25%, most

of the correlations overpredicted the thermal boiling resistance. *Shirashi* predicted the thermal boiling resistance within 40%. For a FR of 50% most of the correlations predicted the boiling resistance within 40%. In case of a FR of 75%, *Imura*, *Shirashi*, *Labunstov* and *Rohsenow* achieved a good agreement with experimental values for an experimental boiling resistance lower than 0.02 °C/W, while for a higher boiling thermal resistance, the correlations above did not perform well. *Rohsenow* predicted the experimental value within $\pm 40\%$ apart from an experimental boiling resistance of 0.017 °C/W. *Kiatsiroat* was in good agreement with the experimental value within the range of 0.028 °C/W to 0.036 °C/W, similarly for a FR of 100%, where *Kiatsiroat* predicted the experimental boiling resistance well for a resistance higher than 0.02 °C/W. *Labunstov* behaved similarly.

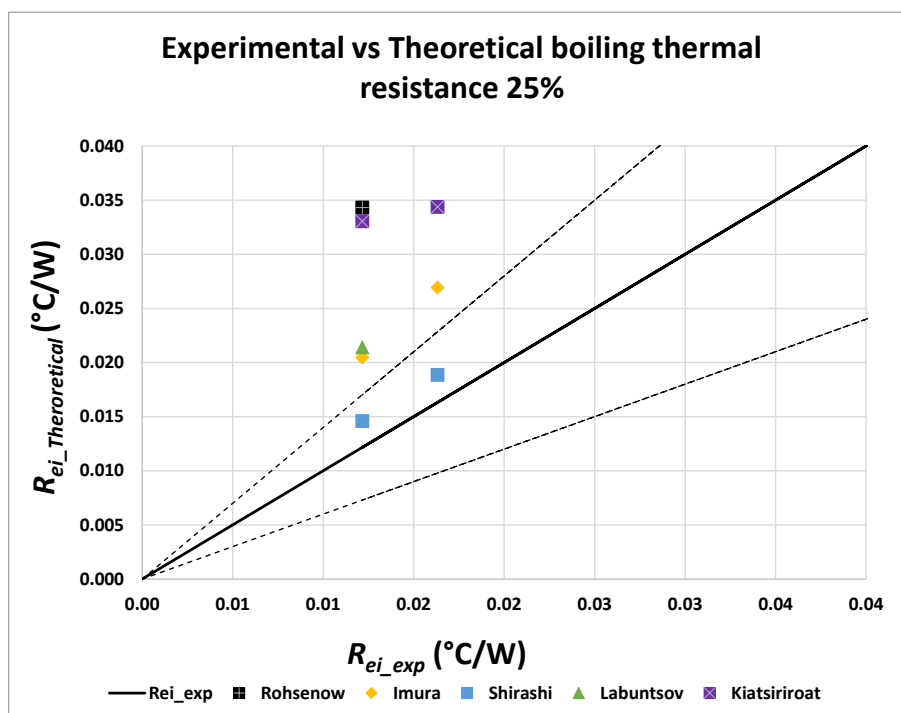


Figure 131 Experimental versus predicted boiling thermal resistance FR25%

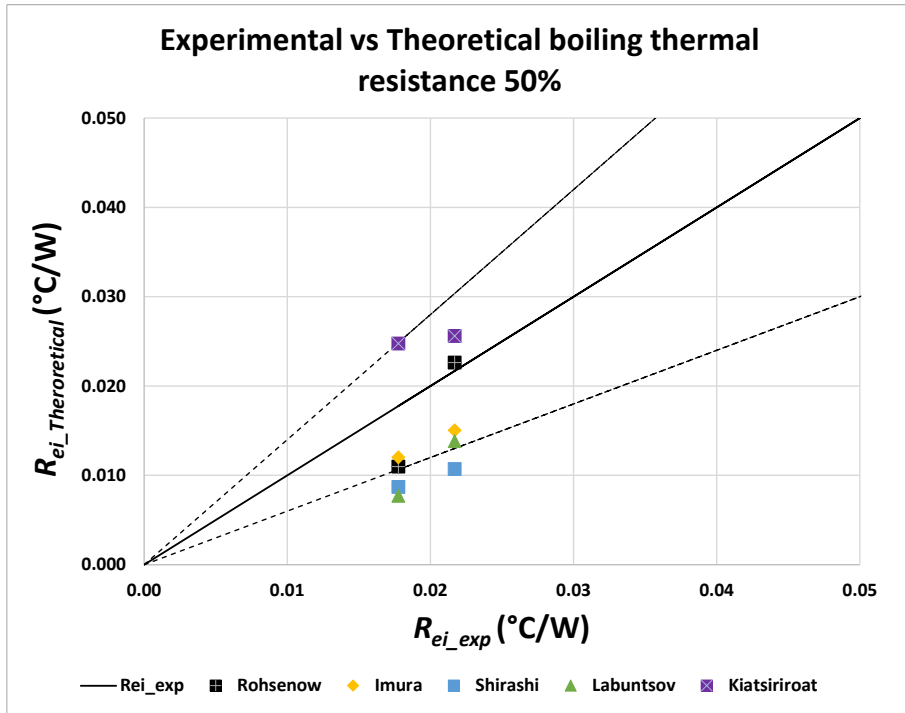


Figure 132 Experimental versus predicted boiling thermal resistance FR50%

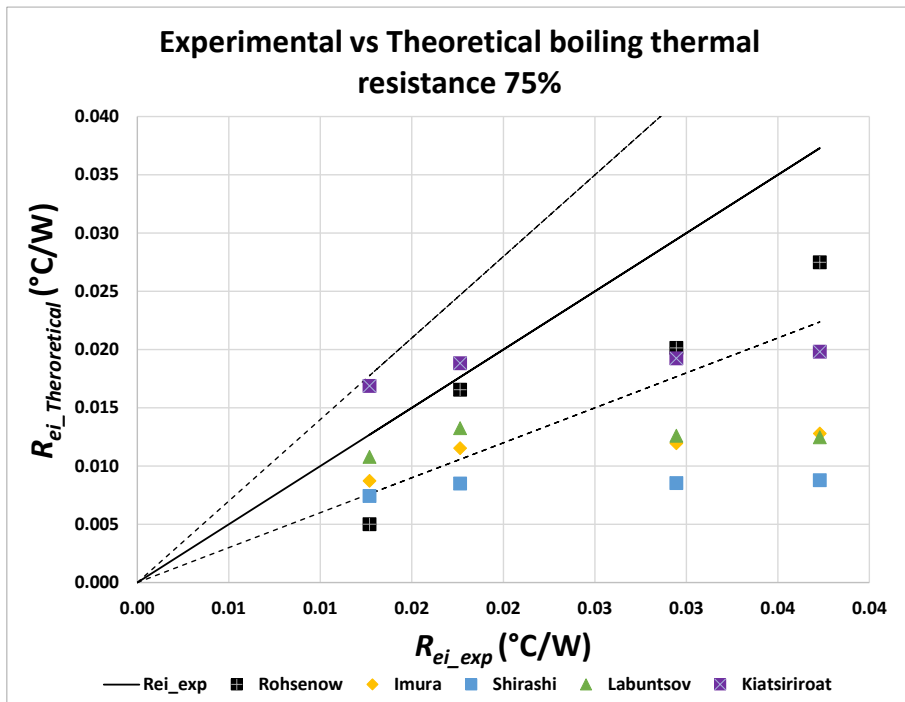


Figure 133 Experimental versus predicted boiling thermal resistance FR75%

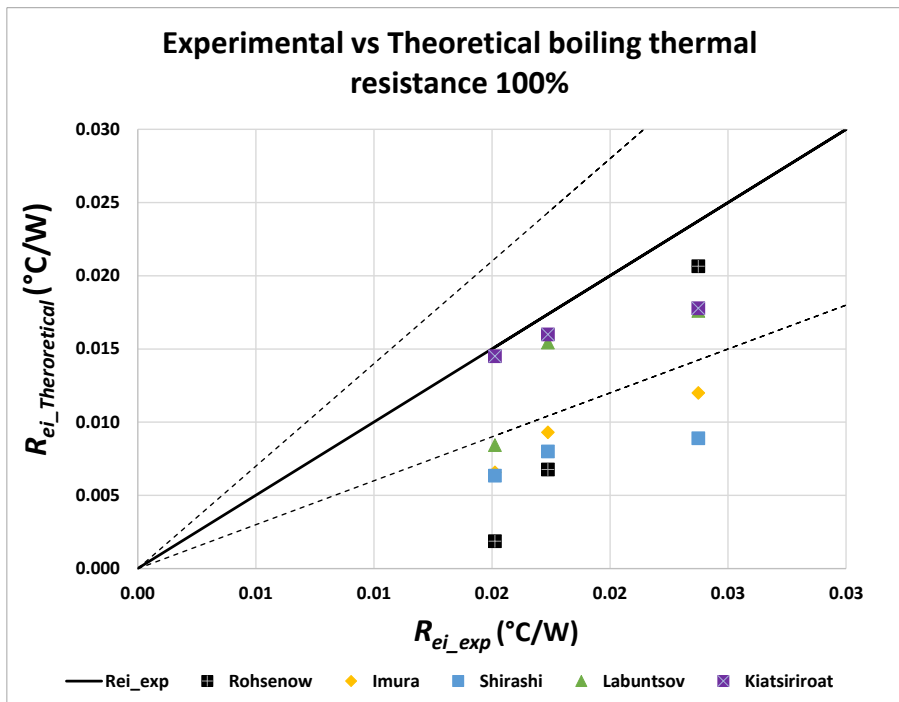


Figure 134 Experimental versus predicted boiling thermal resistance FR100%

6.2.3 Experimental versus theoretical condenser thermal resistance.

To predict the condensation thermal resistance, the predicted values will be calculated for a filling ratio lower than 50%. The experimental values plotted in Figure 135 are compared to the predictions using the correlation developed by Nusselt modified by Rohsenow [97,98]. The predictions show a good agreement with the experimental data with an of error $\pm 25\%$ and within $\pm 35\%$ for two cases.

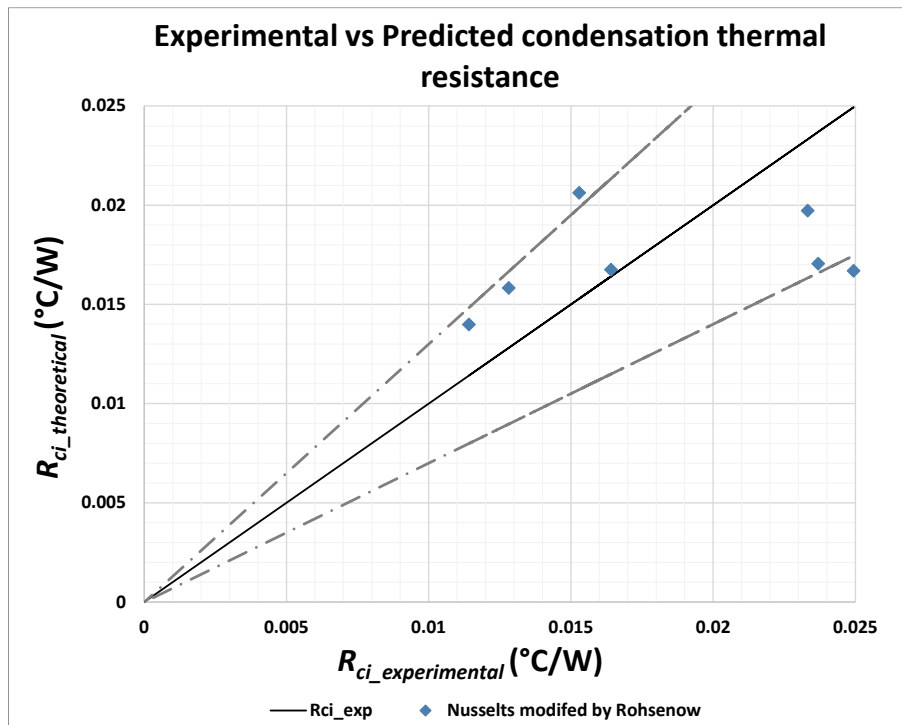


Figure 135 Comparison between the experimental and predicted condensation thermal resistance

6.2.4 Radiation thermal resistance analysis

The thermal radiation resistance is impacted by a variety of factors that need to be taken into account. The emissivity of the tile and the heat pipe will change as the temperature of the respected surfaces change during the different test set points. The resistance associated with the surface is identified as the radiation surface resistance. This resistance will depend on the temperatures of the radiating surfaces. The second component of the overall radiation thermal resistance is the radiation space resistance. This resistance is not impacted by the temperature of the surfaces and is driven by the view factor between the surfaces. This component of the overall radiation resistance will not change as the design of the heat pipe is similar for all the tests. The main contributor to the space radiation resistance is linked to the view factor. It can be seen in Figure 136 that the predicted theoretical resistance is within $\pm 30\%$ for most of the cases and within $\pm 50\%$ for lower heater temperatures. It can be noted that the theoretical radiation resistance did not change with the different conditions, however, the experimental thermal resistance did change. In order to approach an accurate value for the theoretical thermal resistance, a correction factor needs to be applied for the different test conditions.

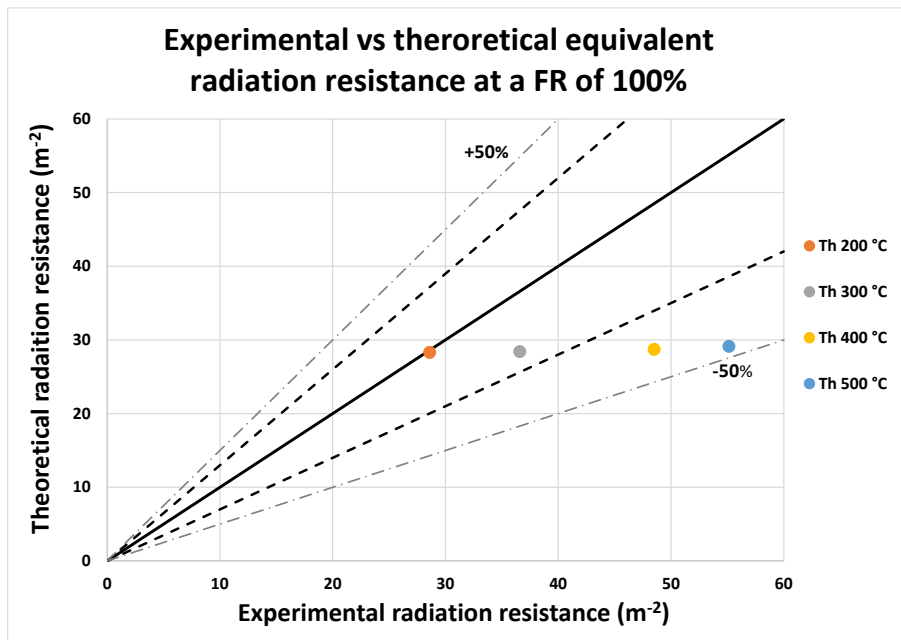


Figure 136 Experimental vs Theoretical thermal radiation resistance

6.2.5 Theoretical analysis of the forced convection at the condenser

The experimental thermal resistance of forced convection at the condenser cannot be determined as there was no possibility of placing a thermocouple on the external surface of the condenser section. The forced convection was calculated using *Haussen* correlation for a Reynolds number lower than 3000 and *Gnielinski* for a Reynolds number higher than 3000. The results are shown in Table 22.

Table 22 Forced convection thermal resistance

FR	Heater temperatures (°C)	Flow rate (L/min)	Heat transfer coefficient (W/m ² .°C)	Forced convection resistance (°C/W)
25%	200	1.1	4400	0.0085
	300	1.1	4400	0.0085
	400	1.1	4420	0.0085
	500	3.7	15000	0.0031
50%	200	0.9	3600	0.0099
	300	3.7	14500	0.0032
	400	3.7	14700	0.0032
	500	3.7	14550	0.0032
75%	200	0.5	630	0.0353
	300	3.7	15140	0.0031

	400	3.7	14810	0.0032
	500	3.7	15000	0.0031
100%	200	0.7	6200	0.0065
	300	3.7	14500	0.0032
	400	3.7	14500	0.0032
	500	3.7	14600	0.0032

6.2.6 Total thermal resistances

The total heat pipe thermal resistance for varying filling ratios and varying heat fluxes is plotted in Figure 137. As the impact of the flooding of the condenser for filling ratios above 50% have a strong influence on the thermal resistance of the heat pipe, they were not plotted apart from heat fluxes lower than 6 kW/m². It can be seen that at lower heat fluxes, the thermal resistance of the heat pipe is high and decreases steadily until it become stable for heat fluxes higher than 6 kW/m². For heat fluxes lower than 6 kW/m² the overall thermal resistance was high due to the occurrence of geyser boiling.

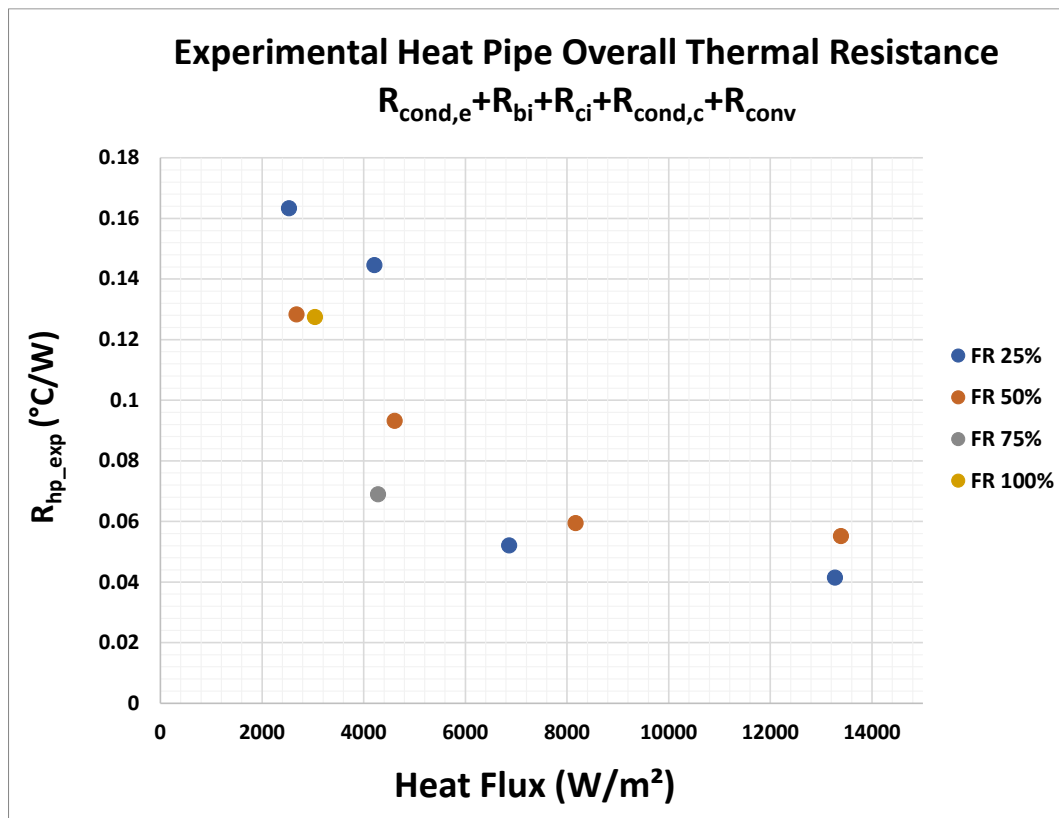


Figure 137 Experimental overall thermal resistance of the single heat pipe

6.2.7 Validation of the single heat pipe theoretical modelling predictions

6.2.7.1 Heat transfer rate prediction

The theoretical modelling tool was used to compare the experimental results and the theoretical predictions of the heat recovered by the single heat pipe. The values obtained are plotted in Figure 138. The prediction tool shows good agreement with the experimental data and predicted the heat recovery of the single heat pipe with an error of $\pm 15\%$ for most of the cases and within $\pm 25\%$ for one case at a filling ratio of 100%.

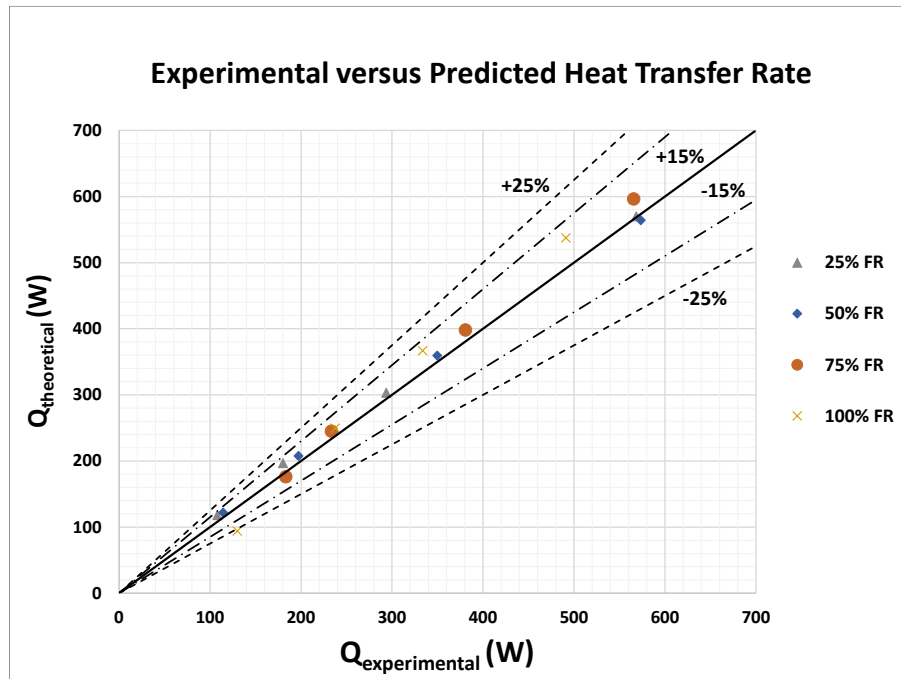


Figure 138 Experimental vs predicted heat transfer rate

6.2.7.2 Heat pipe temperature prediction

The heat pipe temperatures were predicted using the modelling tool. As the number of cases is large, the model was used to simulate two cases at a filling ratio of 75% with a high and low heat flux applied to the evaporator. It can be seen in Figure 139 that for a low heat flux, the temperature difference for the water outlet is less than $0.12\text{ }^{\circ}\text{C}$. The evaporator temperature difference is $0.29\text{ }^{\circ}\text{C}$. The vapour temperature is overpredicted by $3.86\text{ }^{\circ}\text{C}$. Similarly, for a higher heat flux plotted in Figure 140, the temperature difference for the water outlet is less than $0.05\text{ }^{\circ}\text{C}$ and the difference at the evaporator is $4.1\text{ }^{\circ}\text{C}$. As the first case study, the vapour temperature is overpredicted by $3.12\text{ }^{\circ}\text{C}$. It can be concluded that the prediction tool provides an excellent agreement with the measured temperature at the outlet of the water jacket.

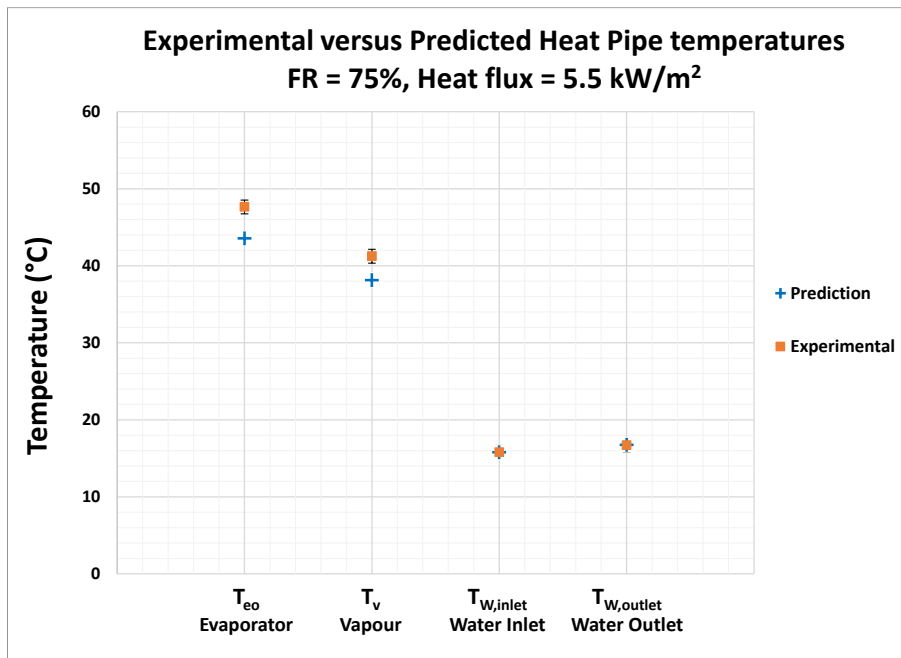


Figure 139 Experimental vs predicted heat pipe temperatures, case study 1

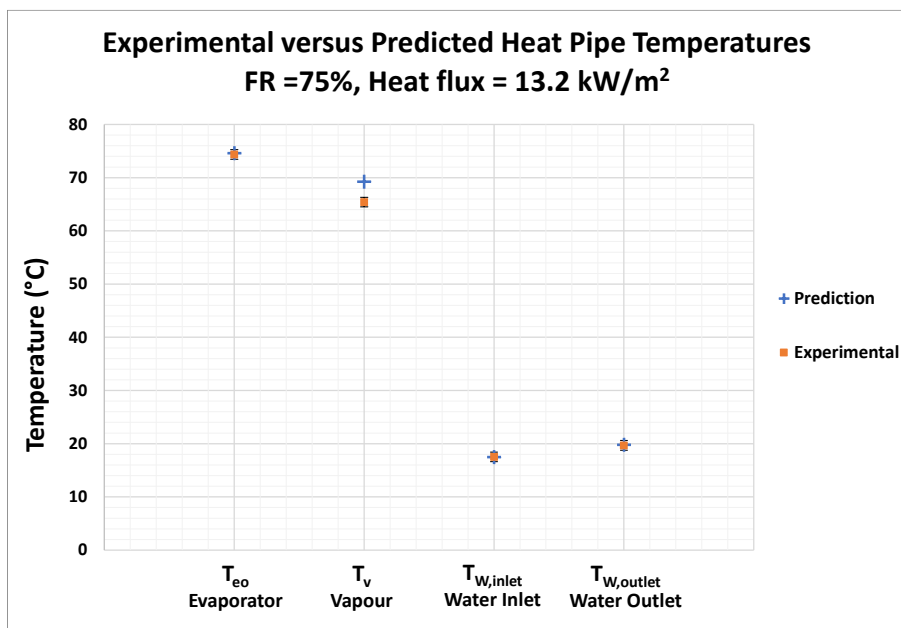


Figure 140 Experimental vs predicted heat pipe temperatures, case study 2

6.3 Multi module laboratory-scale radiative heat pipe ceiling

This section will present and discuss a new evaporator section design coupled with a shell and tube type condenser section. As the condenser section in the single pipe exposed some flooding issues due to the splashing of the working fluid onto the condenser, the module heat pipe condenser section was increased and redesigned. Three modules with varying heat pipe evaporator areas were tested for different heater temperatures and flow rates. The module 15 presents the highest density of pipe with a pipe separation of 15 mm. Module 25 is an

intermediate density with a pipe separation of 25 mm. The low evaporator area is for module 35 with a pipe separation of 35 mm.

The impact of the evaporator section area on the heat pipe temperatures, the heat transfer rate and the contribution of natural convection was investigated. As the evaporator section changes, the boiling resistance area will also be modified, and so the impact of the change on the evaporator for the boiling thermal resistance was investigated.

To verify the assumption on the filling ratio made in the previous section, module 15 was tested with a filling ratio of 25% and 75%.

The change in the condenser section involved the use of different correlations from the one used for the single heat pipe. As the correlations available in the literature for condensation on tube bundles were determined to not be applicable, new correlations were developed.

The prediction model developed in the single pipe was modified to take into account the new heat pipe design and the correlations to be used. The model was then used to predict the heat transfer rate and the heat pipe temperatures.

6.3.1 Module experimental results

6.3.1.1 Module heat pipe temperature measurements

A variation of the heat pipe temperatures occurred at the different flow rates tested. The temperature of the heat pipe will impact the limitation on the potential heat transfer and the operating range of the heat pipe module. The results presented are for the module 15 which has the highest heat transfer area at the evaporator section. The module was tested at four different flow rates, 5 L/min, 10 L/min, 15 L/min, and 20 L/min. The variation of the heat pipe temperatures was also investigated for different evaporator heat fluxes.

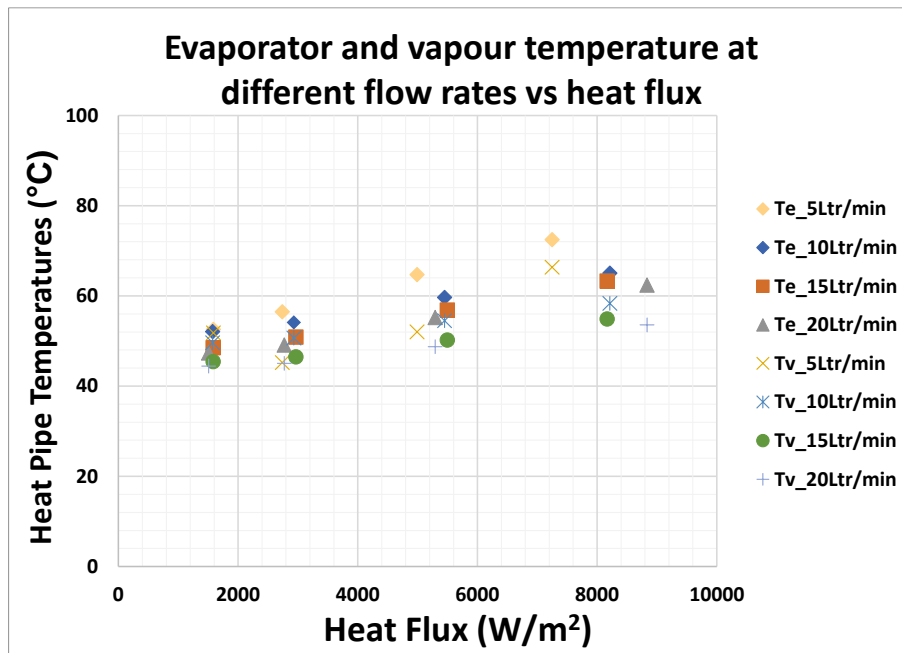


Figure 141 Variation of the temperature measurements of module 15 heat pipe system at various flow rates for a heater temperature of 500°C

Figure 141 presents the variation of the heat pipe temperature for the evaporator section and the vapour temperature. It can be noted that as the flow rate increases, the temperature of the heat pipe will decrease. The impact of the flow rate can be seen from the vapour temperature dropping from 62.3 °C to 46.6 °C. The evaporator section temperature also decreased as the steam temperature decreased from a maximum of 76.1 °C to 67.9 °C for flows of 5 L/min and 20 L/min, respectively. As the flow rate increases in the condenser section, the heat transfer coefficient for forced convection will increase, mainly due to the modification in the Reynolds number. The increase in the heat transfer coefficient, reducing the thermal resistance at the condenser, will decrease the condenser outer wall temperature thus reducing the internal temperature of the heat pipe.

The coolant inlet at the condenser was constant during the test. The outlet temperature varied from 24.87 °C to 18.86 °C. The difference between the inlet and outlet of the coolant changed from 8.90 °C to 2.71 °C for flows of 5 L/min and 20 L/min, respectively.

6.3.1.2 Experimental heat transfer rate

It can be seen from Figure 142 that the impact of the flow rate on the heat recovery of the heat pipe does not have a major impact when the flow rate is above 5 L/min. It can also be seen that, as the temperature of the heater increases, the heat recovered by the heat pipe module will increase.

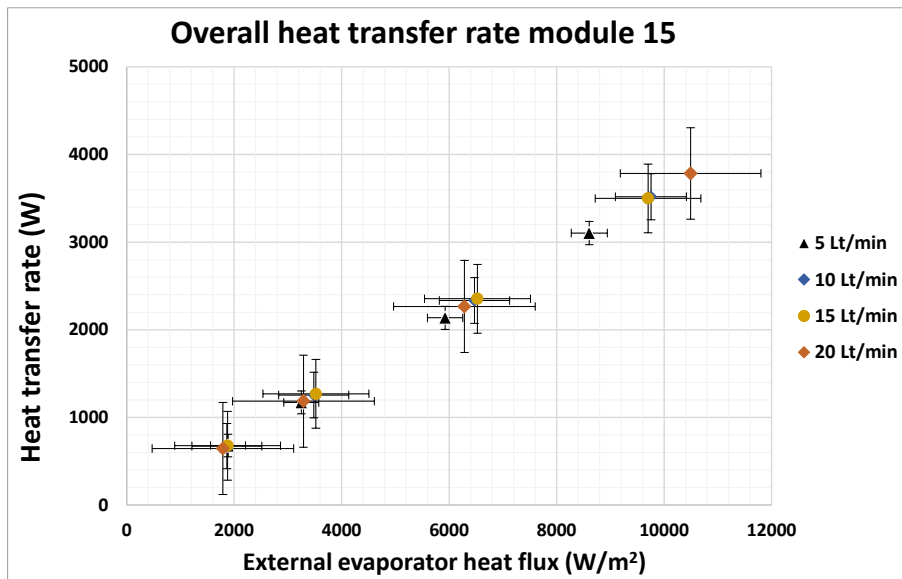


Figure 142 Experimental heat recovery under varying conditions.

6.3.1.3 Filling ratio impact on the module

The impact of the filling ratio was investigated for a single radiative heat pipe. In order to ensure that the conclusion drawn for the experimental results of the single radiative heat pipe can be applied to the module, a test of the module 15 at 25% FR was also carried out under similar conditions to the test at 75% FR.

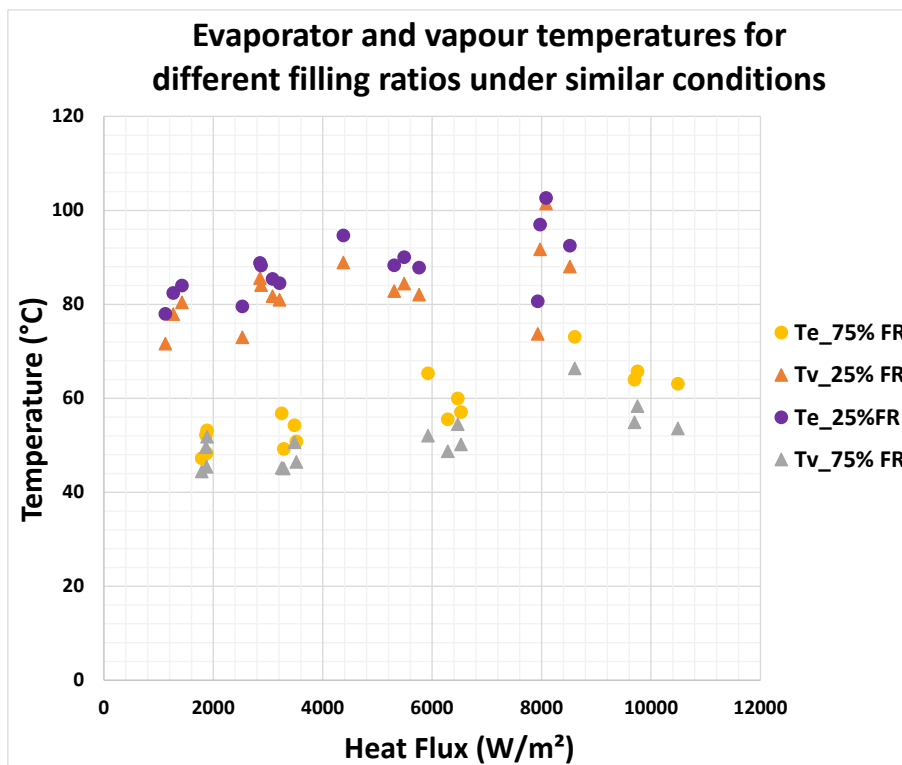


Figure 143 Heat pipe module temperature at filling ratios of 25% and 75% for a tile temperature of 500°C.

It can be seen from Figure 143 that the temperatures of the evaporator section and the vapour are significantly higher for a filling ratio of 25%. The highest difference can be witnessed for a flow rate of 5Ltr/min; the temperatures of the evaporator and the vapour for a filling ratio of 25% are respectively 102.64 °C and 101.46 °C, where for a filling ratio of 75%, the temperatures are 73.11 °C and 66.36 °C. This difference is mainly due to the area of pool boiling in the evaporator section. The pool boiling for the module 15 filled at 75% will occupy the entirety of the surface directly exposed to the radiative heat from the heater. In the case of the module charged at only 25%, the pool volume is greatly reduced with half of the surface area exposed to the heater not covered by the pool. In this case, falling film boiling occurs in the upper section of the heat pipe, thus increasing the temperature of the heat pipe module. Figure 144 presents the heat recovered for both filling ratios under four different flow rates at a heater temperature of 500 °C. Similar to the single heat pipe, the module tends to recover larger amounts of heat at the higher filling ratio.

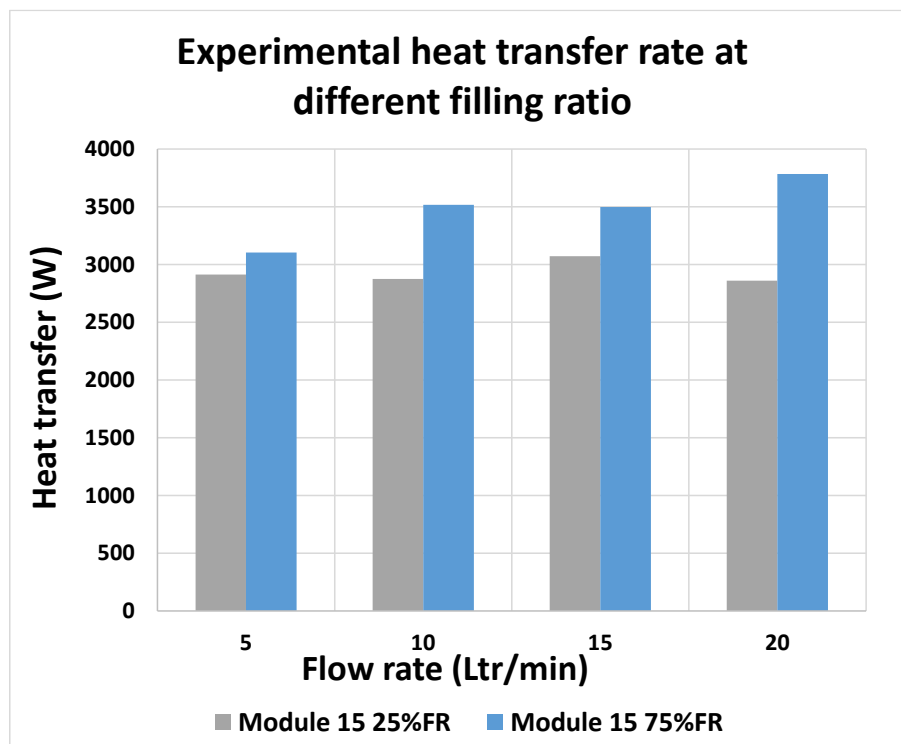


Figure 144 Heat recovery at similar conditions for a FR of 25% and 75% at 500 °C

6.1.3.4 Impact of the evaporator surface area

In order to implement a system that will be able to fine tune the need of heat recovery depending on the tile temperature, thus equalising the temperature in the cross section of the tile, the module was tested and compared with a varying evaporator heat pipe density. The variation in the density of the pipe at the evaporator section will mainly impact the temperature of the heat pipe module and the heat recovered. Figure 145 shows the impact of the

evaporator surface area on the vapour and evaporator temperatures. It can be noted that the highest temperature for the vapour and the evaporator are for Module 15. The maximum temperature is for a flow rate of 5 L/min. The module 15 average evaporator temperature is higher than that for module 35. This is mainly due to the difference in the temperatures of the water supply. It can be determined from Figure 145 that as the density of the evaporator section increases, the temperature of the heat pipe will also increase. This can be a limiting factor in the design of the heat pipe as the maximum safe working temperatures can be reached.

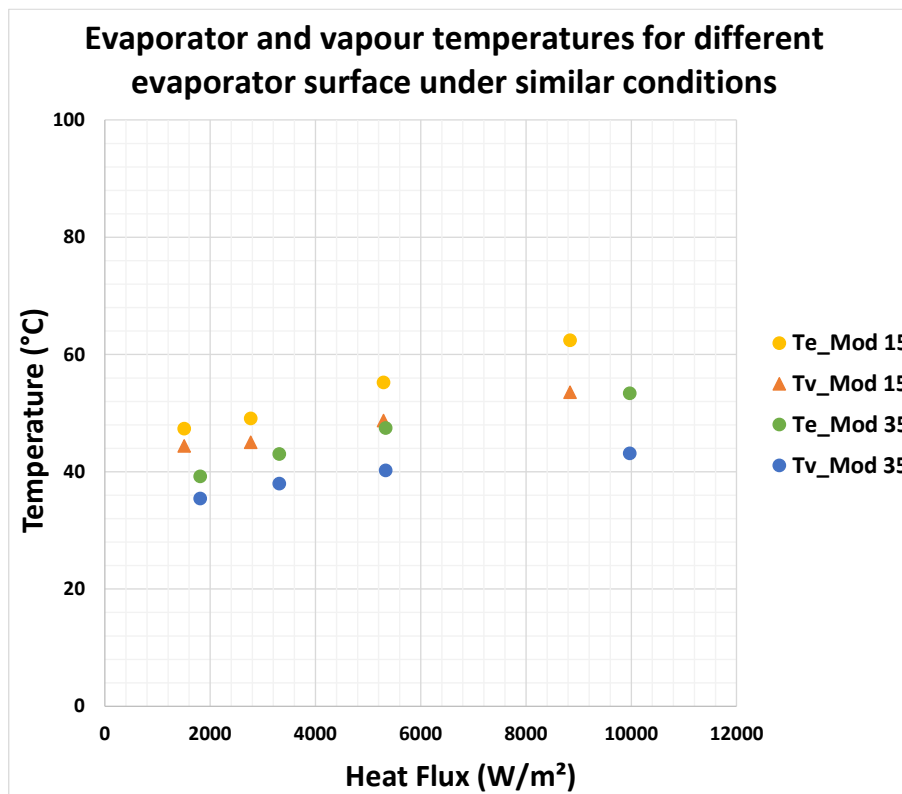


Figure 145 Heat pipe module temperatures at various flow rates

As mentioned previously, the heat recovered by the heat pipe modules increases with the heater temperature. It can be noted from

Figure 146 that at low heater temperatures, the heat recovered by the modules are similar. For 200 °C and 300 °C, the heat recovered by the modules is close to 700 W and 1100 W, respectively. The change in heat transfer between the modules can be seen for a heater temperature of 400 °C, module 15 recovered more heat than the module 25 and module 35. The change in behaviour after 300 °C can be attributed to the contribution of the radiation to the heat transfer compared to the natural convection. At higher heater temperatures, the heat from the tile is mainly transferred through radiation. In this case, the impact of the surface area

at the evaporator section is more important as the view factor will be higher for module 15 than for the other modules.

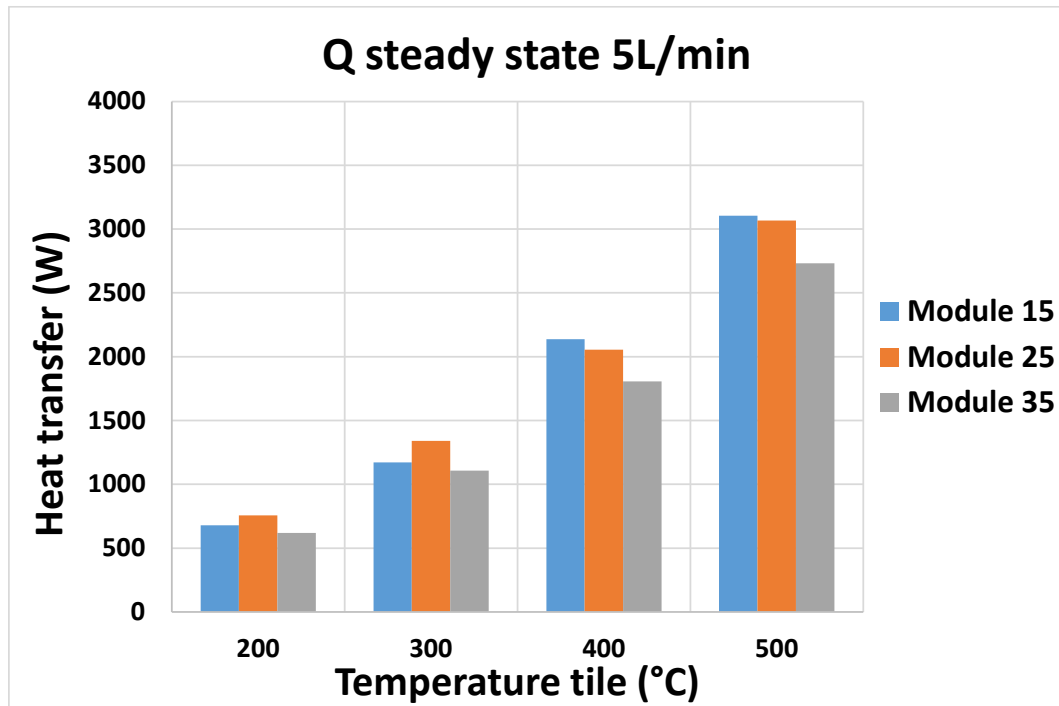


Figure 146 Heat recovered at a flow rate of 5 L/min at various heater temperatures

The variation of heat recovery for the different modules can clearly be seen in Figure 147. Similar to

Figure 146 the variation of heat transfer is not significant for a heater temperature below 400 °C. At 400 °C, module 15 was able to recover up to 2300 W while module 25 and module 35 recovered 1970 W and 1790 W. At 500 °C, module 15 recovered 3500 W, module 25 recovered 3020 W and module 35 recovered 2700 W.

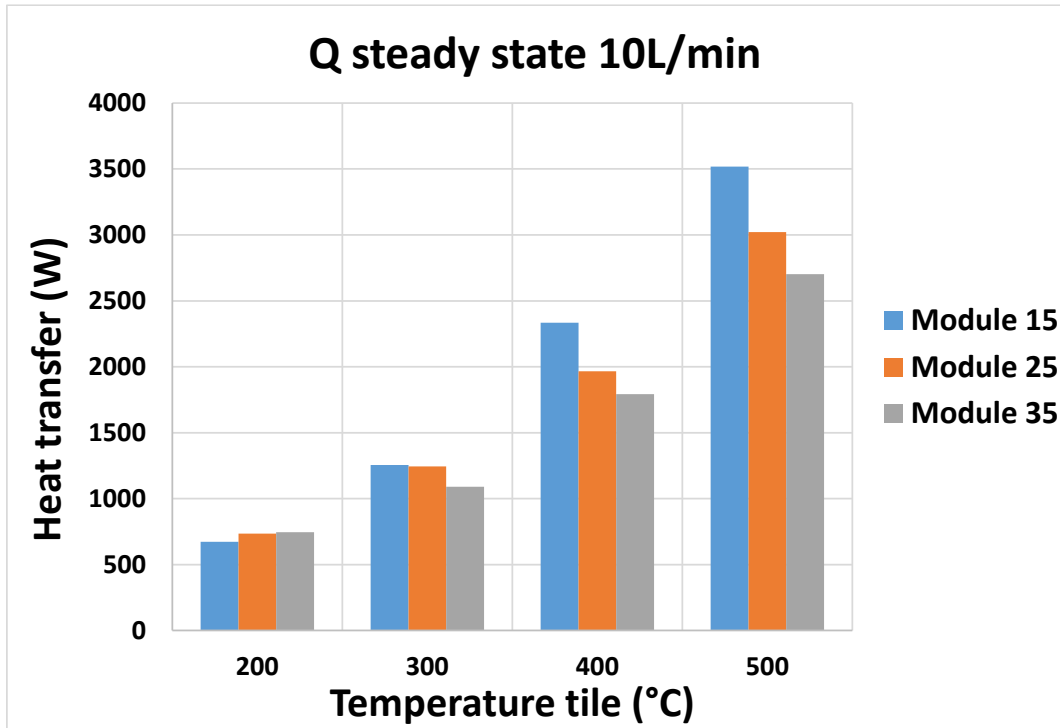


Figure 147 Heat recovered at a flow rate of 10 L/min at various heater temperatures

The density of pipes in the evaporator section is driving the amount of the heat the system will be able to recover. To achieve a uniform temperature on the tile temperature on a full-scale installation, the heat recovered by the heat pipe modules will need to vary in the cross section of the kiln. By using modules with varying evaporator surface areas, the system will be able to control the uniformity of the tile temperature.

6.1.3.5 Contribution of natural convection to the overall heat transfer rate

The surface area occupied by the heat pipe in the kiln is larger than for the single pipe. It can be seen from Figure 148 that the contribution of natural convection to the overall heat transfer rate is much larger. It can be noted that as the heater temperature increases, the contribution diminishes as radiation heat transfer will be the main components for high heater temperatures. Also, as the surface of the evaporator decreases, the natural convection contribution is lower. For a heater temperature of 200 °C, the contribution of natural convection to the overall heat transfer rate is 53%, while under the same condition it is 39% for module 35.

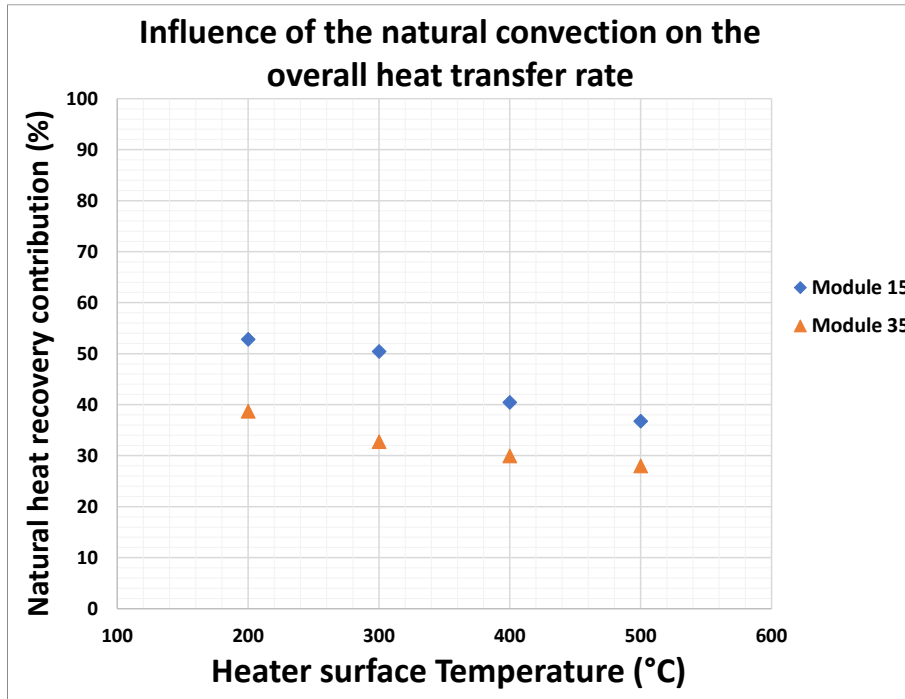


Figure 148 Influence of natural convection overall heat transfer rate for modules 15 and 35 under a flow rate of 15 L/min

6.3.2 Boiling thermal resistance.

6.3.2.1 Experimental results

Impact of the evaporator surface area on the boiling thermal resistance

The boiling thermal resistance is strongly impacted by the area of the evaporator as the boiling thermal resistance depends on the heat flux at the evaporator surface. In order to assess the impact of the evaporator area on the boiling resistance, the different conditions are plotted in Figure 149. As the correlations developed in the literature apply for a steady and uniform boiling regime, selection of the best cases had to be carried out. To achieve a uniform boiling regime, the variation of temperatures in the evaporator needs to be minimal, thus, only cases with a temperature variation below 5 °C were selected for comparison with predictions. The thermal boiling resistance for all the modules decreases as the heat flux increases. As the maximum temperature at the heater is achieved at 500 °C for all of the modules, the maximum boiling heat flux achieved in module 15 will be lower than for the other modules. The maximum thermal resistance for module 15 was achieved at a heat flux of 6.1 kW/m² with a value of 0.00918 °C/W. The thermal resistance is at the lowest for a heat flux of 18.3 kW/m² with a value of 0.001759 °C/W. The thermal resistance for module 25 is higher at lower heat fluxes apart from one case. When the heat flux is above 10 kW/m², the thermal resistances are similar. In the case of module 35, the value of the boiling resistance is higher for most of the cases.

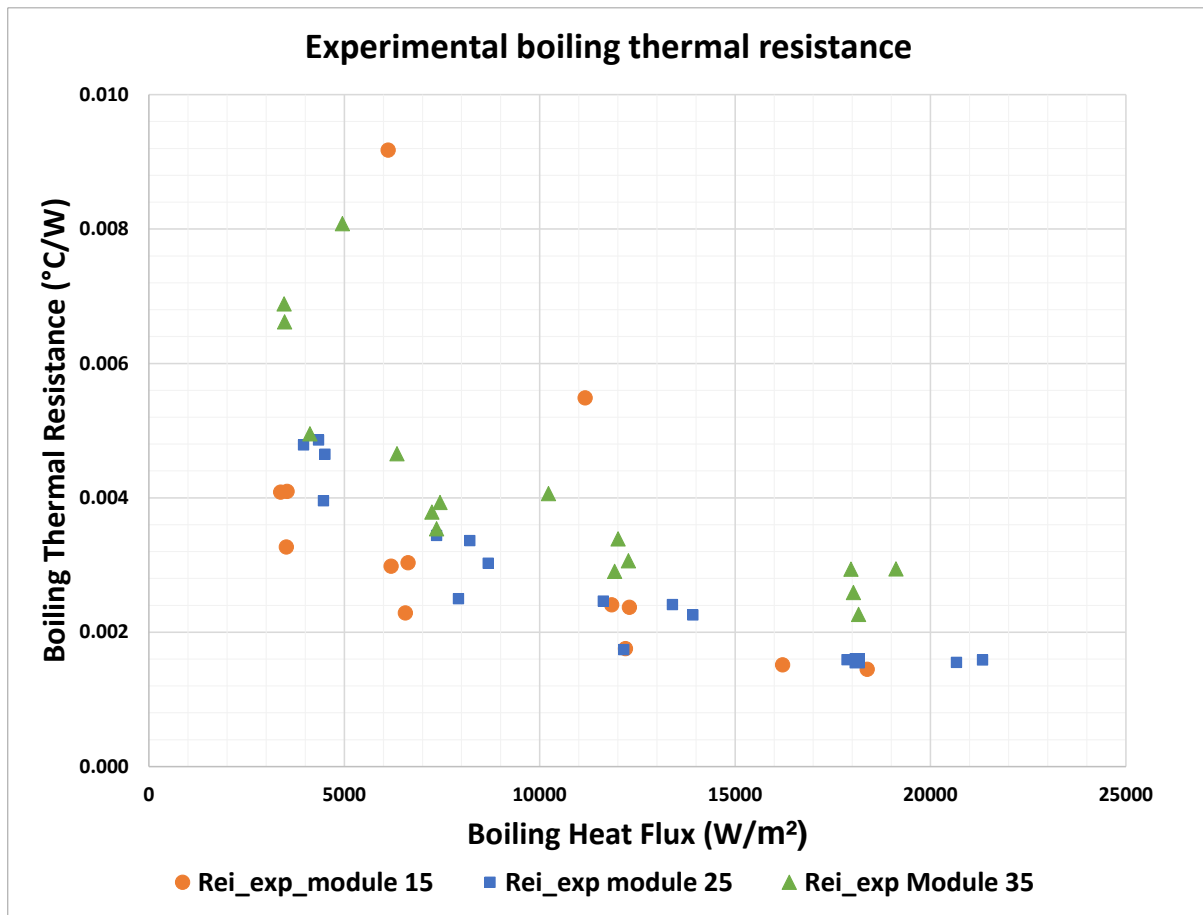


Figure 149 Experimental boiling thermal resistance for three evaporator designs

The boiling thermal resistance was compared to correlations available in the literature. The predictions obtained for module 15 are presented in Figure 150. It can be seen that the predictions for a heat flux below 11 kW/m² did not achieve a good agreement with the experimental data. *Imura*, *Shirashi* and *Kiatsiriroat* predicted a much lower thermal resistance than the experimental value. *Labunstov* overpredicted the experimental thermal resistance at low heat flux. *Kiatsiriroat* was in good agreement with the experimental value for heat fluxes between 15 kW/m² and 19 kW/m². Similarly, for *Imura* and *Shirashi* the predicted boiling thermal resistance was close to the experimental boiling resistance. *Labunstov* overpredicted the thermal resistance for heat fluxes between 15 kW/m² and 19 kW/m² but good agreement remains.

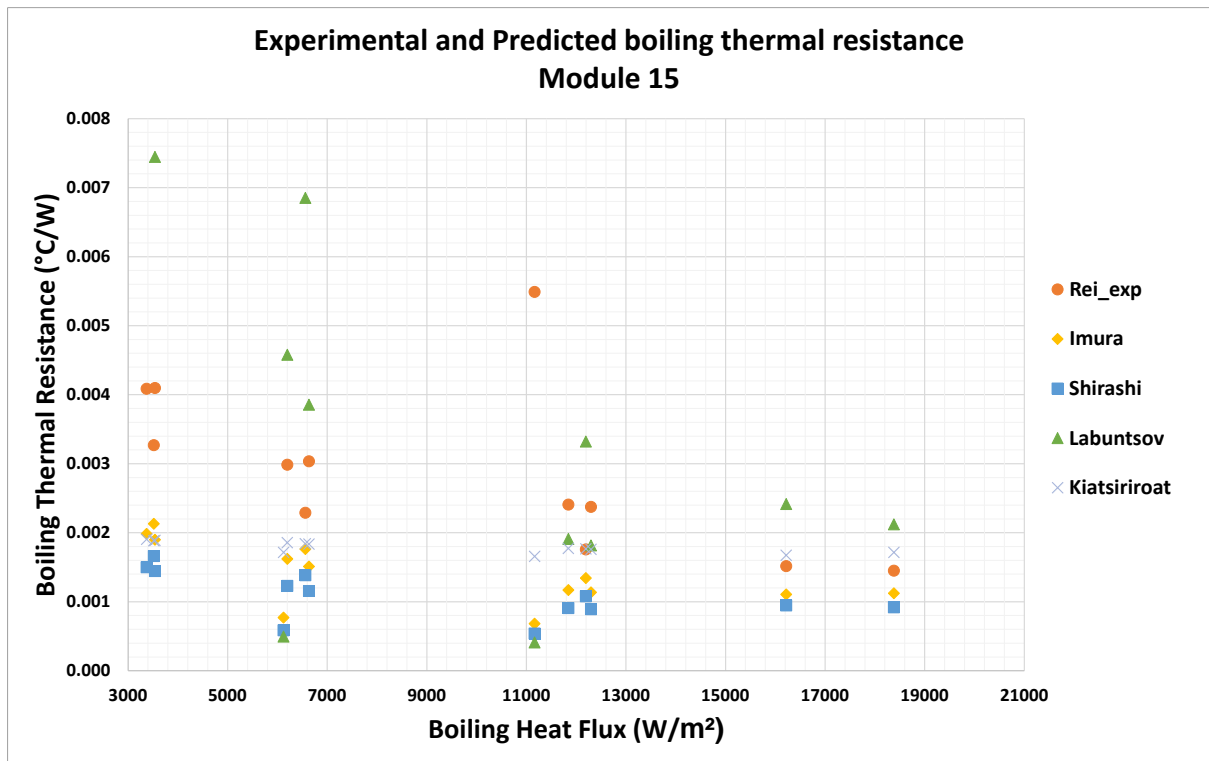


Figure 150 Experimental and predicted boiling thermal resistance for Module 15

The predicted values for the module 25 are plotted in Figure 151. A similar trend to the predicted boiling resistances in the module 15 can be seen. In the module 25 at low heat flux all the correlations gave results lower than the experimental values apart from those from *Labunstov*, that have a good agreement from 3 kW/m² to 9 kW/m². At higher heat fluxes, *Imura*, *Kiatsiriroat*, and *Labunstov* achieved predictions close to the experimental values. *Shirashi* obtained values lower than the experimental boiling resistances. Like Module 15, the best predictions are achieved for heat fluxes higher than 15 kW/m².

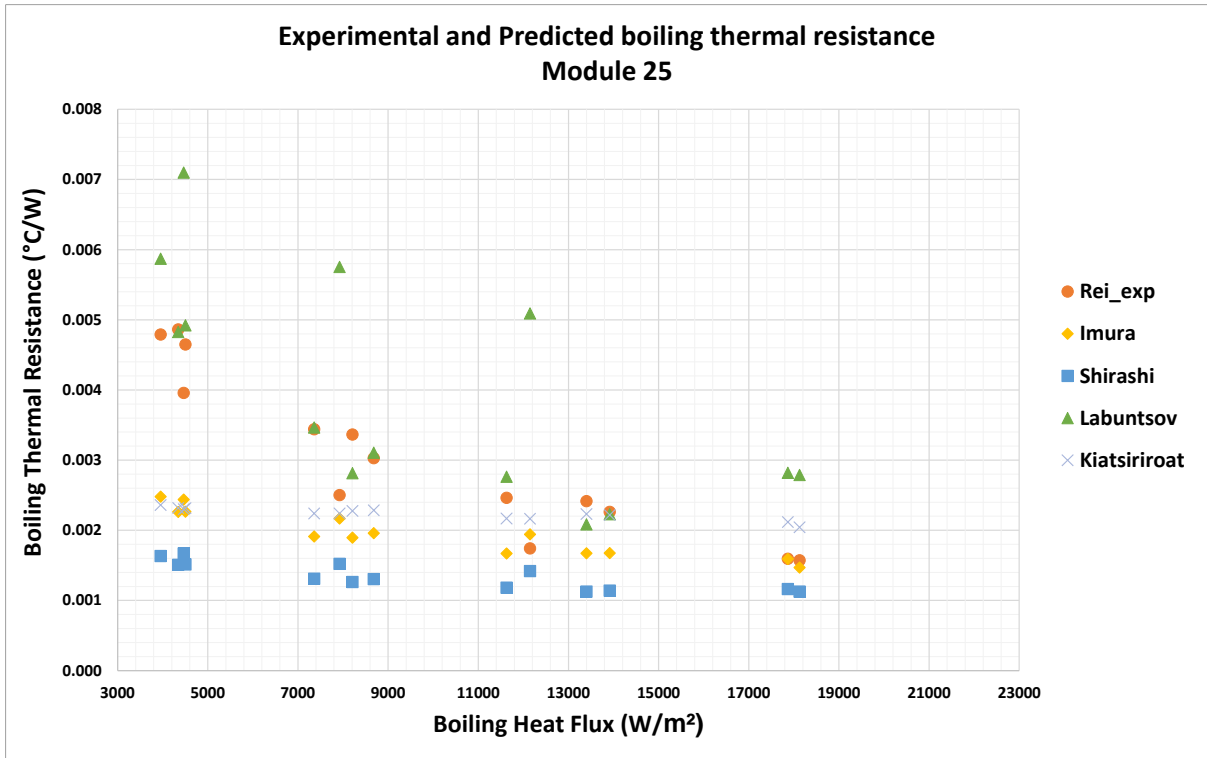


Figure 151 Experimental and predicted boiling thermal resistance for Module 25

The predicted values for the module 35 are plotted in Figure 152. Like the previous predictions, *Imura*, *Kiatsiroat* and *Shirashi* obtained lower boiling resistances at heat fluxes below 15 kW/m² for all the cases. *Labunstov* is in good agreement with the predicted values for most of the cases below 9 kW/m². Between 9 kW/m² and 13 kW/m² all the predictions were below the experimental values. For heat fluxes higher than 17 kW/m², *Kiatsiroat* achieved a good agreement with the experimental values.

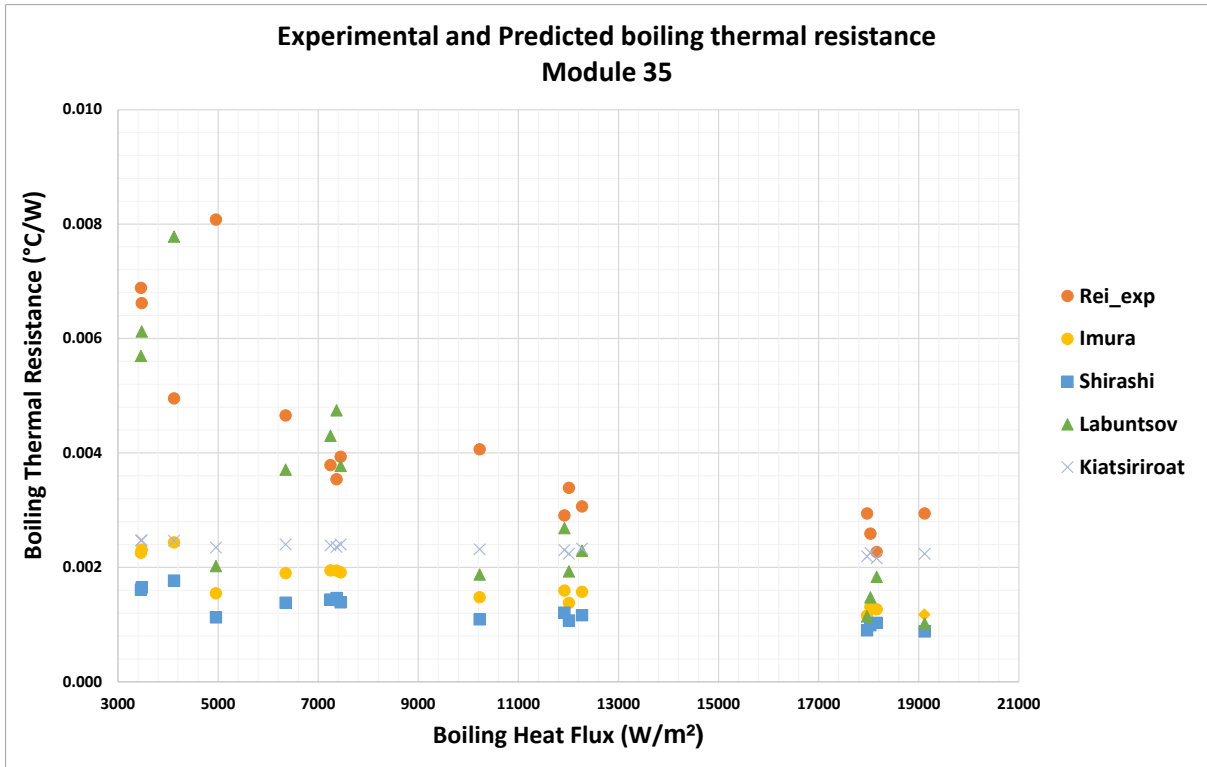


Figure 152 Experimental and predicted boiling thermal resistance for Module 35

It can be seen that the change in surface area did not have a major impact on the predictions, the value for most of the cases below a heat flux of 15 kW/m² are not performing well. It can be noted that the thermal resistance values in all the cases are below 0.008 °C/W. The influence of the thermocouple error on the determination of the thermal boiling resistance will be large. The determination of the accuracy of the correlations for the modules are plotted in Figure 153.

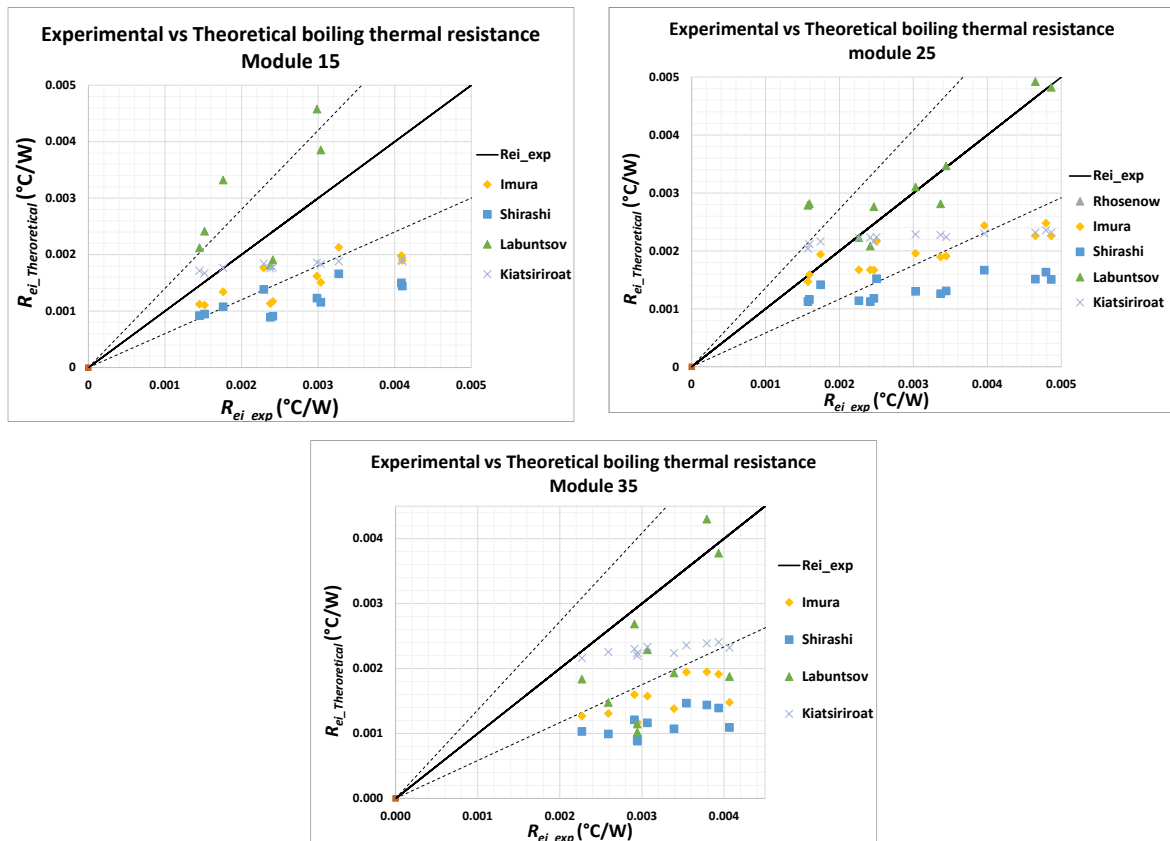


Figure 153 Comparison between the theoretical and experimental thermal resistance

Impact of the filling ratio on the boiling thermal resistance

The module 15 was used in two configurations to assess the impact of the filling ratio on the boiling thermal resistance. At low filling ratio, geyser boiling occurs for heat fluxes below 6 kW/m² as seen on Figure 154. It can be noted that the thermal boiling resistance decreases to 0.002 °C/W for both filling ratios and becomes stable for heat fluxes above 15 kW/m². The variation in the thermal resistance at different filling ratios is minimal, thus the impact of the filling ratio on the boiling thermal resistance is minimal.

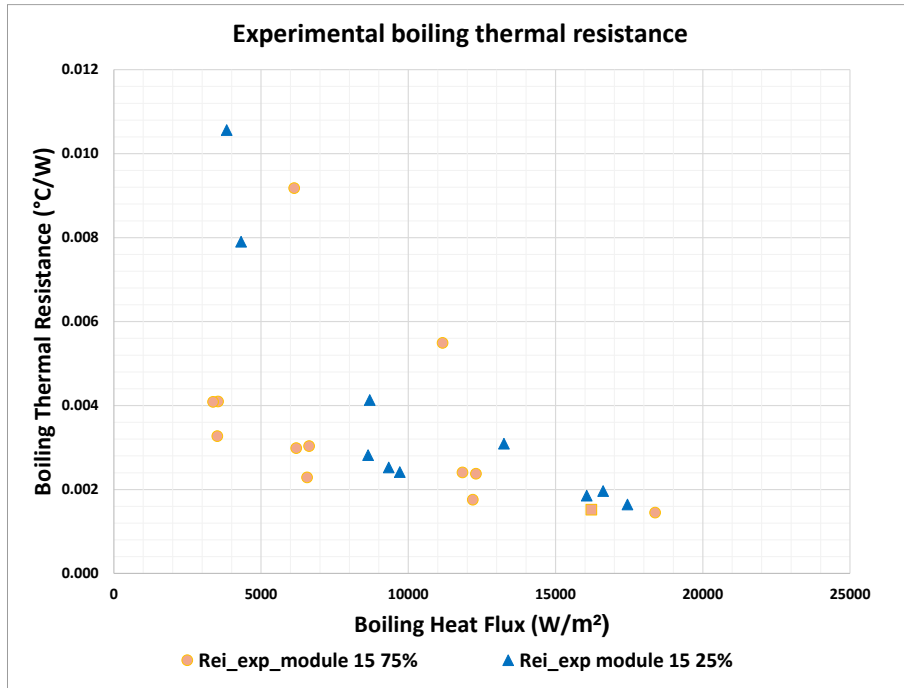


Figure 154 A comparison between the experimental boiling thermal resistance for Module 15 at FR 25% and FR 75%

6.3.2.2 Boiling thermal resistance prediction

The experimental results are compared with correlations available in the literature. The data compared with the correlations were selected under specific conditions. The correlations are validated for uniform evaporator temperatures and heat fluxes. To achieve the best accuracy on the correlations, the variation at the evaporator temperature did not exceed 6 kW/m². The maximum excess temperature selected did not exceed 9 °C. The results obtained by the correlations are compared to the experimental data and are plotted in Figure 155. At lower heat fluxes, the correlations did not perform well as geyser boiling occurred in the heat pipe. For heat fluxes higher than 8 kW/m², *Imura*, *Shirashi* and *Kiatsiroat* predicted values close to the experimental boiling resistance. *Labunstov* overpredicted the boiling thermal resistance for most of the cases. The prediction error is presented in Figure 156. As the boiling thermal resistance decreases, the prediction accuracy for most of the presented correlations decreases. For heat fluxes higher than 15 kW/m², the accuracy of the correlations is within ±40% for all the correlations except for *Labunstov*.

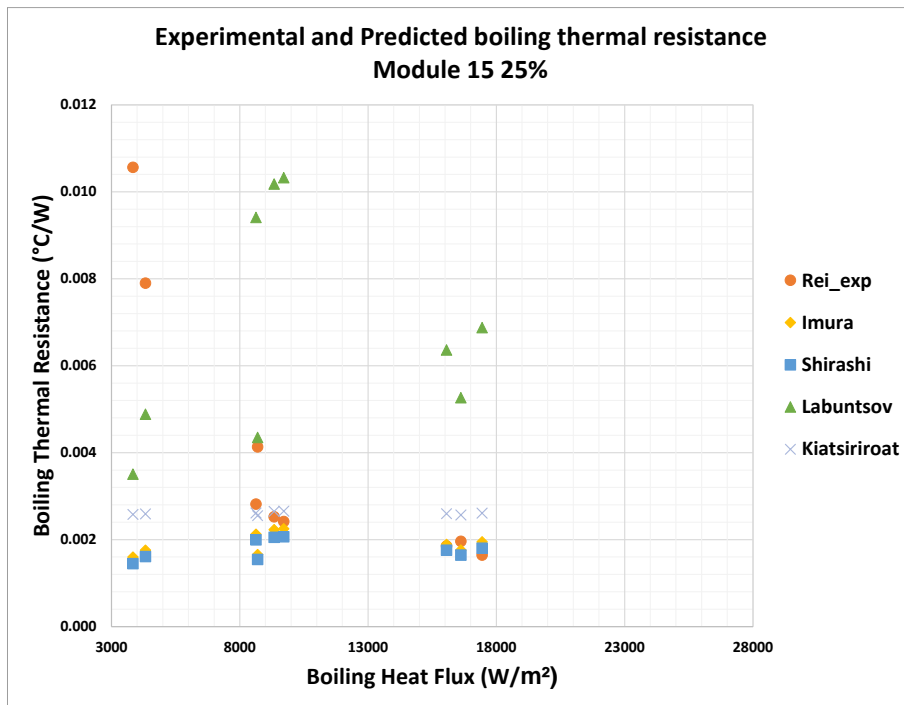


Figure 155 Experimental and predicted boiling thermal resistance Module 15 25%

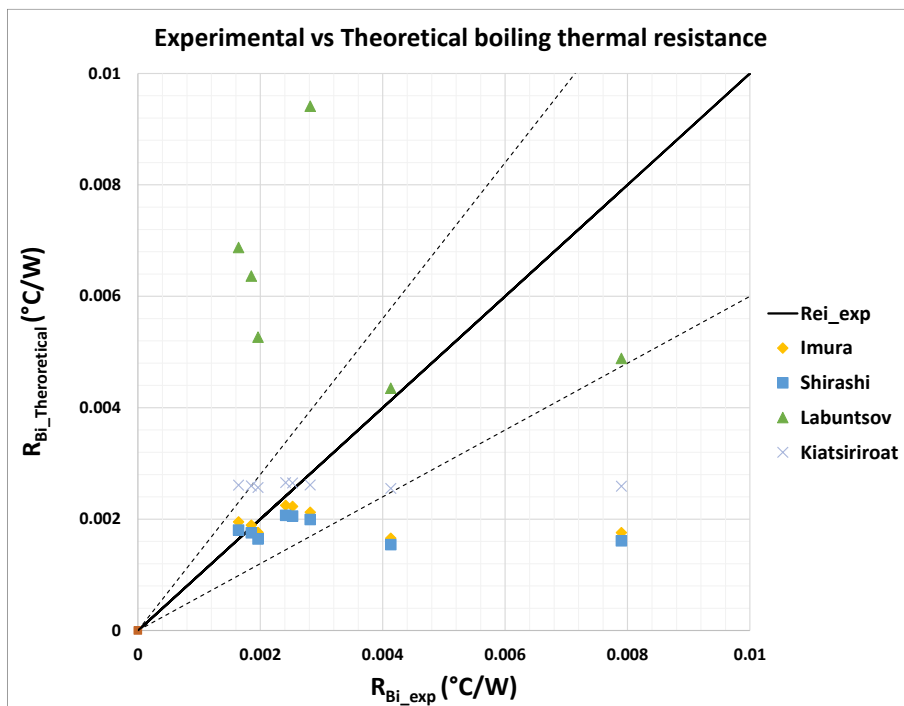


Figure 156 Experimental vs theoretical prediction boiling thermal resistance for Module 15 at FR 25%

6.3.3 Condenser thermal resistance.

6.3.3.1 Experimental results

The condensation resistance cannot be calculated directly as the design of the heat pipe did not allow the positioning of a thermocouple on the inner or outer surface of the condenser

section. To determine the temperature of the surface at the vapour/condenser interface, a similar method to the single pipe had to be carried out. The determination of the internal temperature of the pipe can be made by using the logarithmic mean temperature differential, the forced convection resistance and the heat transfer rate determined by the flow rate and water temperature at the inlet and outlet of the system. The error associated to this method is $\pm 20\%$. Once the temperature of the internal wall of the shell and tube is obtained, the temperature of the outer wall can be determined by the conduction thermal resistance. The condensation resistances for all the modules are plotted in Figure 157. Module 15 and Module 35 follow a similar trend, the condensation thermal resistance decreases with the increase in heat flux. A maximum is reached at 5 kW/m^2 and 3.9 kW/m^2 for a value of $0.0439 \text{ }^\circ\text{C/W}$ and $0.0423 \text{ }^\circ\text{C/W}$ for, respectively, module 15 and module 35. The minimum is achieved for heat fluxes higher than 20 kW/m^2 for a thermal resistance of less than $0.01 \text{ }^\circ\text{C/W}$.

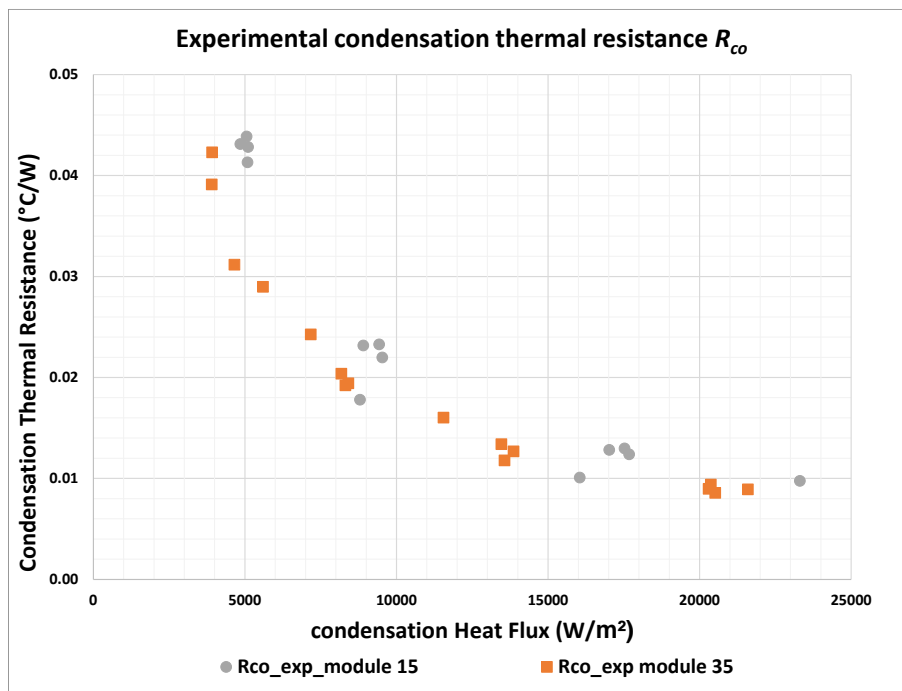


Figure 157 Experimental condensation resistance modules

The condensation resistance is calculated based on forced convection heat transfer correlations. To verify that the forced convection correlations are applicable in the current condenser section design, the UA value for the heat exchanger is calculated and presented in Figure 158. The UA values for the module 15 and 35 are similar. The dimensions of the heat pipe condenser section are similar, and the test were conducted for similar flow rates for all the experiments. The correlations used to determine the forced convection are correct.

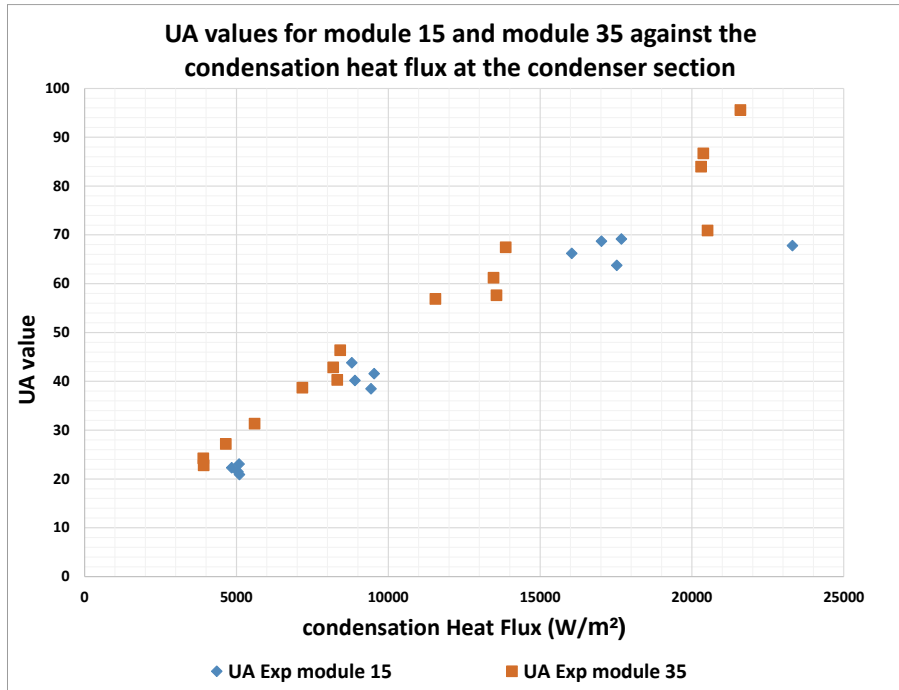


Figure 158 U values for the heat pipe module condenser section

6.3.3.2 Condenser thermal resistance prediction

The experimental values are compared to correlations available in the literature. *Nusselt* developed a correlation for the condensation of vapour on N rows. The results of the prediction using *Nusselt* [97] can be seen in Figure 159. The predicted thermal resistance is much lower than the experimental thermal resistance. The maximum value reached for the predicted value is 0.000485 °C/W for a heat flux of 28 kW/m². The trend of the predicted resistance across the heat fluxes is to increase as the heat flux increases. *Chen* [100] develop a correlation using the *Jakob* number which represents the ratio between the sensible heat and the latent heat released during the phase change occurring in the condenser section. The correlation results are not in agreement with the experimental data. *Rohsenow* [98] included a correction factor to the *Nusselt* correlation to account for the pressure in the condenser during condensation. The correlations did not perform well. Due to the design of the condenser and the non-uniform behaviour of the vapour in the condenser, the correlations used cannot be applied to predict the temperature of the outer wall of the condenser. To determine the temperature of condenser surface, new correction factors to the *Nusselt* correlation had to be developed.

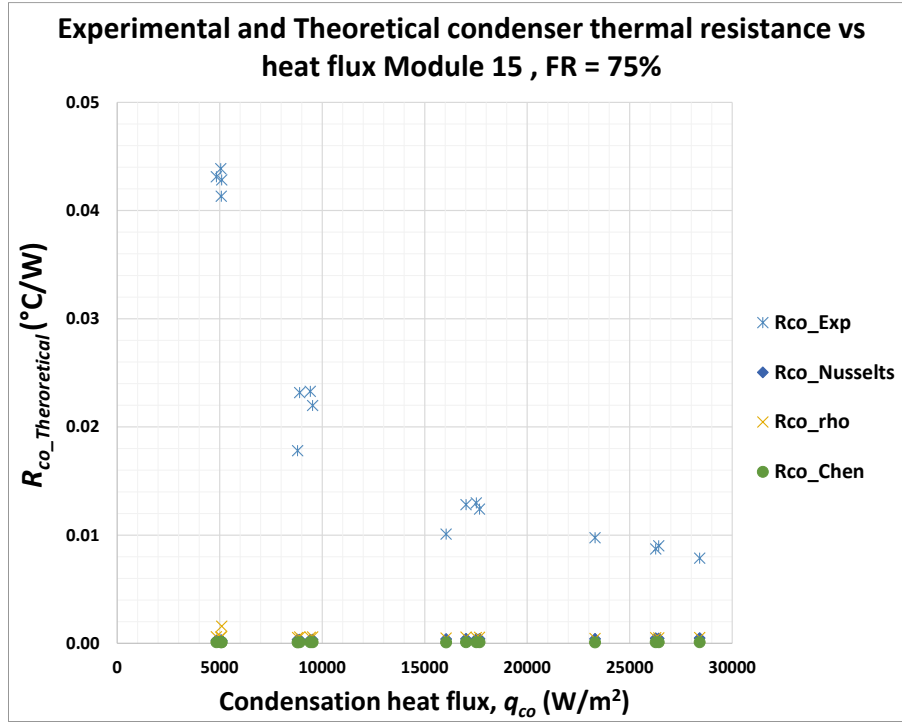


Figure 159 Experimental vs theoretical condenser thermal resistance for module 15 at FR =75%

6.3.3.3 Modified correlation for condensation thermal resistance prediction

The different elements of the Chen correlation were isolated to see the impact of the different components on the heat transfer coefficient. It was noted that the impact of the Jakob on the heat transfer coefficient was low. By removing the Jakob number from the second term of the correlation, the Jakob number will strongly impact the heat transfer coefficient. It was also noted that the modification of the numbers of rows of pipe did not change the heat transfer coefficient. By extrascing the Jakob number from the second termn of the correlation, a new correlation with a correction factor was introduced.

$$h_{co} = 0.725[1 + 0.2(N - 1)]Ja \left[\frac{\rho_l(\rho_l - \rho_v)gh_{fg}^*k_l^3}{ND\mu_l(T_v - T_{eo})} \right]^{\frac{1}{4}} \quad (260)$$

In order into account for the pressure in the condenser during the two phase process, the correction factor developed by Rohsenow was introduced to (260). The correlation is presented below.

$$h_{co} = 1.51 \left(\frac{P_v}{P_{crit}} \right)^{0.14} 0.725 [1 + 0.2(N - 1)]Ja \left[\frac{\rho_l(\rho_l - \rho_v)gh_{fg}^*k_l^3}{ND\mu_l(T_v - T_{eo})} \right]^{\frac{1}{4}} \quad (261)$$

$$\text{For } h_{fg}^* = h_{fg} + 0.68C_p(T_v - T_{eo})$$

By applying (260) and (261) and using the experimental data, the heat transfer coefficient is plotted in Figure 160. For a heat flux of 5 kW/m², (261) performed better with a heat transfer coefficient close to the experimental value. As the heat flux increases, it can be seen that (261) is lower than the experimental values, for heat fluxes higher than 15 kW/m², correlation (260) is in good agreement with the experimental condensation resistance. At 10 kW/m², the experimental value is between the predictions of the two correlations. It can be concluded that the correlations developed perform well for heat fluxes between 5 kW/m² and 30 kW/m². An approach can be deduced from the prediction. At heat fluxes lower than 5 kW/m², correlation (261) should be used. For heat fluxes from 5 kW/m² to 10 kW/m², an average value of both correlations is recommended to predict accurately the heat transfer coefficient. For heat fluxes higher than 10 kW/m², correlation (261) is recommended.

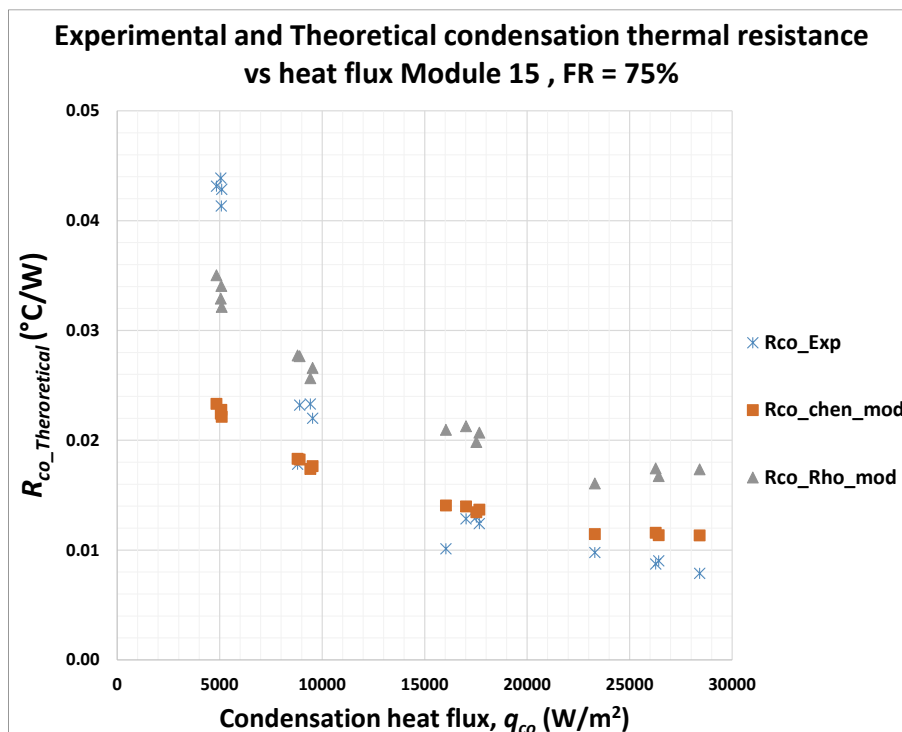


Figure 160 Experimental and theoretical prediction of the condensation heat transfer coefficient against the condensation heat flux.

The accuracy of the correlations is shown in Figure 161. The thermal resistance predicted for low heat fluxes is within $\pm 30\%$ for both correlations. The average of both correlations at lower heat fluxes is close to the predicted value. A deviation for (261) can be seen at higher heat fluxes while (260) remains within $\pm 30\%$ for most of the experimental data points.

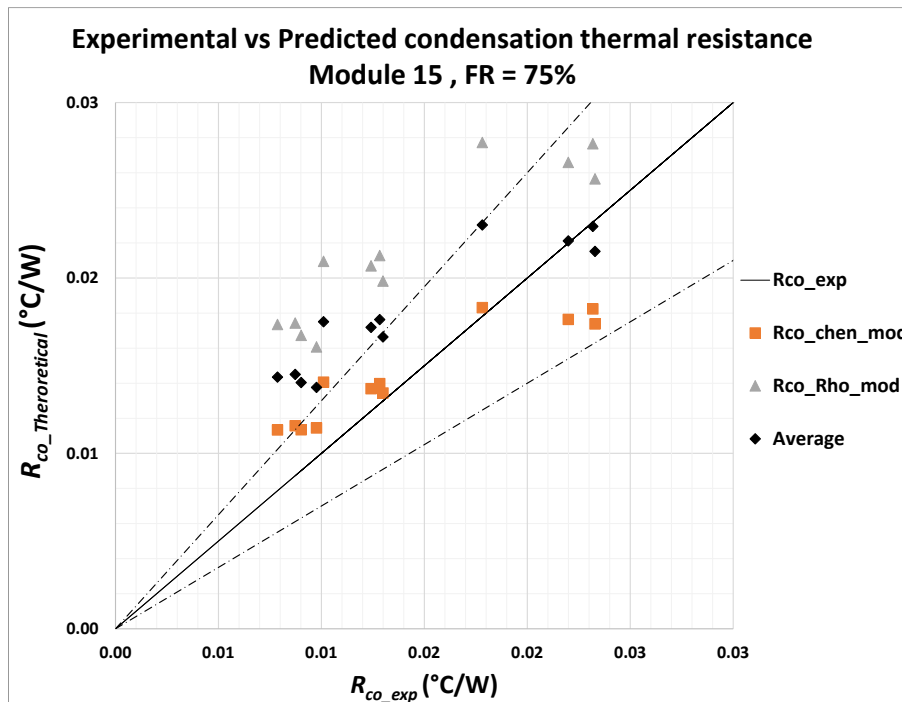


Figure 161 Experimental vs predicted condensation thermal resistance for Module 15 at 75% FR

To validate the developed correlations, the predictions using module 35 were made and are plotted in Figure 162. At heat fluxes lower than 5 kW/m^2 , a similar behaviour can be seen, (261) outperformed (260) with an error lower than $\pm 25\%$. The average between the correlations performed well for heat fluxes from 5 kW/m^2 to 7 kW/m^2 . For heat fluxes higher than 7 kW/m^2 the performance of (260) is in good agreement with the experimental values, the error is within $\pm 25\%$ for heat fluxes between 7 kW/m^2 and 15 kW/m^2 . For higher heat fluxes the error increases to $\pm 40\%$. The correlations behave similarly for different evaporator surfaces and different vapour temperatures. The heat transfer rate also varied between the two sets as module 35 tends to recover less heat than module 15.

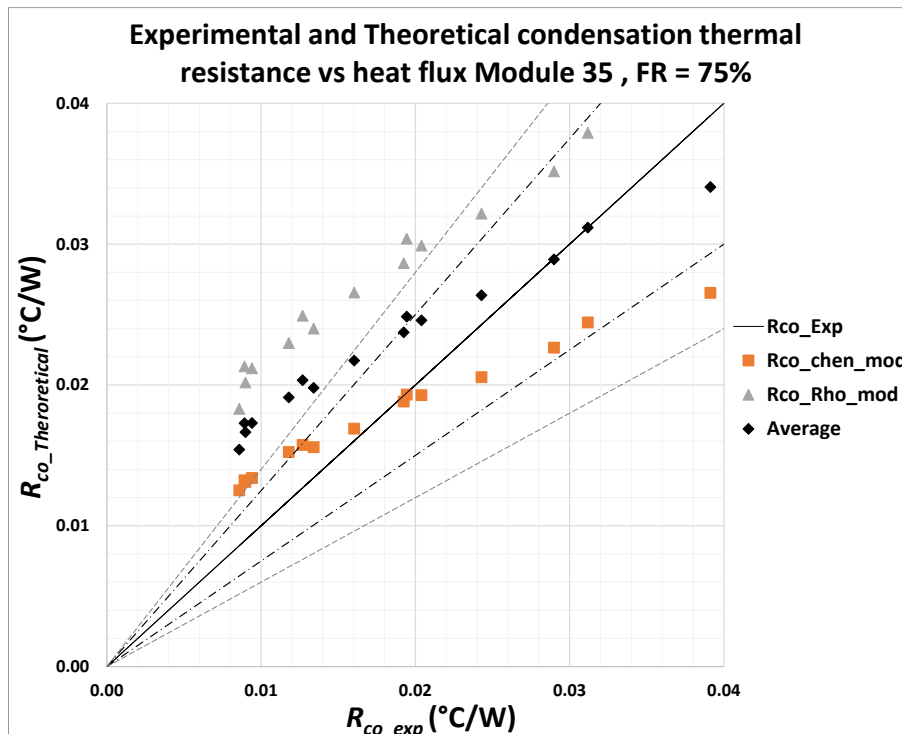


Figure 162 Experimental and theoretical condensation thermal resistance vs the heat flux for module 35 with 75% FR

6.3.4 Experimental overall thermal resistance

The overall thermal resistance of the heat pipe modules for different heat fluxes can be seen in Figure 163. The overall thermal resistance for each model is decreasing as the heat flux applied to the evaporator section increases. It can be noted that for heat fluxes below 8 kW/m², the overall thermal resistance of module 15 is higher than for module 35. For heat fluxes above 8 kW/m², the thermal resistance for each module is similar. The difference is mainly due to the working temperature of the heat pipe, which is higher for module 15.

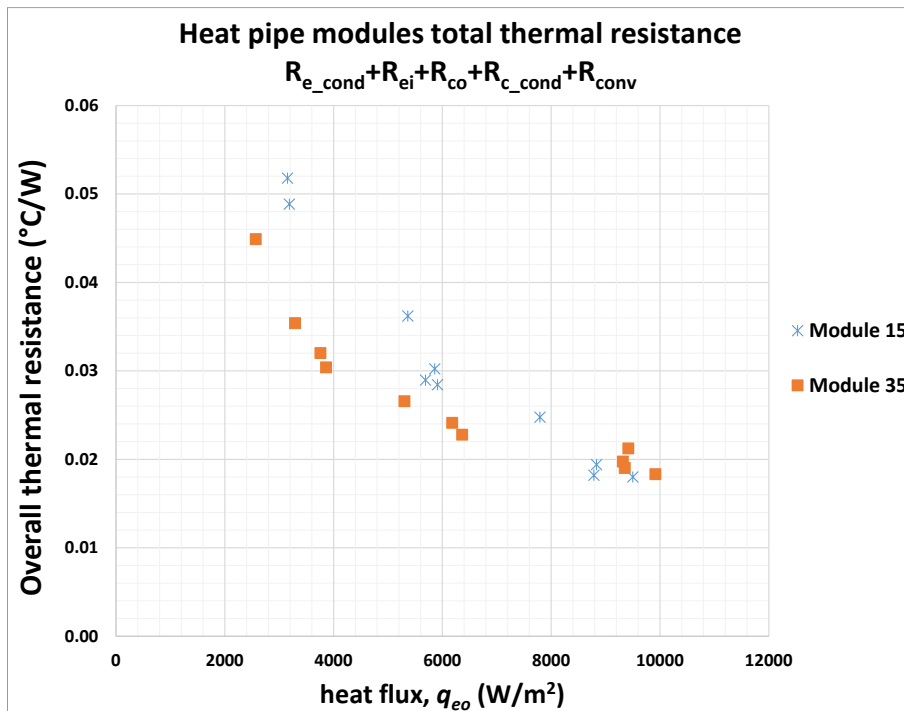


Figure 163 Heat pipe modules overall thermal resistance

6.3.5 Validation of the theoretical modelling predictions

The model developed in the theoretical chapter is applied to the modules for four cases under different conditions. The impact of the flow rate, the change in evaporator surface and different heat fluxes are investigated.

6.3.5.1 Heat pipe temperature prediction

The experimental measurements and the predicted temperatures for the module 15 at a heat flux of 6.5 kW/m² are presented in Figure 164. The predicted value for the vapour temperature and water outlet are close to the experimental value with a maximum difference of 0.02 °C. The evaporator temperature predicted by the model is 2.65 °C higher than the experimental evaporator temperature.

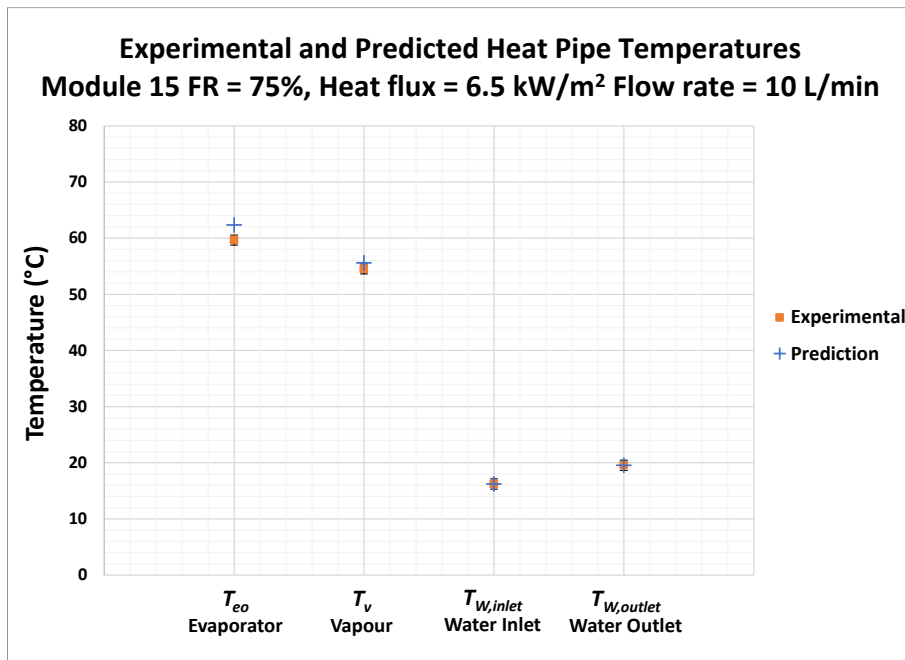


Figure 164 Experimental and predicted heat pipe temperatures, module 15, FR 75%, 10 L/min

Similar predictions of the heat pipe temperatures were made for a similar heat flux with a flow rate of 15 L/min at the condenser section and they are plotted in Figure 165. The predicted value for the water outlet is 0.01 °C higher than the experimental value. For the evaporator and the vapour temperature, the model overpredicted the experimental values by 3 °C.

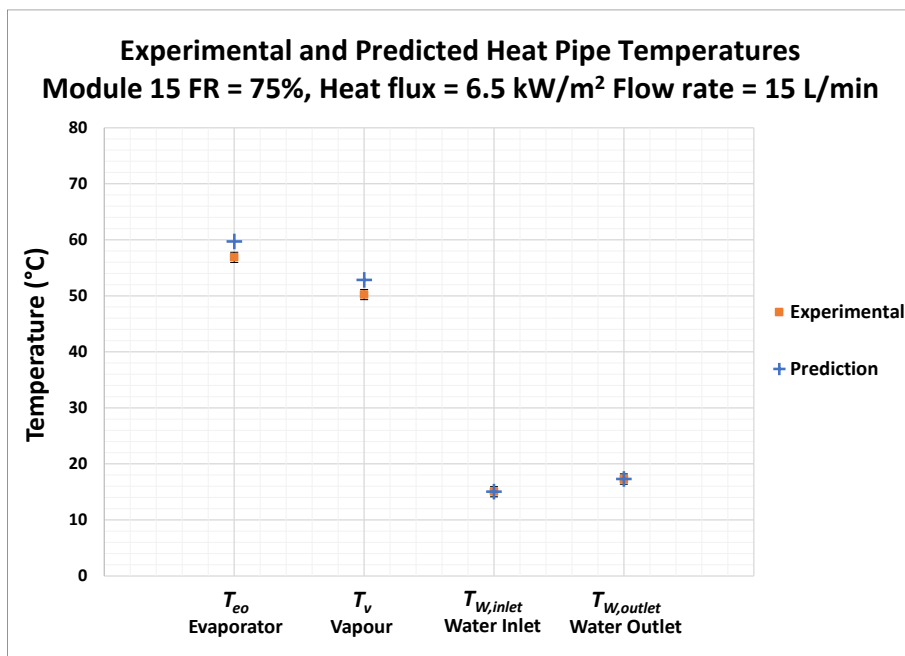


Figure 165 Experimental and predicted heat pipe temperatures, module 15, FR 75%, 15 L/min

To verify the validity of the model at different evaporator section heat transfer areas, the model was applied to module 35. The results for the heat pipe temperatures are plotted in Figure

166. The temperatures predicted by the model with module 35 are in excellent agreement with the experimental temperatures. The maximum temperature difference can be observed for the vapour temperature with a value of 1.08 °C. The maximum evaporator and water outlet temperature differences are 0.48°C and 0.02 °C, respectively.

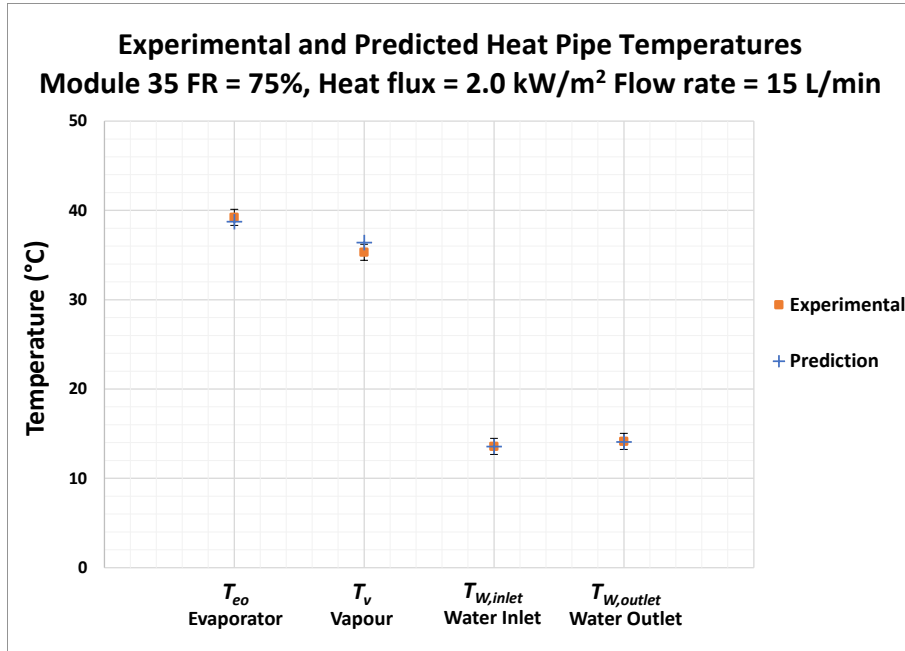


Figure 166 Experimental and predicted heat pipe temperatures, module 35, FR 75%, 15 L/min

6.3.5.2 Heat recovery prediction

The heat recovery predicted by the model for module 15 is presented in Figure 167. The variation of heat recovery between the predicted value and the experimental heat transfer rate is $\pm 10\%$. The agreement between the predicted value and the experimental heat transfer rate is excellent.

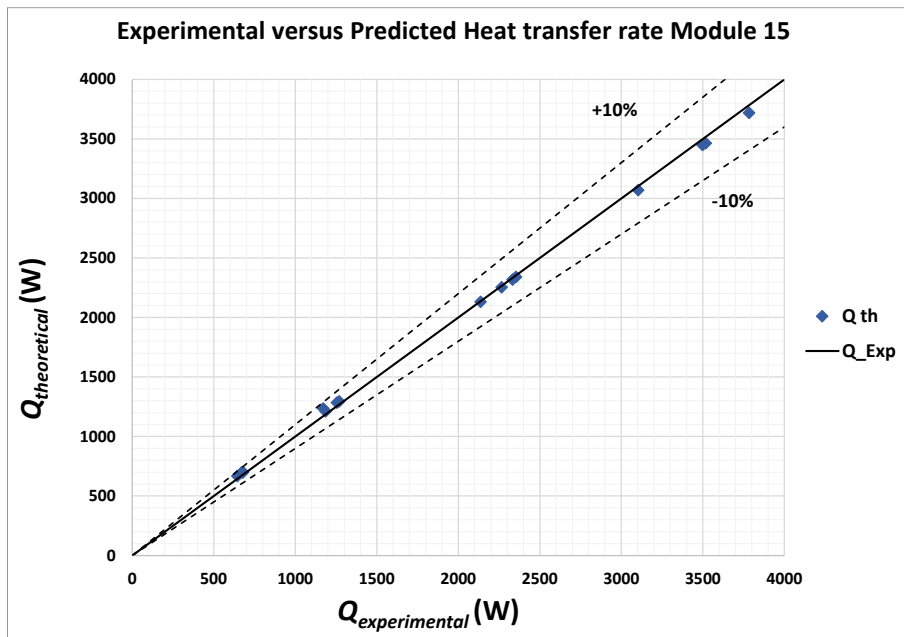


Figure 167 Theoretical versus experimental heat transfer rate module 15

As the surface area of the evaporator will have a major impact on the overall heat transfer rate of the heat pipe module, the model was applied to the module 35 to see the accuracy of the model with a lower evaporator heat transfer area. The results are plotted in Figure 168. The model accurately predicted the experimental heat transfer rate within $\pm 10\%$ error.

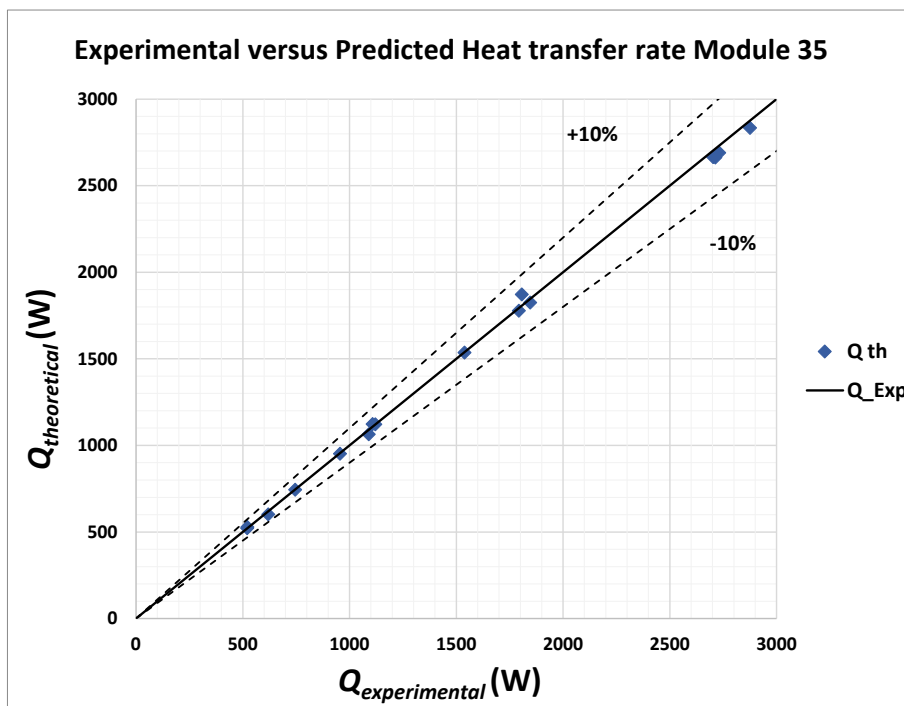


Figure 168 Theoretical versus experimental heat transfer rate module 35

6.4 General discussion on lab test modules

The single heat pipe was able to extract heat from a kiln at varying filling ratios for a heater temperature varying between 200 °C and 500 °C. The system managed to recover a minimum of 110 W for a filling ratio of 25% and a maximum of 580 W for a filling ratio of 50%. The respective heat fluxes were 2.5k W/m² and 26 kW/m². The tests and the analysis done on the single pipe highlighted the benefit of having a near horizontal evaporator section coupled with a vertical condenser section. This presents new opportunities for the application of the heat pipe as the limitation on the inclination of the heat pipe can be problematic for certain applications where the condenser needs to be external to the heated area and when the space in the kiln is limited. The heat pipe presents some limitations related to the behaviour of the pool in the heat pipe. It can be concluded that if the filling ratio in the evaporator is higher than 50%, the impact on the condenser resistance is large. The liquid projected onto the condenser and the increase in the falling film thickness drastically increase the condenser thermal resistance of the heat pipe, thus increasing the heat pipe temperature. This phenomenon can be a strong limitation as it will impact on the potential application of the heat pipe if the filling ratio is higher than 50% in terms of safe working temperature and overall heat transfer rate. For filling ratios lower than 50%, the occurrence of geyser boiling is also a problem as the heat pipe will not be able to provide a steady heat recovery. Also, the occurrence of geyser boiling in repetitive cycles will reduce the life span of the system. The liquid hitting the end cap of the condenser will damage the shell over time, leading to the destruction of the heat pipe.

In order to cover the entirety of a kiln cross section and after validating the suitability of a near horizontal evaporator section combined with a vertical condenser section, the module heat pipe composed of rows of tubes was developed. As the condenser section in the single heat pipe was not suitable due to the limited heat transfer area, a new condenser heat pipe was used. The module heat pipe was tested for different designs and conditions. The main achievement is the modularity of waste heat recovery by modifying the evaporator surface area. The module performed well under the test conditions. Module 15 achieved a maximum heat recovery of 3.7 kW and a minimum of 650 W. Module 25 recovered up to 3.6 kW and a minimum of 670 W. Module 35 with the lowest evaporator density achieved a maximum of 2.9 kW and a minimum of 520 W. The correlations selected for the boiling on the modules and the single pipe behaved in a similar way. However, as the surface area in the modules is higher than for the single pipe, the thermal resistance was better for the module. Geyser boiling did not occur during the module testing. It can be concluded that the new module design prevents the occurrence of geyser boiling at low heat flux. This is an advantage as geyser boiling strongly impacts the stability and the life span of a heat pipe.

The new design in the condenser section involved the use of different correlations between the single pipe and the modules. The correlations available in the literature for condensation on tube bundles did not perform well. New correlations had to be used in order to assess the condensation thermal resistance. It can be noted that the new condenser design greatly improved the condensation thermal resistance compared to the single pipe.

The module design presents good advantages as discussed above. The disadvantages of this type of heat pipe is the difficulty in assessing the condenser thermal resistance. The correlations developed for the condensation resistance will need more data in order to be validated across a spectrum of conditions. Also, the design of the heat pipe can be difficult to implement as the evaporator section will present challenges for installation in a retrofit kiln. The manufacturing of the heat pipe also presents limitations. The distance between the pipes cannot be reduced for module 15 because of welding requirements. Indeed, this type of system is classified as pressure equipment, following rules that regulate the minimum space between welds.

The development and validation of the heat pipe module however open new opportunities for waste heat recovery in a variety of applications that require a near horizontal heat pipe evaporator section.

The use of a near horizontal evaporator section coupled to a vertical condenser section is an innovative way to recover heat for a kiln. A similar study using a straight heat pipe was conducted by *Almahmoud*. This heat pipe was inserted in a kiln and exposed to a heat source with different inclination angles. The values obtained in terms of heat transfer rate were similar to the single heat pipe with a range of 73 W to 573 W. The study focused on the impact of the inclination angle and the treatment of the evaporator surface. The surface treated with black paint showed a significant increase in the radiation heat recovery.

Almahmoud [113] also developed a novel flat heat pipe application for the steel industry. The heat pipe is composed of rows of pipes connected at the bottom by a collector and at the top with a shell and tube condenser section. The system was exposed to a high intensity radiative source composed of electrical heater lamps. The heat pipe was tested at varying conditions. The surface of the evaporator was coated with a black paint that enabled the heat pipe to reach a heat transfer rate of 8.5 kW. The use of a back plate on the flat heat pipe to enhance the heat transfer rate was also investigated. A potential modification to the module heat pipes could be the use of a back plate and a coating on the heat pipe to enhance the heat transfer rate. However, a higher heat source will need to be used as the heat source used in the module test reached a maximum of 3.8 kW.

Jouhara [114] investigated a single pipe with a horizontal evaporator section charged with water and an azeotropic fluid. The heat pipe was tested at a heat transfer rate varying from 50 W to a maximum of 800 W. The heat pipe was also tested at different inclination angles from 0° to 90°. In the case of the single pipe presented in this thesis, the heat flux applied to the heat pipe was not uniform as the radiation heat transfer rate was only on one side of the heat pipe. Jouhara used a heater that provided a uniform heat flux across the heat pipe. A similar result for the overall thermal resistance can be observed. As the heat transfer rate increased, the overall thermal resistance decreased. At heat transfer values above 300 W for the water, the thermal resistance became stable. The comparison on the type of working fluid highlighted the impact of the fluid properties on the temperature distribution of the heat pipe evaporator section, which is more uniform for the azeotropic fluid than for the water at a horizontal evaporator section. However, the impact of the filling ratio in the evaporator section was not investigated. An interesting study could be carried out on the impact of the fluid properties on the heat transfer rate, the thermal resistance of the heat pipe and geyser boiling.

It can be concluded that the experimental results of the single heat pipe and the module heat pipes proved the validity of a near horizontal evaporator section. The condenser section in the module heat pipe should be used. It can be also concluded that the heat transfer area at the evaporator section can be used as a means to tune the heat transfer rate at different locations of a kiln depending on the need. As the heater temperature increased, the heat transfer rate significantly increased. The use of such a system is applicable for heat sources above 200 °C but will perform better for heat sources higher than 400 °C.

The developed modelling tool has been validated through experimental data. The selections of the correlations to be applied for different conditions participate in the accuracy of the predictions. The theoretical model can be used for large scale applications to predict the heat transfer rate, the heat flux, the heat pipe working temperatures and the water outlet at the condenser section. The model will accurately predict the values mentioned by an accurate determination of the view factor and the tile emissivity. It can be concluded that the use of such a heat pipe can cover a large domain of application in industrial sectors.

6.5 Industrial application of the radiative heat pipe ceiling.

6.5.1 Introduction

The theoretical tool developed for the module with the associated developed or available correlations was applied to an industrial roller earth kiln to fine tune the temperature of the tile after the firing section. The predictions for the heat transfer rate and the related temperature at the condenser outlet are discussed in this section. As the use of the module heat pipe

presents challenges in a retrofit case, and for timeline reasons, the system could not be validated experimentally.

6.5.2 Description of the full scale set up

The module heat pipe is applied in the roller earth kiln. The system positioned above the tile as shown in Figure 169 will recover the heat emitted by the tile through radiation. It can be seen in Figure 169 that the evaporator pipe density is higher in the centre of the heat pipe than at the side. This will allow a customized heat transfer rate to achieve a uniform temperature on the tile.

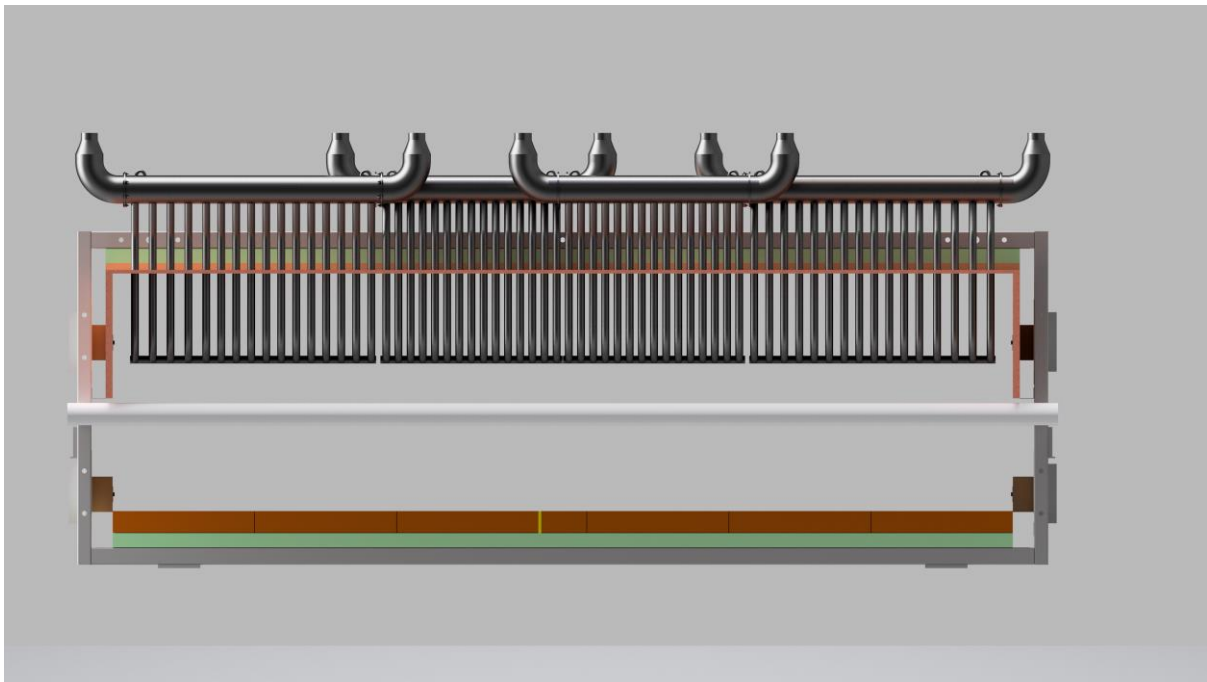


Figure 169 Cross section of the kiln with the heat pipe ceiling installed

The heat pipe design at the evaporator section is designed in a similar way to the module tested in the experimental section. The evaporator section for the heat pipe located in the middle of the kiln is composed of 15 tubes of 28 mm diameter and 755 mm length connected at the bottom by a collector. The evaporator section is connected to the shell and tube via an adiabatic section 415 mm long. The shell and tube condenser includes a 100 mm diameter external tube with a length of 672 mm. The condenser is composed of 22 condensing tube of 15 mm external diameter and 11 mm internal diameter. The heat pipe ceiling located on the side of the tile is composed of a similar evaporator section with varying heat pipe separations. The condenser section is a similar design to the module located in the middle of the kiln. The condenser section is 903 mm long. The drawings of the heat pipe ceiling are presented in Figure 170 to Figure 172.

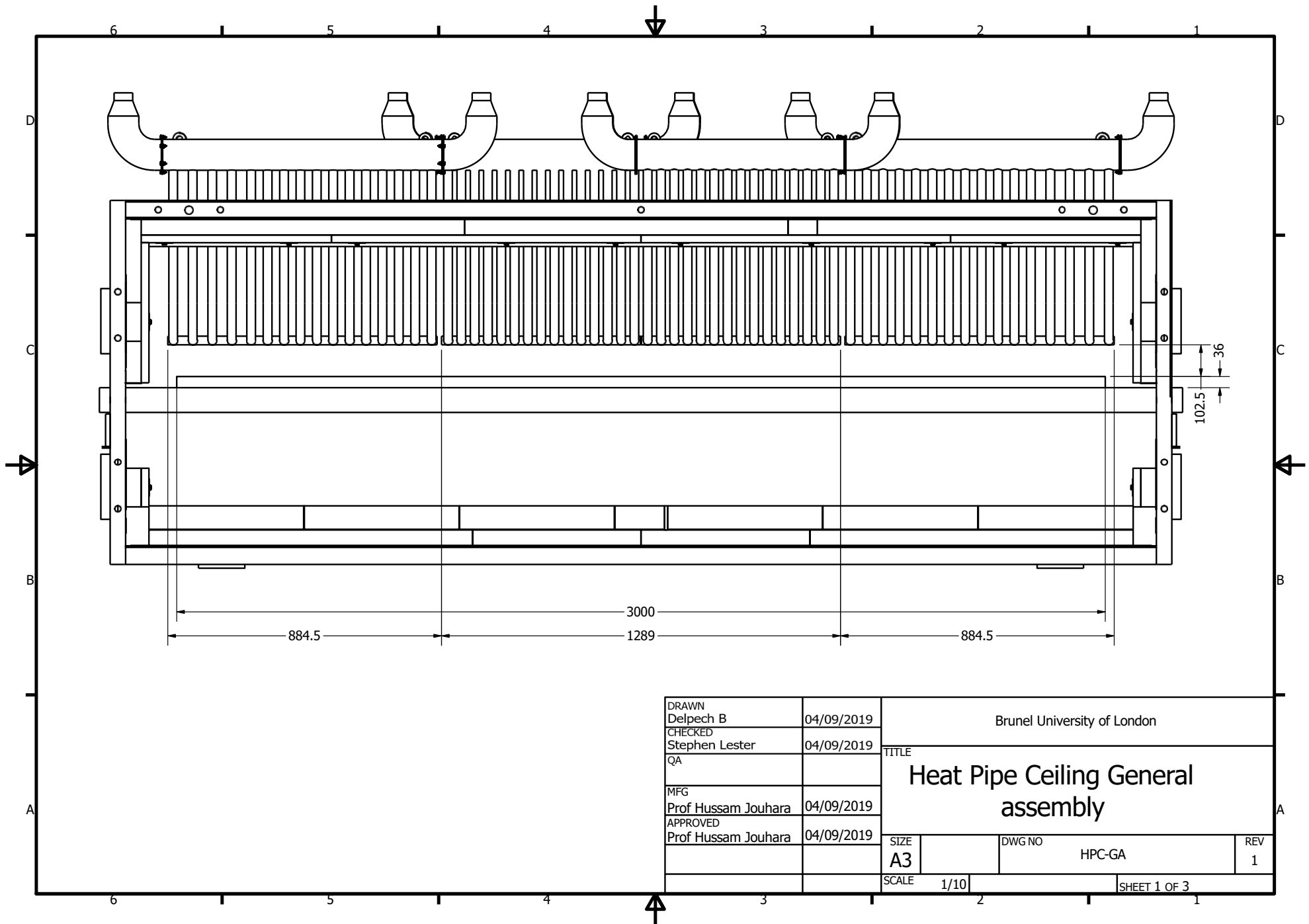
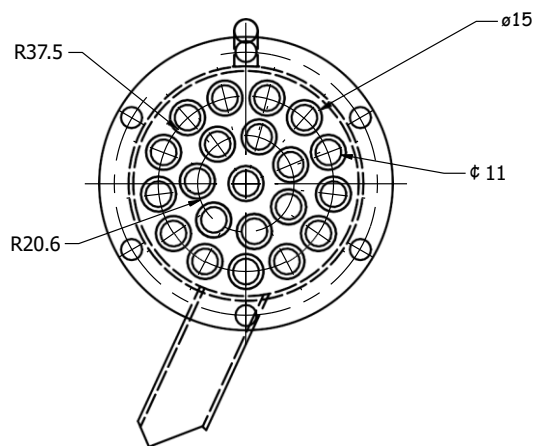
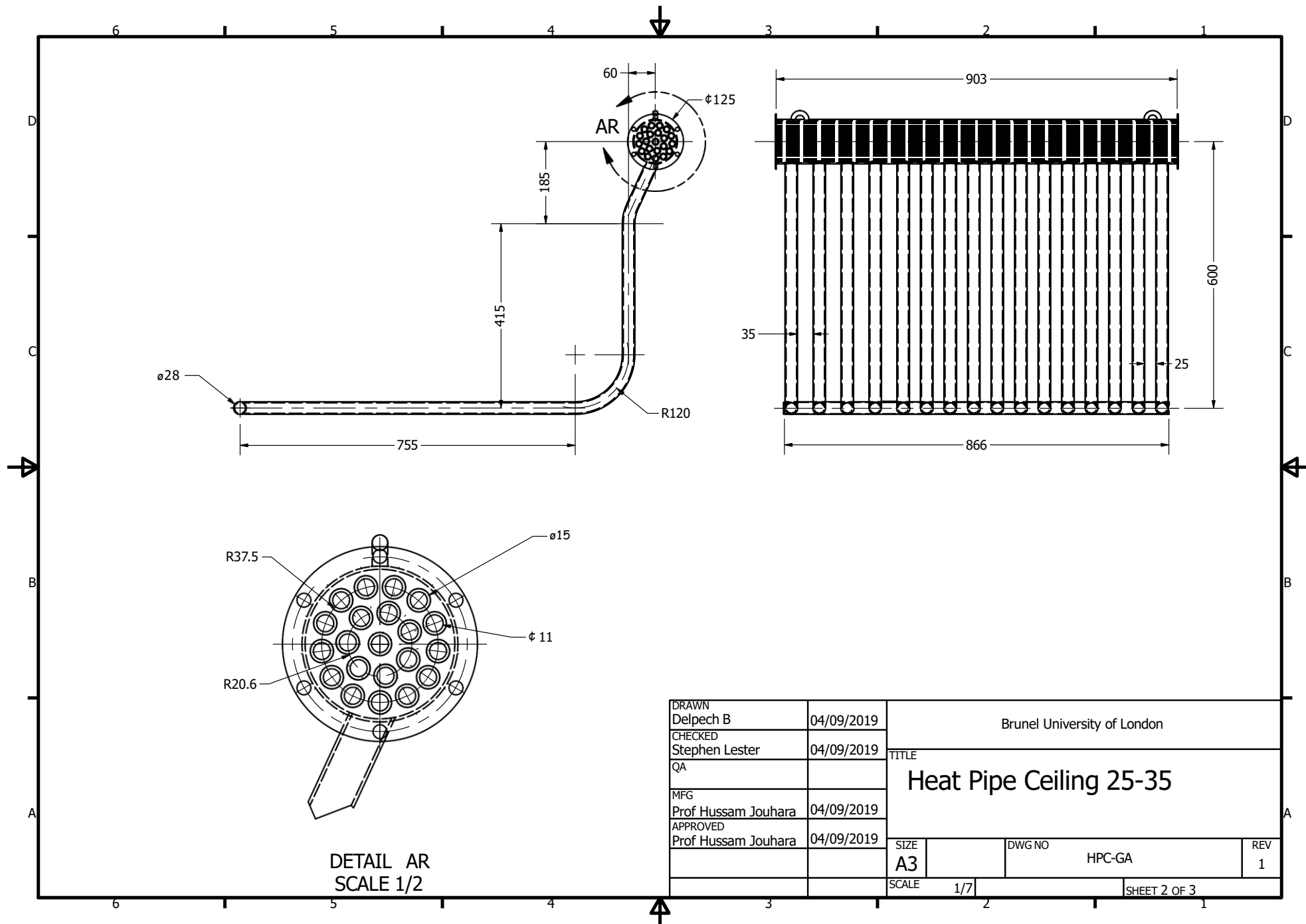


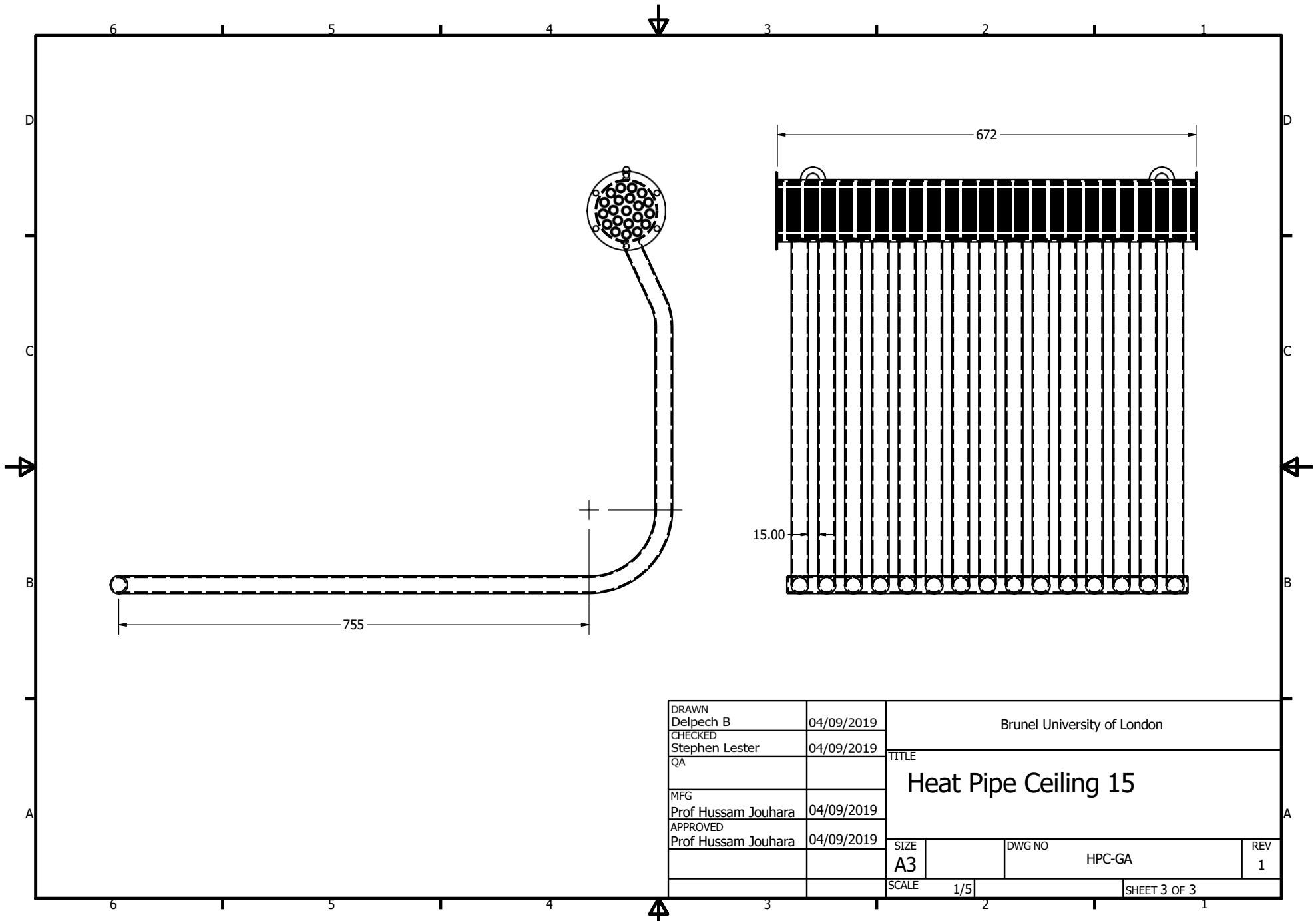
Figure 170 Heat pipe ceiling assembly



DETAIL AR
SCALE 1/2

DRAWN Delpch B	04/09/2019	Brunel University of London		
CHECKED Stephen Lester	04/09/2019	TITLE		
QA		Heat Pipe Ceiling 25-35		
MFG Prof Hussam Jouhara	04/09/2019	REV		
APPROVED Prof Hussam Jouhara	04/09/2019	SIZE A3	DWG NO HPC-GA	1
		SCALE 1/7	SHEET 2 OF 3	

Figure 171 Heat Pipe Ceiling 25-35



DRAWN Delpech B	04/09/2019	Brunel University of London		
CHECKED Stephen Lester	04/09/2019	TITLE		
QA		Heat Pipe Ceiling 15		
MFG Prof Hussam Jouhara	04/09/2019	SIZE A3	DWG NO HPC-GA	REV 1
APPROVED Prof Hussam Jouhara	04/09/2019	SCALE 1/5	SHEET 3 OF 3	

224
Figure 172 Heat pipe ceiling 15

6.5.3 Prediction for the full-scale model

A similar approach to the model was done to calculate the prediction on the heat transfer rate for each heat pipe ceiling. The forced convection in the kiln section was not included in the prediction model. The results of the prediction for a uniform tile temperature of 500 °C are plotted in Figure 173. The module 35 located on the side of the kiln will be strongly impacted by the side wall and the view factor from the tile to the evaporator heat pipe resulting in a low heat transfer rate. The heat transfer rate for the section with a pipe distance of 35 mm is 3.5 kW. Module 25 achieved a heat transfer rate of 5.8 kW. The maximum heat transfer rate in the kiln is achieved for the module located at the middle of the kiln. Module 15 achieved a heat recovery of 8.9 kW, the increase is mainly due to a higher view factor and a higher heat transfer area at the evaporator section. The total heat transfer rate achieved by the entirety of the heat pipe ceiling is 72.9 kW at a heat flux of 18.4 kW/m².

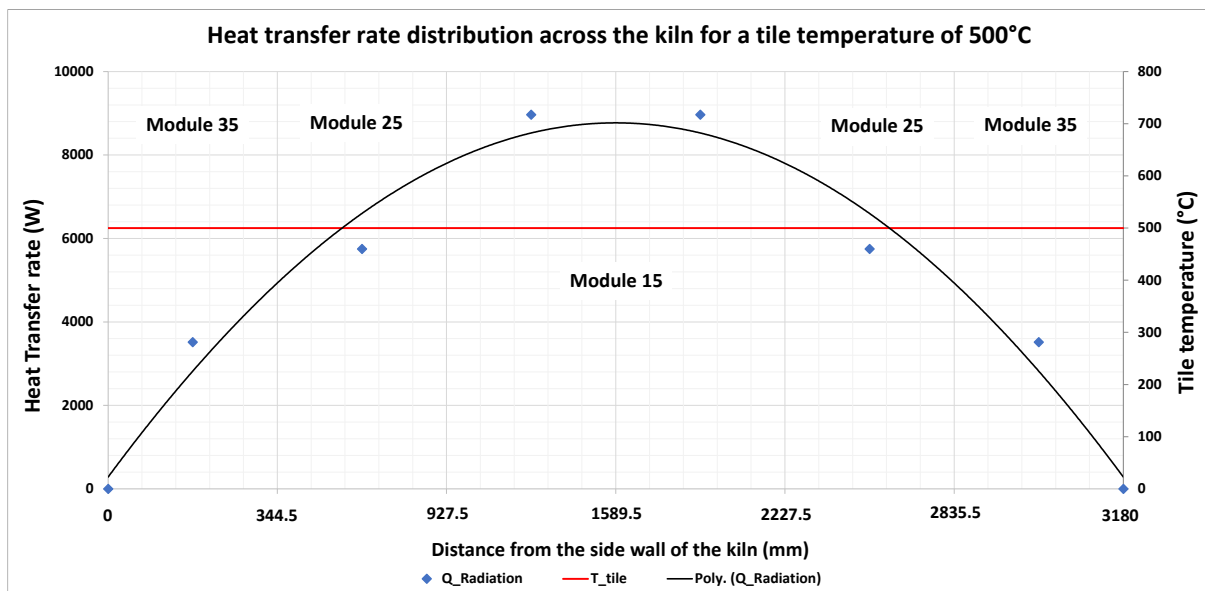


Figure 173 Heat transfer rate distribution across the kiln at a tile temperature of 500 °C

The prediction model was tested at a lower temperature and the predicted values for the heat transfer rate are plotted in Figure 174. A similar trend can be seen. Module 35 will recover up to 435W. The predicted value for the heat transfer rate at module 25 is higher at 707 W. The maximum heat transfer rate is achieved for module 15 located at the middle of the kiln cross section with a heat transfer rate of 1.1 kW. The total heat transfer rate of the heat pipe ceiling is 9 kW at a heat flux of 2.3 kW/m².

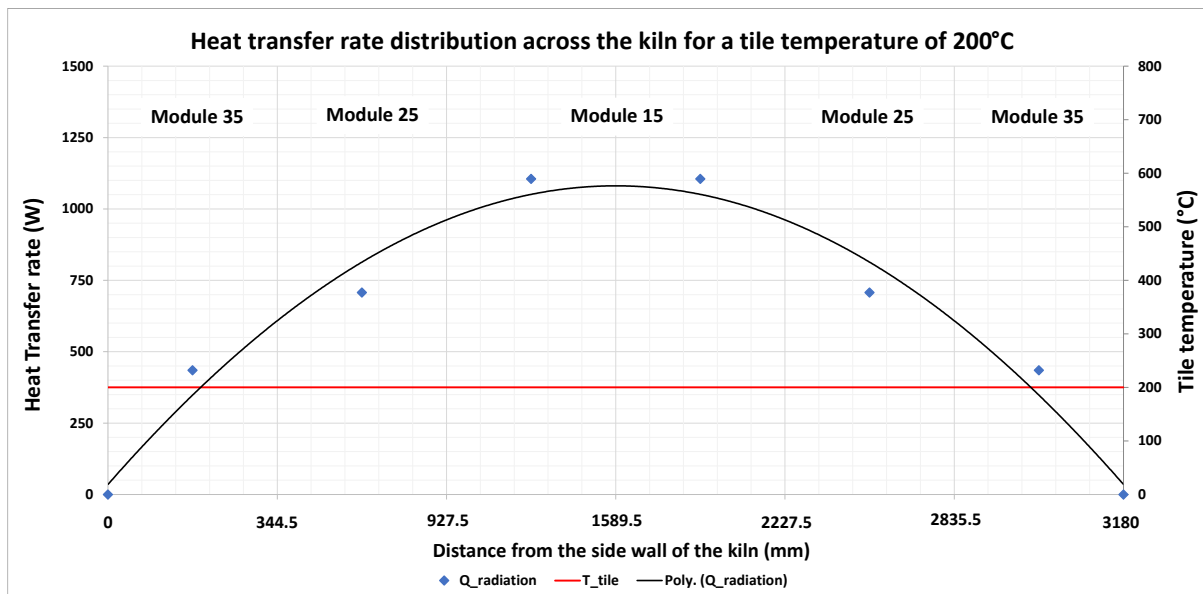


Figure 174 Heat transfer rate distribution across the kiln at a tile temperature of 200°C

6.5.4 Discussion and conclusion

By applying the methodology developed in the module testing, an innovative heat pipe ceiling was designed to fine tune the temperature of the tile in a roller earth kiln. The heat pipe ceiling is predicted to recover up to 72.9 kW when exposed to a tile temperature of 500 °C. As the temperature of the tile decreases in the roller earth cooling section, the heat transfer rate will diminish and the impact of the heat pipe ceiling on the tile temperature will be less. Indeed, as the temperature of the tile decreases, the radiation heat transfer will be less. It is recommended to use the heat pipe ceiling for a tile temperature of 200 °C or above.

The variation in the distribution of the heat transfer area in the cross section of the kiln will allow for a uniform temperature of the tile resulting in a higher tile quality.

The application of the model in an industrial scenario highlights the potential for waste heat recovery of the heat pipe ceiling. The use of this type of heat pipe in roller earth kilns could potentially reduce the amount of product waste, decrease the cool down time of the tile, thus reducing the overall cost of the product. As the system could not be installed in an experimental set up, the results from the prediction could not be validated.

The heat pipe ceiling offers a significant advantage. However, the installation of such a system presents a challenge. In a retrofit situation, the roof of the kiln will need to be removed to fit the radiative ceiling. Ideally, the heat pipe ceiling should be used in new generations of roller earth kilns.

The use of the heat pipe ceiling is not limited to the tile manufacturing sector. Indeed, the heat pipe ceiling could potentially be installed in a variety of applications to cool down products with limited head space. The heat pipe ceiling also provides a remote cooling section that is not exposed to the hot product. In certain applications, a higher temperature cooling fluid will be needed such as thermal oil. The thermal oil is considered as flammable when exposed to hot surfaces (above the flashing point). This risk is removed by using a radiative heat pipe ceiling as the condenser section can be placed outside the kiln. The heat pipe could be applied to the steel industry to cool down products on a conveyor belt. *Jouhara* [58] investigated the use of a flat heat pipe to recover heat from steel wire on a conveyor. The heat pipe ceiling could also be applied in this configuration. However, the need to remove the heat pipe and change the inclination angle was required.

By applying the heat pipe ceiling to the entirety of the kiln indirect cooling section, the system will recover up to 1277 MWh per year. A novel ORC system was presented by *Tian* [14], the energy saving per year represented a value of 115 MWh by installing the ORC at the exhaust stack of the kiln. It can be seen that the heat pipe ceiling will recover significantly more energy. However, the ORC system does not need a retrofitting of the kiln as it is installed in the exhaust stack. The use of ORC in a kiln could be an addition to the heat pipe ceiling to increase the overall energy efficiency of the roller earth kiln. A study was done by *Delpech* [7] on the installation of a full-scale cross flow heat pipe heat exchanger recovering heat from the cooling section exhaust stack. The potential heat recovered from the exhaust stack represented 863 MWh per year. The fact that the heat pipe heat exchanger does not impact the kiln is a significant benefit to the technology. In both cases, the heat pipe ceiling will recover more heat and will bring the benefit of uniform cooling temperature.

Chapter 7: Conclusion from the study and suggestions for future work

7.1 Conclusion from study

Experimental and theoretical studies of a single heat pipe and module heat pipes were conducted.

The investigation on the single heat pipe demonstrated the applicability of a near horizontal evaporator section with a vertical condenser for waste heat recovery. The impact of the filling ratio was investigated and it was concluded that this will have a strong influence on the condenser resistance due to the splashing of the working fluid onto the condenser section, increasing the falling film thickness and the condensation thermal resistance. The boiling resistance was not strongly influenced by the filling ratio when geyser boiling did not occur. The occurrence of geyser boiling was strongly impacted by the filling ratio as the occurrence of geyser boiling is stronger for lower filling ratios. The main influence of the filling ratio was on the boiling heat flux and the heat pipe working temperature. The boiling heat flux increased as the filling ratio decreased due to the reduction in surface area for a similar heat transfer rate. The heat pipe temperature increased as the filling ratio increased due to the limited amount of vapour reaching the condenser section and the high condensation thermal resistance. The heat transfer rate was highest for a filling ratio of 75% for a heater temperature between 200 °C to 400 °C. The maximum heat transfer rate of 573 W was observed for a filling ratio of 50% at a heater temperature of 500 °C. At filling ratios below 25%, the heat transfer rate tended to be lower.

Correlations were selected from the literature to predict the value of the boiling thermal resistance and the condensation thermal resistance for the different test conditions. The thermal resistances predicted by the correlations were compared to the experimental thermal resistances calculated. It was noticed that for the boiling thermal resistance, *Rohsenow* and *Kiatsiriroat* were able to predict boiling thermal resistance values close to the experimental boiling thermal resistances. As geyser boiling occurred in the heat pipe for low heat fluxes and low filling ratios, the comparison between the predicted and experimental thermal resistance had to be done under certain conditions such as heat pipe evaporator temperature uniformity and the excess temperature at the evaporator section. The temperature difference between the maximum and the minimum temperature at the evaporator section did not exceed 7 °C and the excess temperature did not exceed 9 °C. A similar approach was made for the prediction of the condensation thermal resistance. Correlations were selected from the literature to predict the condensation thermal resistances for comparison with the experimental values. Nusselt modified by Rohsenow's correction factor was selected for comparison and

showed agreement with the experimental values. Due to the flooding of the condenser section by the vapour splashing the condenser with working fluid, the condensation thermal resistance drastically increased for high filling ratios as the falling film thickness increased. The predicted value was then made for filling ratios below 50%.

A prediction tool was created to predict the heat pipe temperature at the different conditions. The tool was able to predict the heat pipe temperatures and the heat transfer rate of the single heat pipe. The model predicted the heat transfer rate for all the conditions within 10%. As the number of conditions is substantial, only a few were used to predict the heat pipe temperatures. The modelling tool was tested at a filling ratio of 50% for heat fluxes of 2.7 kW/m² and 13.4 kW/m². For the test on low heat flux, the evaporator temperature was predicted to within ± 4.1 °C, the vapour temperature within ± 3.1 °C and the water outlet temperature was predicted within ± 0.1 °C. For a heat flux of 13.4 kW/m², the evaporator temperature was predicted to within ± 0.3 °C, the vapour temperature within ± 3.5 °C and the water outlet temperature within ± 0.1 °C. The modelling tool was able to predict accurate values for the heat pipe temperature and heat transfer rate for different conditions within 10% error.

To account for the high condensation resistance observed in the single heat pipe tests and to reduce the space occupied by the condenser, a new condenser design was used for the heat pipe modules based on a shell and tube heat exchanger. To control the temperature of the tile, the heat pipe needed to provide different local heat transfer rates depending on the heat pipe location in the kiln. Three modules with varying evaporator section areas were designed and tested. The systems were tested for flow rates from 5 L/min to 20 L/min to investigate the influence of the forced convection heat transfer coefficient on the heat pipe module at heater temperatures varying from 200 °C to 500 °C. It was concluded that the main impact of the flow rate was on the heat pipe temperatures. As the flow rate increased the temperatures of the heat pipe decreased. However, the flow rate did not have a major impact on the heat transfer rate. The flow rate can then be used to protect the heat pipe from overheating. The overall thermal resistance was calculated to determine the influence of the evaporator section area. It was concluded that as the evaporator section area decreases, the overall thermal resistance increases. Similarly, the experimental condensation resistance was assessed, it was observed that as the heat flux increased, the condensation thermal resistance decreased. The condensation thermal resistance presented some challenges, as no correlations currently available in the literature accurately predicted the experimental results. A new correlation to account for the row of tubes and the Jakob number was derived from *Chen* and applied to the experimental results. The correlations were in agreement with the experimental data for high heat flux. For low heat flux, the Rohsenow correction factor was applied on the modified

correlation to account for the pressure in the vapour side of the tube bundle. The heat transfer rate for each module was calculated and shown to be decreasing as the evaporator surface area decreased. Predictions of the heat pipe resistance and heat transfer rate were carried out to verify the accuracy of the selected correlations. The modelling tool developed for the single heat pipe was modified to account for the correlations tested for the module heat pipes. The modelling tool was tested under three different conditions. Module 15 at a filling ratio of 75% at a heat flux of 6.5 kW/m² for a flow rate of 10 L/min was tested. The modelling tool predicted the evaporator temperature within ± 2.7 °C, the vapour temperature within ± 1.0 °C and the water outlet temperature within ± 0.1 °C. The modelling tool was then tested at a similar heat flux for a flow rate of 15 L/min for module 15. The evaporator temperature was predicted to within ± 2.8 °C, the vapour temperature ± 2.6 °C and the water outlet temperature ± 0.1 °C. To assess the impact of a change in the heat pipe design, the modelling tool was tested for module 35 at a heat flux of 2 kW/m² for a flow rate of 15 L/min. The evaporator temperature was predicted to within ± 0.5 °C, the vapour temperature within ± 1.1 °C and the water outlet temperature within ± 0.1 °C. The modelling tool developed using the correlations selected was able to accurately predict the heat pipe temperatures. A similar approach was made on the heat transfer rate. The heat transfer rate for module 15 was predicted within 10% error. The modelling tool was also applied to module 35 and predicted the heat transfer rate within 10% error.

The modelling tool developed for the module was applied to a full-scale industrial heat pipe ceiling composed of three types of heat pipe modules. The density of the heat pipe ceiling was increased in the middle section of the kiln. The modelling tool was then used for a constant tile temperature. The heat pipe ceiling was able to recover heat at different levels for each section of the kiln. The variation of heat transfer rate across the tile will allow a uniform temperature of the tile. The maximum heat transfer rate was achieved for a tile temperature of 500 °C at 72.9 kW for a heat flux of 18.4 kW/m²

The use of heat pipes for waste heat recovery and uniform cooling was investigated. The main objective of the study was to demonstrate the capacity of the heat pipe technology to recover waste heat and provide a uniform cooling temperature at the tile surface, theoretically and experimentally. The full-scale system successfully recovered waste heat while providing a uniform tile temperature, thus reducing the amount of waste product, and increasing the overall quality of the tiles. The module systems were developed to validate experimentally the correlations used in the theoretical modelling tool.

The heat recovered by the heat pipe ceiling can potentially be used in other applications in the facility such as air preheating for the burners or hot air for the dryers. The outlet temperatures

of the module were not high grade as the condenser sections were separated. By using a single condenser section, the water temperature output could be higher. Also, the use of a different cooling fluid such as thermal oil could bring a benefit to the heat pipe ceiling.

7.2 Impact of the study on the research field

Heat pipes for waste heat recovery have been widely investigated for cross flow heat exchangers or wick heat pipe systems. However, only a limited number of papers and theses report on the use of heat pipes to recover heat from radiative heat sources. Moreover, the use of a radiative heat pipe with a horizontal section and a shell and tube heat exchanger was not previously investigated. The development of this technology will extend the field of research for heat pipe applications where limited space is available and for a high intensity heat source parallel to the heat pipe evaporator section.

The correlation modified for the condensation on a tube bundle could have a large impact on the research field as no correlations for condensation on a tube bundle for a heat pipe condenser section exists. However, the correlation modified in this thesis is only applicable for a heat pipe with a similar heat pipe design. Due to the limitations of the test rig design, more investigations will be needed to evaluate the accuracy in the prediction using the developed correlations for different heat pipe designs.

The extensive work on the two-phase process of the heat pipe allows a better understanding of the behaviour of the pool in a near horizontal evaporator section heat pipe. It was noticed that the area occupied by the pool has a major impact on geyser boiling, the heat pipe temperatures, thermal resistances, and the heat transfer rate. It was also noticed that on a near horizontal evaporator section, the area occupied by the pool cannot be defined as the volume occupied by the liquid, as when boiling occurs, the area occupied by the liquid on the top internal surface of the tube will be replaced by vapour. The conclusion observed from the experimental study carried out on the single heat pipe will contribute to enhance future heat pipe design using a similar evaporator section.

The impact of the filling ratio for this type of heat pipe is important. Indeed, it was noted during the test that at high filling ratios, liquid is projected onto the condenser internal surface. The filling ratio will then need to be lower to allow a low condensation resistance.

The design of such a heat pipe will have a major impact on the potential for waste heat recovery in difficult applications with limited space available. Also, this type of heat pipe could bring a major benefit to applications where finely tuned cooling is needed to obtain uniform temperatures on a product. The industrial application developed in this thesis will provide a finely tuned cooling of the tile temperature across the kiln to obtain a uniform temperature.

This system will significantly reduce the internal residual stresses of the tile during the cool down process, thus increasing the structural integrity of the tile. This heat pipe design will also decrease the number of tiles that would be rejected because of a lack of quality, while increasing the overall efficiency of the kiln.

7.3 Suggestions for future work

The work presented in this thesis has some limitations. Indeed, the use of a heat flux sensor at the evaporator section could have presented some advantages such as an accurate heat flux measurement that could be used for the prediction model and the determination of the pool area. A reduced uncertainty associated with the experimental data at low heat flux will also be achieved by using a heat flux sensor. The surface area for the pool was calculated based on the filling ratio and a factor to account for the vapour. By using a heat flux sensor, the pool area could have been determined. Also, the use of thermal imaging to observe the temperature distribution could have enhanced the accuracy of the study. It is recommended that the test should be carried out again with both types of equipment.

The lack of a thermocouple located on the condensation surface introduced an error in the prediction, as the temperature of the condenser surface for each test was evaluated on the heat transfer rate at the coolant. By placing a thermocouple on the condensing surface, the correlations developed above will be validated experimentally. A potential future work would be to install a thermocouple on the condenser surface. Also, simulation and tests at higher heat fluxes should be performed to observe the deviation of the correlation for the condensation thermal resistance. This work could lead to the development or validation of correlations for condensation on a tube bundle in a heat pipe condenser.

More investigation needs to be done on the single heat pipe condenser resistance for high filling ratios to understand the behaviour of the vapour and the liquid at the liquid/vapour interface. Ideally, the development of a glass heat pipe following a similar design could be done to understand the behaviour of the splashing occurring at the interface.

The study carried out on the radiation resistance introduced an error, as the resistance could not be assessed properly due to the assumptions made. Indeed, in the model the walls are considered as reradiating surfaces and the effect of the natural convection on the wall was neglected. Also, the assumptions for the view factor had a major impact on the thermal resistance. Numerical analysis should be carried out to determine the value of the view factor, which should result in a view factor correlation that is applicable for an inclined cylinder exposed to a flat surface. Computational Fluid Dynamics (CFD) analysis will also bring value in the assessment of the natural convection from the re-radiating wall. A similar approach should be done for the radiation resistance. The impact of the *Rohsenow* correction factor

applied to the correlation developed should also be assessed. The installations of pressure sensors in the bundle could provide an idea of the behaviour of the two-phase process in the bundle.

The main limitation of the presented work is the lack of experimental validation for the full-scale system and the impact of uniform cooling on the structure of the tile. The installation of such a system for the validation is quite challenging as the system is invasive. It can be challenging to install this type of system on an industrial site with no previous validation of the technology. To validate the system, a full-scale simulation of the kiln will be carried out, including the heat pipe ceiling. The impact of the cooling on the tile structure will also be assessed by Finite Element Analysis to ensure that the uniform tile temperature enhances the structural integrity of the tile. Once validated by numerical analysis, a full or laboratory scale installation could be tested to validate the impact of the heat pipe on the tile and the theoretical modelling tool developed in this work.

References

- [1] Ciacco EFS, Rocha JR, Coutinho AR. The energy consumption in the ceramic tile industry in Brazil. *Appl Therm Eng* 2017;113:1283–9. <https://doi.org/10.1016/j.applthermaleng.2016.11.068>.
- [2] Abdelaziz EA, Saidur R, Mekhilef S. A review on energy saving strategies in industrial sector. *Renew Sustain Energy Rev* 2011;15:150–68. <https://doi.org/10.1016/j.rser.2010.09.003>.
- [3] Ceramics-unie. Ceramic Unie facts and figures 2017. <http://cerameunie.eu/ceramic-industry/facts-figures/> (accessed December 20, 2017).
- [4] Ceramics-unie. Ceramic Unie facts and figures 2017.
- [5] E, Monfort, A. Mezquita, R. Granel, E. Vaquer, A. Escrig, A. Miralles VZ. Analysis of energy consumption and carbon dioxide emissions in ceramic tile manufacture. *Bol La Soc Esp Ceram y Vidr* 2010;49:303–10.
- [6] Agrafiotis C, Tsoutsos T. Energy saving technologies in the European ceramic sector: a systematic review. *Appl Therm Eng* 2001;21:1231–49. [https://doi.org/10.1016/S1359-4311\(01\)00006-0](https://doi.org/10.1016/S1359-4311(01)00006-0).
- [7] Delpech B, Milani M, Montorsi L, Boscardin D, Chauhan A, Almahmoud S, et al. Energy efficiency enhancement and waste heat recovery in industrial processes by means of the heat pipe technology: Case of the ceramic industry. *Energy* 2018;158:656–65. <https://doi.org/10.1016/j.energy.2018.06.041>.
- [8] European Commission. Reference Document on Best Available Techniques in the Ceramic Manufacturing Industry 2007:210–1.
- [9] Peng J, Zhao Y, Jiao L, Zheng W, Zeng L. CO₂ Emission Calculation and Reduction Options in Ceramic Tile Manufacture-The Foshan Case. *Energy Procedia* 2012;16:467–76. <https://doi.org/10.1016/j.egypro.2012.01.076>.
- [10] Laboratory LLN. U.S. energy use drops in 2008 n.d. <https://www.llnl.gov/news/us-energy-use-drops-2008>.
- [11] Mezquita, A.a, Monfort, E.a, Zaera V. Ceramic tiles manufacturing and emission trading scheme: Reduction of CO₂ emissions, European benchmarking. *Bol La Soc Esp Ceram y Vidr* 2009;48:211–22.
- [12] Anonymous. Industrial microwave drying makes the breakthrough 1995;5:230–1.

- [13] Peris B, Navarro-Esbrí J, Molés F, Mota-Babiloni A. Experimental study of an ORC (organic Rankine cycle) for low grade waste heat recovery in a ceramic industry. *Energy* 2015;85:534–42. <https://doi.org/10.1016/j.energy.2015.03.065>.
- [14] Tian H, Shu GQ. 17 – Organic Rankine Cycle systems for large-scale waste heat recovery to produce electricity. *Org. Rank. Cycle Power Syst.*, 2017, p. 613–36. <https://doi.org/10.1016/B978-0-08-100510-1.00017-X>.
- [15] Mezquita A, Boix J, Monfort E, Mallof G. Energy saving in ceramic tile kilns: Cooling gas heat recovery. *Appl Therm Eng* 2014;65:102–10. <https://doi.org/10.1016/j.applthermaleng.2014.01.002>.
- [16] Rentz O, Schmittinger A, Jochum R, Schultmann F. Exemplary Investigation into the State of Practical Realisation of Integrated Environmental Protection within the Ceramics Industry under Observance of the IPPC-Directive and the Development of BAT Reference Documents, French- German Institute for Environ 2001:44–52.
- [17] Beltran J. Cogeneration systems in the ceramics tile sector, Proceedings of the Workshop on New Technologies for the Rational Use of Energy in the Ceramics Tiles Industry. DG for Ene. Castellon de La Plana, Spain: EC; 1994.
- [18] Enterprise I. Managing the firing process of ceramics tiles to reduce convexity defect : design of experiment approach Fikri Dweiri * Sharfuddin Ahmed Khan 2013;2:46–63. <https://doi.org/10.1504/IJIE.2013.057341>.
- [19] Mirbolouk S. *International Journal of Advanced Research* in 2013;3:805–9.
- [20] Boukouvalas C, Kittler J, Marik R, Mirmehdi M, Petrou M. *Structural Defects* n.d.
- [21] Hanzaei SH, Afshar A, Barazandeh F. Automatic detection and classification of the ceramic tiles??? surface defects. *Pattern Recognit* 2017;66:174–89. <https://doi.org/10.1016/j.patcog.2016.11.021>.
- [22] Eren E, Kurama S, Solodov I. Characterization of porosity and defect imaging in ceramic tile using ultrasonic inspections. *Ceram Int* 2012;38:2145–51. <https://doi.org/10.1016/j.ceramint.2011.10.056>.
- [23] Laranjeira J, Simões N, Simões I, Tadeu A, Serra C. Passive thermography evaluation of bonding defects in adhered ceramic tiling : experimental and in-situ assessments. QIRT2014 Conférence 2014.
- [24] Revel GM, Rocchi S. Defect detection in ceramic materials by quantitative infrared thermography . 8th Conf Quant Infrared Thermogr 2006.

- [25] Cantavella V, Moreno A, Mezquita A, Jarque JC, Palanques A. Evolution of Stresses and Curvatures in Porous Bodies During Cooling. *Qualicer* 2008;241–55.
- [26] Singhinolfi D. Experimental Study of Deformations and State of Tension in Traditional Ceramic Materials. *Mater Ceram /Ceramic Mater* 2011;63:226–32.
- [27] Jouhara H, Robinson AJ. Experimental investigation of small diameter two-phase closed thermosyphons charged with water, FC-84, FC-77 and FC-3283. *Appl Therm Eng* 2010;30:201–11. <https://doi.org/10.1016/j.applthermaleng.2009.08.007>.
- [28] Fadhl B, Wrobel LC, Jouhara H. CFD modelling of a two-phase closed thermosyphon charged with R134a and R404a. *Appl Therm Eng* 2015;78:482–90. <https://doi.org/10.1016/j.applthermaleng.2014.12.062>.
- [29] Chan CW, Siqueiros E, Ling-Chin J, Royapoor M, Roskilly AP. Heat utilisation technologies: A critical review of heat pipes. *Renew Sustain Energy Rev* 2015;50:615–27. <https://doi.org/10.1016/j.rser.2015.05.028>.
- [30] Shi C, Wang Y, Liao Q, Yang Y. Analysis and application of variable conductance heat pipe air preheater. *J Therm Sci* 2011;20:248–53. <https://doi.org/10.1007/s11630-011-0466-5>.
- [31] Leriche M, Harmand S, Lippert M, Desmet B. An experimental and analytical study of a variable conductance heat pipe: Application to vehicle thermal management. *Appl Therm Eng* 2012;38:48–57. <https://doi.org/10.1016/j.applthermaleng.2012.01.019>.
- [32] Srimuang W, Amatachaya P. A review of the applications of heat pipe heat exchangers for heat recovery. *Renew Sustain Energy Rev* 2012;16:4303–15. <https://doi.org/10.1016/j.rser.2012.03.030>.
- [33] Alhuyi Nazari M, Ahmadi MH, Ghasempour R, Shafii MB, Mahian O, Kalogirou S, et al. A review on pulsating heat pipes: From solar to cryogenic applications. *Appl Energy* 2018;222:475–84. <https://doi.org/10.1016/j.apenergy.2018.04.020>.
- [34] Jouhara H, Meskimmon R. Experimental investigation of wraparound loop heat pipe heat exchanger used in energy efficient air handling units. *Energy* 2010;35:4592–9. <https://doi.org/10.1016/j.energy.2010.03.056>.
- [35] Jouhara H, Ezzuddin H. Thermal performance characteristics of a wraparound loop heat pipe (WLHP) charged with R134A. *Energy* 2013;61:128–38. <https://doi.org/10.1016/j.energy.2012.10.016>.
- [36] Jouhara H, Meskimmon R. An investigation into the use of water as a working fluid in

- wraparound loop heat pipe heat exchanger for applications in energy efficient HVAC systems. *Energy* 2018;156:597–605. <https://doi.org/10.1016/j.energy.2018.05.134>.
- [37] Busse CA. Theory of the ultimate heat transfer limit of cylindrical heat pipes. *Int J Heat Mass Transf* 1973;16:169–86. [https://doi.org/10.1016/0017-9310\(73\)90260-3](https://doi.org/10.1016/0017-9310(73)90260-3).
- [38] David R, Ryan M, Peter K. *Heat Pipes: Theory, Design and Applications*. 6th, Revised ed. Butterworth-Heinemann; 2013.
- [39] Solomon AB, Ramachandran K, Pillai BC. Thermal performance of a heat pipe with nanoparticles coated wick. *Appl Therm Eng* 2012;36:106–12. <https://doi.org/10.1016/j.applthermaleng.2011.12.004>.
- [40] Nam Y, Sharratt S, Cha G, Ju YS. Characterization and Modeling of the Heat Transfer Performance of Nanostructured Cu Micropost Wicks. *J Heat Transfer* 2011;133:101502. <https://doi.org/10.1115/1.4004168>.
- [41] Youngsuk Nam, Sharratt S, Byon C, Sung Jin Kim, Ju YS. Fabrication and Characterization of the Capillary Performance of Superhydrophilic Cu Micropost Arrays. *J Microelectromechanical Syst* 2010;19:581–8. <https://doi.org/10.1109/JMEMS.2010.2043922>.
- [42] Odagiri K, Nagano H. Heat transfer characteristics of flat evaporator loop heat pipe under high heat flux condition with different orientations. *Appl Therm Eng* 2019;153:828–36. <https://doi.org/10.1016/j.applthermaleng.2019.02.022>.
- [43] Bai L, Fu J, Lin G, Zhou C, Wen D. Quiet power-free cooling system enabled by loop heat pipe. *Appl Therm Eng* 2019;155:14–23. <https://doi.org/10.1016/j.applthermaleng.2019.03.147>.
- [44] Yong T, Ping C, Xiaowu W. Experimental investigation into the performance of heat pipe with micro grooves fabricated by Extrusion-ploughing process. *Energy Convers Manag* 2010;51:1849–54. <https://doi.org/10.1016/j.enconman.2010.01.001>.
- [45] Yu F, Yu C, Cao J, Chen Y. Experimental analysis of the evaporation regimes of an axially grooved heat pipe at small tilt angles. *Int J Heat Mass Transf* 2018;126:334–41. <https://doi.org/10.1016/j.ijheatmasstransfer.2018.05.112>.
- [46] Li Y, Li Z, Chen C, Yan Y, Zeng Z, Li B. Thermal responses of heat pipes with different wick structures under variable centrifugal accelerations. *Appl Therm Eng* 2016;96:352–63. <https://doi.org/10.1016/j.applthermaleng.2015.11.016>.
- [47] Jiang LL, Tang Y, Zhou W, Jiang LZ, Xiao T, Li Y, et al. Design and fabrication of

- sintered wick for miniature cylindrical heat pipe. *Trans Nonferrous Met Soc China* (English Ed 2014;24:292–301. [https://doi.org/10.1016/S1003-6326\(14\)63060-0](https://doi.org/10.1016/S1003-6326(14)63060-0).
- [48] Zhong G, Ding X, Tang Y, Yu S, Chen G, Tang H, et al. Various orientations research on thermal performance of novel multi-branch heat pipes with different sintered wicks. *Energy Convers Manag* 2018;166:512–21. <https://doi.org/10.1016/j.enconman.2018.04.066>.
- [49] Li H, Wang X, Liu Z, Tang Y, Yuan W, Zhou R, et al. Experimental investigation on the sintered wick of the anti-gravity loop-shaped heat pipe. *Exp Therm Fluid Sci* 2015;68:689–96. <https://doi.org/10.1016/j.expthermflusci.2015.06.020>.
- [50] Faghri A. *Heat Pipe Science and Technology*. 2nd editio. Global Digital Press; 2016.
- [51] Imura H, Sasaguchi K, Kozai H, Numata S. Flux thermique critique dans un thermosyphon ferme et diphasique. *Int J Heat Mass Transf* 1983;26:1181–8. [https://doi.org/10.1016/S0017-9310\(83\)80172-0](https://doi.org/10.1016/S0017-9310(83)80172-0).
- [52] Liu X, Chen Y, Shi M. Dynamic performance analysis on start-up of closed-loop pulsating heat pipes (CLPHPs). *Int J Therm Sci* 2013;65:224–33. <https://doi.org/10.1016/j.ijthermalsci.2012.10.012>.
- [53] Sözen A, Menlik T, Gürü M, Boran K, Kılıç F, Aktaş M, et al. A comparative investigation on the effect of fly-ash and alumina nanofluids on the thermal performance of two-phase closed thermo-syphon heat pipes. *Appl Therm Eng* 2016;96:330–7. <https://doi.org/10.1016/j.applthermaleng.2015.11.038>.
- [54] Han H, Cui X, Zhu Y, Sun S. A comparative study of the behavior of working fluids and their properties on the performance of pulsating heat pipes (PHP). *Int J Therm Sci* 2014;82:138–47. <https://doi.org/10.1016/j.ijthermalsci.2014.04.003>.
- [55] Reay D, Kew P. *Heat Pipes* 2006.
- [56] Bejan A, Kraus AD. *Heat Pipes*. Heat Transf. Handb. New Jersey: 2003.
- [57] Rohsenow WM, Hartnett JP, Cho YI. *Handbook of heat transfer*. Third. 1998.
- [58] Jouhara H, Almahmoud S, Chauhan A, Delpech B, Nannou T, Tassou SA, et al. Experimental investigation on a flat heat pipe heat exchanger for waste heat recovery in steel industry. *Energy Procedia* 2017;123:329–34. <https://doi.org/10.1016/j.egypro.2017.07.262>.
- [59] Delpech B, Milani M, Montorsi L, Boscardin D, Chauhan A, Almahmoud S, et al. Energy efficiency enhancement and waste heat recovery in industrial processes by

- means of the heat pipe technology: Case of the ceramic industry. *Energy* 2018;158:656–65. <https://doi.org/10.1016/j.energy.2018.06.041>.
- [60] Meena P, Rittidech S, Poomsa-ad N. Application of closed-loop oscillating heat-pipe with check valves (CLOHP/CV) air-preheater for reduced relative-humidity in drying systems. *Appl Energy* 2007;84:553–64. <https://doi.org/10.1016/j.apenergy.2006.09.006>.
- [61] Lukitobudi AR, Akbarzadeh A, Johnson PW, Hendy P. Design, construction and testing of a thermosyphon heat exchanger for medium temperature heat recovery in bakeries. *Heat Recover Syst CHP* 1995;15:481–91. [https://doi.org/10.1016/0890-4332\(95\)90057-8](https://doi.org/10.1016/0890-4332(95)90057-8).
- [62] Jouhara H, Milko J, Danielewicz J, Sayegh MA, Szulgowska-Zgrzywa M, Ramos JB, et al. The performance of a novel flat heat pipe based thermal and PV/T (photovoltaic and thermal systems) solar collector that can be used as an energy-active building envelope material. *Energy* 2016;108:148–54. <https://doi.org/10.1016/j.energy.2015.07.063>.
- [63] Jouhara H, Szulgowska-Zgrzywa M, Sayegh MA, Milko J, Danielewicz J, Nannou TK, et al. The performance of a heat pipe based solar PV/T roof collector and its potential contribution in district heating applications. *Energy* 2017;136:117–25. <https://doi.org/10.1016/j.energy.2016.04.070>.
- [64] Al-Arabi M, Salman YK. Laminar natural convection heat transfer from inclined surfaces. *Int J Heat Mass Transf* 1980;23:45–51.
- [65] Oosthuizen PH. Experimental study of free convective heat transfer from inclined cylinders. *J Heat Transfer* 1976;98:672–4.
- [66] Rani N, Setia H, Dutt M, Wanchoo R. K. Natural Convection Heat Transfer from Inclined Cylinders : A Unified Correlation. *Int J Math Comput Phys Electr Comput Eng* 2014;8:100–5.
- [67] Bansal JC. Natural convection heat transfer from inclined cylinders. Panjab university, 1976.
- [68] AL-Arabi M, Khamis M. Natural Convection Heat Transfer from inclined cylinders. *Int J Heat Mass Transf* 1982;25:3–15. <https://doi.org/10.1002/9781119476962.ch5>.
- [69] Li J, Tarasuk JD. Local free convection around inclined cylinders in air: An interferometric study. *Exp Therm Fluid Sci* 1992;5:235–42.

- [https://doi.org/10.1016/0894-1777\(92\)90010-3](https://doi.org/10.1016/0894-1777(92)90010-3).
- [70] Morgan VT. The overall convective heat transfer from smooth circular cylinders. *Adv. heat Transf.*, vol. 11, Elsevier; 1975, p. 199–264.
- [71] Heo JH, Chung BJ. Natural convection heat transfer on the outer surface of inclined cylinders. *Chem Eng Sci* 2012;73:366–72. <https://doi.org/10.1016/j.ces.2012.02.012>.
- [72] Frank Kreith, Raj Manglik MB. *Principles of Heat Transfer, Seventh Edition*. 2011.
- [73] Incropera FP, Dewitt DP, Bergman TL, Lavine AS. *Principles of Heat and Mass Transfer Seventh Edition*. 7th ed. Global Engineering;; 2011.
- [74] Howell JR. A catalog of radiation heat transfer configuration factors. [Http://Www Me U texas Edu/~ Howell/Sectionc/C11 Html](Http://Www.Me.Utexas.Edu/~Howell/Sectionc/C11.Html) 2001.
- [75] Hottel HC. Radiant heat transmission between surfaces separated by non-absorbing media. *Trans ASME* 1931;53.
- [76] Hamilton DC, Morgan WR. Radiant-interchange configuration factors 1952.
- [77] Ehlert JR, Smith TF. View factors for perpendicular and parallel rectangular plates. *J Thermophys Heat Transf* 1993;7:173–5.
- [78] Gross U, Spindler K, Hahne E. Shapefactor-equations for radiation heat transfer between plane rectangular surfaces of arbitrary position and size with parallel boundaries. *Lett Heat Mass Transf* 1981;8:219–27.
- [79] Boeke W, Wall L. Radiative exchange factors in rectangular spaces for the determination of mean radiant temperature. *Build Serv Eng* 1976;43:244–53.
- [80] Chekhovskii IR, Sirotkin V V, Chu-Dun-Chu I V, Chebanov VA. Determination of radiative view factors for rectangles of different sizes. *High Temp Sci* 1979;17:116–9.
- [81] Holman J. *Heat Transfer*. McGraw-Hill Education; 2009.
- [82] Rohsenow WM. A method of correlating heat transfer data for surface boiling of liquids. Cambridge, Mass.: MIT Division of Industrial Cooperation,[1951]; 1951.
- [83] Cooper MG. Heat Flow Rates in Saturated Nucleate Pool Boiling-A Wide-Ranging Examination Using Reduced Properties. In: *Transfer JPH and TFIBT-A in H*, editor. vol. Volume 16, Elsevier; 1984, p. 157–239. [https://doi.org/http://dx.doi.org/10.1016/S0065-2717\(08\)70205-3](https://doi.org/http://dx.doi.org/10.1016/S0065-2717(08)70205-3).
- [84] Gorenflo D. Pool Boiling in VDI-Heat Atlas (English Version). VDI-Verlag, Dusseldorf,

- Ger 1993.
- [85] McNelly MJ. A correlation of the rates of heat transfer to nucleate boiling liquids. *J Imp Coll Chem Eng Soc* 1953;7:18–34.
- [86] Forster HK, Zuber N. Bubble dynamics and boiling heat transfer. *AIChE J* 1955;1:531–5.
- [87] Mostinski IL. Application of rule of corresponding states for the calculation of heat transfer and critical heat flux to boiling liquids. *Br Chem Eng Abstr FOLIO* 1963:580.
- [88] Stephan K, Abdelsalam M. Heat-transfer correlations for natural convection boiling. *Int J Heat Mass Transf* 1980;23:73–87. [https://doi.org/http://dx.doi.org/10.1016/0017-9310\(80\)90140-4](https://doi.org/http://dx.doi.org/10.1016/0017-9310(80)90140-4).
- [89] Imura H, Kusuda H, Ogata J, Miyazaki T, Sakamoto N. Heat transfer in two-phase closed-type thermosyphons. *Trans Japan Soc Mech Eng Ser B* 1979;45:712–22. <https://doi.org/10.1299/kikaib.45.712>.
- [90] Labuntsov DA. Heat transfer problems with nucleate boiling of liquids. *Therm Eng* 1973;19:21–8.
- [91] T. Kiatsiriroat, A. Nuntaphan JT. Thermal Performance Enhancement of Thermosyphon Heat Pipe with Binary Working Fluids. *Exp Heat Transf* 2000;13:137–52. <https://doi.org/10.1080/089161500269517>.
- [92] Shiraishi M, Kikuchi K, Yamanishi T. Investigation of heat transfer characteristics of a two-phase closed thermosyphon. *J Heat Recover Syst* 1981;1:287–97. [https://doi.org/10.1016/0198-7593\(81\)90039-4](https://doi.org/10.1016/0198-7593(81)90039-4).
- [93] Kopchikov IA, Voronin GI, Kolach TA, Labuntsov DA, Lebedev PD. Liquid boiling in a thin film. *Int J Heat Mass Transf* 1969;12:791–6. [https://doi.org/10.1016/0017-9310\(69\)90182-3](https://doi.org/10.1016/0017-9310(69)90182-3).
- [94] El-Genk MS, Saber HH. Determination of operation envelopes for closed, two-phase thermosyphons. *Int J Heat Mass Transf* 1999;42:889–903. [https://doi.org/10.1016/S0017-9310\(98\)00212-9](https://doi.org/10.1016/S0017-9310(98)00212-9).
- [95] Gogonin II. The dependence of boiling heat transfer on the properties and geometric parameters of heat-transfer wall. *High Temp* 2006;44:913–21.
- [96] Chun KR, Seban RA. Heat transfer to evaporating liquid films. *J Heat Transf* 1971;93:391–6. <https://doi.org/10.1115/1.3449836>.

- [97] Nusselt W. Die Oberflächenkondensation des Wasserdampfes the surface condensation of water. *Zetschr Ver Deutch Ing* 1916;60:541–6.
- [98] Rohsenow WM. Heat transfer and temperature distribution in laminar film condensation. *Trans Asme* 1956;78:1645–8.
- [99] Kutateladze SS. *Fundamentals of Heat Transfer* (2nd Edn.) Edward Arnold. New York 1963:247.
- [100] Chen MM. An analytical study of laminar film condensation: part 2—single and multiple horizontal tubes. *J Heat Transfer* 1961;83:55.
- [101] Rose JW. Some aspects of condensation heat transfer theory. *Int Commun Heat Mass Transf* 1988;15:449–73. [https://doi.org/10.1016/0735-1933\(88\)90043-7](https://doi.org/10.1016/0735-1933(88)90043-7).
- [102] Lee WC, Rose JW. Forced convection film condensation on a horizontal tube with and without non-condensing gases. *Int J Heat Mass Transf* 1984;27:519–28. [https://doi.org/10.1016/0017-9310\(84\)90025-5](https://doi.org/10.1016/0017-9310(84)90025-5).
- [103] Fujii T, Uehara H, Hirata K, Oda K. Heat transfer and flow resistance in condensation of low pressure steam flowing through tube banks. *Int J Heat Mass Transf* 1972;15:247–60. [https://doi.org/10.1016/0017-9310\(72\)90072-5](https://doi.org/10.1016/0017-9310(72)90072-5).
- [104] McNaught JM. TWO-PHASE FORCED CONVECTION HEAT-TRANSFER DURING CONDENSATION ON HORIZONTAL TUBE BUNDLES. *Proceeding Int. Heat Transf. Conf. 7, Connecticut: Begellhouse; 1982, p. 125–31.* <https://doi.org/10.1615/IHTC7.490>.
- [105] Hausen H. Darstellung des Wärmeüberganges in Rohren durch verallgemeinerte Potenzbeziehungen. *Z VDI Beihefte Verfahrenstech* 1943:91–8.
- [106] Petukhov BS. Heat Transfer and Friction in Turbulent Pipe Flow with Variable Physical Properties. *Adv Heat Transf* 1970;6:503–64. [https://doi.org/10.1016/S0065-2717\(08\)70153-9](https://doi.org/10.1016/S0065-2717(08)70153-9).
- [107] Sieder EN, Tate GE. Heat transfer and pressure drop of liquids in tubes. *Ind Eng Chem* 1936;28:1429–35.
- [108] Knudsen JG. DL Katz *Fluid dynamics and heat transfer*. Chem Eng Ser McGraw-Hill, New York, NY 1958.
- [109] Gnielinski V. New equations for heat and mass-transfer in turbulent pipe and channel flow. *Int Chem Eng* 1976;16:359–68.

- [110] Sleicher CA, Rouse MW. A convenient correlation for heat transfer to constant and variable property fluids in turbulent pipe flow. *Int J Heat Mass Transf* 1975;18:677–83.
- [111] Khazaee I, Hosseini R, Noie SH. Experimental investigation of effective parameters and correlation of geyser boiling in a two-phase closed thermosyphon. *Appl Therm Eng* 2010;30:406–12. <https://doi.org/10.1016/j.applthermaleng.2009.09.012>.
- [112] Jouhara H, Fadhl B, Wrobel LC. Three-dimensional CFD simulation of geyser boiling in a two-phase closed thermosyphon. *Int J Hydrogen Energy* 2016;41:16463–76. <https://doi.org/10.1016/j.ijhydene.2016.02.038>.
- [113] Almahmoud S, Jouhara H. Experimental and theoretical investigation on a radiative flat heat pipe heat exchanger. *Energy* 2019;174:972–84. <https://doi.org/10.1016/j.energy.2019.03.027>.
- [114] Jouhara H, Ajji Z, Koudsi Y, Ezzuddin H, Mousa N. Experimental investigation of an inclined-condenser wickless heat pipe charged with water and an ethanol-water azeotropic mixture. *Energy* 2013;61:139–47. <https://doi.org/10.1016/j.energy.2012.09.033>.

Appendices

Appendix 1: Error analysis

Background

In order to anticipate any deviation in the experimental results, an error analysis on the experimental data need to be done. In every equipment's or sensors that are used for experimental testing, an error is associated to the outputs. The error can also be propagated by human error, equipment's usage, inaccurate set up, wrong positioning of sensors ect. The error that will be generated by those actions will propagate throughout the data reduction, thus, the error need to be analysed and calculated to evaluate the impact on the final results. Each equipment's is usually supplied with a data sheet including the error associated to the reading of the data. Once all the sensors errors have been established, the error associated with the value calculated using those data can be determined. A set of errors analysis equation are presented in Table 23.

Table 23 Error analysis equations

Mathematical operation	Example	Associated error

Addition/subtraction	$x = a + b + c \dots$	$S_x = \sqrt{S_a^2 + S_b^2 + S_c^2 \dots}$
Multiplication/division	$x = a * b/c \dots$	$S_x = x \sqrt{\left(\frac{S_a}{a}\right)^2 + \left(\frac{S_b}{b}\right)^2 + \left(\frac{S_c}{c}\right)^2 \dots}$
Exponentiation	$x = a^b$	$S_x = x * b * \frac{S_a}{a}$
Logarithm	Base 10 $x = \log_{10} a$	$S_x = 0.434 * \frac{S_a}{a}$
	Base e $x = \ln(a)$	$S_x = \frac{S_a}{a}$
Antilog	Base 10 $x = 10^a$	$S_x = 2.303 * x * S_a$
	Base e $x = e^a$	$S_x = x * S_a$

In this thesis, the results used in the data reduction are the thermocouples values and the flow rate in the condenser section. The list of reading and associated error are presented in the Table 24.

Table 24 Associated errors

	Read from	Associated error	Associated error
T	National instrument PXle-1071-9213	0.03 % \pm 0.02 °C between - 210°C to 760°C 0.03 % \pm 0.02 °C between - 270°C to 1260°C	0.02
T	K type thermocouple	\pm 1.1 °C	1.1
\dot{V}	Gems Sensors RotorFlow Electronic Flow Sensor	6.0 to 45.0 l/min \pm 7% 15.0 to 75.0 l/min \pm 15%	1.5

Results

The heat transfer rate at the condenser is calculated by

$$Q_{out} = \dot{V} \rho C_p \Delta T \quad (262)$$

The results of one experimental test are shown below

T _{in}	18.74 °C
T _{out}	20.94 °C
Delta T	2.20 °C

Flow rate	3.70	Ltr/min
Heat recovery	568.48	W
T _v	34.88	°C
T _{eb1}	43.9	°C
T _{eb2}	46.1	°C
T _{eb3}	44.0	°C
T _{et1}	43.3	°C
T _{et2}	44.3	°C
T _{et3}	38.9	°C
T _{AD,C}	34.4	°C
T _{heater top}	506.3	°C
T _{heater bottom}	581.6	°C
T _{wall1}	137.1	°C
T _{wall2}	198.8	°C
T _{wall3}	327.3	°C
T _{wall4}	117.8	°C
T _{wall top}	426.5	°C
T _{air}	465.0	°C

The errors were determined for each condition using the correlations below.

Table 25 Error propagations

Variable	Equation	Associated error
ΔT	$\Delta T = T_{out} - T_{in}$	$S_{\Delta T} = \sqrt{S_{T_{in}}^2 + S_{T_{out}}^2}$
Q_{out}	$Q_{out} = \dot{V} \rho C_p \Delta T$	$S_{Q_{out}} = Q_{out} \sqrt{\left(\frac{S_{\dot{V}}}{\dot{V}}\right)^2 + \left(\frac{S_{\Delta T}}{\Delta T}\right)^2}$

Table 26 Error analysis for the single heat pipe

			Sx	error
T _{in}	18.7	°C	1.207672	0.41%
T _{out}	20.9	°C	1.208332	0.41%
Delta T	2.2	°C	1.70837	0.62%
Flow rate	3.7	L/min	0.259	7.00%
Heat recovery	570	W	40.05602	7.03%
T _v	34.9	°C	1.130	0.37%
T _{eb1}	43.9	°C	1.133	0.36%
T _{eb2}	46.1	°C	1.134	0.35%
T _{eb3}	44.0	°C	1.133	0.36%
T _{et1}	43.3	°C	1.133	0.36%
T _{et2}	44.3	°C	1.133	0.36%

Tet3	38.9	°C	1.132	0.36%
TAD,C	34.4	°C	1.130	0.37%
Theater top	506.3	°C	1.272	0.16%
Theater bottom	581.6	°C	1.294	0.15%
Twall1	137.1	°C	1.161	0.28%
Twall2	198.8	°C	1.180	0.25%
TWall3	327.3	°C	1.218	0.20%
TWall4	117.8	°C	1.155	0.30%
Twall top	426.5	°C	1.248	0.18%
Tair	465.0	°C	1.260	0.17%

The calculate error for each value extracted from the data logger will be taken into account in the results section.

Table 27 Error analysis for module 15 testing

			Sx	error
Tin	16.1	°C	1.206865	0.42%
Tout	25.5	°C	1.209691	0.40%
Delta T	9.4	°C	1.708764	0.60%
Flow rate	5.00	L/min	0.35	7.00%
Heat recovery	3300	W	231.8583	7.03%
Tv	67.4	°C	1.222	0.36%
Te1	75.2	°C	1.225	0.35%
Te2	72.3	°C	1.224	0.35%
Te3	74.6	°C	1.224	0.35%
Te4	73.6	°C	1.224	0.35%
Te5	75.1	°C	1.225	0.35%
Te6	72.4	°C	1.224	0.35%
Te7	77.8	°C	1.225	0.35%
Te8	73.8	°C	1.224	0.35%
Te9	75.9	°C	1.225	0.35%
TAD,C	63.7	°C	1.221	0.36%
Theater top	506.3	°C	1.354	0.17%
Theater bottom	581.6	°C	1.377	0.16%
Twall1	137.1	°C	1.243	0.30%
Twall2	198.8	°C	1.262	0.27%
TWall3	327.3	°C	1.300	0.22%
TWall4	117.8	°C	1.237	0.32%
Twall top	426.5	°C	1.330	0.19%
Tair	465.3	°C	1.342	0.18%

It can be seen in Table 27 it can be see that the absolute error for the module 15 is higher for the heat transfer rate. However the percentage of error remain the same. This will be taken into account when discussing the heat transfer rate.

The error in the collected data will be implement in the results section when applicable.

Appendix 2: Pressure drop measurements

Introduction

The pressure drop in the shell and tube condenser section of the module heat pipe was measured at different flow rate in the water coolant.

Experimental set up

Different experimental data were gathered to assess the pressure drop in the shell and tube bundle. The temperature of the team was measured by a thermocouple installed in the heat pipe at the adiabatic section, the inlet and outlet temperatures of the water coolant were measured suing K types thermocouple placed in the middle of the flow. The water flow rate was measured with a turbine flow meter (FTB-371) at the inlet of the shell and tube condenser. A schematics of the condenser section can be seen in

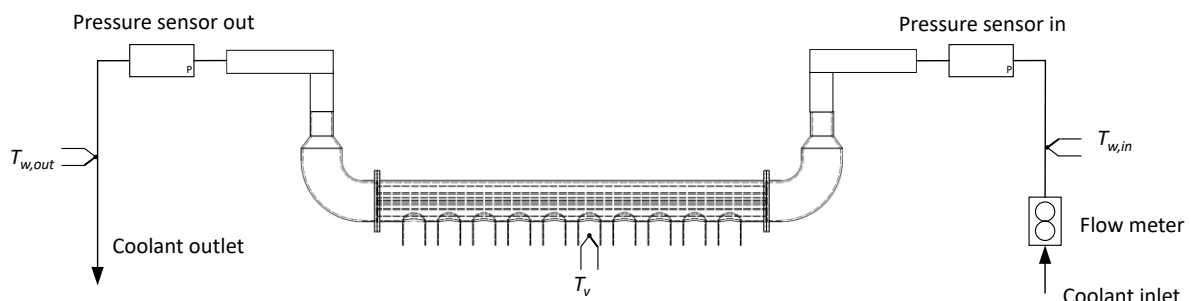


Figure 175 Pressure drop experimental set up

A hydraulic resistance model was developed and can be seen in Figure *. In order to determine the pressure drop at the condenser section, the impact of the different elbow and expansion pieces connected to the shell and tube need to be determined. The connection to the shell and tube is composed of elbows, expander, reducer and the change in diameter for the 9 tubes in the condenser.

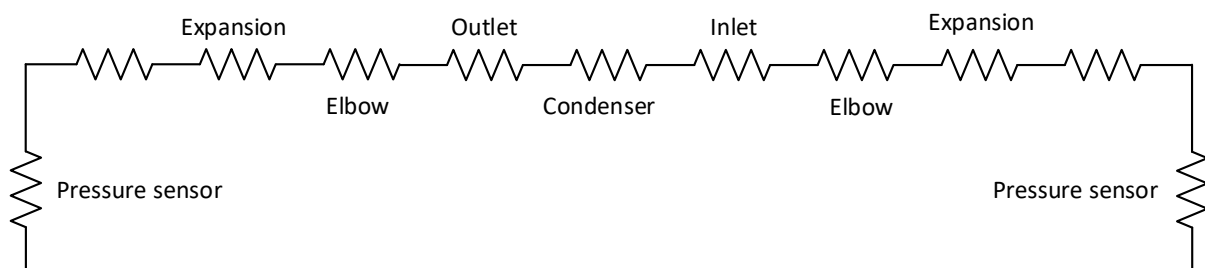


Figure 176 modelling of the pressure resistances at the coolant

Experimental procedures

The test on the pressure drop was carried out for module 35 at different vapour temperature and flow rates at the condenser section.

Results

The pressure drop for each flow rate is presented in Figure 177.

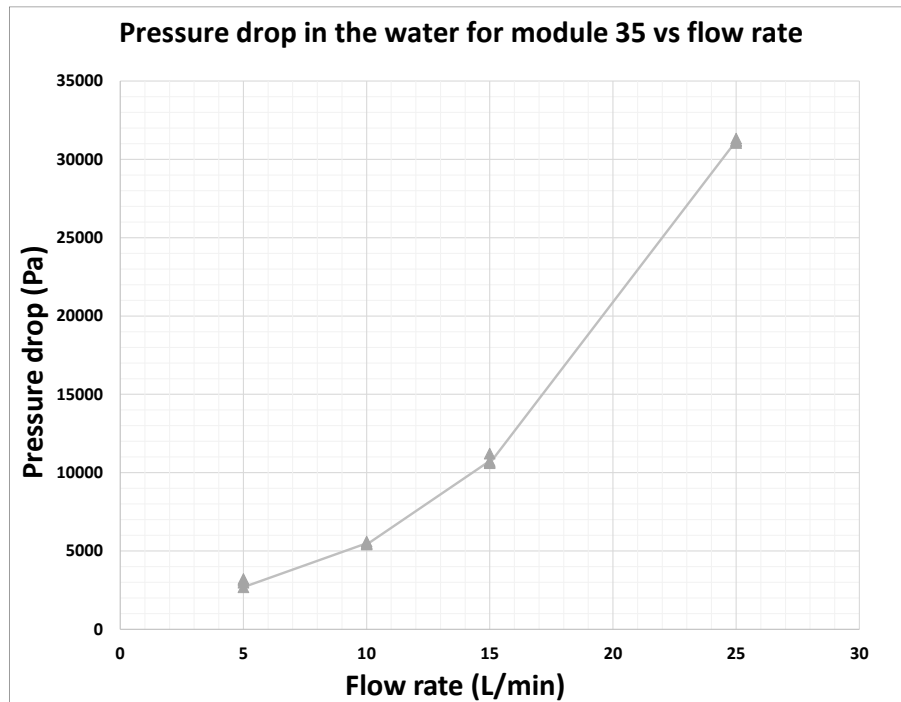


Figure 177 Pressure drop in the water for module 35 vs flow rate

It can be seen that as the flow rate increase, the pressure drop at the condenser section increase exponentially. The Reynolds number obtain is higher for higher flow rate, thus increasing the overall pressure resistance at the condenser.

Table 28 Pressure drop results for various flow rates and vapour temperature

Flow rate (L/min)	Flow rate for each pipes (L/min)	T_{heater} (°C)	T_v (°C)	Water inlet (°C)	Water outlet (°C)	Heat transfer rate (W)	Pressure drop (Pa)	Pipe diameter (m)	Velocity (m/s)	Reynolds number
5	0.56	200	37.8	14.1	15.9	620	3207	0.008	0.537	3657
		300	44.0	14.9	18.1	1108	3099			
		400	48.6	14.6	19.8	1807	2980			
		500	57.3	14.7	22.5	2732	2686			
10	1.11	200	38.2	13.9	15.0	745	5491		1.074	7314
		300	40.4	14.2	15.7	1090	5448			
		400	44.7	14.1	16.7	1793	5605			
		500	48.7	14.5	18.4	2703	5408			
15	1.67	200	35.3	13.6	14.1	520	10750		1.611	11197
		300	37.9	13.2	14.3	1120	11210			

		400	40.7	12.4	14.2	1846	10664		
		500	44.7	12.1	14.7	2713	10599		
25	2.78	200	35.4	12.4	12.7	522	31181	2.685	18662
		300	38.0	13.0	13.7	955	31330		
		400	40.3	12.7	13.8	1538	31188		
		500	43.1	12.2	13.9	2876	31046		

Table 28 shows the result for the different test carried out on the pressure drop at the condenser section. It can be seen that the pressure drop increase with the increase in the flow rate at the coolant. Also, it can be noted that for a flow rate of 5L/min, the pressure drop decreased with higher vapour temperature. For tests above 5 L/min, the vapour temperatures did not significantly change enough to impact the pressure drop.

Conclusion

The condenser section used for the module heat pipe was examined to determine the impact of the increased flow rate at the water coolant. As the system will be installed in an industrial scenario, it is important to determine the pressure drop at the condenser section to size the pumps needed to supply the condenser. It can be noted that the pressure drop occurring in the condenser are low. This is due to the design of the condenser in one passes with limited number of elbows.

It was also noted that when the temperature of the vapour is elevated, the pressure drop at the condenser section slightly decrease.

It is recommended for the full scale system to reduce the number of elbow and increase the internal diameter of the condenser tube to further reduce the pressure drops.